# UNIVERSITAT POLITÈCNICA DE VALÈNCIA

## INSTITUTO INTERUNIVERSITARIO DE INVESTIGACIÓN DE RECONOCIMIENTO MOLECULAR Y DESARROLLO TECNOLÓGICO


UNIVERSITAT POLITÈCNICA DE VALÈNCIA

# "Study, development and improvement of MCM-41-type MSN synthesis oriented to biomedical applications"

PhD. THESIS

Submitted by

**Vicente Candela Noguera**

PhD. Supervisors:

**Prof. María Dolores Marcos Martínez**

**Dra. Elena Aznar Gimeno**

València, December 2021

María Dolores Marcos Martínez, PhD in Chemistry and Professor at the Universitat Politècnica de València, and Elena Aznar Gimeno, PhD in Chemistry and lecturer at the Universitat Politècnica de València.

CERTIFY:

That the work "Study, development and improvement of MCM-41-type MSN synthesis oriented to biomedical applications" has been developed by Vicente Candela Noguera under their supervision at the Instituto Interuniversitario de Investigación de Reconocimiento Molecular y Desarrollo Tecnológico (IDM) of the Universitat Politècnica de València, as a Thesis Project in order to obtain the degree of PhD in Chemistry at the Universitat Politècnica de València.

Valencia, December 2021.

Prof. María Dolores Marcos Martínez Dra. Elena Aznar Gimeno

“Es preciso soñar, pero con la condición de creer en nuestros sueños. De examinar con atención la vida real, de confrontar nuestra observación con nuestros sueños, y de realizar escrupulosamente nuestra fantasía”. *V. Ilich Uliánov.*

**Acknowledgments**

**Agredecimientos**

Casi 6 años en el IDM dan para mucho y es imposible plasmarlo todo en un par de páginas. Después de escribir, borrar, volver a escribir y volver a borrar una introducción para esta dichosa parte de la tesis, me doy cuenta de que esto no lo tiene que revisar ningún evaluador, que no tengo por qué evitar los tópicos y que dejarse llevar tampoco está tan mal.

En primer lugar, agradecer a mis directoras de tesis Elena y Loles, así como a Ramón, la oportunidad que me brindaron en su momento para empezar esta aventura en el IDM, abrirme un hueco en el laboratorio y posibilitarme la obtención de becas y contratos que me permitieron desarrollar esta aventura.

Quería mostrar un especial agradecimiento a Andrea y María. Haciendo de mis hermanas mayores, mis confidentes y mis muletas. Ellas son las grandes responsables de que no tirara la toalla en los momentos más difíciles de la tesis. Si una tesis es resultado de un trabajo colectivo, ellas han sido mis enfermeras y capataces. Gracias de corazón.

Gracias también a Pedro Amorós y Mar Orzáez, que en diferentes ocasiones me han echado una mano ya sea en el mundo de los materiales, o en el mundo de la biología molecular y las células.

No sé si será posible nombrar a todas las personas que han pasado por este grupo desde 2015 a 2021, y es que será probablemente un listado que supere las 50 personas. En cualquier caso, aquellos con los que he compartido algo y han estado ahí saben perfectamente que me los llevo en una porción de mi memoria y mi corazón.

Y es que han pasado muchas personas desde que estábamos sólo en el Departamento de Química y la CPI, a expandirnos por el laboratorio 1.2, la Fe y el CIPF. Aquellas personas que estaban ya en el laboratorio cuando yo llegué: Lorena, Àngela, Luis Pla, Bea Lozano, Lluís Pascual, Alba, Irene, Amelia, Cris T, Cris Marín, Cris G., Sameh, Edgar, María, Mar, Carol, Marta, Mónica, Adrián, Elisa, Toni, Santi, Mari Carmen, Carmen… Los que llegaron una vez estaba yo: Hazem, Ismael, Marcia, Àngels, Pablo, Eva, Bea de Luis, Paula, Angy, Tania, Andy, Serena, Gonçalo, Andrea Escudero, Borja, Elena Lucena, Alejandra, Araceli, Iris, Gema, Blanca, JuanFran, etc.

Siempre recordaré el decálogo de Toni, que a muchos nos guio como un buen *mister* en este mundo de la investigación; las conversaciones científicas con Luis V, que él sabe que me fueron muy útiles; las frases de la campana (o de la *campeing*), las cervezas después del labo y los planes en el Clandestí (y las decepciones del Chico Ostra), la bandera de Moderdonia que no quemamos, los *brownies* que volaban por el laboratorio, las carreras en la UPV, ununpentio saliendo del humo del hielo seco, y un largo etcétera que nos hizo hacer del laboratorio un lugar más humano.

Quería hacer también una mención especial a mis “parejas bio” del labo, a Iris y Gema. Podría decir mil cosas de vosotras, pero se puede resumir en: sois las mejores. También a Eva, que me ha soportado como compi de bancada durante mis últimos años, que se ha comido tantos *brownies* y que ha mantenido a flote el “Eva’s Lab”. Y finalmente a Borja, por su ayuda necesaria y las risas que trajo al laboratorio.

No quería olvidarme de agradecer a Eduardo la oportunidad que me dio en su laboratorio en Dublín durante mi estancia. Para mí esa estancia significó mucho, a nivel personal, pero también a nivel profesional y aún la recuerdo con orgullo. Fue un punto de inflexión para darme cuenta

de lo que sabía hacer, de lo que había aprendido y lo que podía aportar a los demás. Un saludo para Sara y Luiza, que fueron unas estupendas anfitrionas allí.

A mi familia, mis padres y mis hermanas, que me han dado las condiciones para poder llegar hasta aquí con el esfuerzo de toda una vida y han sido mi ejemplo a seguir en muchos aspectos. A Celia, gràcies per ser el meu recolzament i guia els 3 últims anys.

Pensé que este momento nunca iba a llegar y el peso que se libera cuando veo que llego al final es muy difícil de describir. Los dos últimos años han sido frenéticos y me han dejado agotado, física y mentalmente. Escribir la tesis durante el confinamiento ha hecho que la experiencia sea más intensa si cabe, y parecía una rutina que no iba a acabar. Pero ello no quita el orgullo de haber sacado esto adelante.

En definitiva, me llevo un poquito de todos vosotros. Espero que yo también os deje algo de mí. Sin duda, una de las cosas que han hecho todo esto valga la pena es vuestra compañía.

A esas personas que estáis empezando o estáis a mitad, decir que el camino es duro, tiene muchas piedras y muchos agujeros. Tirar para adelante a veces no se ve como una opción. Pero sí se puede. Hay que coger la tesis por los cuernos, hay que meter las manos en el barro. Lo que tenéis que aprender es que vuestra tesis depende al final de vosotros y vosotras. Depende de la garra que le pongáis. Apoyaros de vuestros compañeros, que siempre van a estar ahí, mirad en perspectiva y tirad para adelante.

## Abstract

The present PhD thesis, entitled "Study, development and improvement of MCM-41-type mesoporous silica nanoparticles (MSN) synthesis oriented to biomedical applications" is focused on the synthesis, characterisation, study and evaluation of different MCM-41-type MSN samples to improve the knowledge of MSN as nanomaterials involved in biomedical applications.

The first chapter of this work is a general introduction about the items that are going to be treated throughout the thesis. On the one hand, the main concepts about the mesoporous silica nanoparticles, and in particular MCM-41-type MSN, are introduced, such as their discovery, their properties, advantages, and applications, their synthesis and the chemistry involved, and the possibility of being functionalised or doped to acquire additional and unique properties. On the other hand, a wide range of MSN characterisation techniques are presented highlighting their importance in the current thesis. Finally, the concepts of nanomedicine and nanomaterials are reviewed, including the set of requirements the nanomaterials must accomplish to be validated, the types of nanomaterials developed thus far, and the main bottlenecks found in clinical translation of nanomaterials. In this context, the studies of MSN in nanomedicine are reviewed, illustrating the challenges of MSN within the nanomedicine and the opportunity their offer to material science.

Second chapter exposes the general objectives of present PhD thesis, which are addressed in the following chapters.

Third chapter is based on an in-depth study of the synthesis mechanism of MCM-41-type MSN, considering the silica templating mechanism, the nucleation, the growth and the aging processes. Particularly, the early stages of the MSNs synthesis are substantially analysed. In addition, the different models reported about the silica templating mechanism, which are widely studied, are reviewed.

Fourth chapter is focused on the investigation of the effect of some disregarded parameters on the synthesis and formation of MCM-41-type MSN, such as synthesis time, stirring rate, the magnetic stir bar used, TEOS addition rate and the neutralisation method once nanoparticles are formed. A review of the influence of the most studied synthesis parameters on MCM-41-type MSN is also introduced.

Fifth chapter is based on the study of the obtaining, characterisation and manipulation of colloidal MCM-41-type MSN. First, a critical review of works that report the obtaining of colloidal, well-suspended or discrete MSN is presented. Second, a methodology to characterise the colloidal stability of MSN is introduced. Third, the colloidal behaviour of several nanoparticles under different conditions is studied and compared. And finally, a conceptual and operational framework about the principles governing the colloidal stability of nanoparticles is developed.

Sixth chapter is a comprehensive study of the implications of the use of different surfactant removal procedures on standard MCM-41-type MSN, such as calcination at different temperatures and solvent extraction. The physicochemical properties of MSN studied are the surfactant removal efficiency, the silica condensation degree, the mesostructured framework, the colloidal stability and the surface reactivity. Additionally, the biocompatibility of nanoparticles was tested regarding their cytotoxicity and their degradation in a simulated physiological environment, to validate their use in biomedical applications.

Finally, seventh chapter gathers the general conclusions of the current thesis, which summarise the conclusions obtained in each chapter, but also provide new perspectives and the big picture of the studied matter.

**Resumen**

La presente tesis doctoral, titulada "Estudio, desarrollo y mejora de la síntesis de nanopartículas mesoporosas de sílice (MSN) tipo MCM-41 orientada a aplicaciones biomédicas" se centra en la síntesis, caracterización, estudio y evaluación de diferentes MSN tipo MCM-41, con el objetivo de ampliar el conocimiento de las MSN como nanomateriales implicados en aplicaciones biomédicas.

El primer capítulo de este trabajo es una introducción general sobre los temas que se van a tratar a lo largo de la tesis. Por un lado, se introducen los principales conceptos sobre las nanopartículas de sílice mesoporosas, y en particular las MSN de tipo MCM-41, como su descubrimiento, sus propiedades, ventajas y aplicaciones, su síntesis y la química implicada, y la posibilidad de ser funcionalizadas o dopadas para adquirir propiedades adicionales y únicas. Por otro lado, se presenta un amplio abanico de técnicas de caracterización de MSN, destacando su importancia en la presente tesis. Por último, se revisan los conceptos de nanomedicina y nanomateriales, incluyendo el conjunto de requisitos que deben cumplir los nanomateriales para ser validados, los tipos de nanomateriales desarrollados hasta el momento y los principales cuellos de botella encontrados en la traslación clínica de los nanomateriales. En este contexto, se revisan los estudios de las MSN en nanomedicina, señalando los retos de las mismas dentro de esta especialidad y la oportunidad que ofrecen a la ciencia de los materiales.

En el segundo capítulo se exponen los objetivos generales de la presente tesis doctoral, que son abordados en los siguientes capítulos.

El tercer capítulo se basa en un estudio en profundidad del mecanismo de síntesis de las MSN de tipo MCM-41, considerando el mecanismo de estructuración de la sílice, la nucleación, el crecimiento y los procesos de envejecimiento. En particular, se analizan detalladamente las primeras etapas de la síntesis de MSN. Además, se revisan los diferentes modelos descritos sobre el mecanismo de estructuración de la sílice, que han sido ampliamente estudiados.

El cuarto capítulo se centra en la investigación del efecto de algunos parámetros tradicionalmente poco estudiados en la síntesis y formación de MSN de tipo MCM-41, como el tiempo de síntesis, la velocidad de agitación, el núcleo de agitación magnética utilizado, la velocidad de adición del TEOS y el método de neutralización una vez formadas las nanopartículas. También se introduce una revisión de la influencia de los parámetros de síntesis más estudiados en las MSN tipo MCM-41.

El quinto capítulo se basa en el estudio de la obtención, caracterización y manipulación de MSN de tipo MCM-41 coloidales. En primer lugar, se presenta una revisión crítica de los trabajos que informan sobre la obtención de MSN coloidales, correctamente suspendidas o discretas. En segundo lugar, se introduce una metodología para caracterizar la estabilidad coloidal de las MSN. En tercer lugar, se estudia y compara el comportamiento coloidal de diferentes nanopartículas en diferentes condiciones. Y, por

último, se desarrolla un marco conceptual y de trabajo sobre los principios que rigen la estabilidad coloidal de las nanopartículas.

El sexto capítulo es un estudio exhaustivo de las implicaciones del uso de diferentes procedimientos de eliminación de surfactantes en las MSN de tipo MCM-41, como la calcinación a diferentes temperaturas y la extracción con disolventes. Las propiedades fisicoquímicas de las MSN estudiadas son la eficiencia de eliminación de surfactantes, el grado de condensación de la sílice, la porosidad, la estabilidad coloidal y la reactividad superficial. Además, se comprobó la biocompatibilidad de las nanopartículas en cuanto a su citotoxicidad y su degradación en un entorno fisiológico simulado, para validar su uso en aplicaciones biomédicas.

El séptimo capítulo recoge las conclusiones generales de la presente tesis, que resumen las conclusiones obtenidas en cada capítulo, pero también aportan nuevas perspectivas y la visión global del tema estudiado.

**Resum**

L'actual tesi doctoral, titulada "Estudi, desenvolupament i millora de la síntesi de nanopartícules mesoporoses de sílice (MSN) de tipus MCM-41 orientada cap a aplicacions biomèdiques" se centra en la síntesi, caracterització, estudi i avaluació de diferents mostres de MSN de tipus MCM-41 amb l'objectiu de millorar el coneixement de les MSN com nanomaterials implicats en aplicacions biomèdiques.

El primer capítol d'aquest treball és una introducció general sobre els elements que es tractaran durant tota la tesi. D'una banda, s'introdueixen els conceptes principals sobre les nanopartícules mesoporoses de sílice, i en particular les de tipus MCM-41, com el seu descobriment, les seues propietats, avantatges i aplicacions, la seua síntesi i la química implicada, i la possibilitat de ser funcionalitzades o dopades per adquirir propietats addicionals i úniques. D'altra banda, es presenta una àmplia gamma de tècniques de caracterització de MSN destacant la seua importància en la tesi actual. Finalment, es revisen els conceptes de nanomedicina i nanomaterials, incloent-hi el conjunt de requisits que els nanomaterials han d'aconseguir per ser validats, els tipus de nanomaterials desenvolupats fins ara, i els principals colls d'ampolla trobats en la translació clínica de nanomaterials. En aquest context, es revisen els estudis de les MSN en nanomedicina, assenyalant els seus reptes dins de la nanomedicina i l'oportunitat que ofereixen a la ciència dels materials.

El segon capítol exposa els objectius generals de la tesi doctoral actual, que són abordats en els següents capítols.

El tercer capítol es basa en un estudi en profunditat del mecanisme de síntesi de les MSN tipus MCM-41, considerant el mecanisme d'estructuració de la sílice, la nucleació, el creixement i els processos de maduració. Particularment, les primeres etapes de la síntesi de MSNs s'analitzen en detall. A més, es revisen els diferents models reportats sobre el mecanisme d'estructuració de sílice, que ja han sigut àmpliament estudiats.

El quart capítol es centra en la investigació de l'efecte d'alguns paràmetres tradicionalment menys estudiats en la síntesi i formació de l'MSN de tipus MCM-41, com: el temps de síntesi, la velocitat d'agitació, el nucli d'agitació magnètica utilitzat, la velocitat d'addició de TEOS i el mètode de neutralització una vegada que es formen les nanopartícules. També s'introdueix una revisió de la influència dels paràmetres de síntesi més estudiats en les MSN de tipus MCM-41.

El cinqué capítol es basa en l'estudi de l'obtenció, caracterització i manipulació de les MSN de tipus MCM-41 col·loidals. En primer lloc, es presenta una revisió crítica dels treballs que descriuen l'obtenció de MSN col·loidals, correctament suspeses o discretes. En segon lloc, s'introdueix una metodologia per caracteritzar l'estabilitat col·loidal de les MSN. En tercer lloc, s'estudia i compara el comportament col·loidal de diverses nanopartícules en diferents condicions. I finalment, es desenvolupa un marc conceptual i de treball sobre els principis que regeixen l'estabilitat col·loidal de les nanopartícules.

El sisé capítol és un estudi exhaustiu de les implicacions de l'ús de diferents procediments d'extracció de surfactants a les MSN de tipus MCM-41, com la calcinació a diferents temperatures i l'extracció de dissolvents. Les propietats fisicoquímiques de les MSN estudiades són l'eficiència d'extracció de surfactant, el grau de condensació de sílice, la mesoporositat, l'estabilitat col·loidal i la reactivitat de la superfície. A més, la biocompatibilitat de les nanopartícules es va provar pel que fa a la seua citotoxicitat i la seua degradació en un entorn fisiològic simulat, per validar el seu ús en aplicacions biomèdiques.

El seté capítol recull les conclusions generals de la tesi actual, que resumeix les conclusions obtingudes en cada capítol, però també proporciona noves perspectives i una visió global de la matèria estudiada.

## Abbreviations and Acronyms

| | |
|---|---|
| **ABC** | accelerated blood clearance |
| **ACN** | acetonitrile |
| **ADC** | antibody-drugs conjugated |
| **AgNPs** | silver nanoparticles |
| **APTES** | 3-aminopropyltriethoxysilane |
| **AuNPs** | gold nanoparticles |
| **BBB** | blood–brain barrier |
| **BET** | Brunauer-Emmet-Teller |
| **BJH** | Barrett-Joyner-Halenda |
| **BSA** | bovine serum albumin |
| **CARPA** | complement activation–related pseudoallergy |
| **CMC** | critical micelle concentration |
| **ChMC** | Chemistry, Manufacturing, and Controls |
| **CTAB** | cetyltrimethylammonium bromide |
| **CTAC** | cetyltrimethylammonium chloride |
| **CTATos** | cetyltrimethylammonium p-toluenesulfonate |
| **CQA** | Critical Quality Attributes |
| **DLS** | dynamic light scattering |
| **DEA** | diethanolamine |
| **DFT** | density functional theory |
| **DK** | degree of condensation |
| **DMEM** | Dulbecco's Modified Eagle Medium |
| **DMSO** | dimethyl sulfoxide |
| **DNA** | deoxyribonucleic acid |
| **DTA** | differential thermogravimetric analysis |
| **EA** | elemental analysis |
| **EDX** | energy-dispersive X-ray spectroscopy |
| **ELS** | electrophoretic light scattering |
| **EMA** | European Medicines Agency |
| **EPR** | enhanced permeation and retention |
| **EtOH** | ethanol |
| **FBS** | fetal bovine serum |
| **FDA** | Food and Drug Administration |
| **FTIR** | Fourier-transform infrared spectroscopy |
| **FWHM** | full width at half maximum |
| **GSH** | glutathione reduced |
| **HDLs** | high-density lipoproteins |
| **HPLC-UV** | high-performance liquid chromatography–ultraviolet |
| **HPLC-MS** | high-performance liquid chromatography–mass spectrometry |
| **IONP** | iron oxide nanoparticles |
| **IPTES** | (3-isocyanatopropyl)triethoxysilane |
| **IUPAC** | International Union of Pure and Applied Chemistry |
| **KIT-6** | ordered mesoporous $SiO_2$ |
| **LCT** | liquid crystal templating |

| | |
|---|---|
| **LDLs** | low-density lipoproteins |
| **MCM-41** | Mobile crystalline material 41 |
| **MCM-48** | Mobile crystalline material 48 |
| **MCM-50** | Mobile crystalline material 50 |
| **MPS** | mononuclear phagocyte system |
| **γ-MPS** | 3-(methacryloxy)propyl trimethoxy silane |
| **MPTMS** | 3-mercaptopropyl trimethoxy silane |
| **MSN** | mesoporous silica nanoparticles |
| **MRI** | magnetic resonance imaging |
| **NLDFT** | nonlocal density functional theory |
| **NMR** | nuclear magnetic resonance |
| **NPs** | nanoparticles |
| **NTA** | nanoparticle tracking analysis |
| **PBS** | phosphate-buffered saline |
| **PDI** | polydispersion index |
| **PEG** | polyethylene glycol |
| **PCL** | poly(caprolactone) |
| **PEI** | polyethyleneimine |
| **PLA** | polylactic acid |
| **PLGA** | poly(lactic-co-glycolic acid) |
| **PSD** | particle size distribution |
| **PTFE** | polytetrafluoroethylene |
| **PXRD** | powder X-ray diffraction |
| **QDs** | quantum dots |
| **RCF** | relative centrifugal force |
| **RES** | reticuloendothelial system |
| **RNA** | ribonucleic acid |
| **ROS** | reactive oxygen species |
| **SANS** | small-angle neutron scattering |
| **SAS** | small-angle scattering |
| **SAXS** | small-angle X-ray scattering |
| **SBA-15** | Santa Barbara Amorphous-15 |
| **SBF** | simulated buffer fluid |
| **SEDDSs** | self-emulsifying drug delivery systems |
| **SEM** | scanning electron microscopy |
| **siRNA** | small interfering RNA |
| **SPION** | superparamagnetic iron oxide nanocrystals |
| **ssNMR** | solid–state nuclear magnetic resonance |
| **TEA** | triethanolamine |
| **TEM** | transmission electron microscopy |
| **TBOS** | tetrabutyl orthosilicate |
| **TGA** | thermogravimetric analysis |
| **TPAB** | tetrapropylammonium bromide |
| **TEOS** | tetraethyl orthosilicate |
| **TMOS** | tetramethyl orthosilicate |
| **TPOS** | tetrapropyl orthosilicate |

| | |
|---|---|
| **UV** | ultraviolet |
| **UV-Vis** | ultraviolet-visible |
| **VLP** | virus-like particles |

**Table of contents**

# CHAPTER 1: GENERAL INTRODUCTION

# 1. MESOPOROUS SILICA NANOPARTICLES AND NANOMEDICINE

## 1.1 MESOPOROUS SILICA NANOPARTICLES

Mesoporous silica nanoparticles (**MSN**), within the mesoporous materials, have been highly attractive since **their discovery** in the earlies 2000 thanks to the studies carried out by Lu et al. in 1999 [1], Cai et al. in 2001 [2], Fowler et al. in 2001 [3], Nooney et al. in 2002 [4] and Suzuki et al. in 2004 [5], among others. Their **unique characteristics** have made them highly employed for a wide range of uses. Their properties come from the combination of several concepts, such as silica composition, mesoporosity and nanoscale field [6].

On the one hand, the synthesis of **silica composed** nanoparticles is very simple, low cost, environmentally friendly and quick [7]. Furthermore, simple modifications in the synthesis allow the obtaining of tuneable particle size and shape. The manipulation of silica nanoparticles is based on simple chemistry reaction steps, as well as their easy functionalisation with alkoxysilanes [8]. Besides, the materials obtained have high transparency, inertness and thermal stability[9][10]. On the other hand, the presence of **mesopores** contribute to the obtaining of high surface area and pore volume capacity. Mesopore size can be variable, according to IUPAC from 2 to 50 nm [11] (Fig. 1A) and it can be tailored using different long chain surfactants or swelling agents. This is one of the main differences between mesoporous materials and zeolites, which are composed of micropores templated by small organic molecules [7]. Mesoporous structure can follow either ordered or disordered arrangement [12]. Finally, what concerns to **nanoscopic scale**, in the order to 100 nm (Fig. 1B), it provides some unique electronic, magnetic, optical, mechanical, and chemical features [11]. For example, nanoscale maximises the surface/volume ratio, offers the ability to develop Mie scattering with UV-Visible light [13] and this is also related to quantum confinement effects when nanoparticles are doped with semiconductor elements [14]. Furthermore, nanosized features open their use in fields like the biomedical, nanotechnology and nanoengineering ones [15].

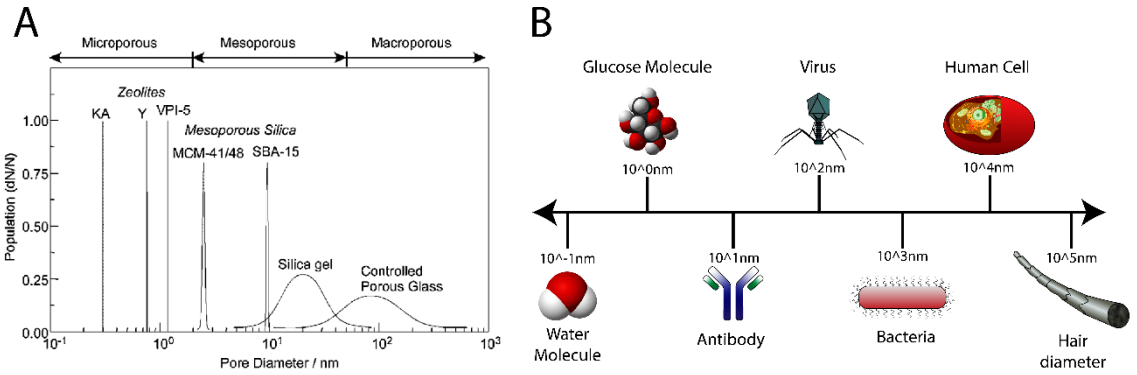


*Figure 1. A) Classification of porous materials into microporous, mesoporous, and macroporous materials according to their pore diameters. Reprinted from reference* [16]*. Copyright © 2012 Chemical Society of Japan. B) Biological and chemical elements on a scale from 0.1 nm to 1 mm. Adapted from reference* [17]*. Copyright © 2017 MDPI.*

Thanks to these characteristics a wide range of **applications** has been developed. Some examples of their varied applications described in the literature are sensing [18], catalysis [19][20], selective adsorption [21][22], gas storage [23] and controlled release systems [24].

Starting from this point, it was developed a wide set of different nanoparticle types. One of the most used and studied nanoparticles are **MCM-41 type MSN.** This type of sieve was **launched** by Mobil Oil Corporation scientists for the first time in 1992 as large particles [25][26]. In 1997 and 1999, Grun et al. got MCM-41 type submicrometer-size spheres ca. 0.5 µm [27][28], but it was not until 2001 when Cai et al. [2] and Fowler et al. [3] published practically in parallel the obtaining of MCM-41 type nanoparticles around 100 nm. MCM-41 materials are the most investigated within the **M41S family** materials because the other members in this family are either thermally unstable or difficult to obtain. As we can see in Figure 2, within M41S family there are different pore geometries: MCM-41 (hexagonal phase) MCM-48 (cubic phase) or MCM-50 (lamellar phase)[29][11]. MCM-41 materials can have a pore diameter between 1.5 and 10 nm and, depending on the surfactant used, a relative surface area around 1000 $m^2/g$ and a pore volume in the order 1 $cm^3\ g^{-1}$. Besides, this geometry gives a narrow pore size distribution and an ordered porous structure.

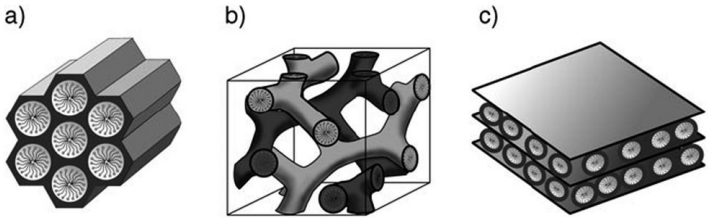


*Figure 2. M41S family materials (a) MCM-41, (b) MCM-48 and (c) MCM-50. Reprinted from reference* [30]. *Copyright © 2014 Royal Society of Chemistry.*

Specifically, these nanomaterials are extensively used for **biomedical applications**, due to their biocompatibility, inertness and high uptake capability in vitro and in vivo, [9], in addition to the characteristics already mentioned. MSN have been used in drug [31][32], gene [10][33] and RNA [34][35] delivery, bioimaging [36][37], theragnostic [38] and tissue engineering [39][40]. In recent years, there has been a rise in *in vitro* and *in vivo* studies with MCM-41-type MSN, whose properties make them especially interesting in controlled release systems.

## 1.2. SYNTHESIS OF MSN

### 1.2.1. MSN synthesis

Since MSN discovery, a plenty of **different synthesis methods** has been developed. Principally, MSN can be prepared via four approaches [41]: template-directed method, sol-gel method, chemical etching technique, and microwave assisted technique. Nevertheless, template-directed method is the most used over the last years and the one that is going to be developed throughout the document.

Generally, in order to prepare MSN via templated method the use of four components is required, such as solvent, silica precursor, surfactant and catalyser.

On the one hand, the **solvent** used can be water or a mixture of water and ethanol. The presence of ethanol causes a decrease in the hydrolysis rate of the silica precursor [42]. For this reason, the use of ethanol produces an increase in the nanoparticles size with a narrow distribution and the formation of accurately smooth spherical and monodisperse nanoparticles [43][44][45][46][47][48][49]. Besides, there is a mesophase transformation from hexagonal to

cubic and lamellar phase which can drive to radial porous arrangement [43][44]. Both processes were described by Stöber and his method is one of the first standardised procedure that used ethanol to synthesise mesoporous silica particles [50].

On the other hand, the **silica precursor** used is normally a tetraalkoxysilane. There are different types of tetraalkoxysilanes, such as tetrabutyl orthosilicate (TBOS), tetrapropyl orthosilicate (TPOS), tetraethyl orthosilicate (TEOS) or tetramethyl orthosilicate (TMOS), which have increasing hydrolysis rate, affecting the nanoparticles size and the number of nucleation sites [51][52][53][54] (Figure 3). In addition, other sources of silica as sodium silicate solution or hydrophilic fumed silica, which forms silicate double-four-ring [55], can be used as silica precursor.

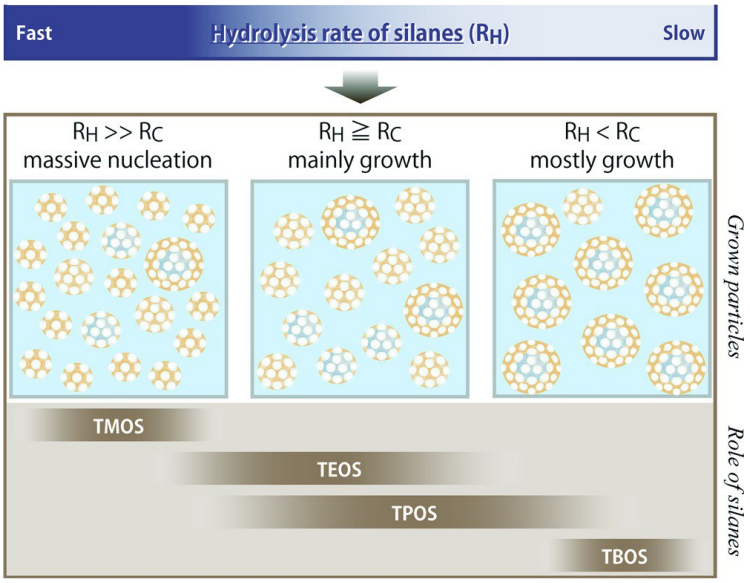


*Figure 3. Hydrolysis rate variation of different types of tetraalkoxysilanes. Reprinted from reference* [52]. *Copyright © 2015 Wiley Online Library.*

Regarding the **surfactant** used, it can be classified into neutral, anionic and cationic. Neutral surfactants usually are triblock copolymers such as Pluronic [56][57] or detergents as Brij [58][59], Triton X-100 [60] or Tween [61]. Normally, they are formed by a hydrophilic part (polyethylene and other polar groups) and alkylic chains in the hydrophobic part. Cationic surfactants are usually formed by a quaternary ammonium salts as cetyltrimethylammonium bromide (CTAB) [62][63], chloride (CTAC) [64][65] or p-toluenesulfonate (CTATOS) [66][67], or tetrapropylammonium bromide (TPAB) [68]. Anionic surfactants generally are formed by a sulfonic, carboxylate or phosphate hydrophobic head as N-lauroylsarcosine sodium [69]. The charge of surfactant employed depends on the pH the reaction is performed, which determines the silica source charge.

Surfactants are used as a template agent to form the mesoporous structure, since they form supramolecular structures as micelles above certain concentration, which is also known as critical micelle concentration (CMC). The use of surfactants with different hydrophilic head size or hydrophobic tail length, even the use of higher or lower concentrations of surfactant, drive to a specific mesostructured arrangement and pore shape and size [42]. In this context, the different members of M41S family are obtained by employing increasing amounts of CTAB as surfactant and temperature, such as Figure 4 shows.

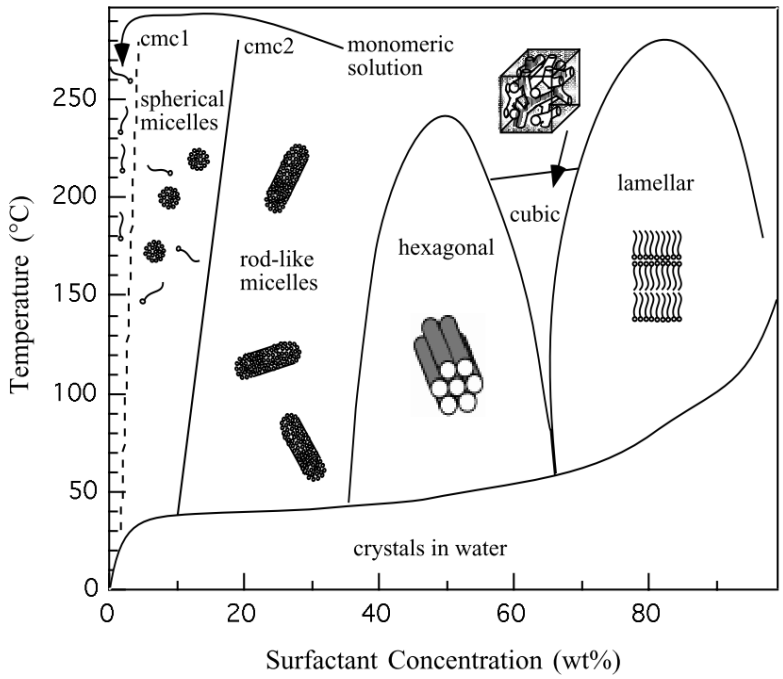


*Figure 4. Phase diagram and schematics of the corresponding surfactant liquid crystal phases of the surfactant CTAB in water.* Reprinted from reference [70]. *Copyright © 1996 American Chemical Society.*

In addition, some synthesis have been reported without the use of a surfactant as a template, but using other organic compounds as sugars [71], urea [72] or β-cyclodextrin [73] acting as structure directing agents.

Finally, acidic or alkaline conditions can also be used as **catalyser** agent. In case of alkaline conditions, the compounds most often used are sodium hydroxide (NaOH) [2][3][4][74], ammonia ($NH_3$) [62][50], triethanolamine (TEA) [75][76][77][78], and diethanolamine (DEA) [75][79]. Each of them has a different basic strength so they affect differently to hydrolysis and condensation rate. In case of acidic condition, hydrochloric acid (HCl) [69][80][81] is the most often used catalyser.

### 1.2.2. MCM-41-type MSN synthesis

Nevertheless, synthesis of MCM-41 nanoparticles is quite specific. As it is mentioned above, first synthesis of MCM-41 type MSN was reported by Cai et al. [2] and Fowler et al. [3] in 2001.

In the synthesis developed by Cai, distilled water was used as solvent, TEOS as a silica precursor, CTAB as surfactant and NaOH as alkaline catalyst. The molar ratio of the reagents added were 1197 $H_2O$ : 0.31 NaOH : 0.125 CTAB : 1 TEOS. The reaction was performed at 80°C, stirring for 2 hours. Then, the resulting product was filtered and washed with distilled water and dried at room temperature.

On the other hand, the method developed in parallel by Fowler and co-workers employed similar molar ratios of the same reagents but at lower dilutions in a first step (130 $H_2O$ : 0.5 NaOH : 0.12 CTAB : 1 TEOS). In a second step, the reaction was quenched after 40 s of the TEOS addition by diluting it (adding 918.5 moles of $H_2O$) obtaining a composition similar to previous

work. After that, the mixture was neutralised with HCl at 60 s and 220 s. Then, solid samples were obtained by evaporation of the water in air for 24 h.

Practically all reported studies that synthesise MCM-41 type MSN are based on the method reported by Cai. However, over the time other reported works have introduced some modifications to the general synthesis to modulate some features of the materials [4][76][77][84][85][86].

### 1.2.3. Reaction chemistry

The synthesis of MCM-41 type MSN uses tetraethyl orthosilicate (TEOS) as the silica precursor. The polymerisation of silica is based on the formation of siloxane bonds (Si – O – Si), which is divided in two steps: hydrolysis and condensation [78][79], as it is show in Scheme 1.

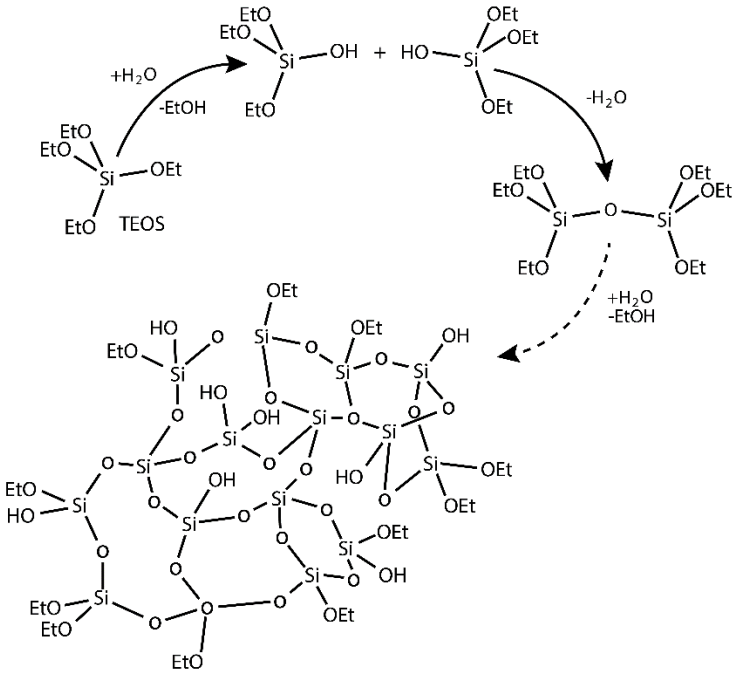


*Scheme 1. Hydrolysis and condensation reactions in silica polymerisation process.*

The hydrolysis reaction means the replacement of an ethoxide group by a hydroxyl group, leading to the generation of a silanol group (Si – OH), as follows:

$$Si(OEt)_4 + H_2O \longrightarrow Si(OEt)_3OH + EtOH \quad (1)$$

As it can be seen in the equation 1, an ethanol or ethoxide molecule is produced each time the reaction takes place. The hydrolysis is catalysed under acid or basic conditions, having a low rate at neutral pH. However, the synthesis of MCM-41 type MSN is mostly performed using basic conditions conferred by NaOH or $NH_4OH$. The mechanism of hydrolysis is influenced on the water-alkoxide ratio and the solvent used, since this ratio modifies the silica precursor solubility [89]. At high pH the number of hydroxide ions ($OH^-$) increases in aqueous solution, acting like stronger nucleophiles than water molecules do.

The condensation step refers to bond formation among silanol groups to form a siloxane bond:

$$R_3SiOH + OHSiR_3 \longrightarrow R_3SiOSiR_3 + H_2O \quad (2)$$

In this case, the reaction rate is favoured when the silicates acquire negatively charge, meaning the silanol groups are deprotonated becoming in silanolate group (Si – $O^-$). The reason behind this is the nucleophilic strength of the negatively charged oxygen in silanolate is much bigger than the negative partial charge of oxygen in silanol. As Figure 5 shows, below the isoelectric point of silica (IEP = 2.0), silica species are positively charged, and the condensation rate is very low. On the contrary, above silica's IEP, the silica species are deprotonating progressively, and the condensation rate increases until slightly alkaline conditions (pH 7.5). It is reported that over pH 7.5 polymerised silicates become unstable, that is why from pH 7.5 the condensation rate starts to decrease. Nevertheless, in the template-directed method MSN synthesis the surfactant–silicate composites can exist in a stable form until higher pH (even around 12), in spite of silicate dissolving, due to strong interactions between silicates and cationic surfactants [90]. Therefore, relatively high condensation rates can be found at alkaline pH in the synthesis of mesoporous materials.

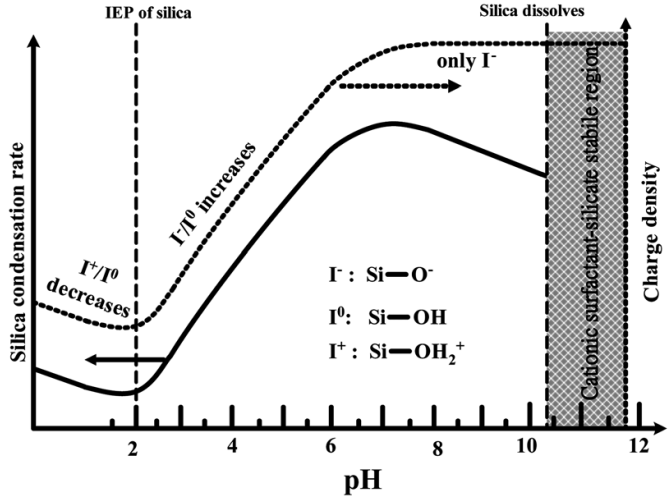


*Figure 5. Diagram of silica condensation rate and charge density of its species at different pH. Reprinted from reference* [90]. *Copyright © 2013 Royal Society of Chemistry.*

There are small pH changes during these processes. pH decreases when hydrolysis takes place, since there is a consumption of OH- groups, which promotes the condensation of silica species. On the contrary, during the condensation reaction OH- groups are formed again, and then pH tends to slightly increase [4][91].

### 1.2.4. Surfactant removal

Once the nanoparticles are prepared, surfactant must be removed to obtain empty pores (Scheme 2). In addition, the presence of surfactant in the nanoparticles is toxic for biomedical applications [92]. The most often used approaches to eliminate the surfactant are calcination and extraction.

**Calcination** is based on burning out the template in an oxygenated and dried atmosphere usually at 550 °C. This method is able to remove totality the surfactant [93]. However, after calcination,

material suffers a significant shrinkage due to reorganisation and condensation of some silanols [94].

**Extraction** method consists of removing the surfactant by washing the nanoparticles in a determined solution. These solutions must be able to weaken the bonds between silica surface and surfactant, and then exchange the surfactant by a cation. HCl/ethanol or methanol solutions have been used very often for this purpose [95][96] but it is also common the use of ammonium nitrate [97]. The extraction can be performed in a round bottom flask under reflux or in a Soxhlet extractor. Extraction causes less shrinkage in the lattice than calcination, since it is less common the silanol condensation without strong heating [90]. Nevertheless, some template can remain in the structure using this method [93] and several extraction cycles should be usually performed.

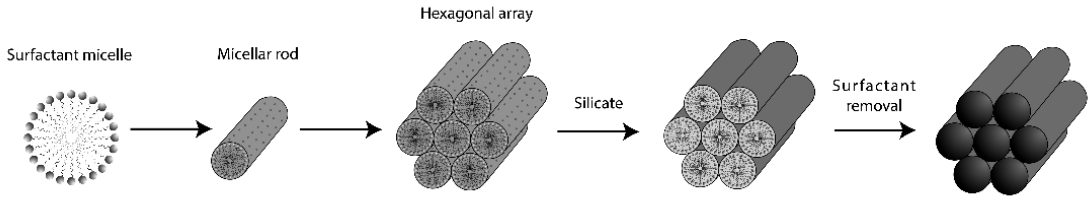


*Scheme 2. The surfactant removal must be done after the silica is templated, as the pores must be emptied. Reprinted from reference* [98]. *Copyright © 2013 Elsevier.*

## 1.3. FUNCTIONALISATION

Most of the named MSN applications, such as controlled drug delivery, sensor technology, catalysis, imaging, and chemisorption,[99][100] require the covalent incorporation of organic compounds (functionalisation) onto their surface. This functionalisation of MSN forms a family of hybrids (organic-inorganic) materials, in which the properties of the organic moiety are as important as the one of the inorganic mesoporous scaffold.

### 1.3.1. Functionalisation chemistry

The chemistry of the silica materials has been well studied over the past century. In spite of the inertness of the silica materials, they are easily functionalised either due to the presence of silanol groups in their surface or through the addition of organic reagents during the silica hydrolysis-condensation process. The reagents most often used for silica functionalisation are organo-trialkoxysilane compounds, i.e., a silicon atom attached to three alkoxy groups and a fourth specific functional group through a Si-C bond. It can be also used other structures less common, like organo-dialkoxysilanes, together with they are generally known as organosilanes [101]. Besides, other types of silanes can be used to functionalise the silica materials, such as Si-Cl, Si-$NR_2$ or Si-NH-Si groups.

The reaction that takes place is an attack of silanol groups of the silica precursor to the silicon atom of the reagent, with the formation of a siloxane bond and the elimination of an (3)

alkoxy group of the reagent, which acts as a leaving group (Equation 3). This reaction is favoured in alkaline conditions because of the stronger nucleophilicity of silanolate group compared to silanol one. Besides, the ability to get out from the attacking molecule of the leaving group also influences the substitution rate. In case of alkoxy groups, this ability is related to its length, since the longer the group, the higher the steric repulsion to form the pentavalent transition states and, then, the slower the substitution rate [88].

$$R_3SiOH + Si(OEt)_3R \longrightarrow R_3SiOSi(OEt)_2R + EtOH$$

The amount of functional groups that can be attached to MSN after functionalisation process varies from 0.1 to 3 mmol $g^{-1}$ of MSN. The concentration of silanol groups can be around 5 mmol $g^{-1}$ for an MSN, which corresponds with around 3 groups per $nm^2$ of surface [102].

### 1.3.2. Methods

MSN can be functionalised either on the external, the internal surface (within the pores) or inside the silica structure. For that purpose, several methods for functionalizing have been developed, being the most common ones co-condensation and grafting methods.

#### 1.3.2.1. Grafting

Grafting, or post-synthesis, method consists on performing the functionalisation after nanoparticles formation (Scheme 3). The specific reaction undertaken is called silylation, and proceeds through the silanol groups on the nanoparticles surface that act as anchoring points for the organosilane reactants. For this reason, the organic groups tend to incorporate in an inhomogeneous manner, being preferably attached onto the external surface, which is more accessible [101].

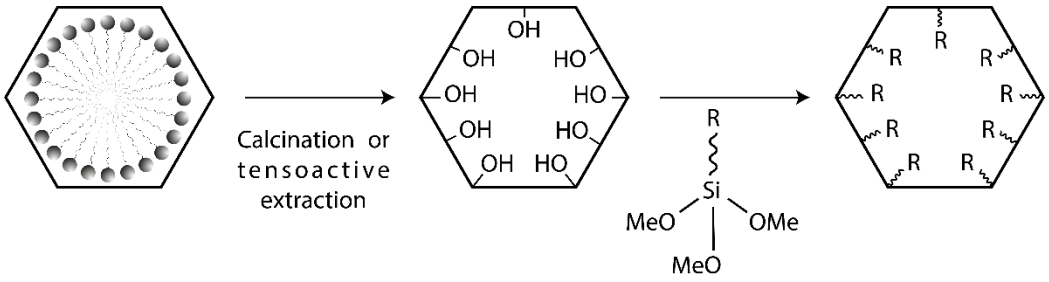


*Scheme 3. Post-synthesis functionalisation method.*

However, controlled dual functionalisation can been achieved by two different approaches that use grafting methods. The first approach is based on functionalising the nanoparticles before removing the surfactant producing a first specific functionalization of the organosilanes on the external surface. This first step must be followed by solvent extraction to remove the surfactant. After that, the inner surface of the pores can be selectively functionalised using a general grafting method as the external surface is already blocked. The second approach lies on functionalising the external surface with a large compound unable to go into the pores. After that, a general grafting method with a small compound allows to functionalise the inner surface

[101]. In either case, functionalizing the inner pores surface requires to choose a compound small enough to fit in the pores.

The main advantage of this method is the original mesoporous arrangement is maintained after grafting, since the nanoparticles are previously consolidated [103]. Therefore, it is a simple method to functionalise the nanoparticles. Besides, this technique is compatible with the calcination method as previous step for surfactant removal.

#### 1.3.2.2. Co-condensation

Co-condensation is a one-pot method based on the addition of the desired organosilane compound [104] during the nanoparticle formation mixed with the silica precursor (Scheme 4). This is the reason why this method tends to give a homogeneous distribution of organic groups in the whole framework, including the external surface, the inner pore surfaces and even inside the silica structure [105]. Hence, co-condensation allows the incorporation of a high amount of functional groups, between 2 and 4 mmol $g^{-1}$ MSN [106].

In this case, the reaction is made in aqueous medium, and thus, the alkoxy groups hydrolyse. Therefore, organosilane molecules behave as silica precursors by means of a nucleophilic bimolecular substitution identical to that of tetralkoxysilanes which leads to the silica polymerisation.

As a limitation, the use of this method can disturb the original mesostructure (pore size, surface area, etc.) and the nanoparticles size and morphology, since the interaction between the surfactant and silica species are altered [105][103]. Furthermore, if large amounts of organic compound are added, the hexagonal mesophase formation can be inhibited [106].

In addition, co-condensation approach limits the surfactant removal choice to solvent extraction since calcination will burn the incorporated organic matter.

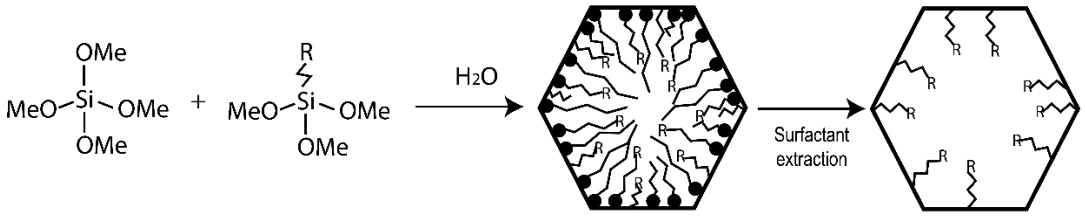


*Scheme 4. Co-condensation functionalisation method.*

### 1.3.3. Properties and applications

Anchoring organic moieties onto the MSN produces **hybrid materials** that can present a wide range of new physical and chemical properties. Indeed, hybrid materials present cooperative and functional behaviour that are not found in their constituents separately. These properties can be tuned depending on the organic groups attached. For example, functionalisation can provide a hydrophobic or hydrophilic behaviour, acidity or basicity, specific reactivity, or affinity with certain molecules, etc. As a result of the new properties acquired by the MSN due to the addition of organic moieties, some interesting functionalities appear. Even, multifunctionalised materials can be synthesised (Figure 6).

On the one hand, it must be mentioned those properties associated with the **loading and release of some cargo**. Functionalisation can control the surface affinity and host-guest chemistry by adding different functional groups, which can be tuned and adapted to the loading requirements of a particular cargo [99][107]. In this context, MSN can carry both hydrophilic and hydrophobic drugs [103].

In addition, an important ability of some functionalised MSN is the controlled release of the payload, associated with the concept of **molecular gates** [100][41][24][108]. Molecular gates are switchable single or supramolecular entities, which are capping the pores and are able to respond to a specific stimulus producing a change in its state from closed to open. Then, molecular gates are usually blocking the pores entrance and avoiding the release of the payload. When the stimulus is applied, the entities acting as molecular gates change their conformation and let the pores entry unblocked, inducing the release of the cargo. A lot of molecular gates have been developed in the last decade, which are able to be sensitive and respond to a wide range of chemical, physical, and biochemical stimuli, such as temperature, pH, light, magnetic and electric fields, redox agents, ultrasounds and biomolecules, among other. In this context, a plenty of materials have been developed for sensing and biosensing applications, in which the payload is a reporter molecule such as a fluorophore, a chromophore or a contrast agent [18].

On the other hand, the incorporation of organic moieties confers some **mechanical and chemical functionalities** such as higher degradation rate or an improvement of dispersibility of the MSN [100]. Other interesting feature is the labelling of MSN with fluorescent or absorbent dyes or isotopes, which is useful for monitoring processes, sensing and bio-imaging. Besides, some functionalisation provide MSN biocatalytic and catalytic ability [41].

Finally, those functional behaviours related to the **interaction of MSN with biological organism** are very useful in the biomedical field. For instance, functionalisation can improve biocompatibility of MSN [37][90][93][99], by using molecules or polymers such as PEG and avoiding the direct contact of silanol groups with the organism [100]. Besides, some moieties such as some charged polymers, peptides or specific ligands, can be used to enhance the cellular uptake and to improve pharmacokinetics of MSN in terms of biodistribution, cell location and excretion [37][90][93]. Related to the latter, there is a wide range of ligands developed to confer targeting abilities [37][90][93][98] to MSN and to improve their bioavailability, principally peptides and antibodies.

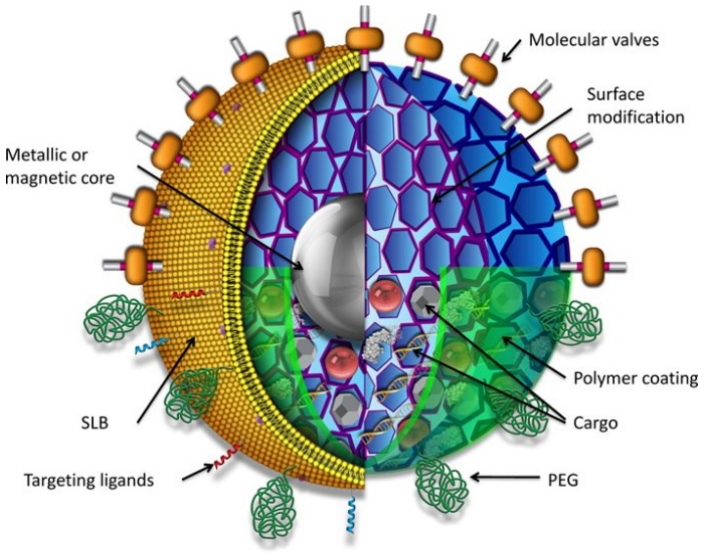


*Figure 6. Scheme of a multifunctional MSN showing multiple types of surface modifications, doping and cargos. Reprinted from* [110]. *Copyright © 2013 American Chemical Society.*

### 1.3.4. Doping

Apart from the mentioned use of organic moieties to functionalise the MSN, it can also be applied the doping or combination with metals or semimetals of MSN (Figure 6). This doping or combination can be either incorporating the metallic and semimetallic atoms into the silica network or assembling the silica nanoparticles with metallic and semimetallic nanoparticles. In the last case, different designs have been used, such as core-shell approach, or decoration or deposition of the metallic nanoparticles over the MSN [111][112].

Metals and semimetals own and confer excellent physic and chemical properties to MSN, such as their thermic and electric conductivity, magnetism or absorbance/fluorescence [113][114]. Therefore, doped MSN can be used in several applications [114][115][112][111], mainly in imaging, magnetic response, catalysis, controlled release and other. Doped MSN with some metals are highly used in magnetic resonance imaging (MRI) were the metal acts as contrast agent, but other imaging applications exist with the addition of fluorescent entities. In relation with the magnetic response, one of the most used application is the hyperthermia therapy, as it is possible to transform alternating magnetic fields into very localised heat. Also, another application of the magnetically doped MSN is the possibility of concentrating the particles in a particular target by applying an external magnetic field. On the catalysis field, dopants can act as heterogenic catalysers or participate in photocatalysis processes. In addition, the combination of MSN with metallic entities can confer alternative functionalities in the response to different stimulus in the field of controlled release. The most employed designs are the cleavage of a thermosensitive or photosensitive bond mediated by the energy conversion of the metallic compound, when a specific stimulus such as light, magnetic field or ultrasound, is applied. Other application can be the facilitation of the storage of different compounds, like hydrogen, through the formation of coordination complexes.

For these purposes a wide range of metals, metal oxides and semimetals have been used for MSN functionalisation [91][100][102]–[105], such as superparamagnetic iron oxide nanocrystals

(SPION), gold nanoparticles (AuNPs), palladium, zinc, aluminium or copper clusters, quantum dost (QDs), and lanthanides atoms ($Gd^{+3}$, $Er^{+3}$, $Yb^{+3}$).

## 1.4. CHARACTERISATION

MSN can be characterised following standard materials and inorganic chemistry characterisation techniques. Characterisation is needed not only to check the proper synthesis and functionalisation of MSN materials, but also to follow the synthesis steps and to understand the synthesis mechanism.

The most common characterisation techniques include powder X-ray diffraction (PXRD), $N_2$ adsorption-desorption, solid–state nuclear magnetic resonance (ssNMR), scanning electron microscopy (SEM) and transmission electron microscopy (TEM), dynamic light scattering (DLS) and electrophoretic light scattering (ELS), thermogravimetric analysis (TGA), Fourier-transform infrared spectroscopy (FTIR), elemental analysis (EA) and UV-visible and fluorescence spectroscopy.

### 1.4.1. Powder X-ray diffraction

Powder **X-ray diffraction is a technique** based on X-ray crystallography and consists of the analysis of the diffracted X-ray beam after hitting a powder sample. A **diffractometer** is formed by an X-ray tube, a small disc-like container to load the powder sample and a detector. X-rays are filtered and collimated to a single wavelength (λ) and direction to obtain clearer results.

The powder diffraction patterns are related to the atomic structure of the material studied, as predicted by **Bragg's law** (Equation 4):

$$n \cdot \lambda = 2d \cdot sin\theta \tag{4}$$

where *n* is an integer number; *λ* is the wavelength used, normally CuKα radiation (λ = 1.54 Å); *d* is the interplanar distance for the family planes in diffraction condition and $\theta$ is the scattering angle. Figure 7 shows a schematic representation of diffraction phenomenon. The positive diffraction condition is satisfied only at certain values of the incident θ angle at which there is a family of planes of the crystalline structure whose interplanar distance *d* fulfils the Bragg's Law. In this way, each family of crystallographic planes of a crystalline solid produces a peak in the diffraction pattern. Besides, the intensity of the scattered radiation depends proportionally to the electron density contained in each family of planes.

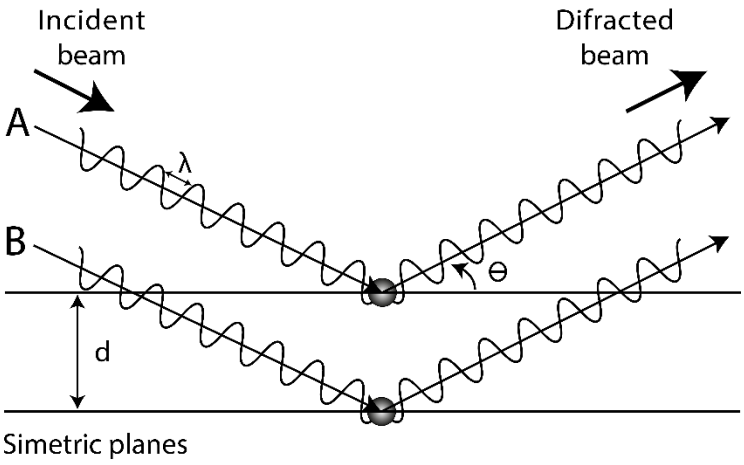


*Figure 7. Schematic representation of diffraction phenomenon and Bragg law.*

In a **crystalline material**, atoms are perfectly ordered giving rise to a set of family planes whose characteristic interplanar distances fall in the order of some Å. Then, diffractograms of crystalline solids appear as a group of narrow peaks with different intensities, located at medium to high 2θ angles. However, **mesoporous silica materials** are built from amorphous silica and then no diffraction signal from the internal distribution of silicon and oxygen atoms is obtained. However, in some cases the pores of the mesoporous material can be ordered in a long-range basis and this repeated geometry can give rise to diffraction phenomena when interacting with x-ray radiation. In this case, the corresponding family planes raised by the pore ordering present quite large d-spacing values and the corresponding diffractograms show peaks only at small 2θ angle, and with a wide profile.

Diffractograms obtained in mesoporous silica materials are useful to characterise the ordered pore structure as the combination of d-spacings and intensities in the diffraction diagram is characteristic of each structure. Specifically, **MCM-41** can be understood as a hexagonal close packing of two-dimensional pores (hexagonal P6mm symmetry). Hence, the crystallographic family planes correspond with a two-dimensional hexagonal system and can be represented with the Miller indices (100), (110), (200) and (210) (Figure 8).

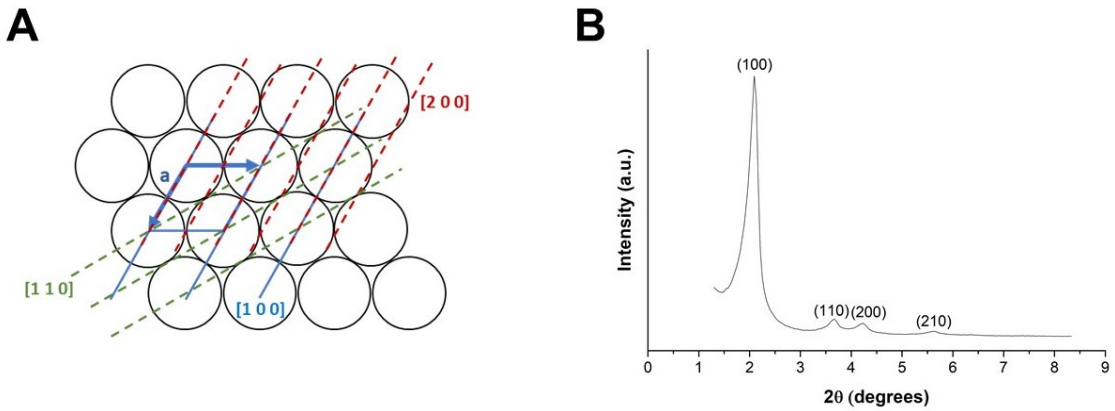


*Figure 8. A) Representation of the main crystallographic family planes of MCM-41 structure. B) Typical diffractogram observed in MCM-41 materials, where the peaks associated with symmetry planes (100), (110), (200) and (210) are shown.*

After the assignation of Miller indices to the peaks in the diffraction diagram of a porous material, the value of the cell parameter in the xy plane, *a*, can be obtained for a hexagonal crystalline system as presented in equation 5:

$$\frac{1}{d^2} = \frac{4(h^2 + hk + k^2)}{3a^2} + \frac{l^2}{c^2} \quad (5)$$

Considering that the pores in MCM-41 structure present only symmetry in two dimensions and that the peak relative to (100) plane is the main peak in x-ray diffractogram of MCM-41 materials, the equation 5 can be simplified (equation 6) to calculate the value $a_0$ (unit cell parameter) according to the distance $d_{100}$.

$$a_0 = \frac{2}{\sqrt{3}} d_{100} \quad (6)$$

Once we have the value of the cell parameter, it is possible to calculate the wall thickness of the silica (*w*) using the value of the pore size (*p*) that can be obtained from $N_2$ adsorption-desorption studies (Equation 7):

$$a_0 = p + w \quad (7)$$

The characterisation by PDXR of this type of materials is **useful for different reasons**. On the one hand, the ordering of the mesostructure can be checked and hence, the evolution of the porous structure along the synthetic procedure, as for example the right drift of the peaks in the diffractogram after the surfactant removal as a result of unit cell contraction, can be followed. On the other hand, it is suitable for ascertain the structure is not damaged with the subsequent functionalisation steps, although the diffraction patterns can suffer some blurring due to the loss of contrast of electron density as materials are loaded and functionalised.

### 1.4.2. $N_2$ ADSORPTION-DESORPTION

**$N_2$ adsorption-desorption** is a technique employed to study the surface of materials. For that purpose, it is measured the amount of $N_2$ gas adsorbed to the material of interest when is pumped in different pressures until reaching a certain of relative pressure at a fixed temperature, and the subsequent amount of $N_2$ that desorbs. Hence, adsorption/desorption isotherms are plotted as the amount of adsorbed/desorbed nitrogen as a function of the partial pressure applied.

The quantity of $N_2$ adsorbed depends on the strength of gas-solid interactions and the topography solid surface. According to that, isotherm can be grouped into different types, (Figure 9A).

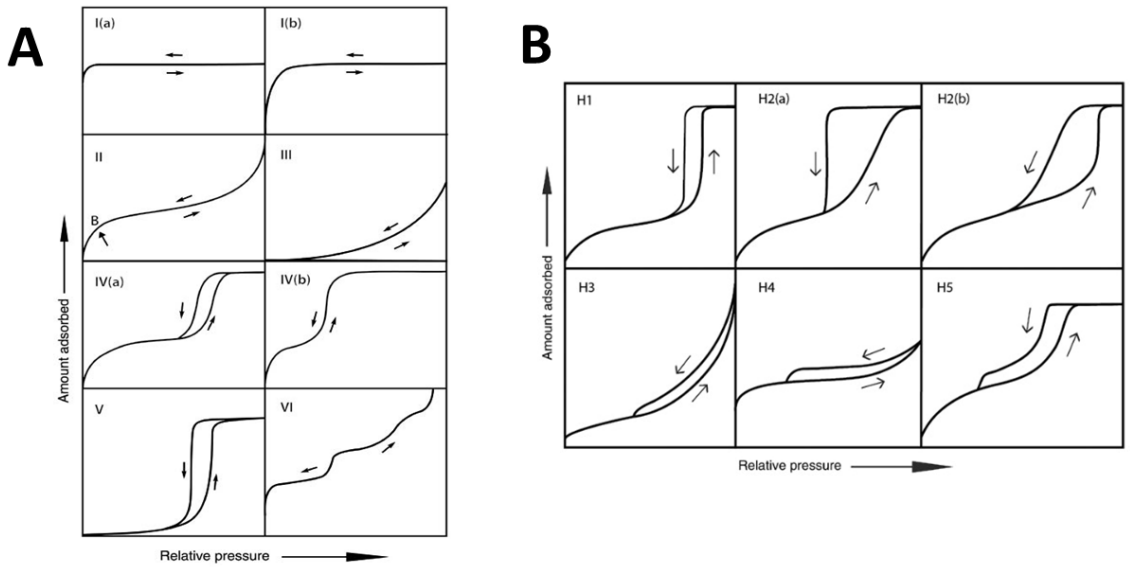


*Figure 9. Representation of the main types of adsorption isotherms (A) and hysteresis loops (B) according to the updated IUPAC classification. Reprinted from* [117]*. Copyright © 2015 De Grutyer.*

$N_2$ adsorption-desorption isotherms are very informative in the **characterisation** of MSN, as the values of the specific surface area, the specific pore volume, the average of pore size and its distribution can be obtained from their adjustment to different adsorption models.

Particularly, **MCM-41 materials** show a type IV (a) isotherm (Figure 10). These isotherms show at low pressures (from 0 to ca. 0.3 $p/p_0$) a quasilinear and progressive rise (Fig. 10, a), whose slope is related to the specific surface area value according to Brunauer-Emmett-Teller (BET) theory. This model considers that at low pressures a $N_2$ monolayer is formed across the whole surface, which presents the same energy of adsorption at each point. Subsequently, at ca. 0.35 $p/p_0$, a sharp increase in the adsorbed volume is observed (Fig. 10, b). This effect corresponds to the capillary condensation, namely, the pores filling. The $p/p_0$ value when the increase occurs is associated with the pore size and the $p/p_0$ range width of this increase gives the amplitude of size distribution. Different models can be used to calculate the size and distribution of the pores, such as the Barrett-Joyner-Halenda (BJH) model, which is based on the Kelvin equation, or the Density Functional Theory (DFT) or the nonlocal DFT (NLDFT), both based on molecular modelling. BJH is greatly used, but DFT and NLDFT are more accurate approximation to materials similar to MCM-41, since BJH can underestimate small sized pores [118]. On the other hand, pore volume is calculated from the total amount of gas adsorbed, taking the value where $p/p_0$ value is considered the pores are totally filled, i.e. where the isotherm reaches a plateau (Fig. 10, c).

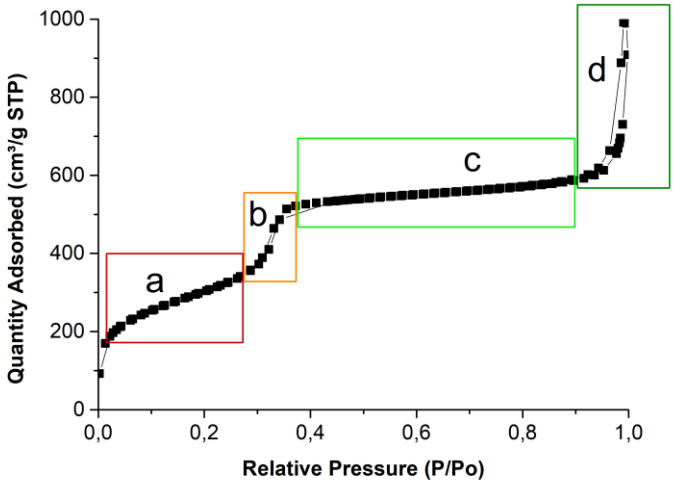


*Figure 10. Typical $N_2$ absorption-desorption isotherm of MCM41-type MSN, in which the marked areas correspond to (a) $N_2$ monolayer adsorption, (b) capillary condensation, (c) plateau region, and (d) interparticle porosity.*

In addition, type IV isotherms can present a hysteresis loop (Figure 9B), indicating the slightly different behaviour when the $N_2$ is added or withdrawn. This difference is due to the capillary condensation during the filling and emptying of mesopores. The shape of the hysteresis loop in these materials, when is present, usually follows a H1 type at the capillary condensation region, which is associated with well-defined cylindrical-like pore channels [7]; and H4 type hysteresis can also be found at high $p/p_0$ values, due to the presence of amorphous silica in the surface of nanoparticles that can be present in the voids between particles when they are close to each other [119].

Finally, it is common to see in MSN an additional sharp increase in the amount of nitrogen adsorbed at the highest pressures (close to 1 $p/p_0$) (Fig. 10, d), which corresponds to the presence of interparticle voids, since it indicates pores larger than 50 nm.

### 1.4.3. Electron microscopy

Electron microscopy allows to obtain images of the nanoparticles. This technique uses a beam of electrons to hit the samples, collecting either the reflected electrons (SEM, scanning electron microscopy) or the transmitted ones (TEM, transmission electron microscopy). These techniques allow to reach high magnification and resolution images, the latter in the order of few nanometres.

**Transmission electron microscopy (TEM)** is based on the image formed by a beam of electrons transmitted through a specimen. The number of electrons which can cross the sample will be inverse to the electron density of each area, so the contrast is related to this density in each point of the specimen. Samples must be in the order of at most few microns thick so as to be able to get some contrast. Bigger samples do not let the electrons through them. Then, this technique allows to see the internal structure of nanoparticles.

**Scanning electron microscopy (SEM)** consists of collecting from above the sample the electrons resulting after the interaction of the beam with the sample. In the SEM mode, the electrons with

higher possibility of escaping from the sample are those hitting the bigger heights and therefore, the image formed will be related to the topography of the sample. In this technique bigger and thicker samples can be used.

Sometimes both techniques can be coupled in order to obtain more information. In addition, **other complementary techniques** can be used, such as energy-dispersive X-ray spectroscopy (EDX), which use the characteristic X-ray emission by the elements of the sample in response to the internal electrons excitation when the sample is hit by the electron beam. Then, this technique can be used to analyse the elemental composition of the sample.

TEM and SEM give information about particle size, morphology, and surface coating. Nevertheless, organic matter does not give as much contrast as silica. TEM can be also used to verify the presence, size, and geometry of the pores. As is shown in Figure 11, pores can be seen in hexagonal distribution or like long channels across the nanoparticles, depending on the orientation of the particles.

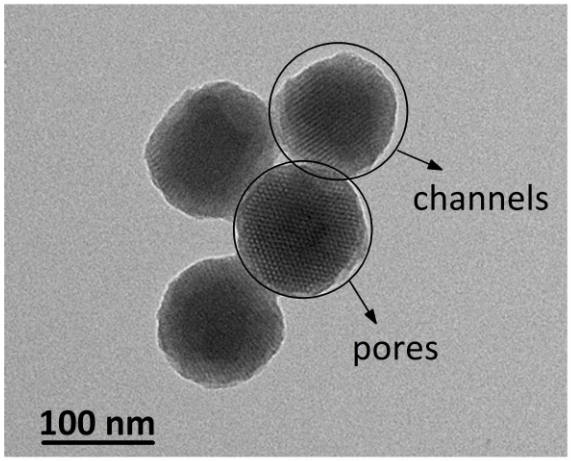


*Figure 11. Example of MSN pictures obtained by TEM, where the mesoporosity can be observed like hexagonally distributed pores or parallel channels.*

### 1.4.4. Dynamic light scattering and related techniques

**Dynamic light scattering** (DLS) is a technique based on the calculation of the size of the particles by measuring the Brownian motion when the sample is irradiated by a laser. The technique analyses the intensity fluctuations over the time in the scattered light by the total amount of nanoparticles. These fluctuations create a set of scattered speckle patterns and the shifts in these patterns over the time are a graphic representation of Brownian motion. Considering that in Brownian motion small particles move quickly and large particles move slowly, according to Stokes-Einstein equation, the DLS technique associates the size of particles with the shifts in the speckle pattern over the time. The behaviour of small and large particles plotted versus the correlation coefficient, meaning the similarity (from 1 to 0) of the speckle patterns over the time, is shown in Figure 12.

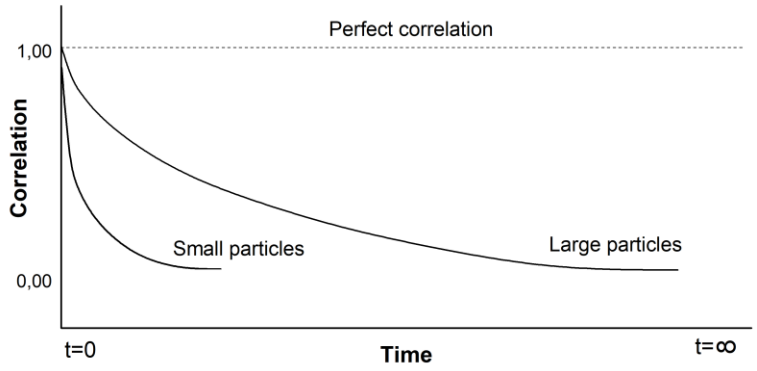


*Figure 12. Typical correlation function, calculated from speckle patterns in DLS measurements, of small and large particles against time.*

After the measurement, a **correlation function** (also called correlogram) is obtained fitting with different mathematical approaches the correlation data obtained. These calculations are then used to calculate the size distribution.

On the other hand, it has to be taken into account that the size measured correspond to the **hydrodynamic diameter**, which is defined as the diameter of a hypothetical spherical particle that diffuses in the same fashion as that of the particle being measured [120][121]. This phenomenon is due to the hydration layer acquired by the particles in suspension. This hydration layer is formed mainly by solvent molecules, but also by ions. This is the reason why measured sizes with DLS are larger than the ones measured with TEM or SEM (Figure 13). Besides, the hydration layer width depends on the properties of the dissolution and of the particles surface.

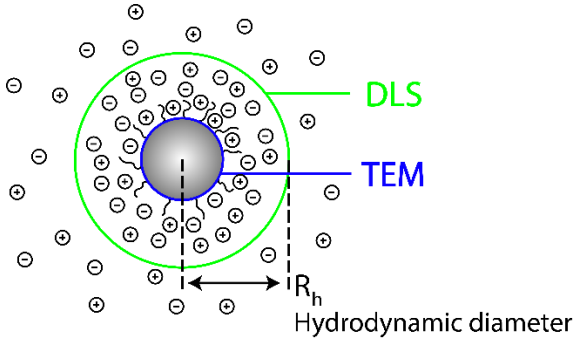


*Figure 13. Representation of hydrodynamic diameter measured in DLS in comparison with the nanoparticle diameter observed at TEM.*

Hence, DLS **is used** in the MSN characterisation to measure the average hydrodynamic diameter of a sample. Specifically, it is useful to compare the sizes of different MSN synthesis and the size changes after each functionalisation step.

As a **limitation**, for DLS to give suitable data, the sample must meet certain conditions as being well suspended and monodispersed, having a narrow size distribution, having minimal fluorescence or absorbance behaviour, not having sediments or large aggregates, etc. These conditions are difficult to achieve with an MSN suspension, making DLS sample preparation a sensitive issue.

The development of the DLS technique has given rise to other derived techniques, as for example the **Electrophoretic Light Scattering (ELS)**. This method is based on determine the Z-potential, which is the electric potential within the electrical double layer around a particle, with a stable entity. To do this, it measures the electrophoretic mobility of particles in a sample, which is the stable movement of charged particles towards the electrode of opposite charge when an electric potential is applied. In order to measure the electrophoretic mobility ELS uses laser Doppler velocimetry. This technique associates the velocity of a particle with the rate of fluctuation in the scattered light intensity that is received in a detector (Figure 14).

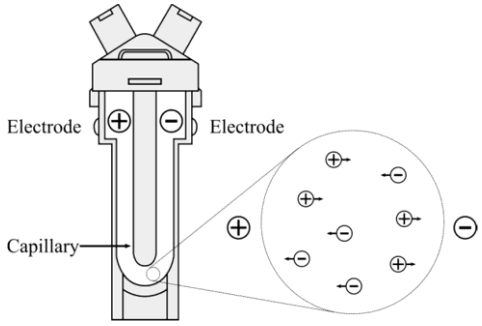


*Figure 14. Scheme of ELS cuvette and measurement. When the electric potential is applied, the charged particles move toward the opposite sign electrode. Reprinted from reference [122].*

The electrophoretic mobility in turn depends on the potential applied, the dielectric constant of the medium, the viscosity of the medium and the z-potential. Only the latter factor is a variable associated with the sample, since the rest of them are fixed for each measurement or can be controlled. The z-potential of the particle can thus be obtained by the application of the Henry's equation.

Therefore, z-potential is used in MSN characterisation to know the stability of the nanoparticles suspensions and to check the proper functionalisation steps that involve a change in the surface charge.

Additionally, other related technic developed is the **nanoparticle tracking analysis** (NTA). It is based on the analysis of both light scattering and Brownian motion of suspended nanoparticles. NTA employs the Stokes-Einstein equation to relate the diffusion coefficient with the particle diameter. In addition, NTA allows visualising the nanoparticles in real time due to the use of a digital camera connected to a microscope (Figure 15).

NTA is generally used to analyse the size dispersion and concentration of nanoparticles, as well as their diffusion coefficient and velocity.

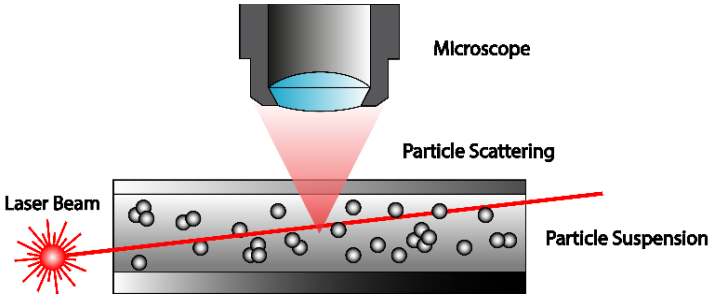


*Figure 15. Scheme of NTA measurement. The samples are placed into a chamber, where disperse the light emitted by a laser beam.*

### 1.4.5. Thermogravimetric analysis (TGA)

**Thermogravimetric analysis** (TGA) consists of measuring the weight of a sample over the time when controlling temperature of the sample. In other words, this technique collects the changes in the sample weight when, for instance, the temperature is raised and, as a result of that heating, some chemical of physical processes take place as evaporation or combustion of some components of the sample. For this purpose, the technique requires of an equipment that measures very small weight changes, so it is equipped with a highly precise microbalance and an anti-vibration system to avoid interferences in the weight measurements.

One of the main applications of TGA is the analysis of the sample composition of the sample as for example the percentage of solvents, organic matter, or the silanol concentration.

In addition, some complementary techniques can be incorporated to TGA, such as **differential thermogravimetric analysis** (DTA). The latter provides information about the endothermic/exothermic character of the transformations that occur to the sample while the heating program takes place. It is based on registering the difference in temperature between the sample and a standard material, giving to positive or negative peaks when the thermally induced process is exothermic or endothermic, respectively.

The **utility** of this technique to characterise the MSN is to give information about the organic matter present in the sample, which can come from surfactant, loaded cargo or functionalised moieties. It is usually difficult to discern between different organic moieties using this technique, since decomposing temperatures overlap each other. Therefore, it is used to know the total amount of organic matter. Nevertheless, some strategies can be used to distinguish the combustion processes, like plotting the TGA derivative, which resolves the inflexion points in the curve to minimums. Hence, it makes the processes visual and differentiable. Other strategy can be running separately every component of the sample to identify the specific behaviour of each one.

**Plotting** the mass of the sample against temperature, as it is showed in Figure 16, the loss of mass can be analysed. It is generally considered that solvents (ethanol, methanol, acetonitrile) and water are evaporated in the temperature interval from room temperature to 100 °C or 150 °C [3]. However, some works reported the water adsorbed on the surface and deep within the pore walls remains in the sample until 300 °C [123]. This loss of mass is related to solvent traces from the synthesis and functionalisation and the moisture of the nanoparticles, which can be very variable depending on the hygroscopic behaviour of compounds. Organic matter decomposition starts above 100 °C, depends on the decomposition temperature of each moiety, and usually are observed up to 600 °C. Silanol condensation to form the stable siloxane bond starts in the range from 190 °C to 400 °C [3][124], depending on the silanol type and their position (vicinal, geminal, nearby or spaced silanols, etc.) and can be found until 1000 °C.

Additionally, the first derivative of TGA curve can be represented to help in the separation of subsequent decomposition processes and the calculation of the corresponding mass loss. On the other hand, DTA can also provide information to assign the different thermal decompositions steps to its corresponding process. For example, the evaporation of solvents

and silanol condensation are endothermic processes, while combustion is an exothermic process.

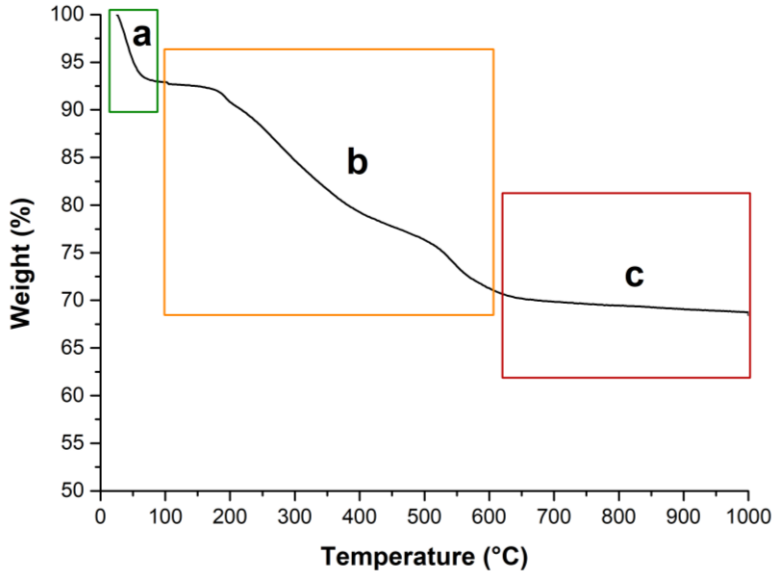


*Figure 16. Typical TGA curve of functionalised MSN sample, in which different regions can be distinguished: (a) solvents and moisture evaporation, (b) organic matter decomposition, and (c) silanols condensation.*

### 1.4.6. Fourier-transform infrared spectroscopy

**Fourier-transform infrared spectroscopy** is a technique used to obtain the infrared spectrum a specimen, which is related to molecular vibrations. Fourier-transform is needed to convert the raw data collected as an interferogram into a spectrum, according to the vibration's frequencies.

Each molecular bond has a particular manner to vibrate when it is excited. Then, irradiating a sample with infrared light will induce the absorption of those frequencies that coincide with the energy required to make vibrate each bond within the sample. Therefore, the spectrum produced is like a fingerprint of the sample. There are some bonds which absorbs in recognisable frequencies, as C=O, C–C (aromatic bond), C=C, C–N, N–O, etc.

Silica framework has an associated spectrum due to Si–O–Si, and Si–OR and Si–OH bonds. Normally, silica infrared spectrum shows as a set of mainly wide bands at 1217, 1056, 954, 795 and 435 (see Figure 17) due to the non-regular arrangement of the silica tetrahedron in the long-range [124]. Therefore, the additional bands which appear in the sample would indicate the presence of other functional groups. In this sense, FTIR is used in the characterisation of MSN to check that the different steps along the functionalisation process are correct, providing every step adds new bonds absorbing at different frequencies. In addition, the silica condensation level can be approximated through the signals coming from Si—OH bonds (located at 950 $cm^{-1}$). Finally, FTIR spectroscopy can be used to confirm the complete template removal more accurately than thermal analysis, being that even traces of the template can be readily detected [93].

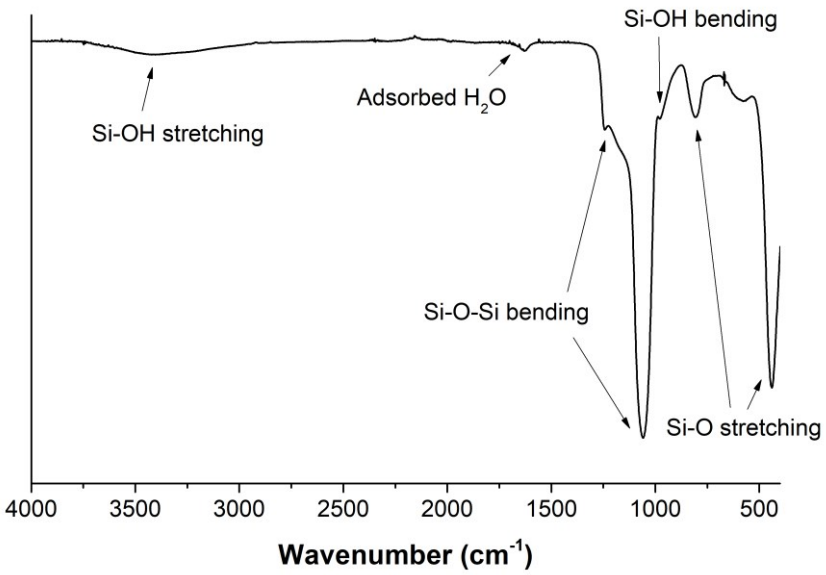


*Figure 17. Typical FTIR spectrum of calcined MSN, in which the bands associated to the bending and stretching of SI-O-Si and Si-OH bonds are observed.*

### 1.4.7. Solid state NMR

**Solid-state nuclear magnetic resonance (ss-NMR)** spectroscopy is based on NMR focussed on solid samples. NMR elucidate the structure of a molecule measuring the resonance frequency of specific atoms when the sample is subjected to a magnetic field. This frequency is related on the strength of the magnetic field that reach the atomic nucleus, which depends on the electronic density in the proximity of the named atom by means of the electromagnetic shielding. In case of ss-NMR, most of the interaction of the atom with the surroundings are anisotropic due to reduced mobility in solid matter. These anisotropic interactions have a substantial influence on the nuclear spins producing very broad signals in the spectrum.

In the case of MSN characterisation, $^{29}$Si-ss-NMR is generally performed since it gives information about the nanoparticle siliceous framework. In other words, it allows to determine the silica condensation level. Mainly in a mesoporous silica nanoparticle a silica tetrahedron can be linked to 1, 2 or 3 other ones. These silicon connectivity states are called Q2, Q3 and Q4, and they give differentiable resonance peaks in the $^{29}$Si-ss-NMR spectrum, as can be observed in Figure 22. Q2, Q3 and Q4 can be observed at ca. -92, -101 and -110 ppm, respectively. Spectra obtained usually show overlapping peaks, which have to be deconvolved to obtain the percentage of each population in the sample. Furthermore, the use of ss-NMR to measure other nuclei, such as the carbon ($^{13}$C-ss-NMR), can be useful to analyse the functionalisation of the samples, according to the same reasoning as for silicon. In this case, the carbon resonance peaks are called T1, T2, T3 regarding the number of silicon tetrahedrons bonded to the silica bonded to the organic moiety (Figure 18).

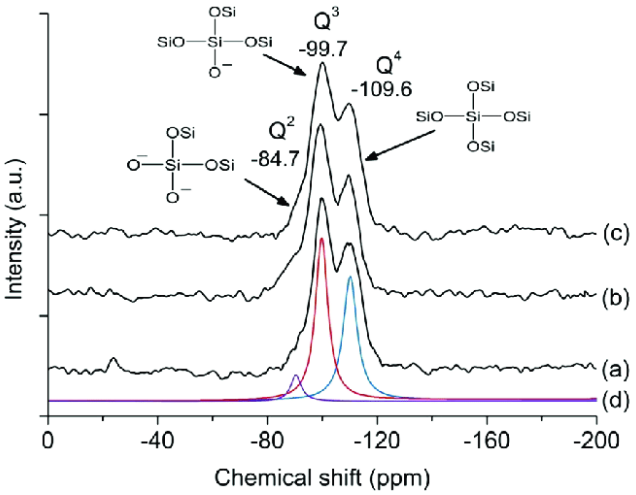


*Figure 18. Typical ss-NMR spectra of MSN samples, in which the resonance peaks $Q_2$, $Q_3$ and $Q_4$ are overlapped. They must be deconvolved to be quantified and analysed. Reprinted from the reference* [125]. *Copyright © 2013 Springer.*

## 1.5. NANOMEDICINE

### 1.5.1. Introduction to nanomedicine

In the last decades, the **interest in nanomedicine** has been increasing within the biomedical field and there is a growing number of research projects and groups dealing with nanomedicine challenges. Nanomedicine is **based on** making use of the knowledge and tools of nanotechnology in combination with pharmaceutical and biomedical sciences. Then, nanomedicine works in the development of nanoscale materials, as powerful new tools, whose aim is the comprehensive monitoring and control, treatment, repair, defence or medical imaging to achieve a medical benefit in biological systems [126].

Hence, nanomedicine does not focus on obtaining new drugs or active agents, since it is an expensive and time-consuming procedure, but rather on **improving** the safety, prolonged activity and efficacy index of traditional therapeutic or sensing species, i.e the modulation and improvement of the pharmacokinetic of biomedical species [127]. For instance, the aim of nanocarriers containing anti-cancer species is to increase their concentration in tumour area and to decrease the contact with healthy tissues [128]. This is where nanotechnology takes the main role, through development of supramolecular chemistry, in dosed and monitored titration or delivery, as well as selective and targeted devices, even in the pursuit of personalised therapies [129].

**Pharmacokinetic** is generally based on four stages: absorption, distribution, metabolism, and elimination, also known as ADME. Besides, in case of compound release systems it can be added an additional parameter: liberation [130]. Nanomedicine is involved in each one of these stages, being that the carried agent adopts the carrier's pharmacokinetics until it is released [127]. Thereby, nanomaterials could offer improvements in a) **absorption**, like higher membrane permeability or bioavailability, and versatility to use different administration routes [131]; b) **biodistribution**, like the ability to carry poorly water soluble compounds, targetability and avoid or reduce drug leakage, the capability to cross cell or tissue membranes; c) **metabolism**, as

higher metabolic stability due to protection from the outside, avoiding formation of undesirable by-products; d) **elimination**, as carrying the drugs to kidney or liver; e) **liberation,** as the ability to control, sustain, delay and target the delivery [128], as well as to escape from endosomes and to reach the nucleus or target compartment [109].

### 1.5.2. Introduction to nanomaterials

Nanoscaled materials, as FDA defines, are those materials which are designed with at least one dimension or structure within the interval from one to some hundreds of nanometres [132]. These dimensions confers them a number of **features**, which make them very interesting to biomedical purposes and are much less significant in macroscopic materials [93][111]. From a physical and chemical point of view, these features are the high surface area to volume ratio, major sensitivity to nanoscale phenomena (Brownian motion, magnetism…), molecular precision or control, high mechanical stability [107], etc. Therefore, these objects show some differential properties to micrometre and micrometre ones, which are related to their biochemical, magnetic, optical and electronic behaviour [133]. On the other hand, from the biological point of view, nanoscale matches with the dimension in which molecular interactions take place in the cellular environment. Thus, nanodevices are able to operate at cellular or sub-cellular level in an accurately manner [126].

The **development** in nanomedicine field has given rise to a wide range of nanomaterials, which can also be called in some cases nanotransporters, nanocarriers, nanodevices, among others. It could be found within this field inorganic nanoscaffolds and nanoparticles, liposomes, lipid-based nanostructures, micelles, organic polymers, and biological structures, such as virus (Figure 19). Each one of these nanomaterials has some advantages and some limitations, which condition their applications and their achievement to clinical trials and commercialisation. Besides, these nanomaterials have been used in a broad range of **applications** such as drug and gene delivery, imaging and contrast enhancement, biosensing, tissue engineering, hyperthermia, photodynamic therapy, etc. [134]

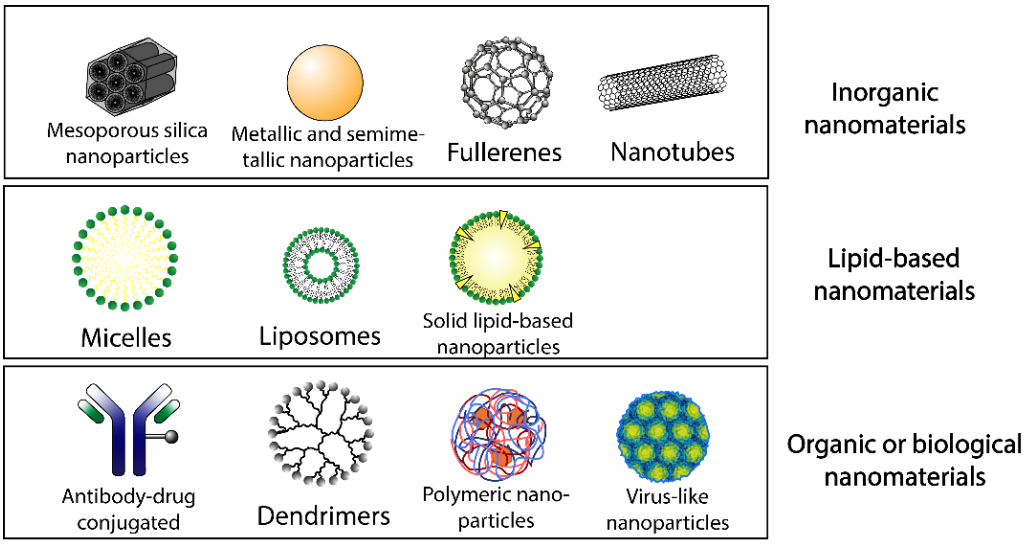


*Figure 19. Schematic representation of the main developed nanomaterials grouped with regard to their nature: (a) lipid-based nanomaterials, (b) organic or biological nanomaterials, and (c) inorganic nanomaterials.*

### 1.5.3. Nanomaterials requirements and challenges in biomedicine

An in-depth study and **characterisation of the properties of nanomaterials** is necessary to achieve in vivo and clinical trials. In particular, with regard to their interactions with biological components and their behaviour under physiological conditions which may differ from *in vitro* or isolated materials [129]. In this context, the study of the **pharmacokinetics** of nanomaterials**,** taking into account their systemic exposure, acquires considerable importance. This includes the analysis of absorption rate, circulation in blood, distribution to tissues, metabolism and decomposition, elimination and accumulation, and toxicity or biocompatibility [135].

Ideal nanomaterials for biomedical applications should be non-cytotoxic and **biocompatible, non-immunogenic or thrombogenic** [128]. The toxicity of nanodrugs depends on their size, shape, physicochemical characteristics, surface properties, etc. Generally, toxicity is associated with how the nanoscale materials interact and affect biological processes [103], such as the production of ROS and free radicals, impairment of mitochondrial function, membrane peroxidation, glutathione depletion, inflammation and formation of apoptotic bodies, disruption of coagulation process, alternations in gene expression, hemolysis of erythrocytes, disturbances of cell cycle regulation, etc.[131] In addition to the biocompatibility of nanodevices, it must be paid attention also to the potential toxicity of **degradation products**, and thus, stability studies must be done. In this context, it is recommended to do assays to check the stability in a biological environment (e.g. 37 °C in foetal bovine serum (FBS)), in which the size and surface charge as a function of time must be measured [129].

In addition, other properties could be required, as their **biodegradability** and final removal from the body once the nanomaterial achieved its function [128]. Then, in most of cases, bioaccumulation could be not desirable due to the potential and associated toxicity. Oppositely, in the case of tissue engineering, the permanence of the nanomaterial in the organism may be a goal.

Besides, a crucial factor is the ability of nanotransporters to penetrate into the desired area and to interact with cells so they must be **internalised** by them [129] (if it is required). This ability depends on their size, the surface properties and the binding activity [128][136]. Nanomaterials are generally internalised by endocytosis receptor-mediated [129], being caveolar-mediated in case of materials below 60 nm and clathrin-mediated for those below 120 nm [135]. Coating the nanomaterials with polymers or surfactants allows to improve the interaction with the cell surface receptors and ligands, increasing the permeability and uptake of nanomedicines. In order to follow the cellular uptake and internal location, dyes or contrast agents can be attached to the nanomaterials [129].

Beyond these prerequisites, nanomaterials have to deal with some biological phenomenon once they reach in vivo trials. On the one hand, one of the main obstacles is the **reticuloendothelial system** (RES) [93][110][111][119], also called mononuclear phagocyte system (MPS). RES is part of the immune system, which is mainly composed by macrophages, responsible for cleaning by phagocytosis the blood circulation from colloidal, damaged, or foreign particles. Therefore, some nanomaterials are fast eliminated from the blood, and thus, their biodistribution is affected. Once RES captures the nanocarriers, they are mainly accumulated in liver, spleen,

lungs, kidney, bone marrow and lymph nodes, and subcutaneous tissues, as they are generously blood irrigated and also are tissue-resident phagocytic cells organs. RES elimination is initiated by opsonisation, i.e., the adsorption of plasma proteins (as lipoproteins, immunoglobulin, fibronectin, complement proteins) in the carrier surface. RES uptake occurs principally for particles larger than 100 nm, meanwhile particles smaller than 10 nm are quickly removed by the kidneys[130][135]. In order to evade this clearance system, nanotransporters can be synthesised with elongated shape [129] or decorated in the external surface. For the latter purpose, the molecule most commonly used is PEG (polyethylene glycol), which slows the uptake by macrophages [109], but other hydrophilic molecules as carbohydrates or polymers as monosialoganglioside [135] or sarcosine [138] have a similar effect. Nevertheless, RES can be favourably used in case of antiparasitic or antimicrobial treatments or inflammatory diseases, where the pathology is localised in the macrophages and RES associated organs [139].

In addition to the adsorption of opsonisation proteins, when nanomaterials circulate in the blood, a set of serum proteins and ions attach to them, forming the known **protein corona**. This layer is related not only with opsonisation by RES, but also with the alteration of pharmacokinetics processes, such as the cellular uptake, and with the nanomaterials properties, such as size, surface charge, toxicity, coating denaturalisation and aggregation of nanocarriers. Protein corona formation is prevented or minimised by coating the nanomaterial surface by PEG or other polymeric compounds [108][135]. For this reason, knowing the nanomaterials interaction with proteins is interesting. Some assays as DLS and ELS, electrophoresis or immunomethods can be performed to test the interaction with proteins and its consequences as aggregation [129].

On the other hand, in case of tumour or inflammatory pathologies treatment, another phenomenon to bear in mind as the **enhanced permeation and retention** (EPR) effect [140]. This effect is provoked by an increased vascular permeability and angiogenesis development, alongside the disrupted lymphatic system [130], located in the damaged tissue in some of these pathologies. Therefore, nanomaterials can show passive targeting because of EPR effect. EPR effect depends on various factors such as tumour size and type and the size of the nanocarrier, being mostly active between 40-800 kDa or 20-100 nm [128]. Nevertheless, in spite of that, nanomaterials also tend to accumulate in organs related to RES. Furthermore, another limitation around EPR effect is their highly heterogeneity among organisms, even within the same subject. Consequently predicting the nanomaterials accumulation and pharmacokinetic becomes more complicated [131]. In addition, all downstream processes as cell uptake and delivery can act as bottlenecks in the improvement of efficacy [109].

Another important goal in nanomaterials development is the ability to **cross many physiological barriers** and reach the desired tissues. Some bioadhesive polymers, permeation accelerators and chelators can be used to opening reversibly tight junctions and increase the membrane permeability [135]. Besides, an endosomal escape strategy has to be followed to reach intracellular environment [103]. In this context, blood–brain barrier (BBB) is one of the hardest to cross, and its crossing is essential to achieve the brain. Some approaches used to reach the central nervous system are the addition of ligands that stimulate the receptor-mediated transcytosis [127].

As it can be seen along this introduction chapter, **nanoparticle size** plays an important role in processes such as particle adhesion, cell uptake, biodistribution and accumulation [93][118][122]. Generally, it is desired that nanoparticles used in nanomedicine are around 50 to 300 nm, being that smaller nanoparticles are removed by renal clearance and that larger nanoparticles can be removed by RES, cannot cross physical membranes, can be absorbed by intestinal cells, penetrate the bloodstream [128][142] and can cause membrane disruption in the cells [103]. In addition, these sizes maximise the EPR effect.

The strategy chosen to tip the balance toward the accumulation in desired organs or tissues and then improve the biodistribution is adding some ligands to confer the desired **targetability** to nanomaterials. These ligands can be antibodies, peptides, aptamers, carbohydrates, growth factors or other specific biomolecules.

In addition, other important potential requirement is the ability to **control the release**, of the carried agent in the desirable location, tissue or time. Then, stimuli-responsive triggerable components that can be responsible for this controlled release can be included. There are components able to react to endogenous stimuli (such as pH, redox potential or enzymatic activities) or exogenous stimuli (as hyperthermia, light, ultrasound or electromagnetic field) [143].

As a summary, physical and chemical characteristics such as size, shape, composition, polarity, charge and other surface properties determine the behaviour and effectiveness of nanomaterials in nanomedicine field, affecting to their stay time in blood, their renal clearance, protein absorption, ability to cross membranes, toxicity, uptake into cells, targeting efficiency, etc.[131][141]

### 1.5.4. Developed nanomaterials in biomedicine

#### 1.5.4.1. Liposomes

**Liposomes are** the most common and well-investigated nanocarriers for drug delivery and are considered by some authors to be the most successful drug-carrier system. Liposomes are spherical vesicles composed of a phospholipidic bilayer as a central element. Therefore, they are biocompatible and biodegradable, since they are based on endogenous-like molecules (natural phospholipids), but some cytotoxicity can be found associated with the surfactant used [135]. Besides, liposomes have a high internal loading capacity [139].

The size of liposomes applied to biomedical field are in the range of 50 to 450 nm. They can be classified depending on the amount of concentric bilayers, as unilamellar or multilamellar [127][144], having different release kinetics and properties. For example, unilamellar liposomes are smaller and enclose higher amount of water, which made them suitable to encapsulate hydrophilic compounds, including DNA, siRNA and contrast agents[139]. Multilamellar liposomes are larger and more appropriate to entrap hydrophobic compounds into the phospholipid bilayer, due to the great amount of lipid bilayers internally. In this sense, liposomes are inappropriate to carry highly hydrophobic species, since they are hardly retained in the vesicles, due to their ability to cross the lipid bilayer.

**First-generation liposomes,** which were firstly developed, are composed basically by lipids and the loaded molecule. This model has some critical limitation such as the fast elimination from blood due to their uptake by the RES, and high accumulation in liver and spleen, in spite of EPR effect. Beside the opsonisation agents, other vesicles like high-density lipoproteins (HDLs) and low-density lipoproteins (LDLs) can interact with liposomes reducing their stability. Another main limitation of first-generation liposomes is the cargo leakage due to instability and insufficient strength of bonds between lipids[139].

In order to minimise these problems, **second-generation liposomes** were developed modulating the lipid composition, their size and their surface charge. This allows improving the liposome characteristics, such as stability, pharmacokinetic properties, and therapeutic efficacy. For instance, the addition of cholesterol to liposomes increases their stability in vitro and in vivo, decreases the leakage and minimises the osmotic effect. The decoration with PEG or similar polymers creates long-circulating liposomes able to escape from RES for extended time intervals. Then, PEGylated liposomes have shown accumulation in tumour via EPR effect[139]. The addition of some ligands confers them targetability [144]. Other functionality which can be included is the inclusion of **stimuli-responsive** triggerable components. In the case of liposomes, mainly pH-sensitive systems have been developed [127].

Despite all the advances achieved in the development of second-generation liposomes, still there are some limitations in their use. For instance, repeated treatment with PEGylated liposomes has been related to accelerated blood clearance (ABC) phenomenon, which is the loss of long circulating properties. Other liposomal systems have been associated with triggering an innate immune response through the complement system, as a result of acute hypersensitivity syndrome called complement activation–related pseudoallergy (CARPA). This syndrome is related to immunological and inflammatory processes. Some strategies such as using desensitisation protocols with empty liposomes or pre-administration of complement inhibitors have been used to prevent CARPA [137].

The main **advantages** of liposomes in the biomedical context are the biocompatibility, the protection they confer to the pharmaceuticals from the external conditions (enzymatic degradation, immunologic or chemical inactivation, etc.) and their ability for controlled drug delivery. Furthermore, liposomes can be easily adjusted in size, charge and surface simply by variations in the preparation methodology [144]. Even, considerable liposomal drug delivery systems have been approved for their **clinical use** and their commercialisation, and many others are found in clinical trials, being the most advanced nanocarrier in this field.[110][119] However, some **drawbacks** have been found in their clinical applications, as the size polydispersion, instability, toxicity or immunogenicity at repeated administration or ACB and CARPA activation [127], which have also been found in other nanomaterials [145]. In addition, the use of ligand-targeted liposomes tends to be negligible in the clinical trials.

#### 1.5.4.2. Micelles (lipidic and polymeric)

Micelles are formed by self-assembly of amphipathic molecules in aqueous solutions. Therefore, it can be composed by lipids or block copolymers. Their size is around 5 to 50 nm. These carriers are attractive for intravenous delivery of hydrophobic compounds, since they can be physically entrapped in the core of polymers micelles and be transported at high concentrations surpassing

their water solubility. Their chemical composition allows an easy control of the size and morphology by changing their components.

Their hydrophilic heads form hydrogen bonds with surrounding water molecules, which avoid the intake of aqueous solution in the core, creating an effective protection against hydrolysis and enzymatic degradation. Furthermore, micelles can be administered into the circulation via inhalation or transdermally [128]. This type of nanoformulations can be used as a good alternative to liposomes, since they have an improved passive and active targeting, higher membrane permeability and larger water solubility. Even, some synthesis are able to avoid opsonisation and phagocytic clearance by RES, increasing the systemic exposure in the blood [135]. Due to these properties, some micellar formulations have reached their evaluation in clinical trials [146].

Nevertheless, as a drawback, some micellar systems are not able to sustain enough the cargo release. In addition, some cytotoxicity has been described due to the use of surfactants [135].

#### 1.5.4.3. Other lipid-based nanomaterials

Apart from liposomes and lipid-micelles, other lipid-based nanomaterials as emulsions or solid lipid-based nanoparticles have been developed.

**Emulsions**, also known as self-emulsifying drug delivery systems (SEDDSs) [128], are mixtures of oil, surfactant and co-solvent, where drugs are solubilised. In these mixtures, the drug is involved in the microstructure formation and influence their final properties. The most interesting point in these systems are the high bioavailability of hydrophobic drugs when are oral administered. However, this fact may cause a rapid increase of systemic exposure, due to fast gastric emptying, and could result in toxicity. Some emulsion formulations have reached clinical studies [135].

**Solid lipid-based nanoparticles** are colloids composed of solid fats such as monoglycerides, diglycerides, triglycerides, or waxes-surfactant mixtures. The main advantage they have over liposomes is the improved physical stability. In addition, these nanoparticles possess a great ability to modulate the drug release. They have a reduced cost and are simple to produce. Besides, unlike liposomes, they have a versatility to be administered by different routes, such as orally, intravenously, by inhalation and transdermally. Current preclinical experiments have been successful but clinical studies have yet to be conducted [128].

#### 1.5.4.4. Organic materials and polymers

Nanodevices **based on** organic polymers form a wide range of platforms, thanks to the increased control of polymer reaction and combination [130]. They can be composed by natural (e.g. proteins or peptides, cellulose, glycans or starches) or synthetic polymers (e.g. polyesters, polyethylene glycol, polyethyleneimine, polyacrylamide, etc.). [99][111] In addition, the combination with other components or monomers can improve some properties as flexibility, degradability, molecular recognition, etc. [109] Normally, organic polymer based nanomaterials are ranging in size between about 10 and 1000 nm. Their **main advantages** are their versatile applications, their low toxicity and biocompatibility due to the mimic ability, their high half-life and bioavailability [135], their easy biodegradation, whether hydrolytically or enzymatically [128].

Amongst polymeric nanodevices it can be found nanoparticles, nanosponges, dendrimers, nanofibers and nucleic acid nanoformulations, etc. [135]

**Organic nanoparticles** are solid constructions based on the amalgamation of polymers. These nanomaterials usually got a stable and prolonged drug release. Although, as disadvantages, in some cases nanoparticle rupture is early, administration routes are limited and some used polymers are not biodegradable [135]. Albumin-based nanoparticles [128] are one of the most used ones. They are generally used to load low aqueous soluble drugs, since albumin contains hydrophobic moieties to bind vitamins and hormones. Besides, albumin facilitates the endocytosis of compounds that carries through natural receptors [139]. On the other hand, apoferritin is also used to form nanoparticles. Apoferritin is a natural nanotransporter and responsible to storage and transfer iron. As an advantage, apoferritin can provide targetability, since it binds to transferrin receptors, which are overexpressed in some tumours. Both examples potentially are undetected by the immune system, owing to the fact that they are common proteins in the blood circulation [128].

**Nanosponges** are composed by hyper-crosslinked polymer with colloidal cavities, in which compounds can be encapsulates. Normally, they reach the size of 500 nm and are administered topical, parenteral, by aerosol or tablets. β-cyclodextrin and similar molecules are used as cavities [128].

**Dendrimers** are highly branched polymers that form spherical structures, from 1 to 100 nm. Their properties are determined by their tailor-made surface functional groups, which can coordinate different compounds in a host-guest manner and can be modified with ligands to acquire other properties (stability, targetability, etc.). Besides, the inner part allows to encapsulate other molecules.[130] Dendrimers size and functionality can easily be tuned with precision[109]. Other advantages apart from biocompatibility are the easy removal from the body and the highly expressed EPR effect. Nevertheless, as drawbacks the high presence of cationic groups, such as polylysine and poly(amidoamine), and larger dendrimers leads to immunogenicity and cytotoxicity [128][130][135], although it provides high membrane permeability, solubility improvement and controlled release ability [135].

**Nanofibers** are a net based on long filaments with a diameter in the nanometres scale. Normally they are formed by polymers such as PLA, PLGA or PCL. These compounds are optimal in their use as drug delivery systems, owing to their high surface-to-volume ratio and their microporosity. Nanofibers can be used to incorporate and release either hydrophilic or hydrophobic active agents, since they can be tailored functionalised. Nanofibers have been tested to be administered topical for local therapy, normally after surgery [128].

**Formulations based on nucleic acids** can be found as aptamers o DNA origami [147]. For example, triangle-shaped DNA origami can be an efficient platform to carry and deliver compounds. Aptamers recognises specific receptors, and thus, they can provide targetability [113][114].

Other simple nanoformulations have been developed with promising results. On the one hand, **nanocrystals** can also be mentioned [115][128]. They are based on the crystallisation and, sometimes the coating with stabilisers or polymers, of active pharmaceutical ingredients. Normally this method is used to improve the pharmacokinetics of those drugs which have water

solubility problems. Giving their simplicity, nanocrystals have been increasing the number of submissions for clinical trials and approvals processes, being a third of the total nanomedicine submissions. However, due to their simplicity and carrier-free format, they present some challenges to be improved such as their manufacturing and stability and their release control, among others. On the other hand, it could be found the **antibody-drugs conjugated (ADC)** complexes [149][130][131], based on the combination of the specific targeting of antibodies with the therapeutic effect of drug. Due to the simplicity of these nanoformulations, a high number of ADC have been approved for clinical trials and commercialisation.

#### 1.5.4.5. Viral structures

Viruses and virus-like structures have also been studied as nanoscaffolds in biomedicine field [109], which are generally used as virus-like particles (VLP). VLP [152] are based on the virus capsid but lacking o modifying the viral genome, in order to avoid the infection ability. VLP are dynamic, high ordered and self-assembled, and monodisperse structures. They can also be functionalised with other molecules to acquire new properties. VLP can be functionalised not only by chemical addition, but also via genetic fusion, i.e. the genetic information of desired proteins or peptides [133][134]. Their size is around 20–150 nm and they can be produced biologically in bacteria, insect cells, plant cells, and yeast.

VLP are used in a variety of **applications**, such as nanoreactors or **enzyme platforms** [152], i.e. loading enzymes to treat pathologies originated by an enzyme deficiency. Even metabolomes or multi-enzyme systems can also be prepared to simulate whole enzymatic routes. The enzyme concentration loaded inside the virus can be around mM order. In addition, VLPs are porous structures that can allow the substrate internalisation and metabolisation, meanwhile it is conferred enzyme stability and proteolysis resistance. Other important application of VLP is **vaccinology** [152] or immunotherapy, i.e. VLPs can be used to stimulate immune response, due to its strong immunogenicity [153], and then, they can be used to treat infectious diseases or cancer pathologies, respectively. VLPs are also applied as drug and gene delivery platforms [155]. In case of the latter is especially interesting, since viral mechanism can easily achieve the nuclei through transduction. Finally, VLPs have been developed to be used in bioimaging applications and other innovative fields such as metallisation and formation of nanowires [154].

The **advantages** of using viruses are the stability of their structure in physiological environment, the improved ability to load and delivery their cargo, their versatility, high bioavailability, broad biodistribution and safety. They show a high surface area and reactive groups in their surface to be decorated easily and contain large empty cavities able to encapsulate high amounts of cargo. In addition, by their nature they could be simply recognised by specific and endogenous receptors. This property can be used to target the nanodevices to determined cells and be easily internalised [152].

As **drawbacks**, VLPs and other viral structures are not far developed, they need more studies and improve their stability, functionalisation, biodegradation, and biocompatibility. Nevertheless, the most important issue to solve is their high immunogenicity when this is not desired [152]. Another limiting factor of virus in nanomedicine is their labour-intensive production [154].

Some other specific virus used in nanomedicine are oncolytic virus, plant viruses and bacteriophages. **Oncolytic viruses** [156] are able to infecting and killing cancer cells. This is achieved due to the inherent ability of some virus to bind and entry selectively to these cells, and their functionalisation with chemotherapeutic or lytic agents. This action can be combined with the immunotherapy associated with the activation of inflammation, and both adaptive and innate immune response. On the other hand, **plant viruses** are interesting in the development of nanodevices due to their reduced risks in the medical field [154]. The use of **bacteriophage** [155], apart from the safety associated to non-infectivity to mammalian cells, is very interesting because of their small genome, simple structure, and some attractive properties. For example, some filamentous bacteriophages can be decorated with on demand peptides, such as cell binding, cell penetrating or nuclear location ones, via phage display technique.

#### 1.5.4.6. Inorganic nanoparticles

Inorganic nanoparticles are interesting due to their size-dependent **unique physical properties** (optical, electromagnetic, thermo-chemical, etc.), which cannot be found in organic nanomaterials. Besides, inorganic nanoparticles usually are more stable and inert, easier, and cheaper to synthesise and functionalise, as well as more scalable. In addition, control drug release and anchoring of targeting ligands are well developed in inorganic nanoplatforms [141]. **However,** these characteristics are often at the expense of a low biocompatibility, i.e. they can be more cytotoxic [109], mainly by ROS production [130]. Furthermore, larger NPs than 100 nm are mostly retained by RES and smaller NPs can easily accumulate in lymph nodes, damaging these organs [141].

There is a wide variability within the inorganic nanomaterials, such as those derived from metals and their oxides (gold, silver, hafnium oxide, iron oxide), derived from carbon (carbon dots, nanotubes, fullerenes and graphene), semiconductors (quantum dots) and semimetallics (silica) [141][109]. There is a variety of inorganic nanomaterials which are under **clinical trials** (mostly for radiotherapy and tumour diagnostics) based on quantum dots, supermagnetic iron oxide, hafnium and gold oxide nanoparticles, and carbon nanotubes [111][122], but the number is still limited.

**Quantum Dots** (QDs) are innate fluorescent and semiconductor inorganic nanoparticles approximately from 2 to 6 nm. These remarkable optical and electronic properties make them very promising. Their main application is imaging and diagnosing, but they can also be used for delivering attached molecules. QDs present some advantages over standard fluorophores, such as not suffering photobleaching, narrow and tuneable emission wavelengths, and a broad excitation spectrum [109]. QDs are easily functionalised with organic molecules. The most commonly used QDs are Cadmium based, but alternative QDs have been developed due to cadmium toxicity. Cadmium QDs are formed by a metallic core (generally CdSe or CdS), which imparts the fluorescence, and a protecting coating. The alternative QDs are graphene or carbon based, which are more biocompatible, and the latter are easier to synthesise on a large scale. Other metallic biocompatible QDs have been studied as those composed by Indium Phosphide or Zinc Cuprous Indium Sulphide. These alternative QDs can generate ROS, but their functionalization with folate and glucosamine improves their biocompatibility [157].

Metallic-based nanoparticles form stable colloidal and monodisperse suspensions, are generally easy to synthesise and functionalise, and relatively inert [99][122]. **Gold nanoparticles** (AuNPs) are interesting due to its optical and photothermal properties. AuNPs absorb from visible to near infrared, absorption that can be tailored by size and shape. Then, they are used to photothermal therapy and imaging. These nanoparticles can be easily functionalised and attached to drugs due to the Au affinity to thiol groups. Au can be used to synthesise other type of nanostructures as nanoshells, nanorods or nanocages, which can be employed in different applications. **Silver nanoparticles** (AgNPs) are used in molecular diagnostics and different therapies, owing to the physical properties of silver (toughness, ductility, malleability, high electrical and thermal conductivity, etc.). AgNPs can be used for treating infections due to their intrinsic antibacterial activity. Their optical properties, such as visible and near infrared absorption, make AgNPs useful for photothermal and laser therapies. **Hafnium Oxide Nanoparticles** (HfO2) is used generally in radiotherapy. Hafnium, which is chemical stable and non-toxic element, has the ability to create free radicals and ROS when is beamed with X-rays in absence and presence of $O_2$, respectively. **Magnetic Iron Oxide Nanoparticles** (IONP) are the most investigated inorganics NPs. Due to its innate magnetic responsiveness, IONP can be used for resonance imaging, cell separation, biosensing and hyperthermia therapy. They are stable (typically below 10 nm), have a long circulating half-life, are biocompatible and can be easily coated by organic polymers, organic surfactants, or other metallic materials. Other related magnetic nanomaterials composed by cobalt or nickel oxides can also be found [109].

**Carbon-based nanomaterials** as nanotubes, carbon dot, nanodiamonds, fullerenes and graphene have extraordinary features related to their stability, conductivity, and roughness. They can be used to encapsulate contrast agents or loading therapeutic agents [109]. However, it has also been reported that these materials can trigger oxidative stress [131], destroy macrophages, and thus compromising immune system [130].

### 1.5.5. Mesoporous silica nanoparticles in biomedical applications

Within the inorganic nanomaterials, silica-based nanoparticles, and, in turn, the **mesoporous silica nanoparticles** and hybrid nanomaterials derived from them, can be considered the most important systems for control of drug delivery [15]. This fact is principally due to the high ability to encapsulate and control the release of their payload. On the one hand, the high surface area of MSN lead to a great loading efficiency, which can be 1000 fold higher than that of liposomes [108]. In addition, MSN can be tuned to encapsulate a wide variety of bioactive molecules, not only drugs and small organic molecules, but also cytokines, growth factors, enzymes and different types of nucleic acids, such a siRNA and miRNA or plasmids [158]. On the other hand, hybrid materials have the ability to respond in front of a wide range of specific stimuli and they behave as smart devices.

Their properties and principles have been developed throughout the document, but this section focus on those related to the nanomedicine field.

MSN must fulfil **some requirements** for their use in biomedical application. For instance, the particle size must be controlled in the range from 60 and 150 nm to optimise the desired biodistribution [142] (be leaded by EPR effect, penetration ability, escape from RES, etc.); the

mesopores must not be degraded until the controlled drug delivery is completed; and the nanoparticles must be easily dispersible and must not aggregate [86].

MSN revealed no **cytotoxicity**, including histopathological evaluation, in many in vitro and in vivo studies where high concentrations were used (more than 100 µg/mL in case of in vitro assays and 50 mg/kg of mice in vivo studies). Long-term evaluations were performed and no acute or chronic toxicity [103] or inflammation was observed after a month of the MSN treatment. In fact, silica is used in some cosmetics and food industry as an additive. FDA categorise silica as "Generally Recognised as Safe" (GRAS). Therefore, the biocompatibility or cytotoxicity may depend on the molecules used to functionalise the MSN [108]. For instance, MSN surface properties are considered greatly crucial to determine some behaviour as the biocompatibility of nanoparticles [145]. In fact, net surface charge of MSN surface influences on the interactions with cells and nanoparticles stability. For example, positive charged nanoparticles have higher binding affinity to phospholipid bilayer of the cell membrane and is easier to be internalised [98][122], but these induce higher immune response and cytotoxicity [145]. On the other hand, it has been seen that MSN produce ROS at high concentrations, which can damage cells and tissues, whether inducing necrosis or apoptosis, but also inflammatory and mutagenic processes in sublethal concentrations. This ROS production is associated with silanol abundance [110] and mesoporous structure, being that solid dense silica nanoparticles do not cause ROS. Nevertheless, solid dense silica nanoparticles tends to be more cytotoxic and have haemolytic activity [93][139]. This greater cytotoxicity is associated with surface silanol, which can disrupt the membrane components with hydrogen bonds and electrostatic interactions when is deprotonated [110]. In addition, nanoparticle morphology can also affect some cell functions as apoptosis, adhesion, migration, and proliferation, which both are related to cytoskeleton organisation. For instance, long rod-shaped MSN can disrupt the cell cytoskeleton [159]. Anyway, it has to be pointed that most of the in vivo studies were performed in immunodeficient models, where it is not taken into account the potential immune or inflammatory response [108].

MSN tends to **distribute** and accumulate in tumours thanks to EPR effect, and RES associated tissues and organs, especially for larger nanoparticles, such as liver, spleen, kidney, and lung. On the other hand, MSN are not able to cross the blood−brain barrier and reach the brain by themselves. As other nanomaterials, attaching some molecules and ligands to MSN, as well as using controlled and small sized nanoparticles, increases the targeting to the desired location and the time blood circulation, reducing the RES uptake [103][108]. **MSN shape** influences on their interaction with biological systems, and also the cellular uptake or blood circulation time [103]. For example, rod and sphere-like nanoparticles are most internalised by cells and have longer blood circulation than long rod-shaped ones [108].

The **excretion** of MSN from the organism is quick and has a great yield. Some studies determined that more than 90% of administered nanoparticles were excreted within 4 days, principally by renal clearance, which represents the 70%, followed by the 20% in faecal excretion [103]. Generally, MSN tends to be **degraded** in physiological conditions into orthosilicic acid, $Si(OH)_4$, or silica oligomers. These species are soluble in water, and then, removed by renal clearance [103], as well as those particles smaller than 5 nm, where renal cut-off remains. The rate of silica dissolution depends on the nanoparticles concentration, size, structure, functionalisation, and

degree of silica condensation. Nevertheless, some in vivo studies showed that nanoparticles and their remnants were **accumulated** in RES related tissues. Accumulation increased until approximately a week, and then it reduced. A month after the treatment, the nanoparticles were still observable in some of these organs.

MSN are **internalised** by cells via endocytosis, which leads to endosomal-lysosomal pathway. Lysosomes exhibit an acidic pH near to 5, reducing environment and a set of hydrolytic enzymes, by which MSN cargo can be degraded, inactivated, or denatured. Therefore, **endosomal escape** before the fusion with the lysosomes is required when the therapeutic compounds are not permeable to cell membrane, such as hydrophilic drugs, proteins, and other macromolecules, such as nucleic acids. Different strategies for achieving the endosomal escape have been developed for MSN systems. The most common option is to use the "proton sponge effect", which is based on the increase of proton concentration and thus, the influx of counter-ions triggers the osmotic swelling and the endosomal burst. This effect is provoked through decorating the MSN with highly protonable groups, such as poly-ornithine or poly-ethylenimine (PEI). Other strategies developed for endosomal escape are to use fusogenic peptides, proteins or polymers [108], peptides to pierce the endosomal membrane (forming toroidal channels or barrel-stave pores) [160] or photochemical active moieties that form ROS and disrupt the endosomal membrane [143][144]. However, endosomal escape has some limitations as the cytotoxicity associated with the lysosomal breakage [108].

### 1.5.6. Clinical translation of nanomedicine

Nanomaterials that are going to be applied in biomedicine need pre-market authorisation, which is regulated by the FDA (USA) or EMA (Europe), among others. These regulatory agencies require pre-clinical and clinical validation, in which the requirements named throughout the document must be tested and passed.

The number of clinical trials involving nanosized components is increasing. By the year 2020, more than 200 nanomedicines have being tested in clinical trials [135][163][164]. The first nanomedicine system which gained FDA approval was the liposome based drug (Doxil®) in 1995 [165]. Since them, the different regulatory agencies have approved around 100 nanodevices [164][166][167][163], including antibody-drug conjugated complexes, emulsions and lipid based systems, inorganic nanoparticles, liposomes, micelles, viral structures, nanocrystals, organic and polymeric nanoparticles. The number of nanomedicines varies in the literature, being that the term and limits of concept "nanomedicines", "nanodrugs" or "nanomaterials" for biomedical applications are not well stablished. Most of the nanomaterials approved are based on liposomes, polymers, viral structures and nanocrystals [132][148][167][166].

Despite the advantages of MSN mentioned throughout the document, like the high surface area, tuneable pore and particle size, and well know chemistry, they have not still overcome clinical trials, and their clinical use is not approved by FDA [133]. This process is limited due to the specific complexity of MSN and hybrid materials [139]. In fact, there are only some dye-doped silica-based nanodevices already approved for clinical use: Cornell Dots (for bioimaging) [168] and a type of gold nanoparticles-silica composites [169]. On the other hand, currently it has been

reported the achievement of one study related to MSN in a phase 2 study of clinical trials, based on targeted nanoparticles applied for imaging in nodal metastases [170].

#### 1.5.6.1. A bottleneck in clinical translation

In spite of the development of a huge number of new biomedical nanodevices and the growing number of publications about these, it is patent how there is a **bottleneck in their translation** to the clinical use and commercialisation [118][120]–[122][139]. The main limitations found for nanomaterials to be approved in clinical use can be grouped into two fields: those related to manufacturing processes and those related to their interaction with the biological organism.

First, the complexity of the nanodevices **manufacturing** compared to the traditional pharmaceuticals is a weak point. Nanomedicines are three-dimensional complexes composed by different components, which possess specific structures, properties, and functions. In this context, it is difficult to determine a robust manufacturing process for nanomaterials [165]. This results in elevated cost and a questionable effective capability to assure good quality formulations, including stability, size uniformity, well-dispersion, scalability and reproducibility of the final product [111][119][139]. Furthermore, in some cases, the own raw materials are complex, expensive and limiting for their industrial production [163]. Besides, the development of a new molecular entity for clinical applications needs Chemistry, Manufacturing, and Controls (ChMC) assessment, whose standards for nanomedicines are not well established [139], and Critical Quality Attributes (CQA), in order to improve the manufacturing and to focus on critical points, which could be helpful to scale the synthesis [165]. In the context of manufacturing, the encapsulation of sufficient therapeutic agent is also a determinant limitation [145]. On the other hand, this complexity is not only in the manufacturing process, but also in the characterisation steps, including those related to in vitro and in vivo assays [163].

On the other hand, the **interaction with the biological organism** is also a complicated issue that is not well understood [165]. Some common drawbacks found generally in nanomaterials are the undesired tissue accumulation [108] and immunogenicity, as well as unknown long-term exposure consequences, which make the **toxicity** of some nanodevices still to remain problematic [145][163]. In this context, it must be taken into consideration the complexity of organism reality: the huge amount of biomolecules and biological processes present in each tissue and organ, the intra- and inter-species variability, the change of physico-chemical properties of exogenous entities in physiological conditions, and the complex pharmacodynamics and pharmacokinetics derived from that [171]. All these conditions are not controllable by researchers and remain as permanent hurdles. For example, extrapolation of the knowledge and results taken from animal assays to human is not a simple process, since it is not often comparable in terms on quality, safety and efficacy [132][140][130].

Furthermore, an important limitation is that only a small percentage of administered nanodevices **reach the targeted and desired location** [145][163]. In case of tumours, in spite of EPR effect, only the 0.7% reach them, according to Wilhelm et al. [172], less than 1% according to Björnmalm [140], meanwhile Dawidczyk et al. [109] reported a range from 0.1% to 35%. This behaviour is independent from the use of targeting ligands, by which Dawidczyk et al. [109] reported the percentages from 1% to 15%. This fact is attributed to the presence of different biological barriers and the sequestration by the RES.

Last but not least, the **regulatory processes** can be mentioned as a third factor among those which hinder the clinical translation of nanomedicine. Up to date, there is still a lack of guidance and clarity in the standards and regulatory laws, as well as in the examinations and assessments required specifically for nanomedicines [145][147].

All of these drawbacks provoke that some recent clinical trials with nanomedicines are not showing an improved survival benefit compared to conventional treatments, in spite of good results in preclinical studies [140].

#### 1.5.6.2. An opportunity to material science

In this context, nanotechnology devices have to overcome some **handicaps** as having a higher efficacy, improving their safety and toxicological profiles, controlling their formation and synthesis, and escaping from the RES and albumin corona.

Therefore, some authors defend that in order to succeed in the development of nanomaterials and achieving clinical use, researchers must propose realistic goals, identify the limitations of nanoparticle approaches and maximizing the capabilities of current nanoscopic systems. They advocate the idea of "**keep it simple**", looking for robustness, and progressing in a stepwise manner, since in the last years the complexity and sophistication of new nanomaterials were not correlated with their achievement to clinical studies [140][173]. The more complex nanodevices are, the more gaps exist in the understanding of the mechanism of action and their characterisation, as well as the more difficult is to have robust and consistent manufacturing processes [132]. Besides, the simpler nanomaterials are, the easier is their approval for clinical use [139]. The aim in nanodevices should be to employ simple, cost-effective and scalable synthesis methods, which will facilitate the future industrial production and clinical translocation [145].

Accordingly, it is undeniably true that **material science** plays an essential role in the nanomedicine challenges ahead. It is crucial to understand the synthesis mechanism of nanomaterials and to establish the properties derived from the structure. Therefore, a rational design of nanodevices allows the optimisation and fine control of physico-chemical properties, which impacts to feasibility of clinical translation.

In this context, it is important to overcome the gap between the chemist and the medical point of view [121]. Materials scientists and chemists need to work with and not against biology. Both disciplines should reach a better understanding and work synergically.

#### 1.5.6.3. Challenges for MSN

In the context mentioned, controlling the features of MSN, such as those related to the size and morphology reproducibility of nanoparticles and pores, the functionalisation reproducibility, the dispersion and suspendibility and the biodegradability in physiological conditions, is desirable for succeeding in biomedical applications and attaining clinical trials [145]. For example, a non-aggregated MSN dispersion is required to get a suitable biodistribution, cell uptake and degradation, being that aggregation results in rapid uptake by the RES [174][175]. Precise pore-size and shape control may allow selective drug loading, as well as an efficient gate coating. The large pore volume, meaning thin silica wall, would allow better biodegradation. Well-controlled particle size is needed for a good control in particle–cell interactions (uptake process and

cytotoxicity derived) [163] and precise quantitative dose in carrying cargos [90]. Obtaining not only reproducible, but also a scalable manufacturing is also dependent of the good control of synthesis processes.

In addition, is mandatory to improve and standardise the complicated and multiple functionalisation steps required for most of MSN applications. These steps usually limit the industrial scale fabrication, introduce new components that difficult the fine control and characterisation, and potentially tend to aggregate the final MSN [41].

According to this, the main weaknesses in the synthesis of the MCM-41-type MSN, and their translation to clinical, are the obtaining of monodisperse, non-aggregated and biodegradable nanoparticles [142], inasmuch as the pore formation (size and geometry), the nanoparticle specific surface and the nanoparticle size and shape are well stablished in the methods used currently, reaching an acceptable reproducibility [2][176][11].

## 1.6. REFERENCES


[1] Y. Lu, H. Fan, A. Stump, T. L. Ward, T. Rieker, and C. J. Brinker, “Aerosol-assisted self-assembly of mesostructured spherical nanoparticles,” *Nature*, vol. 398, no. 6724, pp. 223–226, 1999, doi: 10.1038/18410.

[2] Q. Cai, Z. S. Luo, W. Q. Pang, Y. W. Fan, X. H. Chen, and F. Z. Cui, “Dilute solution routes to various controllable morphologies of MCM-41 silica with a basic medium,” *Chem. Mater.*, vol. 13, no. 2, pp. 258–263, 2001, doi: 10.1021/cm990661z.

[3] C. E. Fowler, D. Khushalani, B. Lebeau, and S. Mann, “Nanoscale Materials with Mesostructured Interiors,” *Adv. Mater.*, vol. 13, no. 9, pp. 649–652, May 2001, doi: 10.1002/1521-4095(200105)13:9<649::AID-ADMA649>3.0.CO;2-G.

[4] R. I. Nooney, D. Thirunavukkarasu, Y. Chen, R. Josephs, and A. E. Ostafin, “Synthesis of Nanoscale Mesoporous Silica Spheres with Controlled Particle Size,” *Nature*, 2002, doi: 10.1021/cm0204371.

[5] K. Suzuki, K. Ikari, and H. Imai, “Synthesis of Silica Nanoparticles Having a Well-Ordered Mesostructure Using a Double Surfactant System,” *J. Am. Chem. Soc.*, vol. 126, no. 2, pp. 462–463, Jan. 2004, doi: 10.1021/ja038250d.

[6] Z. Li, Y. Zhang, and N. Feng, “Mesoporous silica nanoparticles: synthesis, classification, drug loading, pharmacokinetics, biocompatibility, and application in drug delivery,” *Expert Opin. Drug Deliv.*, vol. 16, no. 3, pp. 219–237, 2019, doi: 10.1080/17425247.2019.1575806.

[7] Z. ALOthman, “A Review: Fundamental Aspects of Silicate Mesoporous Materials,” *Materials (Basel).*, vol. 5, no. 12, pp. 2874–2902, Dec. 2012, doi: 10.3390/ma5122874.

[8] G. J. A. A. Soler-Illia and O. Azzaroni, “Multifunctional hybrids by combining ordered mesoporous materials and macromolecular building blocks,” *Chem. Soc. Rev.*, vol. 40, no. 2, pp. 1107–1150, 2011, doi: 10.1039/c0cs00208a.

[9] E. Yamamoto and K. Kuroda, “Colloidal mesoporous silica nanoparticles,” *Bull. Chem. Soc. Jpn.*, vol. 89, no. 5, pp. 501–539, 2016, doi: 10.1246/bcsj.20150420.

[10] Y. Zhou *et al.*, “Mesoporous silica nanoparticles for drug and gene delivery,” *Acta Pharm. Sin. B*, vol. 8, no. 2, pp. 165–177, 2018, doi: 10.1016/j.apsb.2018.01.007.

[11] S. Bhattacharyya, G. Lelong, and M. L. Saboungi, “Recent progress in the synthesis and selected applications of MCM-41: A short review,” *J. Exp. Nanosci.*, vol. 1, no. 3, pp. 375–395, 2006, doi: 10.1080/17458080600812757.

[12] C. Vanichvattanadecha, W. Singhapong, and A. Jaroenworaluck, “Different sources of silicon precursors influencing on surface characteristics and pore morphologies of mesoporous silica nanoparticles,” *Appl. Surf. Sci.*, vol. 513, p. 145568, May 2020, doi: 10.1016/j.apsusc.2020.145568.

[13] Á. G. U. Helmut H. Telle, *Laser Spectroscopy and Laser Imaging: An Introduction*. Series in Optics and Optoelectronics, 2018.

[14] D. Sumanth Kumar, B. Jai Kumar, and H. M. Mahesh, “Quantum Nanostructures (QDs): An Overview,” in *Synthesis of Inorganic Nanomaterials*, Elsevier, 2018, pp. 59–88.

[15] S. L. Suib, “A Review of Recent Developments of Mesoporous Materials,” *Chem. Rec.*, vol. 17, no. 12, pp. 1169–1183, Dec. 2017, doi: 10.1002/tcr.201700025.

[16] K. Ariga, A. Vinu, Y. Yamauchi, Q. Ji, and J. P. Hill, "Nanoarchitectonics for Mesoporous Materials," *Bull. Chem. Soc. Jpn.*, vol. 85, no. 1, pp. 1–32, Jan. 2012, doi: 10.1246/bcsj.20110162.

[17] C. Fornaguera and M. J. García-Celma, "Personalized nanomedicine: A revolution at the nanoscale," *Journal of Personalized Medicine*, vol. 7, no. 4. MDPI AG, Dec. 01, 2017, doi: 10.3390/jpm7040012.

[18] F. Sancenõn, L. Pascual, M. Oroval, E. Aznar, and R. Martínez-Máñez, "Gated Silica Mesoporous Materials in Sensing Applications," *ChemistryOpen*, vol. 4, no. 4, pp. 418–437, 2015.

[19] D. C. Yu Lai, "Mesoporous Silica Nanomaterials Applications in Catalysis," *J. Thermodyn. Catal.*, vol. 05, no. 01, pp. 10–12, 2014, doi: 10.4172/2157-7544.1000e124.

[20] R. K. Sharma, S. Sharma, S. Dutta, R. Zboril, and M. B. Gawande, "Silica-nanosphere-based organic–inorganic hybrid nanomaterials: synthesis, functionalization and applications in catalysis," *Green Chem.*, vol. 17, p. 3207, 2015, doi: 10.1039/c5gc00381d.

[21] C. Kim, I. H. Yoon, C. H. Jung, S. B. Yoon, W. K. Choi, and J. K. Moon, "Sorption of cobalt by amine-functionalized silica nanoparticles for foam decontamination of nuclear facilities," *J. Radioanal. Nucl. Chem.*, vol. 310, no. 2, pp. 841–847, 2016, doi: 10.1007/s10967-016-4886-2.

[22] S. Nasreen, U. Rafique, S. Ehrman, and M. A. Ashraf, "Synthesis and Characterization of Mesoporous Silica Nanoparticles for Environmental Remediation of Metals, PAHs and Phenols," *Ekoloji*, vol. 27, no. 106, pp. 1625–1637, Nov. 2018.

[23] R. E. Morris and P. S. Wheatley, "Gas storage in nanoporous materials," *Angewandte Chemie - International Edition*, vol. 47, no. 27. John Wiley & Sons, Ltd, pp. 4966–4981, Jun. 23, 2008, doi: 10.1002/anie.200703934.

[24] E. Aznar, M. Oroval, L. Pascual, J. R. Murguía, R. Martínez-Mánez, and F. Sancenón, "Gated Materials for On-Command Release of Guest Molecules," *Chem. Rev.*, vol. 116, no. 2, pp. 561–718, 2016, doi: 10.1021/acs.chemrev.5b00456.

[25] C. T. Kresge, M. E. Leonowicz, W. J. Roth, J. C. Vartuli, and J. S. Beck, "Ordered mesoporous molecular sieves synthesized by a liquid-crystal template mechanism," *Nature*, vol. 359, no. 6397, pp. 710–712, 1992, doi: 10.1038/359710a0.

[26] J. S. Beck *et al.*, "A New Family of Mesoporous Molecular Sieves Prepared with Liquid Crystal Templates," *J. Am. Chem. Soc.*, vol. 114, no. 27, pp. 10834–10843, 1992, doi: 10.1021/ja00053a020.

[27] M. Grün, I. Lauer, and K. K. Unger, "The synthesis of micrometer- and submicrometer-size spheres of ordered mesoporous oxide MCM-41," *Adv. Mater.*, vol. 9, no. 3, pp. 254–257, Mar. 1997, doi: 10.1002/adma.19970090317.

[28] M. Grün, K. K. Unger, A. Matsumoto, and K. Tsutsumi, "Novel pathways for the preparation of mesoporous MCM-41 materials: Control of porosity and morphology," *Microporous Mesoporous Mater.*, vol. 27, no. 2–3, pp. 207–216, Feb. 1999, doi: 10.1016/S1387-1811(98)00255-8.

[29] C. T. Kresge, J. C. Vartuli, W. J. Roth, and M. E. Leonowicz, "The discovery of ExxonMobil's M41S family of mesoporous molecular sieves," in *Studies in Surface Science and Catalysis*, Jan. 2004, vol. 148, pp. 53–72, doi: 10.1016/s0167-

2991(04)80193-9.

[30] L. T. Gibson, “Mesosilica materials and organic pollutant adsorption: Part A removal from air,” *Chemical Society Reviews*, vol. 43, no. 15. Royal Society of Chemistry, pp. 5163–5172, Aug. 07, 2014, doi: 10.1039/c3cs60096c.

[31] M. Vallet-Regí, M. Colilla, I. Izquierdo-Barba, and M. Manzano, “Mesoporous silica nanoparticles for drug delivery: Current insights,” *Molecules*, vol. 23, no. 1, pp. 1–19, 2018, doi: 10.3390/molecules23010047.

[32] M. Vallet-Regi, A. Rámila, R. P. Del Real, and J. Pérez-Pariente, “A new property of MCM-41: Drug delivery system,” *Chem. Mater.*, vol. 13, no. 2, pp. 308–311, 2001, doi: 10.1021/cm0011559.

[33] D. R. Radu, C. Y. Lai, K. Jeftinija, E. W. Rowe, S. Jeftinija, and V. S. Y. Lin, “A polyamidoamine dendrimer-capped mesoporous silica nanosphere-based gene transfection reagent,” *J. Am. Chem. Soc.*, vol. 126, no. 41, pp. 13216–13217, 2004, doi: 10.1021/ja046275m.

[34] J. Morry *et al.*, “Dermal delivery of HSP47 siRNA with NOX4-modulating mesoporous silica-based nanoparticles for treating fibrosis,” *Biomaterials*, vol. 66, no. 1, pp. 41–52, Oct. 2015, doi: 10.1016/j.biomaterials.2015.07.005.

[35] Y. Li *et al.*, “Dual targeting delivery of miR-328 by functionalized mesoporous silica nanoparticles for colorectal cancer therapy,” *Nanomedicine*, vol. 13, no. 14, pp. 1753–1772, 2018, doi: 10.2217/nnm-2017-0353.

[36] B. G. Cha and J. Kim, “Functional mesoporous silica nanoparticles for bio-imaging applications,” *Wiley Interdiscip. Rev. Nanomedicine Nanobiotechnology*, vol. 11, no. 1, pp. 1–22, 2019, doi: 10.1002/wnan.1515.

[37] F. W. Pratiwi, C. W. Kuo, S. H. Wu, Y. P. Chen, C. Y. Mou, and P. Chen, “The Bioimaging Applications of Mesoporous Silica Nanoparticles,” in *Enzymes*, 1st ed., vol. 43, Elsevier Inc., 2018, pp. 123–153.

[38] N. T. Chen, S. H. Cheng, J. S. Souris, C. T. Chen, C. Y. Mou, and L. W. Lo, “Theranostic applications of mesoporous silica nanoparticles and their organic/inorganic hybrids,” *J. Mater. Chem. B*, vol. 1, no. 25, pp. 3128–3135, 2013, doi: 10.1039/c3tb20249f.

[39] L. Polo *et al.*, “Molecular gates in mesoporous bioactive glasses for the treatment of bone tumors and infection,” *Acta Biomater.*, vol. 50, pp. 114–126, 2017, doi: 10.1016/j.actbio.2016.12.025.

[40] Y. Chen, H. Chen, and J. Shi, “In vivo bio-safety evaluations and diagnostic/therapeutic applications of chemically designed mesoporous silica nanoparticles,” *Adv. Mater.*, vol. 25, no. 23, pp. 3144–3176, 2013, doi: 10.1002/adma.201205292.

[41] T. T. Hoang Thi, V. Du Cao, T. N. Q. Nguyen, D. T. Hoang, V. C. Ngo, and D. H. Nguyen, “Functionalized mesoporous silica nanoparticles and biomedical applications,” *Mater. Sci. Eng. C*, vol. 99, no. December 2018, pp. 631–656, 2019, doi: 10.1016/j.msec.2019.01.129.

[42] H. Yamada, H. Ujiie, C. Urata, E. Yamamoto, Y. Yamauchi, and K. Kuroda, “A multifunctional role of trialkylbenzenes for the preparation of aqueous colloidal mesostructured/mesoporous silica nanoparticles with controlled pore size, particle diameter, and morphology,” *Nanoscale*, vol. 7, no. 46, pp. 19557–19567, 2015, doi: 10.1039/C5NR04465K.

[43] L. Luo, Y. Liang, E. S. Erichsen, and R. Anwander, “Monodisperse mesoporous silica nanoparticles of distinct topology,” *J. Colloid Interface Sci.*, vol. 495, pp. 84–93, 2017, doi: 10.1016/j.jcis.2017.01.107.

[44] S. Liu *et al.*, “The Influence of the Alcohol Concentration on the Structural Ordering of Mesoporous Silica: Cosurfactant versus Cosolvent,” *J. Phys. Chem. B*, vol. 107, no. 38, pp. 10405–10411, 2003, doi: 10.1021/jp034410w.

[45] S. Kachbouri, N. Mnasri, E. Elaloui, and Y. Moussaoui, “Tuning particle morphology of mesoporous silica nanoparticles for adsorption of dyes from aqueous solution,” *J. Saudi Chem. Soc.*, vol. 22, no. 4, pp. 405–415, 2018, doi: 10.1016/j.jscs.2017.08.005.

[46] K. S. Rao, K. El-Hami, T. Kodaki, K. Matsushige, and K. Makino, “A novel method for synthesis of silica nanoparticles,” *J. Colloid Interface Sci.*, vol. 289, no. 1, pp. 125–131, 2005, doi: 10.1016/j.jcis.2005.02.019.

[47] L. M. Rossi, L. Shi, F. H. Quina, and Z. Rosenzweig, “Stöber synthesis of monodispersed luminescent silica nanoparticles for bioanalytical assays,” *Langmuir*, vol. 21, no. 10, pp. 4277–4280, 2005, doi: 10.1021/la0504098.

[48] P. Khodaee, N. Najmoddin, and S. Shahrad, “The effect of ethanol and temperature on the structural properties of mesoporous silica synthesized by the sol-gel method,” *J. Tissues Mater.*, vol. 1, no. 1, pp. 10–17, 2018, doi: 10.22034/JTM.2018.67254.

[49] J. Gu, W. Fan, A. Shimojima, and T. Okubo, “Organic–Inorganic Mesoporous Nanocarriers Integrated with Biogenic Ligands,” *Small*, vol. 3, no. 10, pp. 1740–1744, Oct. 2007, doi: 10.1002/smll.200700311.

[50] W. Stöber, A. Fink, and E. Bohn, “Controlled growth of monodisperse silica spheres in the micron size range,” *J. Colloid Interface Sci.*, vol. 26, no. 1, pp. 62–69, Jan. 1968, doi: 10.1016/0021-9797(68)90272-5.

[51] T. N. M. Bernards, M. J. van Bommel, and A. H. Boonstra, “Hydrolysis-condensation processes of the tetra-alkoxysilanes TPOS, TEOS and TMOS in some alcoholic solvents,” *J. Non. Cryst. Solids*, vol. 134, no. 1–2, pp. 1–13, 1991, doi: 10.1016/0022-3093(91)90005-Q.

[52] H. Yamada, C. Urata, E. Yamamoto, S. Higashitamori, Y. Yamauchi, and K. Kuroda, “Effective Use of Alkoxysilanes with Different Hydrolysis Rates for Particle Size Control of Aqueous Colloidal Mesostructured and Mesoporous Silica Nanoparticles by the Seed-Growth Method,” *ChemNanoMat*, vol. 1, no. 3, pp. 194–202, Jul. 2015, doi: 10.1002/cnma.201500010.

[53] M. J. Hollamby, D. Borisova, P. Brown, J. Eastoe, I. Grillo, and D. Shchukin, “Growth of mesoporous silica nanoparticles monitored by time-resolved small-angle neutron scattering,” *Langmuir*, vol. 28, no. 9, pp. 4425–4433, 2012, doi: 10.1021/la203097x.

[54] H. Yamada, C. Urata, Y. Aoyama, S. Osada, Y. Yamauchi, and K. Kuroda, “Preparation of colloidal mesoporous silica nanoparticles with different diameters and their unique degradation behavior in static aqueous systems,” *Chem. Mater.*, vol. 24, no. 8, pp. 1462–1471, Apr. 2012, doi: 10.1021/cm3001688.

[55] J. Frasch, B. Lebeau, M. Soulard, J. Patarin, and R. Zana, “In situ investigations on cetyltrimethylammonium surfactant/silicate systems, precursors of organized mesoporous MCM-41-type siliceous materials,” *Langmuir*, vol. 16, no. 23, pp. 9049–9057, 2000, doi: 10.1021/la000295u.

[56] S. Kerkhofs *et al.*, “Self-Assembly of Pluronic F127 - Silica Spherical Core-Shell Nanoparticles in Cubic Close-Packed Structures,” *Chem. Mater.*, vol. 27, no. 15, pp. 5161–5169, 2015, doi: 10.1021/acs.chemmater.5b01772.

[57] D. R. Dunphy, P. H. Sheth, F. L. Garcia, and C. J. Brinker, “Enlarged pore size in mesoporous silica films templated by pluronic F127: Use of poloxamer mixtures and increased template/SiO2 ratios in materials synthesized by evaporation-induced self-assembly,” *Chem. Mater.*, vol. 27, no. 1, pp. 75–84, 2015, doi: 10.1021/cm5031624.

[58] S. A. El-Safty and J. Evans, “Formation of highly ordered mesoporous silica materials adopting lyotropic liquid crystal mesophases,” *J. Mater. Chem.*, vol. 12, no. 1, pp. 117–123, 2002, doi: 10.1039/b106077p.

[59] A. Sayari and Y. Yang, “Nonionic oligomeric polymer directed synthesis of highly ordered large pore periodic mesoporous organosilica,” *Chem. Commun.*, no. 21, pp. 2582–2583, 2002, doi: 10.1039/b208512g.

[60] M. Ganesh and S. G. Lee, “Synthesis, Characterization and Drug Release Capability of New Cost Effective Mesoporous Silica Nano Particle for Ibuprofen Drug Delivery,” *Int. J. Control Autom.*, vol. 6, no. 5, pp. 207–216, 2013, doi: 10.14257/ijca.2013.6.5.20.

[61] E. Prouzet, F. Cot, G. Nabias, A. Larbot, P. Kooyman, and T. J. Pinnavaia, “Assembly of mesoporous silica molecular sieves based on nonionic ethoxylated sorbitan esters as structure directors,” *Chem. Mater.*, vol. 11, no. 6, pp. 1498–1503, 1999, doi: 10.1021/cm9810281.

[62] Y. S. Lin and C. L. Haynes, “Impacts of mesoporous silica nanoparticle size, pore ordering, and pore integrity on hemolytic activity,” *J. Am. Chem. Soc.*, vol. 132, no. 13, pp. 4834–4842, 2010, doi: 10.1021/ja910846q.

[63] S. Williams *et al.*, “Nanoporous silica nanoparticles as biomaterials: evaluation of different strategies for the functionalization with polysialic acid by step-by-step cytocompatibility testing,” *J. Mater. Sci. Mater. Med.*, vol. 26, no. 3, 2015, doi: 10.1007/s10856-015-5409-3.

[64] S. Han, W. Hou, W. Dang, J. Xu, J. Hu, and D. Li, “Synthesis of rod-like mesoporous silica using mixed surfactants of cetyltrimethylammonium bromide and cetyltrimethylammonium chloride as templates,” *Mater. Lett.*, vol. 57, no. 29, pp. 4520–4524, 2003, doi: 10.1016/S0167-577X(03)00355-0.

[65] N. Mizoshita and H. Tanaka, “Interface-assisted synthesis of mesoporous silica nanoparticles using neat tetraalkoxysilanes,” *Microporous Mesoporous Mater.*, vol. 239, pp. 1–8, 2017, doi: 10.1016/j.micromeso.2016.09.025.

[66] K. Möller and T. Bein, “Talented mesoporous silica nanoparticles,” *Chem. Mater.*, vol. 29, no. 1, pp. 371–388, 2017, doi: 10.1021/acs.chemmater.6b03629.

[67] X. Du, L. Xiong, S. Dai, F. Kleitz, and S. Zhang Qiao, “Intracellular microenvironment-responsive dendrimer-like mesoporous nanohybrids for traceable, effective, and safe gene delivery,” *Adv. Funct. Mater.*, vol. 24, no. 48, pp. 7627–7637, 2014, doi: 10.1002/adfm.201402408.

[68] N. Venkatathri, “Synthesis of mesoporous silica nanosphere using different templates,” *Solid State Commun.*, vol. 143, no. 10, pp. 493–497, 2007, doi: 10.1016/j.ssc.2007.06.017.

[69] J. G. Wang, Q. Xiao, H. J. Zhou, P. C. Sun, D. T. Ding, and T. H. Chen, “Anionic surfactant-

templated mesoporous silica (AMS) nano-spheres with radially oriented mesopores," *J. Colloid Interface Sci.*, vol. 323, no. 2, pp. 332–337, 2008, doi: 10.1016/j.jcis.2008.04.044.

[70] N. K. Raman, M. T. Anderson, and C. J. Brinker, "Template-based approaches to the preparation of amorphous, nanoporous silica," *Chemistry of Materials*, vol. 8, no. 8. American Chemical Society, pp. 1682–1701, 1996, doi: 10.1021/cm960138+.

[71] Y. Wei *et al.*, "A non-surfactant templating route to mesoporous silica materials," *Adv. Mater.*, vol. 10, no. 4, pp. 313–316, 1998, doi: 10.1002/(SICI)1521-4095(199803)10:4<313::AID-ADMA313>3.0.CO;2-M.

[72] J. Bin Pang, K. Y. Qiu, J. Xu, Y. Wei, and J. Chen, "Synthesis of mesoporous silica materials via nonsurfactant urea-templated sol-gel reactions," *J. Inorg. Organomet. Polym. Mater.*, vol. 10, no. 1, pp. 39–49, 2000, doi: 10.1023/A:1009404415925.

[73] J. Y. Zheng, J. Bin Pang, K. Y. Qiu, and Y. Wei, "Synthesis of mesoporous silica materials via nonsurfactant templated sol-gel route by using mixture of organic compounds as template," *J. Sol-Gel Sci. Technol.*, vol. 24, no. 1, pp. 81–88, 2002, doi: 10.1023/A:1015117717642.

[74] F. Catalano and P. P. Pompa, "Design Rules for Mesoporous Silica toward the Nanosize: A Systematic Study," *ACS Appl. Mater. Interfaces*, vol. 11, no. 50, pp. 47237–47246, 2019, doi: 10.1021/acsami.9b16135.

[75] Z. A. Qiao, L. Zhang, M. Guo, Y. Liu, and Q. Huo, "Synthesis of mesoporous silica nanoparticles via controlled hydrolysis and condensation of silicon alkoxide," *Chem. Mater.*, vol. 21, no. 16, pp. 3823–3829, 2009, doi: 10.1021/cm901335k.

[76] Z. Zhang, A. Mayoral, and I. Melián-Cabrera, "Protocol optimization for the mild detemplation of mesoporous silica nanoparticles resulting in enhanced texture and colloidal stability," *Microporous Mesoporous Mater.*, vol. 220, pp. 110–119, Jan. 2016, doi: 10.1016/j.micromeso.2015.08.026.

[77] E. Yamamoto, M. Kitahara, T. Tsumura, and K. Kuroda, "Preparation of size-controlled monodisperse colloidal mesoporous silica nanoparticles and fabrication of colloidal crystals," *Chem. Mater.*, vol. 26, no. 9, pp. 2927–2933, 2014, doi: 10.1021/cm500619p.

[78] K. Möller, J. Kobler, and T. Bein, "Colloidal suspensions of mercapto-functionalized nanosized mesoporous silica," *J. Mater. Chem.*, vol. 17, no. 7, pp. 624–631, 2007, doi: 10.1039/B611931J.

[79] D. Das *et al.*, "Synthesis and physicochemical characterization of mesoporous sio2 nanoparticles," *J. Nanomater.*, vol. 2014, 2014, doi: 10.1155/2014/176015.

[80] J. Schmitt *et al.*, "Outset of the Morphology of Nanostructured Silica Particles during Nucleation Followed by Ultrasmall-Angle X-ray Scattering," *Langmuir*, vol. 32, no. 20, pp. 5162–5172, 2016, doi: 10.1021/acs.langmuir.6b00572.

[81] H. B. S. Chan, P. M. Budd, and T. V. De Naylor, "Control of mesostructured silica particle morphology," *J. Mater. Chem.*, vol. 11, no. 3, pp. 951–957, 2001, doi: 10.1039/b005713o.

[82] M. Varache, I. Bezverkhyy, F. Bouyer, R. Chassagnon, F. Baras, and F. Bouyer, "Improving structural stability of water-dispersed MCM-41 silica nanoparticles through post-synthesis pH aging process," *J. Nanoparticle Res.*, vol. 17, no. 9, 2015, doi: 10.1007/s11051-015-3147-6.

[83] N. Hao, L. Li, and F. Tang, “Facile preparation of ellipsoid-like MCM-41 with parallel channels along the short axis for drug delivery and assembly of Ag nanoparticles for catalysis,” *J. Mater. Chem. A*, vol. 2, no. 30, pp. 11565–11568, 2014, doi: 10.1039/c4ta01820f.

[84] Z. Nan, X. Xue, W. Hou, X. Yan, and S. Han, “Fabrication of MCM-41 mesoporous silica through the self-assembly supermolecule of β-CD and CTAB,” *J. Solid State Chem.*, vol. 180, no. 2, pp. 780–784, 2007, doi: 10.1016/j.jssc.2006.11.011.

[85] G. Lelong, S. Bhattacharyya, S. Kline, T. Cacciaguerra, M. A. Gonzalez, and M.-L. L. Saboungi, “Effect of Surfactant Concentration on the Morphology and Texture of MCM-41 Materials,” *J. Phys. Chem.*, vol. 112, no. 29, pp. 10674–10680, Jul. 2008, doi: 10.1021/jp800898n.

[86] M. Varache, I. Bezverkhyy, L. Saviot, F. Bouyer, F. Baras, and F. Bouyer, “Optimization of MCM-41 type silica nanoparticles for biological applications: Control of size and absence of aggregation and cell cytotoxicity,” *J. Non. Cryst. Solids*, vol. 408, pp. 87–97, 2015, doi: 10.1016/j.jnoncrysol.2014.10.020.

[87] F. D. Osterholtz and E. R. Pohl, “Kinetics of the Hydrolysis and Condensation of Organofunctional Alkoxysilanes: A Review,” *J. Adhes. Sci. Technol.*, vol. 6, no. 1, pp. 127–149, 1992, doi: 10.1163/156856192X00106.

[88] A. A. Issa and A. S. Luyt, “Kinetics of alkoxysilanes and organoalkoxysilanes polymerization: A review,” *Polymers (Basel).*, vol. 11, no. 3, 2019, doi: 10.3390/polym11030537.

[89] J. Wen and G. L. Wilkes, “Organic/inorganic hybrid network materials by the sol-gel approach,” *Chem. Mater.*, vol. 8, no. 8, pp. 1667–1681, 1996, doi: 10.1021/cm9601143.

[90] S. H. Wu and H. P. Lin, “Synthesis of mesoporous silica nanoparticles,” *Chem. Soc. Rev.*, vol. 42, no. 9, pp. 3862–3875, 2013, doi: 10.1039/c3cs35405a.

[91] F. Lu, S. H. Wu, Y. Hung, and C. Y. Mou, “Size effect on cell uptake in well-suspended, uniform mesoporous silica nanoparticles,” *Small*, vol. 5, no. 12, pp. 1408–1413, Jun. 2009, doi: 10.1002/smll.200900005.

[92] B. Arechabala, C. Coiffard, P. Rivalland, L. J. M. Coiffard, and Y. De Roeck-Holtzhauer, “Comparison of cytotoxicity of various surfactants tested on normal human fibroblast cultures using the neutral red test, MTT assay and LDH release,” *J. Appl. Toxicol.*, vol. 19, no. 3, pp. 163–165, 1999, doi: 10.1002/(SICI)1099-1263(199905/06)19:3<163::AID-JAT561>3.0.CO;2-H.

[93] M. Barczak, “Template removal from mesoporous silicas using different methods as a tool for adjusting their properties,” *New J. Chem.*, vol. 42, no. 6, pp. 4182–4191, 2018, doi: 10.1039/c7nj04642a.

[94] A. M. Basso, B. P. Nicola, K. Bernardo-Gusmão, and S. B. C. Pergher, “Tunable effect of the calcination of the silanol groups of KIT-6 and SBA-15 mesoporous materials,” *Appl. Sci.*, vol. 10, no. 3, pp. 1–16, 2020, doi: 10.3390/app10030970.

[95] A. Lodha *et al.*, “Synthesis of mesoporous silica nanoparticles and drug loading of poorly water soluble drug cyclosporin A,” *J. Pharm. Bioallied Sci.*, vol. 4, no. SUPPL., pp. 92–94, 2012, doi: 10.4103/0975-7406.94153.

[96] S. S. Park, M. H. Jung, Y. S. Lee, J. H. Bae, S. H. Kim, and C. S. Ha, “Functionalised mesoporous silica nanoparticles with excellent cytotoxicity against various cancer cells

for pH-responsive and controlled drug delivery," *Mater. Des.*, vol. 184, p. 108187, 2019, doi: 10.1016/j.matdes.2019.108187.

[97] N. Lang and A. Tuel, "A fast and efficient ion-exchange procedure to remove surfactant molecules from MCM-41 materials," *Chem. Mater.*, vol. 16, no. 10, pp. 1961–1966, 2004, doi: 10.1021/cm030633n.

[98] F. Raji and M. Pakizeh, "Study of Hg(II) species removal from aqueous solution using hybrid ZnCl 2 -MCM-41 adsorbent," *Appl. Surf. Sci.*, vol. 282, pp. 415–424, Oct. 2013, doi: 10.1016/j.apsusc.2013.05.145.

[99] J. Kecht and T. Bein, "Functionalization of Colloidal Mesoporous Silica by Metalorganic Reagents," *Langmuir*, vol. 24, no. 24, pp. 14209–14214, Dec. 2008, doi: 10.1021/la802115n.

[100] D. Tarn, C. E. Ashley, M. Xue, E. C. Carnes, J. I. Zink, and C. J. Brinker, "Mesoporous Silica Nanoparticle Nanocarriers: Biofunctionality and Biocompatibility," *Acc. Chem. Res.*, vol. 46, no. 3, pp. 792–801, Mar. 2013, doi: 10.1021/ar3000986.

[101] A. Stein, B. J. Melde, and R. C. Schroden, "Hybrid inorganic-organic mesoporous silicates-nanoscopic reactors coming of age," *Adv. Mater.*, vol. 12, no. 19, pp. 1403–1419, 2000, doi: 10.1002/1521-4095(200010)12:19<1403::AID-ADMA1403>3.0.CO;2-X.

[102] I. I. Slowing, J. L. Vivero-Escoto, B. G. Trewyn, and V. S. Y. Lin, "Mesoporous silica nanoparticles: Structural design and applications," *J. Mater. Chem.*, vol. 20, no. 37, pp. 7924–7937, 2010, doi: 10.1039/c0jm00554a.

[103] T. Asefa and Z. Tao, "Biocompatibility of Mesoporous Silica Nanoparticles," 2012, doi: 10.1021/tx300166u.

[104] Y. R. Han, J. W. Park, H. Kim, H. Ji, S. H. Lim, and C. H. Jun, "A one-step co-condensation method for the synthesis of well-defined functionalized mesoporous SBA-15 using trimethallylsilanes as organosilane sources," *Chem. Commun.*, vol. 51, no. 96, pp. 17084–17087, 2015, doi: 10.1039/c5cc07286g.

[105] T. Suteewong, H. Sai, M. Bradbury, L. A. Estroff, S. M. Gruner, and U. Wiesner, "Synthesis and formation mechanism of aminated mesoporous silica nanoparticles," *Chem. Mater.*, vol. 24, no. 20, pp. 3895–3905, 2012, doi: 10.1021/cm301857e.

[106] R. P. Hodgkins, A. E. Garcia-Bennett, and P. A. Wright, "Structure and morphology of propylthiol-functionalised mesoporous silicas templated by non-ionic triblock copolymers," *Microporous Mesoporous Mater.*, vol. 79, no. 1–3, pp. 241–252, 2005, doi: 10.1016/j.micromeso.2004.10.036.

[107] M. Bouchoucha, M.-F. Côté, R. C.-Gaudreault, M.-A. Fortin, and F. Kleitz, "Size-Controlled Functionalized Mesoporous Silica Nanoparticles for Tunable Drug Release and Enhanced Anti-Tumoral Activity," *Chem. Mater.*, vol. 28, no. 12, pp. 4243–4258, Jun. 2016, doi: 10.1021/acs.chemmater.6b00877.

[108] A. Watermann and J. Brieger, "Mesoporous silica nanoparticles as drug delivery vehicles in cancer," *Nanomaterials*, vol. 7, no. 7, 2017, doi: 10.3390/nano7070189.

[109] C. M. Dawidczyk, L. M. Russell, and P. C. Searson, "Nanomedicines for cancer therapy: State-of-the-art and limitations to pre-clinical studies that hinder future developments," *Front. Chem.*, vol. 2, no. AUG, pp. 1–13, 2014, doi: 10.3389/fchem.2014.00069.

[110] D. Tarn, C. E. Ashley, M. Xue, E. C. Carnes, J. I. Zink, and C. Jeffrey Brinker, “Mesoporous Silica Nanoparticle Nanocarriers-Biofunctionality and Biocompatibility,” *Acc Chem Res*, vol. 46, no. 3, pp. 792–801, 2013, doi: 10.1021/ar3000986.

[111] J. E. Lee, N. Lee, T. Kim, J. Kim, and T. Hyeon, “Multifunctional mesoporous silica nanocomposite nanoparticles for theranostic applications,” *Acc. Chem. Res.*, vol. 44, no. 10, pp. 893–902, Oct. 2011, doi: 10.1021/ar2000259.

[112] Q. Zhang, I. Lee, J. B. Joo, F. Zaera, and Y. Yin, “Core–Shell Nanostructured Catalysts,” *Acc. Chem. Res.*, vol. 46, no. 8, pp. 1816–1824, Aug. 2013, doi: 10.1021/ar300230s.

[113] L. Yu, H. Lin, X. Lu, and Y. Chen, “Multifunctional Mesoporous Silica Nanoprobes: Material Chemistry–Based Fabrication and Bio-Imaging Functionality,” *Adv. Ther.*, vol. 1, no. 8, p. 1800078, Dec. 2018, doi: 10.1002/adtp.201800078.

[114] Y. Klichko *et al.*, “Mesostructured silica for optical functionality, nanomachines, and drug delivery,” in *Journal of the American Ceramic Society*, Jan. 2009, vol. 92, no. SUPPL. 1, p. s2, doi: 10.1111/j.1551-2916.2008.02722.x.

[115] D. Kim, K. Shin, S. G. Kwon, and T. Hyeon, “Synthesis and Biomedical Applications of Multifunctional Nanoparticles,” *Adv. Mater.*, vol. 30, no. 49, p. 1802309, Dec. 2018, doi: 10.1002/adma.201802309.

[116] G. Wang and X. Su, “The synthesis and bio-applications of magnetic and fluorescent bifunctional composite nanoparticles,” *Analyst*, vol. 136, no. 9. Royal Society of Chemistry, pp. 1783–1798, May 07, 2011, doi: 10.1039/c1an15036g.

[117] M. Thommes *et al.*, “Physisorption of gases, with special reference to the evaluation of surface area and pore size distribution (IUPAC Technical Report),” *Pure Appl. Chem.*, vol. 87, no. 9–10, pp. 1051–1069, Oct. 2015, doi: 10.1515/pac-2014-1117.

[118] X. Deng, K. Chen, and H. Tü Ysü, “Protocol for the Nanocasting Method: Preparation of Ordered Mesoporous Metal Oxides,” *Chem. Mater*, vol. 29, p. 47, 2017, doi: 10.1021/acs.chemmater.6b02645.

[119] E. Y. Trofimova, D. A. Kurdyukov, Y. A. Kukushkina, M. A. Yagovkina, and V. G. Golubev, “Synthesis of monodispersed mesoporous spheres of submicron size amorphous silica,” *Glas. Phys. Chem.*, vol. 37, no. 4, pp. 378–384, Aug. 2011, doi: 10.1134/S108765961104016X.

[120] V. A. Hackley and J. D. Clogston, “Measuring the hydrodynamic size of nanoparticles in aqueous media using batch-mode dynamic light scattering.,” *Methods Mol. Biol.*, vol. 697, pp. 35–52, 2011, doi: 10.1007/978-1-60327-198-1_4.

[121] S. E. Harding, “Chapter 7 Protein hydrodynamics,” vol. 2, 1999, pp. 271–305.

[122] A. Lázaro García, “Nano-silica production at low temperatures from the dissolution of olovine synthesis, tailoring and modelling,” 2014, Accessed: Nov. 27, 2021. [Online]. Available: https://www.researchgate.net/publication/263414178_Nano-silica_production_at_low_temperatures_from_the_dissolution_of_olivine_-_Synthesis_tailoring_and_modelling.

[123] K. M. Hello, A. A. Ibrahim, J. K. Shneine, and J. N. Appaturi, “Simple method for functionalization of silica with alkyl silane and organic ligands,” *South African J. Chem. Eng.*, vol. 25, no. April, pp. 159–168, 2018, doi: 10.1016/j.sajce.2018.05.001.

[124] V. V. Potapov and L. T. Zhuravlev, “Temperature dependence of the concentration of

silanol groups in silica precipitated from a hydrothermal solution," *Glas. Phys. Chem.*, vol. 31, no. 5, pp. 661–670, Sep. 2005, doi: 10.1007/s10720-005-0111-z.

[125] E. P. Ng, J. Y. Goh, T. C. Ling, and R. R. Mukti, "Eco-friendly synthesis for MCM-41 nanoporous materials using the non-reacted reagents in mother liquor," *Nanoscale Res. Lett.*, vol. 8, no. 1, pp. 1–8, Dec. 2013, doi: 10.1186/1556-276X-8-120.

[126] M. Saha, "Nanomedicine: Promising Tiny Machine for the Healthcare in Future-A Review," *Oman Med. J.*, vol. 24, no. 4, pp. 242–247, 2009, doi: 10.5001/omj.2009.50.

[127] G. Bozzuto and A. Molinari, "Liposomes as nanomedical devices," *Int. J. Nanomedicine*, vol. 10, pp. 975–999, 2015, doi: 10.2147/IJN.S68861.

[128] K. Kopeckova *et al.*, "Nanodrugs used in cancer therapy," *Biomed. Pap.*, vol. 163, no. 2, pp. 122–131, 2019, doi: 10.5507/bp.2019.010.

[129] C. Fornaguera and C. Solans, "Methods for the in vitro characterization of nanomedicines—biological component interaction," *J. Pers. Med.*, vol. 7, no. 1, 2017, doi: 10.3390/jpm7010002.

[130] R. Rajagopalan and J. V. Yakhmi, *Chapter 8 - Nanotechnological approaches toward cancer chemotherapy*. Elsevier Inc., 2017.

[131] E. Piktel, K. Niemirowicz, M. Watek, T. Wollny, P. Deptuła, and R. Bucki, "Recent insights in nanotechnology-based drugs and formulations designed for effective anti-cancer therapy," *J. Nanobiotechnology*, vol. 14, no. 1, pp. 1–23, 2016, doi: 10.1186/s12951-016-0193-x.

[132] S. Mühlebach, "Regulatory challenges of nanomedicines and their follow-on versions: A generic or similar approach?," *Adv. Drug Deliv. Rev.*, vol. 131, pp. 122–131, 2018, doi: 10.1016/j.addr.2018.06.024.

[133] D. Bobo, K. J. Robinson, J. Islam, K. J. Thurecht, and S. R. Corrie, "Nanoparticle-Based Medicines: A Review of FDA-Approved Materials and Clinical Trials to Date," *Pharm. Res.*, vol. 33, no. 10, pp. 2373–2387, 2016, doi: 10.1007/s11095-016-1958-5.

[134] S. Das, S. Mitra, S. M. P. Khurana, and N. Debnath, "Nanomaterials for biomedical applications," *Front. Life Sci.*, vol. 7, no. 3–4, pp. 90–98, 2013, doi: 10.1080/21553769.2013.869510.

[135] Y. H. Choi and H. K. Han, "Nanomedicines: current status and future perspectives in aspect of drug delivery and pharmacokinetics," *J. Pharm. Investig.*, vol. 48, no. 1, pp. 43–60, 2018, doi: 10.1007/s40005-017-0370-4.

[136] I. Garrido-Cano *et al.*, "Biocompatibility and internalization assessment of bare and functionalised mesoporous silica nanoparticles," *Microporous Mesoporous Mater.*, vol. 310, Jan. 2021, doi: 10.1016/j.micromeso.2020.110593.

[137] L. Sercombe, T. Veerati, F. Moheimani, S. Y. Wu, A. K. Sood, and S. Hua, "Advances and challenges of liposome assisted drug delivery," *Front. Pharmacol.*, vol. 6, no. DEC, pp. 1–13, 2015, doi: 10.3389/fphar.2015.00286.

[138] Y. Hu, Y. Hou, H. Wang, and H. Lu, "Polysarcosine as an Alternative to PEG for Therapeutic Protein Conjugation," *Bioconjug. Chem.*, vol. 29, no. 7, pp. 2232–2238, Jul. 2018, doi: 10.1021/acs.bioconjchem.8b00237.

[139] C. M. Dawidczyk *et al.*, "State-of-the-art in design rules for drug delivery platforms: Lessons learned from FDA-approved nanomedicines," *J. Control. Release*, vol. 187, pp.

133–144, 2014, doi: 10.1016/j.jconrel.2014.05.036.

[140] M. Björnmalm, K. J. Thurecht, M. Michael, A. M. Scott, and F. Caruso, “Bridging Bio-Nano Science and Cancer Nanomedicine,” *ACS Nano*, vol. 11, no. 10, pp. 9594–9613, 2017, doi: 10.1021/acsnano.7b04855.

[141] S. Bayda *et al.*, “Inorganic Nanoparticles for Cancer Therapy: A Transition from Lab to Clinic,” *Curr. Med. Chem.*, vol. 25, no. 34, pp. 4269–4303, 2017, doi: 10.2174/0929867325666171229141156.

[142] D. M. Oliveira and A. S. Andrada, “Synthesis of ordered mesoporous silica MCM-41 with controlled morphology for potential application in controlled drug delivery systems,” *Cerâmica*, vol. 65, no. 374, pp. 170–179, Jun. 2019, doi: 10.1590/0366-69132019653742509.

[143] V. Torchilin, “Multifunctional and stimuli-sensitive pharmaceutical nanocarriers,” *Eur. J. Pharm. Biopharm.*, vol. 71, no. 3, pp. 431–444, 2009, doi: 10.1016/j.ejpb.2008.09.026.

[144] V. P. Torchilin, “Recent advances with liposomes as pharmaceutical carriers,” *Nat. Rev. Drug Discov.*, vol. 4, no. 2, pp. 145–160, 2005, doi: 10.1038/nrd1632.

[145] F. Tang, L. Li, and D. Chen, “Mesoporous silica nanoparticles: Synthesis, biocompatibility and drug delivery,” *Adv. Mater.*, vol. 24, no. 12, pp. 1504–1534, 2012, doi: 10.1002/adma.201104763.

[146] M. Talelli *et al.*, “Nanobody - Shell functionalized thermosensitive core-crosslinked polymeric micelles for active drug targeting,” *J. Control. Release*, vol. 151, no. 2, pp. 183–192, Apr. 2011, doi: 10.1016/j.jconrel.2011.01.015.

[147] Y. Dong and Y. Mao, “DNA Origami as Scaffolds for Self-Assembly of Lipids and Proteins,” *ChemBioChem*, vol. 20, no. 19, pp. 2422–2431, 2019, doi: 10.1002/cbic.201900073.

[148] M. Jarvis, V. Krishnan, and S. Mitragotri, “Nanocrystals: A perspective on translational research and clinical studies,” *Bioeng. Transl. Med.*, vol. 4, no. 1, pp. 5–16, 2019, doi: 10.1002/btm2.10122.

[149] M.-R. Nejadmoghaddam, A. Minai-Tehrani, R. Ghahremanzadeh, M. Mahmoudi, R. Dinarvand, and A.-H. Zarnani, “Antibody-Drug Conjugates: Possibilities and Challenges.,” *Avicenna J. Med. Biotechnol.*, vol. 11, no. 1, pp. 3–23, 2019, Accessed: Sep. 16, 2020. [Online]. Available: https://pubmed.ncbi.nlm.nih.gov/30800238/.

[150] C. Peters and S. Brown, “Antibody–drug conjugates as novel anti-cancer chemotherapeutics,” *Biosci. Rep.*, vol. 35, no. 4, Aug. 2015, doi: 10.1042/BSR20150089.

[151] G. S. Hamilton, “Antibody-drug conjugates for cancer therapy: The technological and regulatory challenges of developing drug-biologic hybrids,” *Biologicals*, vol. 43, no. 5, pp. 318–332, Sep. 2015, doi: 10.1016/j.biologicals.2015.05.006.

[152] R. Koyani, J. Pérez-Robles, R. D. Cadena-Nava, and R. Vazquez-Duhalt, “Biomaterial-based nanoreactors, an alternative for enzyme delivery,” *Nanotechnol. Rev.*, vol. 6, no. 5, pp. 405–419, 2017, doi: 10.1515/ntrev-2016-0071.

[153] K. Cheng, Q. Kang, and X. Zhao, “Biogenic nanoparticles as immunomodulator for tumor treatment,” *Wiley Interdiscip. Rev. Nanomedicine Nanobiotechnology*, no. April, pp. 1–19, 2020, doi: 10.1002/wnan.1646.

[154] J. F. C. Steele *et al.*, “Synthetic plant virology for nanobiotechnology and

nanomedicine," *Wiley Interdiscip. Rev. Nanomedicine Nanobiotechnology*, vol. 9, no. 4, pp. 1–18, 2017, doi: 10.1002/wnan.1447.

[155] Z. Ju and W. Sun, "Drug delivery vectors based on filamentous bacteriophages and phage-mimetic nanoparticles," *Drug Deliv.*, vol. 24, no. 1, pp. 1898–1908, 2017, doi: 10.1080/10717544.2017.1410259.

[156] N. Badrinath, J. Heo, and S. Y. Yoo, "Viruses as nanomedicine for cancer," *Int. J. Nanomedicine*, vol. 11, pp. 4835–4847, 2016, doi: 10.2147/IJN.S116447.

[157] N. S. Kulkarni, Y. Guererro, N. Gupta, A. Muth, and V. Gupta, "Exploring potential of quantum dots as dual modality for cancer therapy and diagnosis," *J. Drug Deliv. Sci. Technol.*, vol. 49, no. October 2018, pp. 352–364, 2019, doi: 10.1016/j.jddst.2018.12.010.

[158] T. T. Hoang Thi, V. Du Cao, T. N. Q. Nguyen, D. T. Hoang, V. C. Ngo, and D. H. Nguyen, "Functionalized mesoporous silica nanoparticles and biomedical applications," *Mater. Sci. Eng. C*, vol. 99, no. November 2017, pp. 631–656, 2019, doi: 10.1016/j.msec.2019.01.129.

[159] X. Huang, X. Teng, D. Chen, F. Tang, and J. He, "The effect of the shape of mesoporous silica nanoparticles on cellular uptake and cell function," *Biomaterials*, vol. 31, no. 3, pp. 438–448, Jan. 2010, doi: 10.1016/j.biomaterials.2009.09.060.

[160] A. K. Varkouhi, M. Scholte, G. Storm, and H. J. Haisma, "Endosomal escape pathways for delivery of biologicals," *J. Control. Release*, vol. 151, no. 3, pp. 220–228, 2011, doi: 10.1016/j.jconrel.2010.11.004.

[161] N. Nishiyama, Arnida, W. D. Jang, K. Date, K. Miyata, and K. Kataoka, "Photochemical enhancement of transgene expression by polymeric micelles incorporating plasmid DNA and dendrimer-based photosensitizer," *J. Drug Target.*, vol. 14, no. 6, pp. 413–424, 2006, doi: 10.1080/10611860600834508.

[162] L. Prasmickaite, A. Høgset, and K. Berg, "Evaluation of Different Photosensitizers for Use in Photochemical Gene Transfection¶," *Photochem. Photobiol.*, vol. 73, no. 4, p. 388, 2001, doi: 10.1562/0031-8655(2001)073<0388:eodpfu>2.0.co;2.

[163] L.-P. Wu, D. Wang, and Z. Li, "Grand challenges in nanomedicine," *Mater. Sci. Eng. C*, vol. 106, p. 110302, Jan. 2020, doi: 10.1016/j.msec.2019.110302.

[164] A. C. Anselmo and S. Mitragotri, "Nanoparticles in the clinic: An update," *Bioeng. Transl. Med.*, vol. 4, no. 3, Sep. 2019, doi: 10.1002/btm2.10143.

[165] R. Foulkes, E. Man, J. Thind, S. Yeung, A. Joy, and C. Hoskins, "The regulation of nanomaterials and nanomedicines for clinical application: current and future perspectives," *Biomater. Sci.*, vol. 8, no. 17, pp. 4653–4664, Sep. 2020, doi: 10.1039/D0BM00558D.

[166] A. J. McGoron, "Perspectives on the Future of Nanomedicine to Impact Patients: An Analysis of US Federal Funding and Interventional Clinical Trials," *Bioconjug. Chem.*, vol. 31, no. 3, pp. 436–447, Mar. 2020, doi: 10.1021/acs.bioconjchem.9b00818.

[167] P. L. Chariou, O. A. Ortega-Rivera, and N. F. Steinmetz, "Nanocarriers for the Delivery of Medical, Veterinary, and Agricultural Active Ingredients," *ACS Nano*, vol. 14, no. 3, pp. 2678–2701, Mar. 2020, doi: 10.1021/acsnano.0c00173.

[168] R. Friedman, "Nano dot technology enters clinical trials.," *Journal of the National*

*Cancer Institute*, vol. 103, no. 19. J Natl Cancer Inst, pp. 1428–1429, Oct. 05, 2011, doi: 10.1093/jnci/djr400.

[169] A. N. Kharlamov, A. E. Tyurnina, V. S. Veselova, O. P. Kovtun, V. Y. Shur, and J. L. Gabinsky, "Silica-gold nanoparticles for atheroprotective management of plaques: Results of the NANOM-FIM trial," *Nanoscale*, vol. 7, no. 17, pp. 8003–8015, May 2015, doi: 10.1039/c5nr01050k.

[170] "Targeted Silica Nanoparticles for Real-Time Image-Guided Intraoperative Mapping of Nodal Metastases - Full Text View - ClinicalTrials.gov," 2020.

[171] A. J. Paula *et al.*, "Topography-driven bionano-interactions on colloidal silica nanoparticles," 2014, doi: 10.1021/am405594q.

[172] S. Wilhelm *et al.*, "Analysis of nanoparticle delivery to tumours," *Nature Reviews Materials*, vol. 1, no. 5. Nature Publishing Group, pp. 1–12, Apr. 26, 2016, doi: 10.1038/natrevmats.2016.14.

[173] K. Park, "Facing the truth about nanotechnology in drug delivery," *ACS Nano*, vol. 7, no. 9. American Chemical Society, pp. 7442–7447, Sep. 24, 2013, doi: 10.1021/nn404501g.

[174] R. Narayan, U. Y. Nayak, A. M. Raichur, and S. Garg, "Mesoporous silica nanoparticles: A comprehensive review on synthesis and recent advances," *Pharmaceutics*, vol. 10, no. 3, pp. 1–49, 2018, doi: 10.3390/pharmaceutics10030118.

[175] Y. S. Lin, K. R. Hurley, and C. L. Haynes, "Critical considerations in the biomedical use of mesoporous silica nanoparticles," *Journal of Physical Chemistry Letters*, vol. 3, no. 3. American Chemical Society, pp. 364–374, Feb. 02, 2012, doi: 10.1021/jz2013837.

[176] C. Lai *et al.*, "A Mesoporous Silica Nanosphere-Based Carrier System with Chemically Removable CdS Nanoparticle Caps for Stimuli-Responsive Controlled Release of Neurotransmitters and Drug Molecules," *J. Am. Chem. Soc.*, vol. 125, no. 15, pp. 4451–4459, Apr. 2003, doi: 10.1021/ja028650l.

# CHAPTER 2: OBJETIVES

## 2. OBJETIVES

The use of MSN into the nanomedicine field has increased in the last decade due to their unique properties, such as their high specific surface area, biocompatibility and ease to being functionalised. Nevertheless, some drawbacks, such as the biodegradability, the colloidal stability and long-term biocompatibility, hinder MSN achieve clinical trials.

In this context, the PhD thesis has been focused in the study, development and improvement of MCM-41-type MSN synthesis oriented towards the biomedical applications.

The specific objectives are:

- To understand mechanism synthesis of MCM-41-type MSN regarding the silica templating mechanism, as well as nucleation, growth and condensation processes.
- To study the influence of some disregarded parameters in the synthesis of MCM-41-type MSN.
- To control the MCM-41-type MSN synthesis in order to obtain more reproducible and tailored nanoparticles.
- To develop some methodology to characterise the colloidal stability in MSN.
- To study the parameters that influence on colloidal stability of MCM-41-type MSN samples.
- To analyse the principles which govern the colloidal stability in MCM-41-type MSN.
- To study systematically the implications of the use of different surfactant removal procedures in MCM-41-type MSN.
- To distinguish the main variables and steps that affect to the use of MCM-41-type MSN in biomedical applications, regard their reproducibility, suspendability and biodegradability.

# CHAPTER 3. IN-DEPTH STUDY OF THE MCM-41-TYPE MSN FORMATION MECHANISM

# 3. IN-DEPTH STUDY OF THE MCM-41-TYPE MSN FORMATION MECHANISM

## 3.1. INTRODUCTION

In the last decade, mesoporous silica nanoparticles have been widely applied to several fields, including chemistry, biomedicine and environmental science as a result of their unique properties. In that context, researchers have pursued the control of the characteristics of the particles since it allows tailoring them according to application requirements. Therefore, understanding the chemistry involved in the synthesis of MSN becomes an important goal in order to control their properties [1]. However, in spite of the efforts made by some groups that shed light on several interesting points, there is no complete understanding of the mechanism of the synthesis of MSN at a nanoscopic level. The most studied issues around the synthesis mechanism are the surfactant templating and the silica polymerization process [1][2].

Within the MSN the most studied are MCM-41-type ones, because of their ordered framework, narrow pore size distribution, cylindrical arrangement of pores and high specific surface area and volume. In addition, versatility of MCM-41 nanoparticles is demonstrated as their synthesis is easily tuneable, producing nanoparticles with different structures, morphologies, sizes or surface features [3][4]. All these properties make MCM-41-type MSN be the most extensively researched silica particles for biomedical applications [5], such as loading and delivery of active pharmaceutical ingredients, compared to other mesostructured materials, such as worm-like, dendrimer-like or disordered pores.

The aim of this project is to shed some more light on the synthesis mechanism of MCM-41-type MSN. To this purpose, we have reviewed the information reported on the synthesis mechanism, focusing on the silica templating mechanism, as well as the nucleation, growth and aging processes. Based on this framework, we have studied the mechanism of the different steps in the synthesis of MCM-41-type MSN.

### 3.1.1 Silica templating mechanism

The first important issue that could allow us to control the synthesis of the nanoparticles is to fully understand the mechanism by which the silica precursor is templated into the corresponding silica-surfactant mesostructures, i.e. the formation of the surfactant micelles, their role as structure directing agent and the interaction with the silica precursor [6]. The importance of this topic is evidenced by the fact that this is one of the most studied processes around the MSN formation and many mechanisms have been proposed to explain these topics around MCM-41-type materials.

#### 3.1.1.1. Liquid crystal templating mechanism.

Liquid crystal templating (LCT) was the mechanism used and accepted originally after the discovery of the M41S materials, inasmuch as the similarities between the geometry of MCM-41 materials and the behaviour of liquid crystal phases [7][8]. This mechanism is based on the

assembly of surfactant molecules into a hexagonal arrangement of cylindrical micelles by themselves prior to the addition of the silica precursors (Scheme 1).

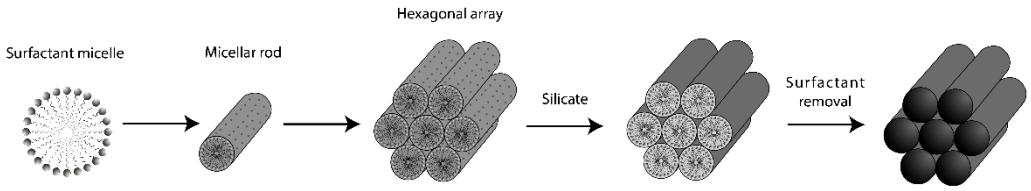


*Scheme 1. Schematic representation of liquid crystal templating mechanism, in which the formation of supramicellar hexagonal arrangement of surfactant precedes the addition of silica precursor. Adapted with permission from* [7]. *Copyright © 1992 American Chemical Society.*

However, this liquid crystal templating mechanism has been lately discarded because the amount of surfactant used is far below the concentration needed [9] for a liquid-crystal phase formation in an aqueous dispersion [10][11]. As we could observe in Figure 4 in Chapter 1, at 80 degrees surfactant molecules form hexagonal supramicellar structure at concentrations above 40 wt% [12]. This surfactant concentration would produce highly viscous solutions difficult to manipulate [2]. Besides, the concentration employed in the synthesis of MCM-41 nanoparticles is only enough to reach the critical micellar concentration to form spherical micelles (CMC1) [13]. Nevertheless, this is the common model represented due to its simplicity and easy viewing.

#### 3.1.1.2. Cooperative assembly model

The most accepted model for explaining the formation of mesostructured micelles in MCM-41-type MSN is the cooperative assembly model, widely studied by Stucky and co-workers [14][15], and Edler [2].

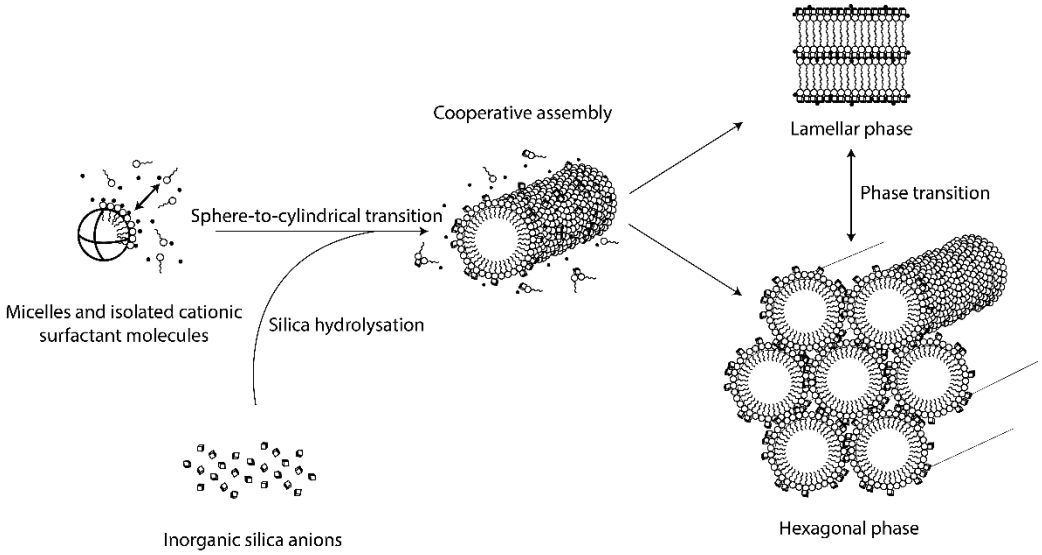


*Scheme 2. Schematic representation of cooperative assembly model, in which the formation of supramicellar hexagonal arrangement is promoted after the addition of the silica precursor. Adapted from reference* [15]. *Copyright © 1995 Science.*

This model is based on the interrelation of three processes: i) the oligomeric silicate species bind with high affinity to the surfactant micelles, positively charged, forming an organic-inorganic interface, ii) there is a preferential polymerisation and formation of silica at the interface region, due to the accumulation of silicate species in the boundary, and iii) the interfacial charge-density formed allows to shield the electrostatic repulsion between the positively-charged micelles, enabling the self-assembly of silica-coated micelles, which in addition can adopt different morphologies due to the stabilisation given by this interface (Scheme 2). In first place silica-surfactant micelles form rod-like quasi spherical structures [16]. Then, sphere-to-cylindrical transition occurs as silica species are attaching and polymerizing around the interface, through which the channel framework is created [17]. These processes occur in a dynamic and cooperative way, and allow to develop silica/surfactant mesostructures at surfactant amounts below those needed for crystal liquid phase formation [18]. In fact, surfactant amounts generally used are near but below the critical micelle concentration where the surfactant remains free or poorly organised as nanoscale spheres or cylinders [19] (Scheme 3).

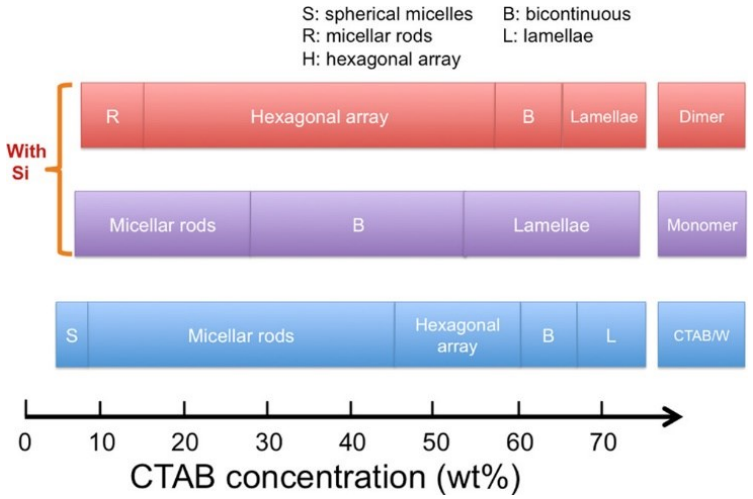


*Scheme 3. Comparison of the simulated mesophases formed according to the CTAB concentration, in presence and absence of silica precursor species (dimers or monomers). Reprinted from the reference* [18]. *Copyright © 2017 American Chemical Society.*

Furthermore, it should be noted that the formation of silica-surfactant mesophases, and therewith, the cooperative assembly process, starts as silica precursor is hydrolysed, i.e. when silicate species are dissolved and acquire negative charges to interact with surfactant molecules [20]. Thus, this process is independent from the silica polymerization and reveals the importance and strength of the binding between silica and surfactant, which drives the cooperative process.[15] In fact, the manner the surfactant-silica interaction acts upon silica hydrolysis and condensation is crucial to precisely forecast the structure and geometry the nanoparticles will adopt [21].

In addition, surfactant-silica micelles can vary their arrangement with some degree of flexibility once formed. This process is called phase transition and can take place meanwhile the silica is not completely condensed [22]–[24], being typical the transition from a lamellar to an hexagonal phase [15]. Hence, when the silica oligomers progressively polymerise, the mesophase begins to stabilise and the charge density of the silica framework decreases. As a result, the flexibility disappears and the morphology of the micelles is fixed.

#### 3.1.1.3. Soft-templating method

Soft-templating method was described by Mann and co-workers in 2002 [25], as an alternative cooperative and templating behaviour for surfactant-silica micelles in MSN formation. They suggest the nucleation of MCM-41 was divided in the following steps: i) formation of ellipsoid-shaped silica-surfactant micelles, in sizes from 5 to 9 nm; ii) aggregation of silica–surfactant micelles to form disordered spherical or ellipsoid nanoparticles; iii) progressive internal reorganisation and cylinder elongation of the silica–surfactant micelles, starting in the near surface regions of the nanoparticles (Scheme 4).

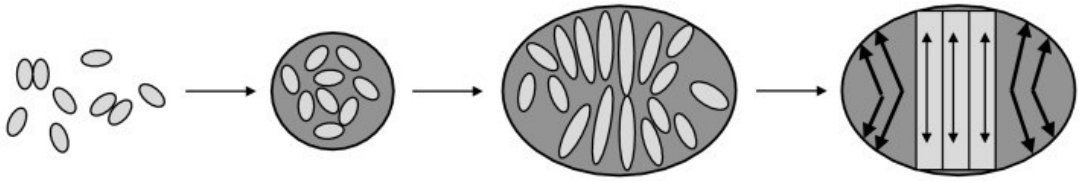

*Scheme 4. Schematic representation of mesoporosity formation according to soft-templating method. First, the silica-surfactant micelles formed are ellipsoid-shaped and disordered. Then, an internal reorganisation and elongation of the micelles form the hexagonal symmetry of MCM-41 nanoparticles. Reprinted from reference* [25]. *Copyright © 2002 Wiley online library.*

The internal reorganization of micelles is associated with two stages. On the one hand, lateral arrangement of the surfactant-silica composites produces a nematic-like effect during the formation of the silica wall between micelles, which is why they are arranged in parallel. On the other hand, the induced shape anisotropy becomes coupled with the subsequent development of the hexagonal structural order.

This method has been referenced in different later works, especially for explaining the formation of ellipsoid nanoparticles [26].

#### 3.1.1.4. Silicate polymerisation model

This theory was suggested from some experimental observations by in situ investigations, which cannot be explained with previous models. It was first described by Frasch and co-workers in 2000 [6].

The silica polymerisation model takes up some reasoning from cooperative assembly process, such as the importance of the interaction between silica species and surfactant molecules to form the mesophase [17]. However, the main statement of this model, and the discussion point, is that the cooperative assembly behaviour can only take place if the silica precursor polymerises in oligomers.

They were based on the fact that no organic mesophase involving the surfactant micelles was observed prior to the addition of the silica precursor. Hence, the presence of silica is necessary to form the mesophase structure, but it is not enough according to this model. It is just when the silica monomers form pre-polymers when they are able to bind to surfactant ions strongly. This ability is bigger as the polymers grow, following a cooperative manner. Before that,

surfactant only binds to counterions (bromide in this case) because the affinity constant of surfactant species towards bromide anions is much higher than the one towards hydroxyl groups belonging to silicate monomers. However, the oligomeric and polymeric silicate ions show higher affinity towards the surfactant moieties as a result of charge density matching and multidentate binding (Scheme 5).

What is more, charged silica polymers do not bind to surfactant micelles, but to the free surfactant cations released from the initial micelles. These micelles just act as reservoirs of surfactant ions, supplying surfactant ions to the silicate polymers, and are progressively consumed [27][28]. Nevertheless, the preferential binding of silicate oligomers to individual surfactant cations remains a controversial subject [17].

To sum up, the mesophase framework formation is due to the condensation of silica in polymers, which bind to surfactant molecules, forming hybrid silica-surfactant micelles in a cooperative way. These micelles undergo a shape modification from spheres to cylindrical structures, a process called sphere-to-rod transition [29]. Micelles can aggregate to form mesostructures through the charges and repulsion quenching provided by multicharged silica oligomers [30].

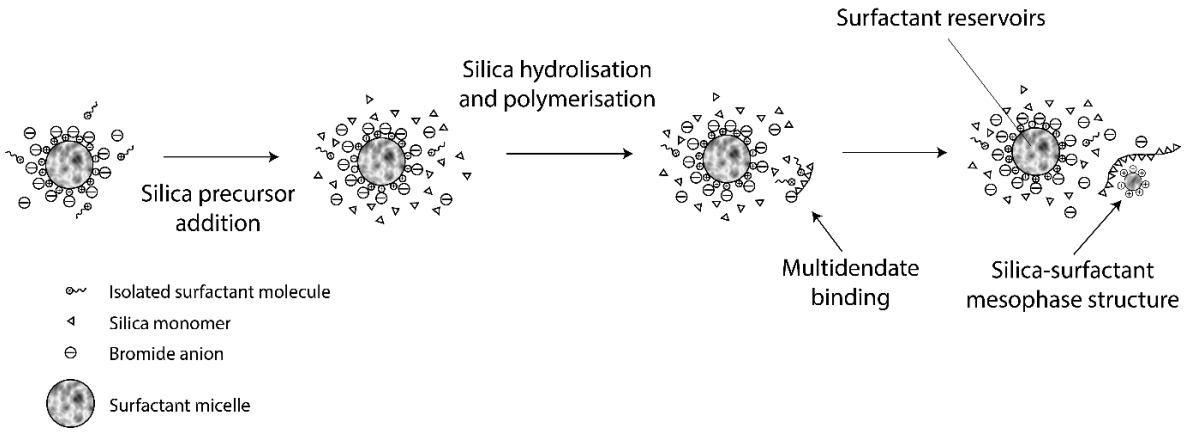


*Scheme 5. Schematic representation of silicate polymerisation model, in which the polymerisation of silica precursors is required to form silica-surfactant micelles. Adapted from reference* [6]*. Copyright © 2000 American Chemical Society.*

#### 3.1.1.5. "Swelling–shrinking" model

Another complementary model for explaining the mesostructure formation is called "swelling-shrinking", which is based on principles of cooperative assembly model, through which the formation of a mesophase is explained in a cooperative way. This model was proposed by Kong and colleagues [21] based on synchrotron time-resolved small-angle X-ray scattering (SAXS) data, which allowed to analyse in real time the formation of micelles and mesostructures.

In that work they propose that, before adding TEOS, CTAB form ellipsoid micelles. This surfactant micelles are positively charged by the quaternary ammonium salt in the head groups and the core is formed by hydrophobic hydrocarbon tails. When TEOS is added, it tends to oil-like solubilize in the micelle core, since TEOS is also hydrophobic. In fact, in this study it was observed that vigorous stirring was needed to emulsify the TEOS oil-drops into the CTAB solution. In this way, CTAB micelles increase their size and change their shape from ellipsoid to spherical. Shortly

after, due to the stirring, water droplets penetrate in the hydrophobic core and tend to hydrolyse TEOS molecules, which become hydrophilic thanks to the gain in negative charge. Thus, silicate species are gradually released into the aqueous solution and binds strongly with positive head groups by electrostatic forces (Scheme 6).

However, the most interesting phenomenon this model suggest is that the micelles are shrinking and becoming smaller due to the TEOS consumption inside the CTAB core. So, meanwhile it is creating a silica shell around micelles, micelles are decreasing their size and realising the TEOS within them. This process is going on until all the TEOS is hydrolysed and the micelles reach the size expected.

In parallel, the interface formed helps to coordinate the assembly of the micelles. Therefore, the neighbouring surfactant-silica micelles start to aggregate and produce the nuclei for the particle growth.

This model could explain how TEOS is able to act as a silica precursor in aqueous MSN synthesis (in absence of any other solvent, as ethanol).

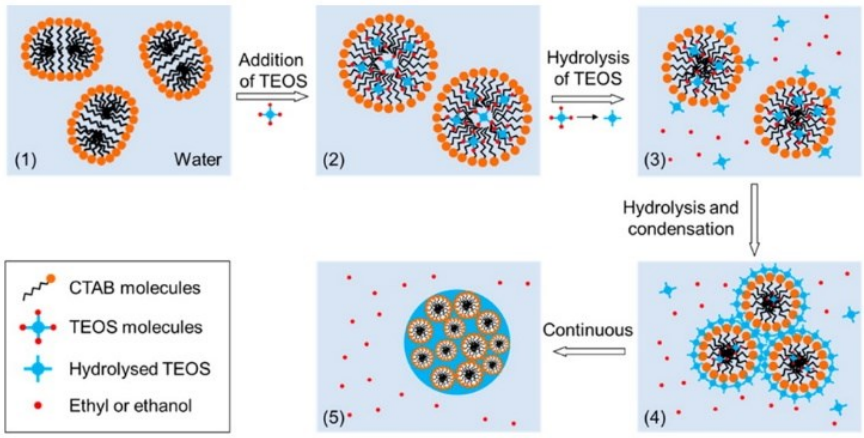


*Scheme 6. Schematic representation of "swelling–shrinking" model, in which the early surfactant micelles act as silica precursor reservoirs. Reprinted from* [21]*. Copyright © 2015 American Chemical Society.*

#### 3.1.1.6. Conclusions

Currently, cooperative assembly and silica polymerisation are the most accepted models. However, due to the lack of knowledge about first stages of mesoporous silica materials formation, it is not clear if silica polymerisation is previous to silica-surfactant micelles and mesophase formation, remaining as a controversial subject. Jin et al. performed some computational simulations and found silica polymerisation had to be posterior to silica-surfactant binding in order to generate mesoscale ordering [17]. On the other hand, Pérez-Sánchez et al., through another simulation method, reported that the presence of silica oligomers is required to form hexagonal liquid crystals from low-concentration surfactant solutions [30].

### 3.1.1. Nanoparticles formation

The basis of nanoparticles synthesis is the formation of a mesophase structure, but this cannot explain the whole process. According to the literature and to the most accepted models, nanoparticles formation is divided in four steps represented in the Scheme 7: silica-surfactant micelles formation, nucleation, growth and aging. [17][31]

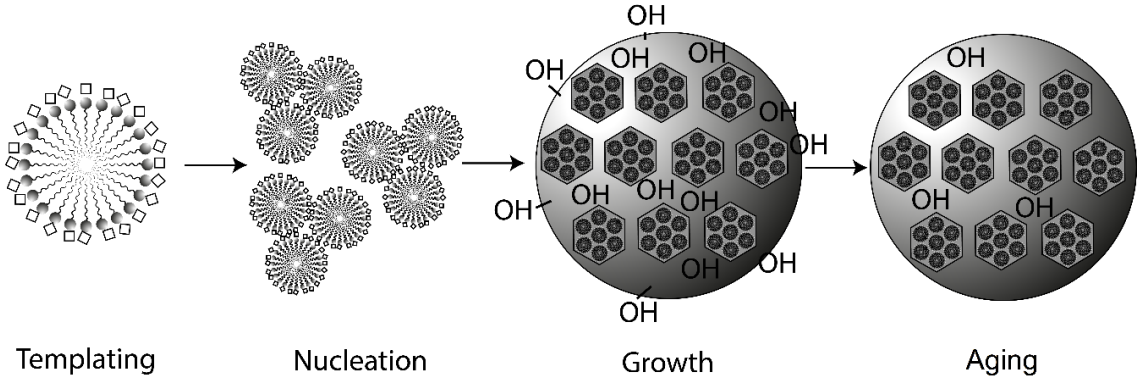


*Scheme 7. Schematic representation of the steps involved in the formation of MSN: (a) silica-surfactant micelles formation, (b) nucleation, (c) growth, and (d) aging.*

**Silica-surfactant micelles formation** has been widely developed in the previous section. Whichever the model proposed, the silica-surfactant templating requires the hydrolysis of the silica precursor and the exposure of its negative charges. Then, this step depends on the silica hydrolysis rate. In addition, for the silicate polymerization model, condensation is also required, and then, depends on both hydrolysis and condensation rate.

**Nucleation** is the formation of initial and small cores, due to the aggregation of silica-surfactant micelles [32]. These aggregations are possible thanks to the shielding of the electrostatic repulsion between the hydrolysed silica species when they bind to the surfactant micelles [33]. These small cores act as nucleation sites, to which the rest of micelles bind and where a preferential silica polymerisation occurs [34][29]. Yamamoto et al. [35] suggested that the nucleation is initiated by condensation and that this process is silica-driven and not a micelle-initiated mechanism since the increase in the surfactant concentration leads to an increase in the particle size rather than to an increase in the number of particles. Under the conditions of their experiments they find that the number of nucleation sites is fixed at an early stage and that is not related with the amount of precursor. Therefore, the rate-limiting step should be the hydrolysis and condensation of the silica precursor, which are mainly influenced by the pH and hence, the addition of higher concentration of silica precursor should lead to the formation of larger nanoparticles rather than more of them [34].

**Growth** means the increase of the cores size by the aggregation or coalescence with other small cores or simple silica-coated micelles, as well as the formation of silica walls. Starting from this point, silica-coated micelles align along crystal planes, as Cai and co-workers proposed [36]. The growth rate is also associated with the hydrolysis and condensation rate of the silica precursor, and then it can be modified by the presence of co-solvents, amines or inorganic compounds [33]. It has been reported that nanoparticles growth is halted when the charge density reaches a certain value that prevents the deposition of new silicate species [3] or when the materials are consumed [20]. Precipitation occurs when the mesostructured complexes reach a certain size and a neutralized charge, even at relatively low silica polymer concentration [6]. At late stages

of particle growth, small nanoparticles, whose radius is below a certain value, are dissolved instead of continuing growing. This tendency generates a mass transfer to larger nanoparticles, which grow at the expenses of the dissolution of smaller nanoparticles. This phenomenon is known as Ostwald ripening. [37]

These three first steps are very quick, since it has been reported that nanoparticles formation starts with a rapid evolution to a hexagonal mesophase. Linden et al. reported that the hexagonal mesophase was formed within 3 minutes [38]. Other studies reported the emergence of a white suspension in the range of 1 to 10 min after the addition of the silica precursor [3][39][40][41][42][43][44]. This indicates the presence of formed nanoparticles and precipitated nanoparticles, which are big enough to show Rayleigh and Mie scattering effect. Other studies described a similar behaviour [26][34].

The **aging** is the formation and reorganisation of silica bonds, which strengthen and consolidate the nanoparticle skeleton. This process is slower than the previous ones. In fact, some studies reported that complete silicate condensation takes at least 1 h [3] or 1.5 h [45]. This is the reason why most of protocols tend to leave the mixture of silica precursor and surfactant at least 2 h.

### 3.1.2. Conclusions and outlook

According to the reviewed information, we present in this work an in-depth study of the early stages of the MSNs synthesis to shed some more light on the mechanism involved in their formation. On the one hand, we have studied silica templating, nucleation and growth processes by taking aliquots during the first stages of MSN synthesis at different conditions, stopping and non-stopping the synthesis reaction. We have also studied the relationship between the hydrolysis and condensation rates and the nucleation process with respect to some reaction parameters. On the other hand, we have studied the growth and aging processes during the formation of the MSNs applying increasing synthesis times. According to our observations, both silica polymerization and cooperative assembly mechanisms are valid models to explain the initial stages of the MSN formation.

## 3.2. MATERIALS AND METHODS

### 3.2.1. Chemicals

Tetraethylorthosilicate (TEOS), 1-hexadecyltrimethylammonium bromide (CTAB) and sodium hydroxide (NaOH) were purchased from Sigma-Aldrich. Hydrochloric acid 37% (HCl) was provided by Scharlab.

### 3.2.2. General techniques

Transmission electron microscopy (TEM), $N_2$ adsorption–desorption isotherms, powder X-ray diffraction (PXRD), dynamic light scattering (DLS), electrophoretic light scattering (ELS) and solid-state nuclear magnetic resonance (ss-NMR) were used in order to characterise the prepared materials. The instruments used were the following: JEOL JEM-1010 microscope for TEM images acquisitions; Bruker D8 Advance diffractometer (Cu Kα radiation) for PXRD measurements; Micromeritics ASAP 2010 automated analyser for recording of $N_2$ adsorption–desorption isotherms, samples were degassed at 120 °C in a vacuum overnight. The specific surface areas were calculated from the adsorption data within the low-pressure range using the BET (Brunauer–Emmett–Teller) model. Pore size was determined following the BJH (Barrett–Joyner–Halenda) method. Particle size (DLS) and ʒ potential (ELS) in solution were measured by ZetaSizer Nano ZS (Malvern Instruments Ltd.) equipped with a laser of 633 nm and collecting the signal at 173°. ss-NMR were performed in Bruker Avance III 400 WB spectrophotometer.

### 3.2.3. Synthesis of nanoparticles

The assays and synthesis performed during the work were based on a standard synthesis. The modifications carried out throughout were specified in each assay (Results and discussion section). The standard synthesis was stablished as follows: 1 g of CTAB (2.74 mmol) was mixed with 480 mL of deionised water in a 1L (10.5 cm of outer diameter) cylindrical beaker. The mixture was heated at 50 °C to dissolve the surfactant and stirred with a cylindrical and plain magnetic stir bar (60mm long and 15mm diameter) at 500 rpm. Then, 280 mg of NaOH (7 mmol) dissolved in 3.5 mL of deionised water were added to reach a pH of 12.16, and the temperature solution was adjusted to 80 °C. A watch glass was placed to cover the beaker to minimize the solvent evaporation and therefore to avoid the volume decreasing during the reaction. When the temperature reached 80 °C, 5 mL of TEOS (25.7 mmol) were added dropwise, using syringe and needle. Soon after, a white precipitate appeared. The mixture was stirred for 2 h. After this time, the suspension was cooled at room temperature (measured pH 11.75), and the solid product was vacuum filtered with a Buchner over a filter paper (Whatman™ Grade 3MM Chr) and deionised water was added until the suspension reached neutral pH. Then, the solid was dried under vacuum and grinded to obtain a white powder. After the synthesis, nanoparticles were calcined at 550 °C using an oxidant atmosphere for 5 h in order to remove the surfactant.

### 3.2.4. Image analysis

Transmission electron microscopy was performed to acquire a wide representation of each sample, in order to check size and shape of synthesized nanoparticles. At least 100 particles for each sample were counted to obtain a representative size distribution of the particles. In the case of non-spherical nanoparticles the size was measured along the longer direction.

### 3.2.5. DLS measurements

DLS measurements coming from aliquots samples were performed directly from aliquots samples or just diluting them with distilled water. The rest of DLS samples were resuspended and generously sonicated in distilled water (1 mg NP/ml). After that, they were briefly spun in a centrifuge (a spin pulse to 10,000 rpm) to remove the presence of large aggregates or sedimentation, which disturbed the DLS measurements. ELS samples were prepared suspending, then generously sonicating nanoparticles in distilled water (10 mg NP/ml) and finally spinning briefly (a centrifuge pulse to 10,000 rpm) to remove the presence of large aggregates or sedimentation, which disturbed the electrophoretic movement measurements of the particles.

## 3.3. RESULTS AND DISCUSSION

As it is mentioned in the introduction, there are plenty of studies and hypothesis about the templating and nucleation mechanism in the formation of MSN, but there is not consensus about it. In order to shed some light on the matter, we have conducted four different assays focused on the first steps of the formation of the MCM-41-type MSN: (i) direct collection of aliquots, (ii) stirring aliquots collection, (iii) hydrolysis and condensation time variations, and (iv) quenched collection of aliquots. Additionally, we have studied the aging process by synthesising nanoparticles at different reaction times.

### 3.3.1. Direct collection of aliquots

The first assay performed consisted of taking five aliquots while adding TEOS in a standard synthesis of MCM-41-type MSN. The aliquots were taken just after the addition of 1 ml, 2 ml, 3 ml, 4ml and 5 ml of TEOS, and they were called DA (direct aliquot): **DA1**, **DA2**, **DA3**, **DA4** and **DA5**, respectively. Each one was placed into an Eppendorf tube once taken. In addition, an aliquot called **A0** was taken before starting the TEOS addition, to check the pre-existence of CTAB micelles. The TEOS addition rate was fixed at 5 ml/min, and then each millilitre took 12 seconds to be added. Each aliquot was prepared and observed in DLS and TEM.

The first issue to point out was the fact that the reaction continued after placing the aliquots in the tubes, as no action was deliberately taken to stop the reaction. The aliquots were then observed to become whiter and opaque over time (Figure 1). **DA4** and **DA5** were already white at the moment they were taken from the reaction. Then, after 15 minutes, a tendency to form large agglomerates and flocculates could be observed, although these are not clearly visible in the photograph (Figure 1). **DA3** was translucent at the time it was taken, but this state could not be recorded because it lasted only a few seconds and then turned white. **DA2** turned white after about 15 minutes and **DA1** remained translucent for several hours.

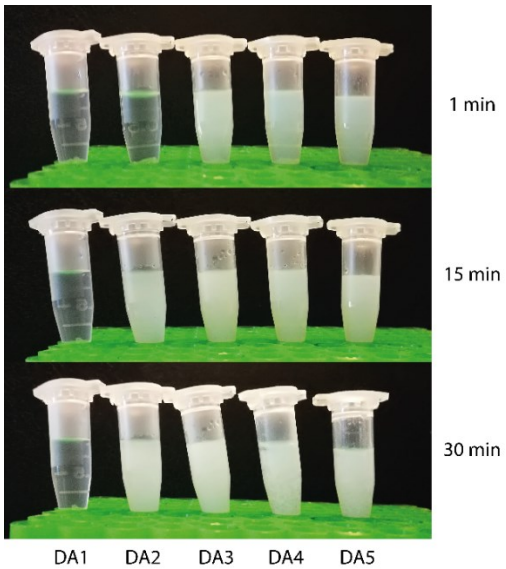


*Figure 120. Photography of DA samples at 1 min, 15 min and 30 min.*

It is assumed that this evolution is due to the fact that the pH of the aliquots is still very alkaline (ca. 12) and the temperature is around 80 degrees and it takes a few minutes to reach room temperature.

DLS measurements and TEM samples were prepared after several hours to assure that the reactions in the aliquots have finished. In the case of **A0** sample, DLS measurement (Figure 2A) revealed a peak ca. 5.5 nm, corresponding to CTAB micelles, and some noise over 100 nm. Nevertheless, the intercept of correlogram functions indicated the weak scattering of the sample, and then, the quality of results could be compromised. Additionally, in spite of the low electron density of organic matter, CTAB micelles can be observed in TEM images (Figure 2B) of this sample. They formed worm-like aggregates of small dots of about 5-6 nm. These images are similar to previously reported TEM observations of CTAB solutions. [46][47][48]

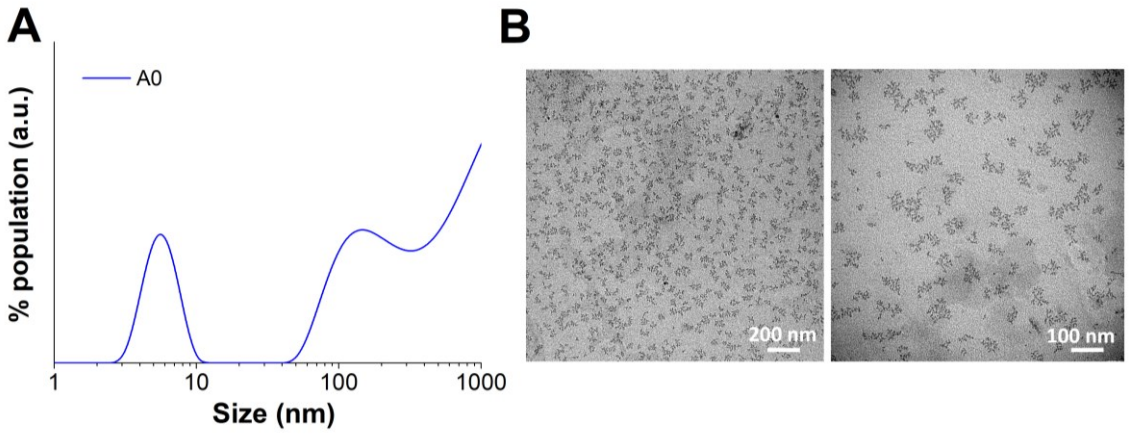


*Figure 2. A) DLS and B) TEM results for **A0** (CTAB) sample.*

The results DLS measurements and representative TEM images of the other samples are shown in the Figure 3 and Table 1. **DA1** showed in DLS measurement the same peak than **A0** sample, at ca. 5.5 nm, which can be interpreted as that there are still some CTAB micelles which have not been assembled with silica or that form single silica-surfactant complexes. In addition, other populations appeared clearly at 43 nm, 82 nm and 310 nm, indicating the presence of some larger entities. These entities were analysed in TEM images, in which some kind of small silica-surfactant complexes were observed in the range of 40 to 80 nm (inset in Figure 3B b), attributable to the peaks observed in DLS measurements. Finally, TEM images also showed some other larger and irregular particles, mainly made up of polymerised and amorphous silica. In addition, CTAB crystallisations were observed. Both could be the responsible for the DLS signal at 310 nm. **DA2** and **DA3** both showed single and clear populations of nanoparticles at 535 nm and 262 nm, respectively. TEM pictures of **DA2** showed the presence of large nanoparticles, in the range from 100 to 700 nm (averaged at 380 nm). Some particles are not spherical, but hexagonal. In the case of TEM images of **DA3** the presence of nanoparticles in the range of 80 to 230 nm (averaged at 150 nm) was observed. These nanoparticles have a spherical but irregular shape. In both cases, nanoparticles are quite fused, even coalesced. Finally, **DA4** and **DA5** were not possible to be measured by DLS due to the presence of large agglomerations and sediments. TEM images confirmed the presence of large floccules. The dilution and sonication of these samples (**DA4** and **DA5**) did not undo the floccules, and then, no DLS measurements could be taken. The appearance in TEM of the nanoparticles is similar to the common MCM-41-

type nanoparticles, but they are highly fused, making it difficult to find individual nanoparticles. The nanoparticles from **DA4** were sized in the range of 60 to 120 nm (centred at 90 nm), while those from **DA5** did so in the range of 70 to 130 nm (centred at 95 nm). In addition, **DA4** formed less spherical nanoparticles than **DA5**.

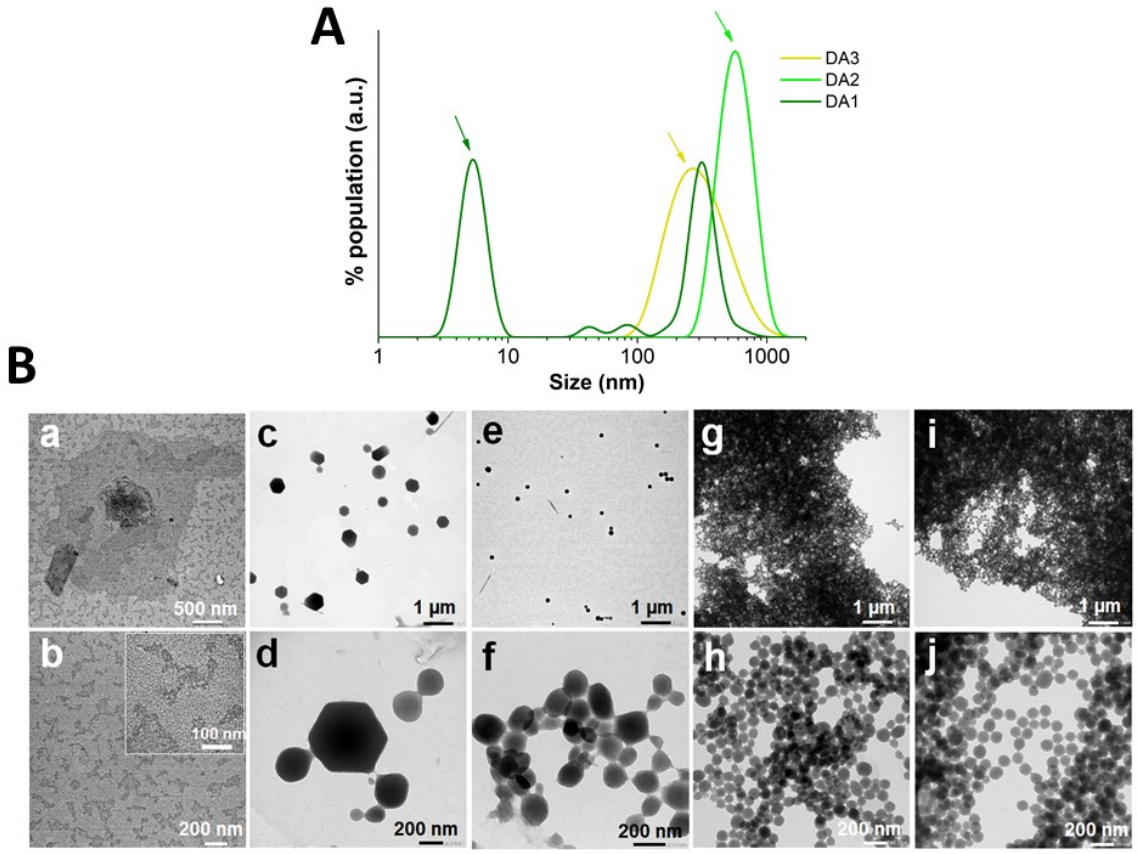


*Figure 3. (A) Size distribution of **DA1**, **DA2** and **DA3**, according to Intensity PSD analysis. (B) TEM images at lower and higher magnification of **DA1** (a, b), **DA2** (c, d), **DA3** (e, f), **DA4** (g, h) and **DA5** (i, j).*

*Table 1. DLS measurements of DA samples.*

| SAMPLE | ATTENUATOR | SIZE (INTENSITY) | PDI |
|---|---|---|---|
| **DA1** | 10 | 5.5 nm, 43 nm, 82 nm and 320 nm | 0.552 |
| **DA2** | 5 | 535 nm | 0.121 |
| **DA3** | 3 | 262 nm | 0.208 |
| **DA4** | 3 | [a] | [a] |
| **DA5** | 3 | [a] | [a] |

[a] *Presence of large aggregates and floccules*

With these results we can argue that **DA1** sample contained silica species able to form silica-surfactant complexes, but not enough dense to nucleate the formation of mesoporous nanoparticles. In this context, the larger entities found in **DA1** correspond to polymerisation of amorphous silica, but they were scarcely frequent. These suggestions are additionally supported by the fact the aliquot did not become white or opaque, and the Attenuator in DLS measurements was 10.

The most striking fact in this assay is the great increase in the particles' size in samples **DA2** and **DA3**, in comparison with the other samples. While the addition of 1 mL of TEOS (**DA1**) was not enough to develop the cooperative assembly and form MSN, the addition of 2 mL of TEOS (**DA2**) promoted the condensation, nucleation and growth processes, forming large nanoparticles. This phenomenon was also observed by other authors [40], but no explanations were found. Thus, we hypothesise that the larger size of **DA2** and **DA3** with regard to those samples which have bigger amount of TEOS (**DA4** and **DA5**) is based on the formation of a lower number of nucleation seeds, and then, a bigger number of silica-surfactant complexes per seed [49]. However, it has been described that the number of nucleation sites is not related with the amount of precursor, but with the hydrolysis and condensation rate of the silica precursor. This is supported by the argument that the amount of silica available to cooperatively assemble with CTAB micelles and condensate to form initial seeds is directly related to hydrolysis-condensation reactions and not to the amount of TEOS added [35]. Then, the number of nucleation centres should be influenced mainly by the pH [35], the temperature and the solvent. Nevertheless, the only differential factor in this assay was the amount of TEOS added. Hence, in these conditions, the low amount of TEOS added acts as bottleneck and limits the amount of silica precursor available to be hydrolysed and condensed. This phenomenon is especially remarkable at the high alkaline pH (ca. 12) of the reaction, where the hydrolysis rate is boosted and condensation rate remains high due to the stability conferred by surfactant. Thus, in highly alkaline conditions and low concentration of TEOS, the number of seeds formed can be directly related with the amount of silica precursor.

In addition, it was also observable the quasi-crystalline growth of nanoparticles in **DA2**, which formed some hexagonal nanoparticles, repeating the internal arrangement of supra-micellar hexagonal structures. This process of crystallisation is supposed to be resulting as a consequence of resting conditions. The low number of seeds formed in **DA2** allowed a high deposition of silica per seed, and then, stimulate this crystalline growth. This phenomenon is also observed in **DA3**, although to a lesser extent. In **DA4** and **DA5** crystallisation was not observed, being that the number of nucleation sites is higher, the silica available per seed is too low and is rapidly consumed.

### 3.3.2. Stirring aliquot collection

In order to evaluate the influence on the growth of nanoparticles by letting the aliquots stand after the addition of TEOS without having stopped the reaction, a different assay was performed. It was called `stirring aliquots collection´, since each aliquot was taken from each sample while stirring for 2 hours in the glass beaker. Then, 4 samples were prepared, in which 1 ml, 2 ml, 3 ml or 4 ml of TEOS were added. 5 ml sample was not prepared, as it was considered equivalent to the standard synthesis of MCM-41-type MSN. Aliquots taken were called SA (stirring aliquots): **SA1**, **SA2**, **SA3** and **SA4**, respectively.

DLS measurements and TEM pictures were taken after 2 hours (Figure 4 and Table 2), when the reaction was considered complete. All the samples except **SA1** had to be diluted in order to be measured in DLS. **SA1** showed a unique peak in DLS at ca. 5.6 nm, which is interpreted to correspond to CTAB micelles, as in **A0**, or to individual silica-surfactant micelles. However, it has

to be noted that the Attenuator level was located at 11 in the measurement, and then their reliability is not ensured (Table 2). TEM images of **SA1** showed small particles from 10 to 20 nm, which can be suggested to correspond with small silica-surfactant micelles. In addition, some large entities, such as CTAB crystals or amorphous silica aggregates can be observed. Regarding to **SA2**, **SA3** and **SA4** clear and single populations were observed on DLS curves, centred at 309, 135 and 132 nm, correspondingly. In all these samples narrow distribution size curves and considerably low PDI values were obtained (0.100, 0.060 and 0.077, respectively). TEM pictures showed that **SA2** material consists of spherical and slightly fused MSNs ranging 300 to 500 nm (centred at 400 nm). Parallel channels corresponding to the mesostructured porosity of these particles can be observed in the inset of the Fig. 4B d. In case of **SA3** and **SA4**, TEM images showed standard MCM41-type MSN, being slightly larger in case of **SA3** (ca. 110 ± 22 nm in **SA3** and 94 ± 12 nm in **SA4**).

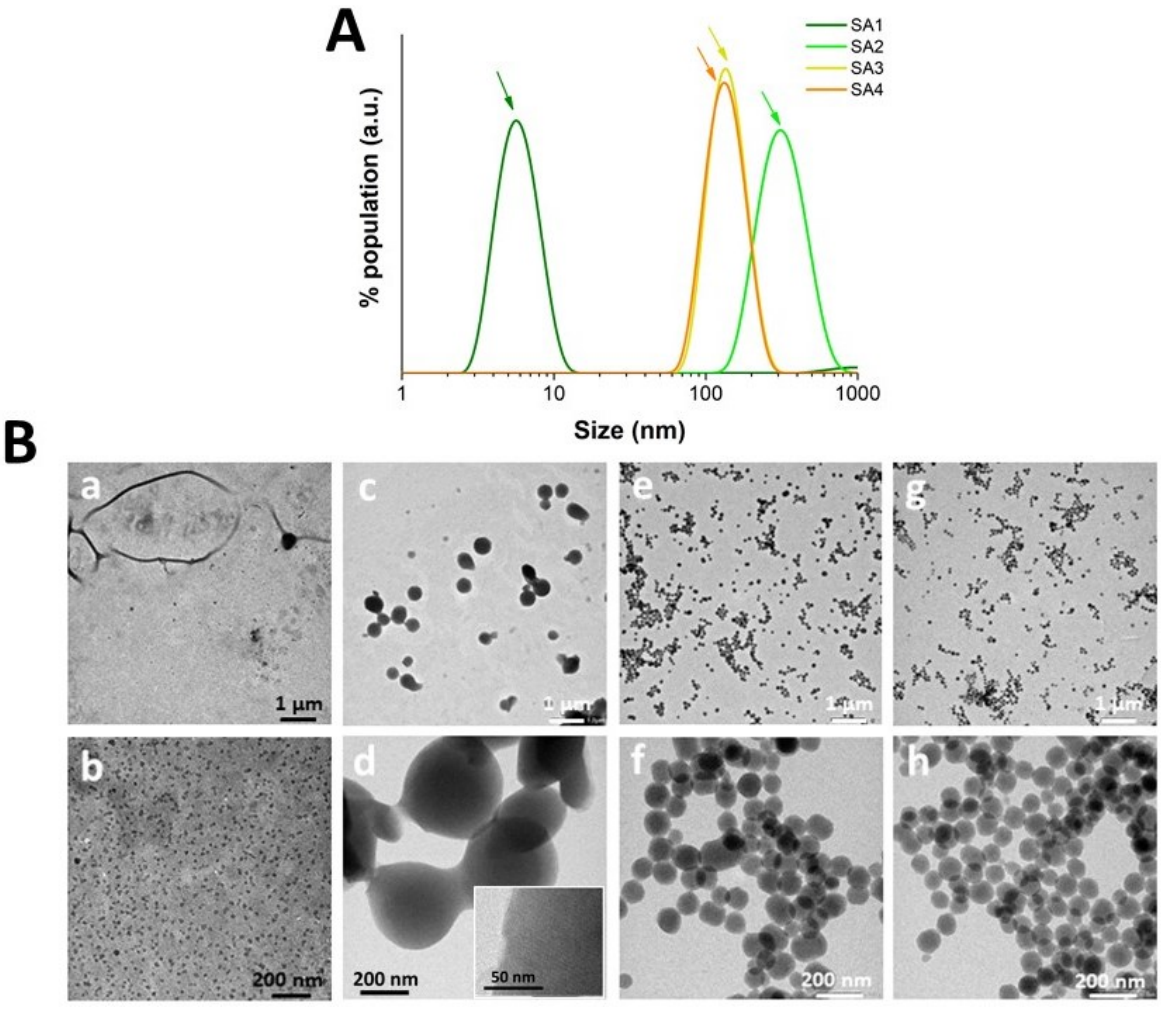


*Figure 4. (A) Size distribution of **SA1**, **SA2**, **SA3** and **SA4**, according to Intensity PSD analysis. (B) TEM images at lower and higher magnification of **SA1** (a, b), **SA2** (c, d), **SA3** (e, f) and **SA4** (g, h).*

*Table 2. DLS measurements of SA samples.*

| SAMPLE | SIZE (INTENSITY) | PDI |
|---|---|---|
| **SA1** | 5.6 nm | 0.237 |
| **SA2** | 309 nm | 0.100 |
| **SA3** | 135 nm | 0.060 |
| **SA4** | 132 nm | 0.077 |

The comparison between DA and SA samples shows an analogous tendency. On the one hand, the addition of 1 mL of TEOS (**DA1** and **SA1**) was not enough to cooperatively assemble with the surfactant micelles and completely or partially form MSNs. On the other hand, intermediate volumes of TEOS (**DA2**, **DA3**, **SA2** and **SA3**) fall in the range in which the amount of TEOS acts as rate-limiting step. As it was explained previously, this means that the amount of TEOS directly influences on the silica availability to assemble with surfactant micelles and, therefore, it limits the formation of nucleation seeds in the early stages of synthesis. However, in the case of stirring conditions, unlike the case of direct collection of aliquots, the growth of nanoparticles (**SA2** and **SA3**) is less pronounced, and the formation of quasi-crystalline nanoparticles is not observed. Then, two complementary explanations can be hypothesised. First, as some authors have reported [21], the stirring increases the contact of silica precursor species with water molecules, thereby improving the rate of hydrolysis. Therefore, the stirring itself causes the increase of silicate species available to condense and, accordingly, the increase of the initial number of nucleation seeds. Second, the stirring avoids the crystallization process, which requires resting conditions, and then limit the accumulation and deposition of silica over the seeds and the overgrowth of the nanoparticles. Accordingly, the importance of the stirring in this procedure is crucial, since it is implicated in not only the mixture and dispersion of reactants, but also in the hydrolysis-condensation regulation and the nucleation process.

Finally, aliquots in which greater amounts of TEOS were added (**DA4**, **DA5** and **SA4**) tended to be similar, since the formation of seeds reach a maximum value for these reaction conditions. In other words, the amount of TEOS present in this solutions allows the hydrolysis and condensation rate progressing at their highest value. Therefore, the MSN formed are sized at the values of the synthesis under standard conditions.

### 3.3.3. Hydrolysis and condensation time variations

Just as it was observed in other assays, hydrolysis and condensation rates are influenced not only by pH [50][21][51][20], temperature [52][53] and solvent [54], which is widely reported, but also by the stirring rate and the amount of silica precursor at some specific conditions (high alkaline pH and low silica precursor concentrations). An easy way to monitor the condensation and growth rates of MSN in a synthesis is to observe the changes of the suspension appearance. First, the hydrolysis of the silica precursor and condensation of the first molecules of supersaturated silicic acid are indicated by the opalescence that appears in the suspension [44]. After that, the suspension turns cloudy white when the small seeds grow and form nanoparticles that reach certain threshold [55]. For example, Lin et al. found that when particles grow over 25

nm the corresponding suspension changes from clear to turbid [56]. In this context, Khlebtsov et al. stablished the dependence of the turbidity with concentration and particle size using silica nanoparticles [57]. As we have seen in the previous sections, the growth process is quick, and then, the turbidity appears soon. In this context, Möller et al. reported that after 1 min they observed the formation of a white suspension in their synthesis reaction. [40]

Hence, in order to stablish the influence of the amount of TEOS added and the stirring rate on the hydrolysis and condensation reactions, we have determined the time it takes for the synthesis reaction mixture to turn turbid white at naked eye, keeping the rest of the parameters unchanged. Two assays were performed in this context and reported in the Table 3. On the one hand, the time to get a turbid white suspension was measured when different amounts of TEOS were added (1 mL, 2 mL, 3 mL, 4 mL and 5 mL). According to previous assays, the white turbidity was immediately reached when the fourth mL of TEOS was added using an addition rate of 5 mL $min^{-1}$. With that in mind, we decided to instantly add the precursor to eliminate the TEOS addition rate as a variable and limiting factor. On the other hand, the influence of the stirring rate in relation to the time it took to become a white cloudy suspension was also observed. Therefore, the assays were repeated adjusting different stirring rates (300 rpm, 900 rpm and 1200 rpm) in the case of 3 mL of TEOS addition.

*Table 3. Cloudy appearance time measurements as a function of stirring rate and TEOS volume added.*

| **ADDED TEOS (mL)** | **STIRRING RATE** | | | |
|---|---|---|---|---|
| | 300 rpm | 500 rpm | 900 rpm | 1200 rpm |
| 1 | - | [a] | - | - |
| 2 | - | 97 s | - | - |
| 3 | 115 s | 63 s | 37 s | 26 s |
| 4 | - | 45 s | - | - |
| 5 | - | 36 s | - | - |

[a] *Cloudy suspension does not appear*

The results obtained showed that the time required to obtain a turbid white suspension, and then well-formed nanoparticles, decreased as the amount of TEOS increases (from 97 seconds for 2 mL to 36 seconds for 5 mL). It should also be noted that 1 mL of TEOS was not enough to obtain nanoparticles (as observed in previous sections). In the case of the stirring rate, the time required also decreases as the stirring rate increases (from 115 seconds at 300 rpm to 26 seconds at 1200 rpm). This behaviour fits with the observations made previously, which suggested that lower amounts of TEOS and lower stirring rate decrease the hydrolysis and condensation rate, and vice versa.

In a standard synthesis, when the TEOS is added at a rate of 5 mL/min, the suspension becomes white turbid after the fourth ml of TEOS (the 80% of total TEOS), namely, at 48 seconds approximately. In the only study we have found in which is accurately reported the time that the white precipitate appears, a TEOS addition rate of 0.5 mL/min was used. In this case, turbidity occurs at 2.8 mL [58], which corresponds to the 56% of the total TEOS addition and more than 5 minutes. Therefore, the rate of TEOS addition also influences the time and amount of TEOS required to form nanoparticles causing the appearance of white turbidity. Therefore, to study this influence on the hydrolysis and condensation rate, another assay was performed using

different TEOS addition rates (0.25 mL $min^{-1}$, 0.5 mL $min^{-1}$, 1 mL $min^{-1}$, 5 mL $min^{-1}$ and instant addition) (Table 4). TEOS was added in each case until the reaction mixture became cloudy.

*Table 4. Time required for the reaction mixture to become cloudy, measured as a function of the rate of TEOS addition. Also the amount and percentage of TEOS added at that moment is included.*

| | **0.25 mL $min^{-1}$** | **0.5 mL $min^{-1}$** | **1 mL $min^{-1}$** | **5 mL $min^{-1}$** | **Instant** |
|---|---|---|---|---|---|
| **Time (s)** | 630 | 336 | 150 | 48 | 36 |
| **TEOS added (mL)** | 2.7 | 2.8 | 2.5 | 4 | 5 |
| **% TEOS added** | 54 | 56 | 50 | 80 | 100 |

As it can be seen in our assays, the time required for the reaction suspension to become cloudy white is also influenced by the rate of TEOS addition. At slower addition rates more time is needed (from 36 seconds for an instant addition to 630 seconds when TEOS is added at 0.25 mL $min^{-1}$). This behaviour can be provoked because the addition rate of TEOS also is associated with the amount of TEOS available to be hydrolysed-condensed, and therewith, slow addition rates are analogous to the presence of low concentration of TEOS. Additionally, the amount of TEOS required to obtain white turbid suspension is lower as TEOS addition rate decreases. This effect can also be observed focusing on the % of TEOS added to obtain a white turbid suspension. Hence, the formation of large enough nanoparticles occurs at lower TEOS amount with slower TEOS addition rates. This phenomenon can be explained considering that at slower addition rates, the TEOS available to be hydrolysed and condensed is lower, and then, less nucleation seeds are formed, and less amount of TEOS is needed to grow the seeds over the observable size. Therefore, in samples where TEOS is not added instantaneously, the rate of addition acts as a rate-limiting step, as this rate influences the time it takes to see the nanoparticles formation.

### 3.3.4. Quenched collection of aliquots

Another assay was performed to study the initial stages of MCM-41-type MSN synthesis. In this case, we decided to "take some shots" along the growing process in a standard synthesis as the TEOS is being added. Therefore, quenching of the reaction was necessary after aliquots were taken ('quenched aliquots collection') to avoid further reaction in the tubes. The method employed to quench was to dilute them and apply rapid cooling. Aliquots were taken just after the addition of 1, 2, 3, 4 and 5 mL of TEOS at 5 mL $min^{-1}$, which were named quenched aliquots (**QA1**, **QA2**, **QA3**, **QA4** and **QA5**, respectively). The quenching was performed by diluting 5 times the aliquots with deionised water and placing them in ice bath immediately.

DLS measurements and representative TEM images are shown in Table 5 and Figure 5. At first glance, a gradual growth of nanoparticles can be observed. **QA1** was too diluted to be measured with quality by DLS, being that the sample did not scatter enough light. However, two peaks could still be measured around 5 nm and 370 nm. The first one is suggested to correspond with CTAB micelles and single silica-surfactant complexes, and the latter to large entities such as CTAB crystallisations or aggregates of amorphous silica. TEM images showed the presence of CTAB crystallisations, but no amorphous silica could be seen. Besides, some small dots like those observed in **A0** and **SA1** were also present in the TEM images. **QA2** was quite polydisperse and

diluted, but DLS was able to resolve a mixture of populations. A peak at ca. 6 nm was observed, which presumably corresponds to unassembled CTAB micelles, and other wide populations centred at 32 nm and 155 nm were recorded. In the TEM images, small nanoparticles still in formation can be seen, with a size ca. 28-30 nm. In addition, some larger particles are observable, whose sizes varies from 30 to 300 nm, in accordance with DLS results. **QA3** showed two clear populations at 38 nm and 205 nm in DLS measurements. TEM images showed a first population that correspond to the small mesoporous nanoparticles in formation, which are highly fused. In addition, there is a scarce population of nanoparticles that have grown much more than the rest, in the range of 150 to 400 nm, observation that fits with the DLS measurement. **QA4** and **QA5**, showed in DLS single populations at 114 nm and 132 nm, respectively. TEM images showed that in **QA4** there is still some MSN in formation in a similar stage to **QA3**, but most of the population are nanoparticles already formed, in the 80 to 100 nm range. Pictures of **QA5** showed nanoparticles already formed with sizes from 90 to 120 nm. No larger size populations were seen.

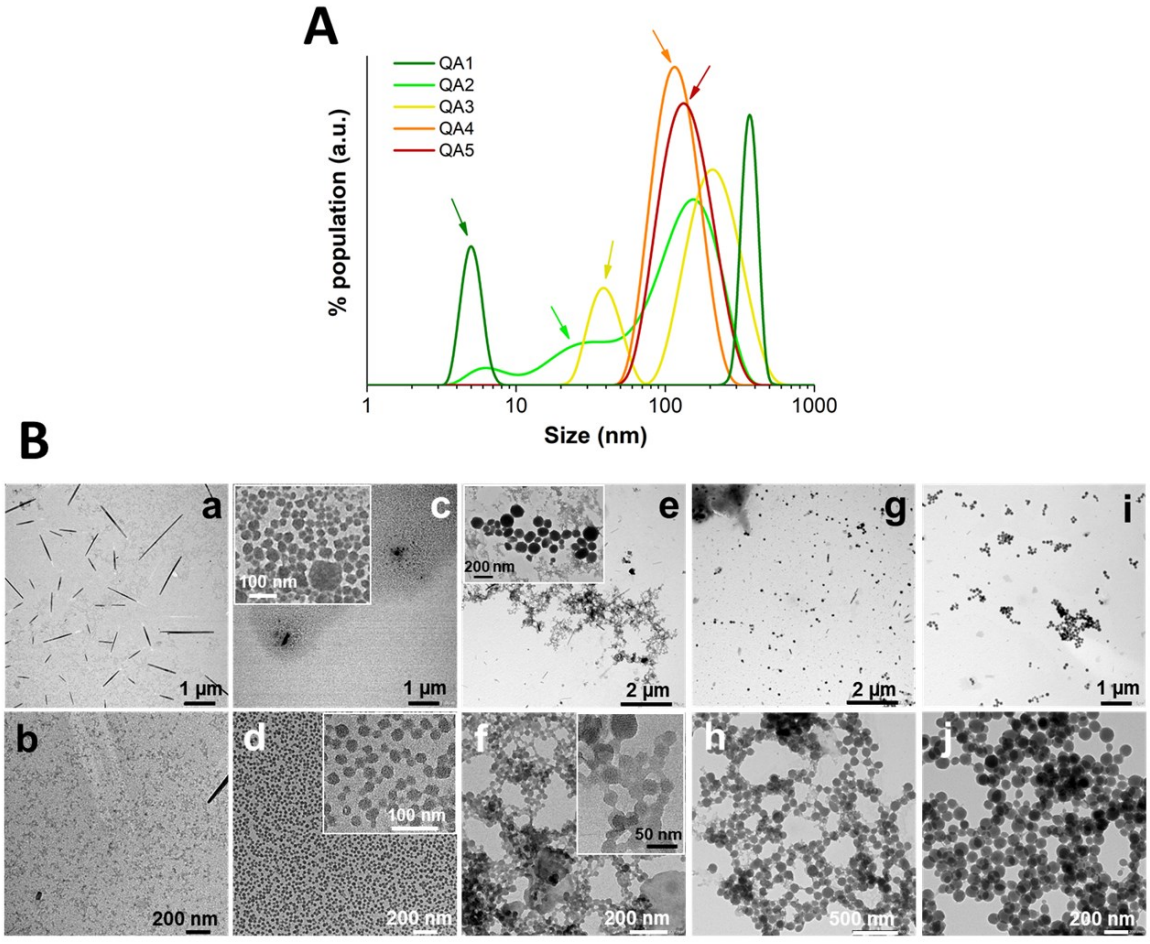


*Figure 5. (A) Size distribution of **QA1**, **QA2**, **QA3**, **QA4** and **QA5**, according to Intensity PSD analysis. (B) TEM images at lower and higher magnification of **QA1** (a, b), **QA2** (c, d), **QA3** (e, f), **QA4** (g, h) and **QA5** (i, j).*

*Table 5. DLS measurements of QA samples.*

| SAMPLE | ATTENUATOR | SIZE (INTENSITY) | PDI |
|---|---|---|---|
| **QA1** | 11[a] | 5 nm and 370 nm | 0.997 |
| **QA2** | 10 | 6 nm, 32 nm and 155 nm | 0.459 |
| **QA3** | 7 | 38 nm and 205 nm | 0.487 |
| **QA4** | 6 | 114 nm | 0.080 |
| **QA5** | 6 | 132 nm | 0.157 |

[a] *Sample too diluted*

The results showed that the nanoparticles are forming and growing progressively, from the 6 nm CTAB micelles, then seeds of 30 and 40 nm approximately, to finally fully formed nanoparticles of 115 and 130 nm. Nevertheless, some bigger size populations are formed at first aliquots (**QA2** and **QA3**), which are not found in following samples, neither by TEM nor by DLS. This phenomenon could be explained because the reaction is not fully quenched, and therefore, the existence of a low number of nucleation seeds in the first stages provokes the remaining silica precursor to develop some large nanoparticles, similar to the process observed in **DA** and **SA** samples.

All of these results suggest that templating, nucleation and growth processes are very quick, with fully formed nanoparticles being observed after 5 min. According to our experience, templating mechanism can occur as defined in both silica polymerisation and cooperative assembly models. Swelling-shrinking model also fits with the obtained results. At initial stages, we have observed that the CTAB micelles and silica-surfactant complexes had around 6 nm, which is quite bigger than the final sizes of channels and pores found in standard MCM-41-type MSN (in the range of 2-3 nm), and even larger than the unit cell of mesostruture, which is usually in the range of 4-5 nm. Therefore, initial micelles should act as CTAB repositories or suffer a rearrangement in presence of silica precursor, as silica polymerization and swelling-shrinking models, on the one side, and cooperative assembly model, on the other, suggest respectively.

Additionally, the results obtained prove the dependence of the hydrolysis and condensation rate on multiple parameters, some of them not widely studied, such as the amount of TEOS at low concentration, the TEOS addition rate and the stirring rate. Our experiences showed a clear relationship between the hydrolysis and condensation rate versus the nucleation process. Nucleation process influences strongly on the growth and formation of nanoparticles, and thus, it is a critical step.

The results obtained also demonstrate that the arrangement and templating of silica occur from the initial stages, in contrast to the observations made by Sadasivan et al. [25], which described the formation of disordered silica-surfactant micelles in nanoparticles below 50 nm. Applying higher magnification in **QA2** TEM image, a 2D quasi-hexagonal arrangement of pores can be observed (Figure 6, red circles).

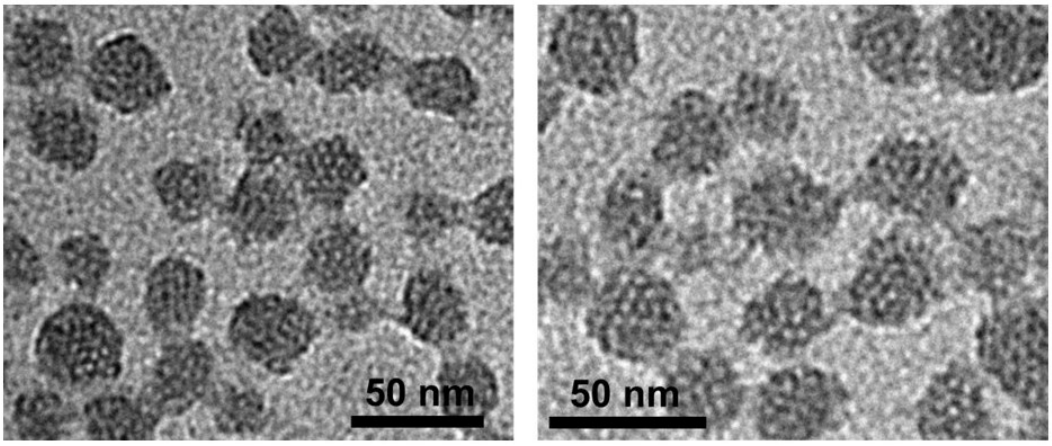


*Figure 6. TEM images of **QA2** at different magnifications, in which the hexagonal arrangement of mesopores can be observed.*

### 3.3.5. Aging and reaction time

As it was described by Linden [38] and Yi [21], and our assays in previous section, the first steps in the synthesis of the nanoparticles (surfactant-silica micelles formation, nucleation and growth) occurs in less than 10 minutes. Then, the additional time the reaction is left should correspond to aging and rearrangement processes. To study these, we have characterised several samples after complete addition of TEOS (5 mL), at different reaction times (5 min, 20 min, 1 hour, 2 hours and 4 hours), which were named **MSN-5min**, **MSN-20min**, **MSN-1hour**, **MSN-2hours** and **MSN-4hours**, respectively. TEM images, DLS and ELS measurements, $^{29}$Si-ssNMR, PXRD and $N_2$ adsorption-desorption isotherms were performed to characterise the nanoparticles synthesised. This study is similar to the one performed by Catalano et al. [3], who analysed samples at 7 min, 30 min, 1 hour, 1.5 hour and 2 hours, and characterised them by TEM pictures, DLS and ELS, small angle XRD and nitrogen adsorption-desorption isotherms. Nevertheless, they obtained some different conclusions, as it will be mentioned throughout the section.

TEM pictures shown in Figure 7 were taken to calcined samples and show that all the samples were composed by nanoparticles completely formed. However, the first samples (**MSN-5min** and **MSN-20min**) show nanoparticles with irregular surface and higher presence of smaller size populations. Nanoparticles were in the range of 94 ± 18 nm (**MSN-5min**), 90 ± 17 nm (**MSN-20min**), 93 ± 16 nm (**MSN-1hour**), 98 ± 15 nm (**MSN-2hours**) and 103 ± 21 nm (**MSN-4hours**). A slight increase (around a 9%) in the average size over the time is observable, although nanoparticles synthesised during 5 min are sized in the range of nanoparticles normally used. These results disagree with Catalano et al. [3] studies, which suggest an increase from 108 nm at 7 minutes to 159 nm at 2 hours. On the other hand, in our experiments it could be observed that the size dispersion slightly decreases from 5 min to 2 hours, but increase at 4 hours. Then, nanoparticles seem to be more homogenous at 2 hours.

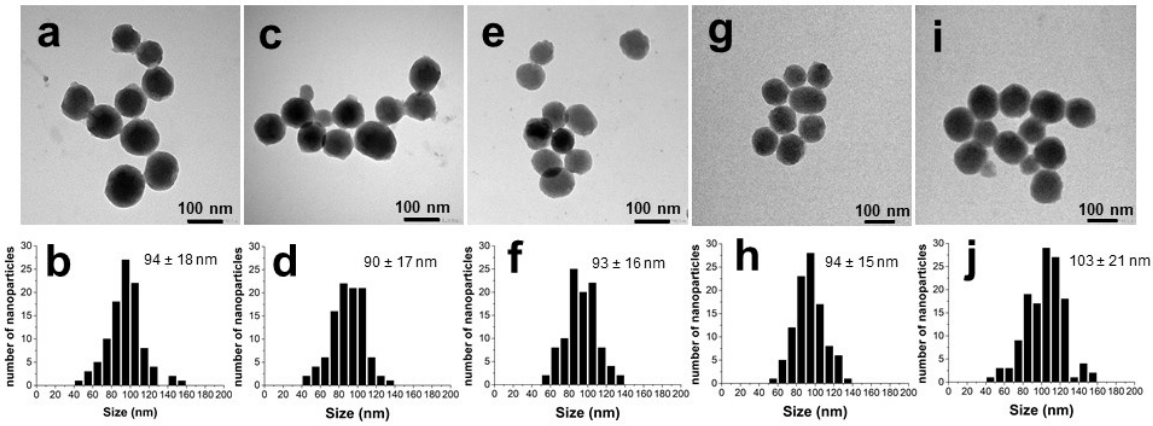


*Figure 7. TEM images at lower and higher magnification and histograms with particle size distribution of **MSN-5min** (a, b, c), **MSN-20min** (d, e, f), **MSN-1hour** (g, h, i), **MSN-2hours** (j, k, l) and **MSN-4hours** (m, n, o). Nanoparticles sizes were measured in TEM images. At least 100 particles for each sample were counted.*

Therefore, it could be affirmed that 5 min of synthesis were enough to obtain common MSN in terms of size and morphology. However, additional time was needed to reduce the polydispersion of the sample, being optimised at 2 hours. In this context, according to Ostwald ripening, smaller size populations disappear in favour of larger ones. In our case, it is observable how the percentage of nanoparticles smaller than 60 nm is decreasing from 5 min to 2 hours, but they increase at 4 hours (4% at **MSN-5min**, 6% at **MSN-20min**, 2% at **MSN-1hour**, 1% at **MSN-2hours** and 3% at **MSN-4hours**).

DLS and ELS measurements of calcined samples are presented in Figure 8 and summarised in Table 6. It can be observed in the DLS curves (Fig. 8A) how the size distribution becomes narrower with time (from 5 min to 2 hours), but increases after 4 hours. This behaviour is also observable on the PDI value (0.406 in **MSN-5min**, 0.283 in **MSN-20min**, 0.260 in **MSN-1hour**, 0.237 in **MSN-2hours** and 0.265 in **MSN-4hours**). Thus, these results fit well with the tendency observed in the TEM pictures. This result is similar to that observed by Möller and co-workers [40], where a very broad distribution was observed in the early stages of synthesis; a distribution that narrowed drastically over time. However, it must be taken into consideration that our measurements were performed with spun samples and therefore, large aggregates and sediments were removed. Then, the populations observed in the DLS curves, correspond to the fraction that is at least moderately suspendable in water. In this context, **MSN-5min** showed two populations at 185 and 702 nm, **MSN-20min** one population at 148 nm, **MSN-1hour** one at 159 nm, **MSN-2hours** one at 158 nm and -**MSN-4hours** one at 174 nm. ELS measurements of calcined samples (Fig. 8B) showed a decrease in the ζ Potential of samples over the time (-35.7 mV for **MSN-5min**, -33.7 mV for **MSN-20min**, -32,2 mV for **MSN-1hour**, -29,9 mV for **MSN-2hours** and -28.4 mV for **MSN-4hours**). This indicates that nanoparticles are losing negative charge on the surface as the reaction progress. The higher negative surface of **MSN-5min**, and **MSN-20min** to a lesser extent, could explain the better suspendibility of larger populations, which are observed in DLS curves in spite of applying a brief spun. The tendency we observed in ζ potential values is also in conflict with the results of Catalano et al. [3], which did not show a correlation between the reaction evolution and the Z potential value. This can be explained regarding the differences observed in the synthesis process (the authors washed the nanoparticles with ethanol and extracted the surfactant refluxing with ethanol-HCl).

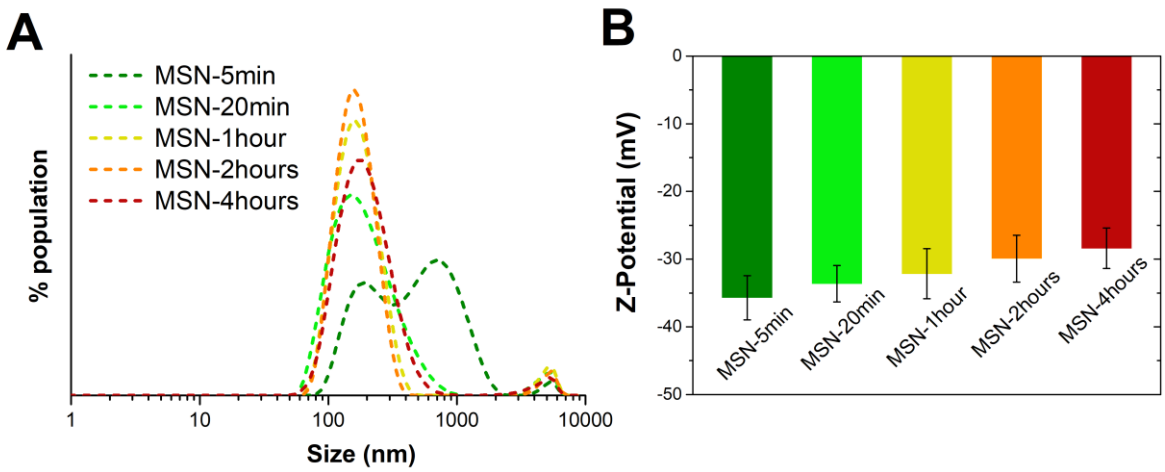


*Figure 8. (A) Size distribution of **MSN-5min**, **MSN-20min**, **MSN-1hour**, **MSN-2hours** and **MSN-4hours**, according to Intensity PSD analysis. Measurement performed in samples resuspended in distilled water at 1 mg/ml and brief spin pulses were applied to remove the larger aggregates. (B) ζ potential measurement of **MSN-5min**, **MSN-20min**, **MSN-1hour**, **MSN-2hours** and **MSN-4hours**. Measurement performed in samples resuspended in distilled water at 10 mg/ml and brief spin pulses were applied to remove the larger aggregates.*

*Table 6. DLS measurements of samples as a function of their reaction time.*

| SAMPLE | SIZE (INTENSITY) | PDI | Z-POTENTIAL |
|---|---|---|---|
| **MSN-5min** | 185 nm and 702 nm | 0.406 | -35,7 mV |
| **MSN-20min** | 148 nm | 0.283 | -33,7 mV |
| **MSN-1hour** | 159 nm | 0.260 | -32,2 mV |
| **MSN-2hours** | 158 nm | 0.237 | -29,9 mV |
| **MSN-4hours** | 174 nm | 0.265 | -28,4 mV |

DLS results seem to indicate that the aging step after the nanoparticles growth is necessary to reorganise and level the size between nanoparticles. This can be done by completing the growth of the nanoparticles with the remaining silica or using some of the silica already condensed into the smaller nanoparticles. It must be noted that during the synthesis there are continuous hydrolysis and condensation reactions of silica entities due to the elevated temperature and the alkaline pH. ELS results allow monitoring the progress of the reaction, since the negative charge of calcined MSN comes from silanolate groups. Therefore, the decrease in ζ potential means the progressive condensation of the silanol groups during this period. Therefore, the degree of condensation of the nanoparticles is expected to be higher in those samples in which the reaction time is longer and vice versa.

As-made and calcined nanoparticles were also studied by powder X-ray diffraction techniques (PXRD), and the results are represented in Figure 9 and Table 7. Diffractograms of the as-made materials were similar in all the samples (from **MSN-5min** to **MSN-4hours**) in terms of both the position of their peaks and their broadness. Therefore, this fact suggests that the supra-micellar hexagonal structure is formed already after 5 minutes with the same characteristics as the standard synthesis ((100), (110), (200) and (210) reflections are present), which was already reported [38]. The main peak, corresponding to the (100) reflection in these samples falls in the narrow range of 2.09 to 2.14 degrees, which corresponds to a unit cell ca. 4.76 to 4.88 nm. Furthermore, the full width at half maximum (FWHM) was calculated for this peak by measuring

their broadness in x-axis at half their height in y-axis. In this sense, it ranges from 0.22 to 0.24. In the case of the calcined nanoparticles, the hexagonal porous arrangement is maintained as the peaks corresponding to the reflections (100), (110), (200) and (210) are still observable. Once again, these results dissent from the study of Catalano et al. [3], who observed unresolved peaks in as made early samples, due to a disruption in the structure, which may be provoked by ethanol washing and surfactant extraction processes. Moreover, our samples showed the typical shift of the diffractogram peaks to higher 2θ values in calcined samples (reduction in d-spacing), which is related to the unit cell contraction or shrinkage provoked by calcination process. In this context, some greater variability in the position and the width of the peaks than the ones of the as-made samples is noticed. On the one hand, the peak [100] was found progressively in lower diffraction angle with the progression of the reaction (at 2.45, 2.47, 2.41, 2.32 and 2.36 for the samples **MSN-5min**, **MSN-20min**, **MSN-1hour**, **MSN-2hours** and **MSN-4hours**, respectively). On the other hand, the broadness of the peak [100] (FWHM) is greater in the first samples (0.32 and 0.30 for **MSN-5min** and **MSN-20min**, respectively) and smaller when the reaction time increase (0.28, 0.26 and 0.28 for **MSN-1hour**, **MSN-2hours** and **MSN-4hours**, accordingly).

In terms of compared results between as-made and calcined samples, it was observable how the unit cell contraction appeared to be lower as the reaction synthesis progressed and vice versa. Then, in **MSN-5min** and **MSN-20min** the unit cell shrank 0.65 and 0.68 nm, respectively, while in **MSN-1hour**, **MSN-2hours** and **MSN-4hours** the unit cell contracted 0.45, 0.49 and 0.49, correspondingly. Besides, the ratio between the FWHM of the [100] peak after and before calcination behaved in the same vein, being higher in **MSN-5min** and **MSN-20min** samples (1.45 and 1.30) and smaller in **MSN-1hour**, **MSN-2hours** and **MSN-4hours** ones (1.17, 1.18 and 1.27). This broadening of the peak after the calcination process reflects the partial loss of structural regularity which is less as the aging time is longer.

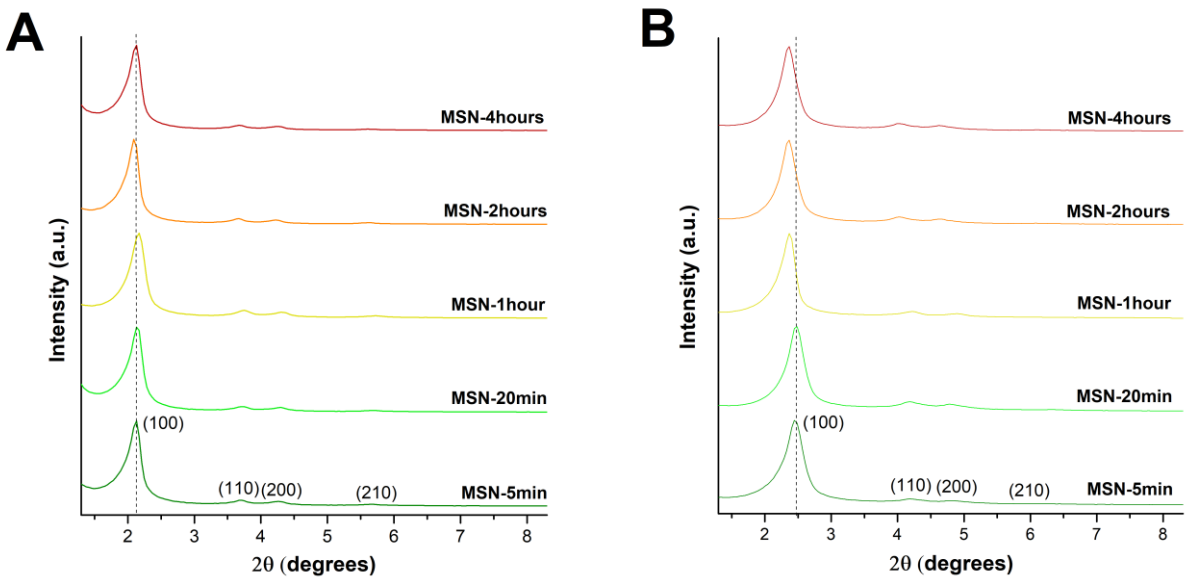


*Figure 9. PRXD patterns of as made (A) and calcined (B) samples. Dotted lines signal the position of peak (100) in the cases of **MSN-5 min** as-made and calcined.*

*Table 7. PXRD measurements of samples as a function of their synthesis time.*

| SAMPLE | AS MADE | | | CALCINED | | | COMPARED DATA | | |
|---|---|---|---|---|---|---|---|---|---|
| | Peak [100] (2θ) | Unit cell (nm) | FWHM peak [100] | Peak [100] (2θ) | Unit cell (nm) | FWHM peak [100] | Peak [100] shift (2θ) | Unit cell contraction (nm) | FWHM ratio |
| **MSN-5min** | 2.12 | 4.81 | 0.22 | 2.45 | 4.16 | 0.32 | 0.33 | 0.65 | 1.45 |
| **MSN-20min** | 2.12 | 4.81 | 0.23 | 2.47 | 4.13 | 0.30 | 0.38 | 0.68 | 1.30 |
| **MSN-1hour** | 2.14 | 4.76 | 0.24 | 2.41 | 4.24 | 0.28 | 0.27 | 0.52 | 1.17 |
| **MSN-2hours** | 2.09 | 4.88 | 0.22 | 2.32 | 4.39 | 0.26 | 0.16 | 0.49 | 1.18 |
| **MSN-4hours** | 2.12 | 4.81 | 0.22 | 2.36 | 4.32 | 0.28 | 0.24 | 0.49 | 1.27 |

Therefore, these results suggest that the cell contraction and structure disruption have an inverse correlation with reaction time and then, with the aging. In this sense, when weak structures such as **MSN-5min** and **MSN-20min** are calcined, they tend to suffer greater contraction and disorder of the mesostructure [59][60], which is reflected in greater peaks shifts (unit cell contraction) and broadening (FWHM ratio). By contrast, the samples **MSN-1hour**, **MSN-2hours** and **MSN-4hours** are more consolidated and suffer less shrinkage and structure disruption.

Measurement of isothermal adsorption-desorption of nitrogen were also performed to characterise the pore size, pore volume, and surface area (Table 8 and Figure 10). The isotherms obtained were similar in all the samples studied. They all exhibited a type IV isotherm typical of mesoporous materials. The main difference observed was that the sharp jump at intermediate partial pressures, corresponding to the capillary condensation region, shifted to the right as the synthesis time increased (from 0.28 $p/p_o$ in **MSN-5min** to 0.32 $p/p_o$ in **MSN-4hours**). This tendency was observed in Table 8, in which the pore size increases progressively with the reaction time (from 2.65 $p/p_o$ in **MSN-5min** to 2.88 $p/p_o$ in **MSN-4hours**). On the other hand, in case of specific surface area, it was observable a decrease oppositely to the reaction time (from 1157 $m^2\ g^{-1}$ in **MSN-5min** to 1082 $m^2\ g^{-1}$ in **MSN-4hours**). Regarding the pore volume, no clear tendency was observed and it seemed to be constant in the different samples (in the range from 0.97 to 1.01 $cm^3\ g^{-1}$).

Taking into account the PXRD and $N_2$ isotherms results, we have calculated the wall thickness for the different materials. In the hexagonal mesoporous materials unit cell correspond to the sum of the pore size and wall thickness. Therefore, the wall thickness was obtained by subtracting the pore size value from the unit cell value but no clear tendency was observed as a function of synthesis time (Table 8).

*Table 8. Mesoporosity of samples as a function of their synthesis time.*

| SAMPLE | BET SURFACE ($m^2 g^{-1}$) | PORE VOLUME ($cm^3 g^{-1}$) | PORE SIZE (nm) | WALL THICKNESS (nm) |
|---|---|---|---|---|
| **MSN-5min** | 1157 | 0.97 | 2.65 | 1.51 |
| **MSN-20min** | 1131 | 0.98 | 2.73 | 1.40 |
| **MSN-1hour** | 1134 | 1.01 | 2.71 | 1.53 |
| **MSN-2hours** | 1101 | 0.98 | 2.84 | 1.55 |
| **MSN-4hours** | 1082 | 0.98 | 2.88 | 1.44 |

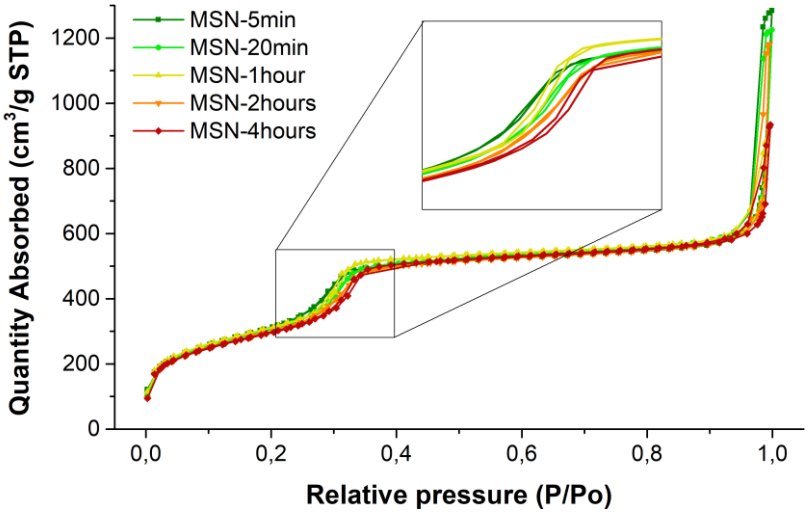


*Figure 10. $N_2$ absorption-desorption isotherms of (a) **MSN-5min**, (b) **MSN-20min**, (c) **MSN-1hour**, (d) **MSN-2hours**, and (e) **MSN-4hours**. Inset: capillary condensation region magnified.*

The results observed in $N_2$ absorption-desorption isotherms fit with the expected tendency in accordance with PXRD data. Then, the consolidation of the structure over reaction time reduces the shrinkage of the mesostructure. As a consequence of that, we found that the pore size is higher as the synthesis time increases. Additionally, the decrease in specific surface area in the samples with longer aging can be also produced by a greater consolidation of their structure, which suffer fewer defects and nooks in the surface, in contrast to those samples stirred only for 5 or 20 minutes. On the other hand, the smalls variation in the wall thickness calculated for the different materials suggest the reaction time is not affecting the to this parameter, and the changes in the unit cell measured in the PXRD analysis correspond with the decrease in pore size obtained with the $N_2$ adsorption measurements.

In order to reliably verify the degree of condensation of the samples, they were analysed by $Si^{29}$-ss-NMR. The Figure 11 shows the obtained spectra and the Table 9 collects the area under the curve (AUC) for each peak obtained by deconvolution of the spectra, fitting them by Gaussian method. The NMR spectra of the samples (Figure 11) showed 3 peaks at ca. -90, -100 and -110 ppm, corresponding to $(HO)_2Si\text{-}(OSi)_2$ ($Q_2$), $(HO)Si\text{-}(OSi)_3$ ($Q_3$) and $Si(OSi)_4$ ($Q_4$) silicon species. Nevertheless, the measurement of the sample **MSN-20min** was ignored for the analysis, since the obtained spectra presented only two peaks ($Q_3$ and $Q_4$), maybe due to some experimental or measurement error. Additionally, it was observed that some peaks of measured samples

showed a very narrow appearance, which we cannot able to explain and which can disturb the calculation of AUC. Taking this into account, at first glance the spectra showed a progressive decrease in of the $Q_2$ signal and an increase of $Q_3$ and $Q_4$ ones. Regarding the AUC calculated from spectra deconvolution and Gaussian fitting (Table 9), it was observed a decreasing tendency in the AUC of $Q_2$ with the progression of reaction time (32.8 > 17.1 > 10.2 > 4.6) with a concomitant increase of the AUC of $Q_3$ (41.7 < 47.4 < 48.6 < 74.0) and $Q_4$, except for **MSN-4hours** (25.5 < 35.6 < 41.2 > 21.4). In this sense, the peak corresponding to $Q_4$ of **MSN-4hours** showed a higher height than the other samples, but its narrowness leads to a low AUC. Besides, the degree of condensation (DK) calculated according to the equation reported by Barczak [61] (eq. 1) has also been included in Table 9.

$$DK = \frac{4 \cdot Q_4 + 3 \cdot Q_3 + 2 \cdot Q_2 + 1 \cdot Q_1}{400} \quad (1)$$

The variation of the DK parameter reflects that the connectivity of silica in the lattice increases progressively with the reaction time, except for **MSN-4hours** (73.2 < 79.6 < 82.8 > 79.2). This agrees with previous reports in which a partial condensation was reported for a solid obtained after 3 minutes stirring [17].

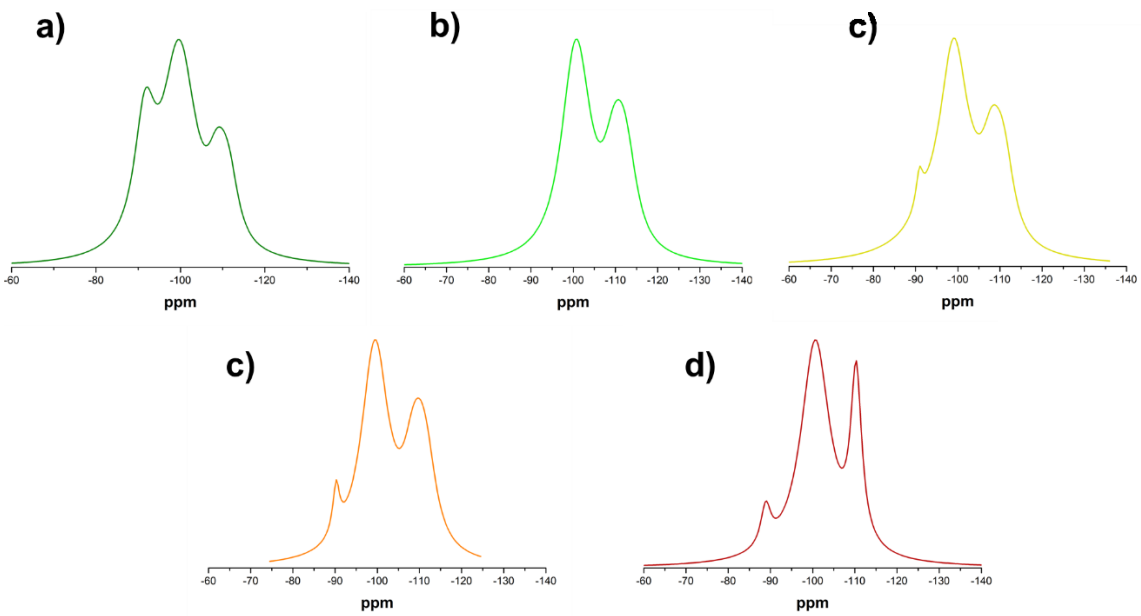


*Figure 11. $Si^{29}$-ss-NMR spectra of (a) **MSN-5min**, (b) **MSN-20min**, (c) **MSN-1hour**, (d) **MSN-2hours,** and (e) **MSN-4hours**.*

*Table 9. Peak areas obtained from the deconvolution of the $Si^{29}$-NMR spectra shown in Figure 12. The peaks were fitted to a pseudo-Voigt function. The degree of silica condensation of samples as a function of their synthesis time is given as the "DK" (degree of condensation) parameter.*

| SAMPLE | $Si^{29}$-ss-NMR | | | |
|---|---|---|---|---|
| | % Q2 | % Q3 | % Q4 | DK |
| **MSN-5min** | 32.8 | 41.7 | 25.5 | 73.2 |
| **MSN-20min** | 0 | 64.1 | 35.9 | 84.0 |
| **MSN-1hour** | 17.1 | 47.4 | 35.6 | 79.6 |
| **MSN-2hours** | 10.2 | 48.6 | 41.2 | 82.8 |
| **MSN-4hours** | 4.6 | 74.0 | 21.4 | 79.2 |

The result obtained suggest that there is an increase in the silica condensation degree as the aging time increases. In addition, it can be affirmed that once nanoparticles are formed the silica condensation inside the material is a slow process which can take several hours. Nevertheless, further assays are required to obtain consistent measurements.

## 3.4. CONCLUSIONS

This chapter presents a systematic study of the MCM-41-type MSN mechanism of formation. Hydrolysis and condensation rate have been found to play a central role in the development of MSN. In this sense, the formation of MSN has been found to be not only affected by the pH and temperature, as it has been widely studied, but also by the amount of TEOS added, the stirring rate and the TEOS addition rate. We demonstrated that these parameters influence on the silica available to be hydrolysed, and then, affect the hydrolysis and condensation rates. In this context, when the hydrolysis rate decrease, the number of initial seeds decrease and larger nanoparticles are formed, and vice versa.

Additionally, the initial stages of MSN formation have been observed and characterised by TEM and DLS, concluding that both silica polymerization and cooperative assembly models are valid according to our observations. Even, swelling-shrinking model fits with the obtained results. We can affirm that since silica-surfactant micelles analysed in the first stages of MSN formation are larger than the mesostructures formed posteriorly, they can act as CTAB repositories or suffer a rearrangement in presence of silica precursor.

Besides, the rapid formation of MCM-41-type MSN has been demonstrated, as 5 min synthesis has been sufficient to prepare MSN with similar characteristics to the ones prepared following standard synthesis. This is possible because the templating, nucleation and growth steps are very quick in the conditions used in a standard synthesis. The evolution and aging of MSN over time was also recorded and characterized. We observed in TEM and DLS that the aging of nanoparticles from 5 minutes does not increase considerably their size, but reduces the size dispersion until certain time, in which the dispersion increase again, being 2 hours the best time. The consolidation of the structure over time, and then, their increased resistance to the shrinkage provoked after calcination was also observed analysing the PXRD spectra and $N_2$ adsorption-desorption isotherms. In this context, the consolidation of the structure minimise the shrinkage of pores, but barely affects the wall thickness. In addition, ELS and NMR data suggested the increase of silica condensation degree over time, since the ζ potential decrease (indicating the loss of silanol/silanolate groups) and the condensation degree (DK) tends to increase.

To sum up, after 5 minutes the reaction works mainly towards the increasing of the silica condensation degree inside the nanoparticles, the consolidation of the structure, the rearrangement of some siloxane bonds to minimize energy and the redistribution of silica between nanoparticles, from the smallest nanoparticles to the largest ones, ending in a more homogeneous suspension at 2 hours.

On account of the studies performed here, a deeper knowledge about the synthesis mechanism of MCM-41-type MSN has been obtained. A clear understanding of this matter could provide a strong basis to improve the control of the synthesis of nanoparticles, which is essential in their development on different applications, especially what concerns to nanomedicine.

## 3.5. REFERENCES


[1] S. H. Wu and H. P. Lin, "Synthesis of mesoporous silica nanoparticles," *Chem. Soc. Rev.*, vol. 42, no. 9, pp. 3862–3875, 2013, doi: 10.1039/c3cs35405a.

[2] K. J. Edler, "Current understanding of formation mechanisms in surfactant-templated materials," *Aust. J. Chem.*, vol. 58, no. 9, pp. 627–643, 2005, doi: 10.1071/CH05141.

[3] F. Catalano and P. P. Pompa, "Design Rules for Mesoporous Silica toward the Nanosize: A Systematic Study," *ACS Appl. Mater. Interfaces*, vol. 11, no. 50, pp. 47237–47246, 2019, doi: 10.1021/acsami.9b16135.

[4] Y. Chen *et al.*, "The complete control for the nanosize of spherical MCM-41," *J. Nanosci. Nanotechnol.*, vol. 12, no. 9, pp. 7239–7249, 2012, doi: 10.1166/jnn.2012.6459.

[5] F. Tang, L. Li, and D. Chen, "Mesoporous silica nanoparticles: Synthesis, biocompatibility and drug delivery," *Adv. Mater.*, vol. 24, no. 12, pp. 1504–1534, 2012, doi: 10.1002/adma.201104763.

[6] J. Frasch, B. Lebeau, M. Soulard, J. Patarin, and R. Zana, "In situ investigations on cetyltrimethylammonium surfactant/silicate systems, precursors of organized mesoporous MCM-41-type siliceous materials," *Langmuir*, vol. 16, no. 23, pp. 9049–9057, 2000, doi: 10.1021/la000295u.

[7] J. S. Beck *et al.*, "A New Family of Mesoporous Molecular Sieves Prepared with Liquid Crystal Templates," *J. Am. Chem. Soc.*, vol. 114, no. 27, pp. 10834–10843, 1992, doi: 10.1021/ja00053a020.

[8] C. T. Kresge, M. E. Leonowicz, W. J. Roth, J. C. Vartuli, and J. S. Beck, "Ordered mesoporous molecular sives synthesized by a liquid-crytal template mechanism," *Nature*, vol. 359, pp. 710–713, 1992, doi: 10.1038/359710a0.

[9] N. K. Raman, M. T. Anderson, and C. J. Brinker, "Template-based approaches to the preparation of amorphous, nanoporous silicas," *Chemistry of Materials*, vol. 8, no. 8. American Chemical Society, pp. 1682–1701, 1996, doi: 10.1021/cm960138+.

[10] E. W. S. J. C. Vartuli, K. D. Schmitt, C. T. Kresge, W. J. Roth, M. E. Leonowicz, S. B. McCullen, S. D. Hellring, J. S. Beck, J. L. Schlenker, D. H. Olson, "Effect of Surfactant / Silica Molar Ratios on the Formation of Mesoporous Molecular Sieves : Inorganic," *Chem. Mater.*, vol. 6, pp. 2317–2326, 1994, doi: 10.1021/cm00048a018.

[11] M. J. Hollamby, D. Borisova, P. Brown, J. Eastoe, I. Grillo, and D. Shchukin, "Growth of mesoporous silica nanoparticles monitored by time-resolved small-angle neutron scattering," *Langmuir*, vol. 28, no. 9, pp. 4425–4433, 2012, doi: 10.1021/la203097x.

[12] J. C. Vartuli *et al.*, "Synthesis of Mesoporous Materials: Liquid-Crystal Templating versus Intercalation of Layered Silicates," *Chem. Mater.*, vol. 6, no. 11, pp. 2070–2077, Nov. 1994, doi: 10.1021/cm00047a029.

[13] C. Y. Chen, S. Q. Xiao, and M. E. Davis, "Studies on ordered mesoporous materials III. Comparison of MCM-41 to mesoporous materials derived from kanemite," *Microporous Mater.*, vol. 4, no. 1, pp. 1–20, 1995, doi: 10.1016/0927-6513(94)00077-9.

[14] A. Monnier *et al.*, "Cooperative formation of inorganic-organic interfaces in the synthesis of silicate mesostructures," *Science (80-. ).*, vol. 261, no. 5126, pp. 1299–1303, 1993, doi: 10.1126/science.261.5126.1299.

[15] A. Firouzi *et al.*, “Cooperative organization of inorganic-surfactant and biomimetic assemblies,” *Science (80-. ).*, vol. 267, no. 5201, pp. 1138–1143, 1995, doi: 10.1126/science.7855591.

[16] C. E. Fowler, D. Khushalani, B. Lebeau, and S. Mann, “Nanoscale Materials with Mesostructured Interiors,” *Adv. Mater.*, vol. 13, no. 9, pp. 649–652, May 2001, doi: 10.1002/1521-4095(200105)13:9<649::AID-ADMA649>3.0.CO;2-G.

[17] L. Jin, S. M. Auerbach, and P. A. Monson, “Simulating the formation of surfactant-templated mesoporous silica materials: A model with both surfactant self-assembly and silica polymerization,” *Langmuir*, vol. 29, no. 2, pp. 766–780, 2013, doi: 10.1021/la304475j.

[18] S. C. Chien *et al.*, “Molecular Simulations of the Synthesis of Periodic Mesoporous Silica Phases at High Surfactant Concentrations,” *J. Phys. Chem. C*, vol. 121, no. 8, pp. 4564–4575, 2017, doi: 10.1021/acs.jpcc.6b09429.

[19] G. Lelong, S. Bhattacharyya, S. Kline, T. Cacciaguerra, M. A. Gonzalez, and M.-L. L. Saboungi, “Effect of Surfactant Concentration on the Morphology and Texture of MCM-41 Materials,” *J. Phys. Chem.*, vol. 112, no. 29, pp. 10674–10680, Jul. 2008, doi: 10.1021/jp800898n.

[20] F. Lu, S. H. Wu, Y. Hung, and C. Y. Mou, “Size effect on cell uptake in well-suspended, uniform mesoporous silica nanoparticles,” *Small*, vol. 5, no. 12, pp. 1408–1413, Jun. 2009, doi: 10.1002/smll.200900005.

[21] Z. Yi *et al.*, “A New Insight into Growth Mechanism and Kinetics of Mesoporous Silica Nanoparticles by in Situ Small Angle X-ray Scattering,” *Langmuir*, vol. 31, no. 30, pp. 8478–8487, 2015, doi: 10.1021/acs.langmuir.5b01637.

[22] C. C. Landry *et al.*, “Phase transformations in mesostructured silica/surfactant composites. Mechanisms for change and applications to materials synthesis,” *Chem. Mater.*, vol. 13, no. 5, pp. 1600–1608, 2001, doi: 10.1021/cm000373z.

[23] P. Ågren *et al.*, “Kinetics of Cosurfactant-Surfactant-Silicate Phase Behavior. 1. Short-Chain Alcohols,” *J. Phys. Chem. B*, vol. 103, no. 29, pp. 5943–5948, 1999, doi: 10.1021/jp984684x.

[24] K. W. Gallis and C. C. Landry, “Synthesis of MCM-48 by a Phase Transformation Process,” *Chem. Mater.*, vol. 9, no. 10, pp. 2035–2038, 1997, doi: 10.1021/cm970482m.

[25] S. Sadasivan, C. E. Fowler, D. Khushalani, and S. Mann, “Nucleation of MCM-41 nanoparticles by internal reorganization of disordered and nematic-like silica - Surfactant clusters,” *Angew. Chemie - Int. Ed.*, vol. 41, no. 12, pp. 2151–2153, 2002, doi: 10.1002/1521-3773(20020617)41:12<2151::AID-ANIE2151>3.0.CO;2-U.

[26] N. Hao, L. Li, and F. Tang, “Facile preparation of ellipsoid-like MCM-41 with parallel channels along the short axis for drug delivery and assembly of Ag nanoparticles for catalysis,” *J. Mater. Chem. A*, vol. 2, no. 30, pp. 11565–11568, 2014, doi: 10.1039/c4ta01820f.

[27] Q. Huo *et al.*, “Organization of Organic Molecules with Inorganic Molecular Species into Nanocomposite Biphase Arrays*,” 1994. doi: 10.1021/cm00044a016.

[28] S. Schacht, Q. Huo, I. G. Voigt-Martin, G. D. Stucky, and F. Schüth, “Oil-water interface templating of mesoporous macroscale structures,” *Science (80-. ).*, vol. 273, no. 5276, pp. 768–771, Aug. 1996, doi: 10.1126/science.273.5276.768.

[29] J. Schmitt *et al.*, “Outset of the Morphology of Nanostructured Silica Particles during Nucleation Followed by Ultrasmall-Angle X-ray Scattering,” *Langmuir*, vol. 32, no. 20, pp. 5162–5172, 2016, doi: 10.1021/acs.langmuir.6b00572.

[30] G. Pérez-Sánchez *et al.*, “Multiscale Model for the Templated Synthesis of Mesoporous Silica: The Essential Role of Silica Oligomers,” *Chem. Mater.*, vol. 28, no. 8, pp. 2715–2727, 2016, doi: 10.1021/acs.chemmater.6b00348.

[31] P. P. Ghimire and M. Jaroniec, “Renaissance of Stöber method for synthesis of colloidal particles: New developments and opportunities,” *J. Colloid Interface Sci.*, vol. 584, pp. 838–865, 2021, doi: 10.1016/j.jcis.2020.10.014.

[32] J. Gu, W. Fan, A. Shimojima, and T. Okubo, “Organic–Inorganic Mesoporous Nanocarriers Integrated with Biogenic Ligands,” *Small*, vol. 3, no. 10, pp. 1740–1744, Oct. 2007, doi: 10.1002/smll.200700311.

[33] R. Narayan, U. Y. Nayak, A. M. Raichur, and S. Garg, “Mesoporous silica nanoparticles: A comprehensive review on synthesis and recent advances,” *Pharmaceutics*, vol. 10, no. 3, pp. 1–49, 2018, doi: 10.3390/pharmaceutics10030118.

[34] R. I. Nooney, D. Thirunavukkarasu, Y. Chen, R. Josephs, and A. E. Ostafin, “Synthesis of Nanoscale Mesoporous Silica Spheres with Controlled Particle Size,” *Nature*, 2002, doi: 10.1021/cm0204371.

[35] E. Yamamoto and K. Kuroda, “Colloidal mesoporous silica nanoparticles,” *Bull. Chem. Soc. Jpn.*, vol. 89, no. 5, pp. 501–539, 2016, doi: 10.1246/bcsj.20150420.

[36] Q. Cai, Z. S. Luo, W. Q. Pang, Y. W. Fan, X. H. Chen, and F. Z. Cui, “Dilute solution routes to various controllable morphologies of MCM-41 silica with a basic medium,” *Chem. Mater.*, vol. 13, no. 2, pp. 258–263, 2001, doi: 10.1021/cm990661z.

[37] N. T. K. Thanh, N. Maclean, and S. Mahiddine, “Mechanisms of nucleation and growth of nanoparticles in solution,” *Chemical Reviews*, vol. 114, no. 15. American Chemical Society, pp. 7610–7630, Aug. 13, 2014, doi: 10.1021/cr400544s.

[38] M. Lindén, S. A. Schunk, and F. Schüth, “In Situ X-Ray Diffraction Study of the Initial Stages of Formation of MCM-41 in a Tubular Reactor,” *Angew. Chemie Int. Ed.*, vol. 37, no. 6, pp. 821–823, Apr. 1998, doi: 10.1002/(SICI)1521-3773(19980403)37:6<821::AID-ANIE821>3.0.CO;2-I.

[39] R. Kumar, H. T. Chen, J. L. V. Escoto, V. S. Y. Lin, and M. Pruski, “Template removal and thermal stability of organically functionalized mesoporous silica nanoparticles,” *Chem. Mater.*, vol. 18, no. 18, pp. 4319–4327, Sep. 2006, doi: 10.1021/cm060598v.

[40] K. Möller, J. Kobler, and T. Bein, “Colloidal suspensions of nanometer-sized mesoporous silica,” *Adv. Funct. Mater.*, vol. 17, no. 4, pp. 605–612, Mar. 2007, doi: 10.1002/adfm.200600578.

[41] S. Kachbouri, N. Mnasri, E. Elaloui, and Y. Moussaoui, “Tuning particle morphology of mesoporous silica nanoparticles for adsorption of dyes from aqueous solution,” *J. Saudi Chem. Soc.*, vol. 22, no. 4, pp. 405–415, 2018, doi: 10.1016/j.jscs.2017.08.005.

[42] A. Lodha *et al.*, “Synthesis of mesoporous silica nanoparticles and drug loading of poorly water soluble drug cyclosporin A,” *J. Pharm. Bioallied Sci.*, vol. 4, no. SUPPL., pp. 92–94, 2012, doi: 10.4103/0975-7406.94153.

[43] J. Kobler, K. Möller, and T. Bein, “Colloidal Suspensions of Functionalized Mesoporous

Silica Nanoparticles," *ACS Nano*, vol. 2, no. 4, pp. 791–799, Apr. 2008, doi: 10.1021/nn700008s.

[44] W. Stöber, A. Fink, and E. Bohn, "Controlled growth of monodisperse silica spheres in the micron size range," *J. Colloid Interface Sci.*, vol. 26, no. 1, pp. 62–69, Jan. 1968, doi: 10.1016/0021-9797(68)90272-5.

[45] J. Zhang, Z. Luz, and D. Goldfarb, "EPR Studies of the Formation Mechanism of the Mesoporous Materials MCM-41 and MCM-50," *J. Phys. Chem. B*, vol. 101, no. 36, pp. 7087–7094, Sep. 1997, doi: 10.1021/jp9709621.

[46] K. Kuperkar *et al.*, "Viscoelastic micellar water/CTAB/NaNO3 solutions: Rheology, SANS and cryo-TEM analysis," *J. Colloid Interface Sci.*, vol. 323, no. 2, pp. 403–409, Jul. 2008, doi: 10.1016/j.jcis.2008.04.040.

[47] V. Agarwal, M. Singh, G. McPherson, V. John, and A. Bose, "Microstructure evolution in aqueous solutions of cetyl trimethylammonium bromide (CTAB) and phenol derivatives," *Colloids Surfaces A Physicochem. Eng. Asp.*, vol. 281, no. 1–3, pp. 246–253, Jun. 2006, doi: 10.1016/j.colsurfa.2006.02.047.

[48] R. M. Pallares, X. Su, S. H. Lim, and N. T. K. Thanh, "Fine-tuning of gold nanorod dimensions and plasmonic properties using the Hofmeister effects," *J. Mater. Chem. C*, vol. 4, no. 1, pp. 53–61, Dec. 2016, doi: 10.1039/C5TC02426A.

[49] H. Yamada, C. Urata, E. Yamamoto, S. Higashitamori, Y. Yamauchi, and K. Kuroda, "Effective Use of Alkoxysilanes with Different Hydrolysis Rates for Particle Size Control of Aqueous Colloidal Mesostructured and Mesoporous Silica Nanoparticles by the Seed-Growth Method," *ChemNanoMat*, vol. 1, no. 3, pp. 194–202, Jul. 2015, doi: 10.1002/cnma.201500010.

[50] C. J. Brinker, "Hydrolysis and condensation of silicates: effects on structure," *J. Non. Cryst. Solids*, vol. 100, pp. 31–50, 1988, doi: 10.1016/0022-3093(88)90005-1.

[51] Z. A. Qiao, L. Zhang, M. Guo, Y. Liu, and Q. Huo, "Synthesis of mesoporous silica nanoparticles via controlled hydrolysis and condensation of silicon alkoxide," *Chem. Mater.*, vol. 21, no. 16, pp. 3823–3829, 2009, doi: 10.1021/cm901335k.

[52] M. Yu *et al.*, "A simple approach to prepare monodisperse mesoporous silica nanospheres with adjustable sizes," *J. Colloid Interface Sci.*, vol. 376, no. 1, pp. 67–75, 2012, doi: 10.1016/j.jcis.2012.03.014.

[53] N. A. Zainal, S. R. A. Shukor, H. A. A. Wab, and K. A. Razak, "Study on the effect of synthesis parameters of silica nanoparticles entrapped with rifampicin," *Chem. Eng. Trans.*, vol. 32, pp. 2245–2250, 2013, doi: 10.3303/CET1332375.

[54] H. Yamada, H. Ujiie, C. Urata, E. Yamamoto, Y. Yamauchi, and K. Kuroda, "A multifunctional role of trialkylbenzenes for the preparation of aqueous colloidal mesostructured/mesoporous silica nanoparticles with controlled pore size, particle diameter, and morphology," *Nanoscale*, vol. 7, no. 46, pp. 19557–19567, 2015, doi: 10.1039/C5NR04465K.

[55] W. H. Fu, Y. Guan, Y. M. Wang, and M. Y. He, "A facile synthesis of monodispersed mesoporous silica nanospheres with Pm3n structure," *Microporous Mesoporous Mater.*, vol. 220, pp. 168–174, 2016, doi: 10.1016/j.micromeso.2015.09.004.

[56] Y. S. Lin and C. L. Haynes, "Impacts of mesoporous silica nanoparticle size, pore ordering, and pore integrity on hemolytic activity," *J. Am. Chem. Soc.*, vol. 132, no. 13,

pp. 4834–4842, 2010, doi: 10.1021/ja910846q.

[57] B. N. Khlebtsov, V. A. Khanadeev, and N. G. Khlebtsov, “Determination of the Size, Concentration, and Refractive Index of Silica Nanoparticles from Turbidity Spectra,” *Langmuir*, vol. 24, no. 16, pp. 8964–8970, Aug. 2008, doi: 10.1021/la8010053.

[58] Y. D. Chiang, H. Y. Lian, S. Y. Leo, S. G. Wang, Y. Yamauchi, and K. C. W. Wu, “Controlling particle size and structural properties of mesoporous silica nanoparticles using the taguchi method,” *J. Phys. Chem. C*, vol. 115, no. 27, pp. 13158–13165, 2011, doi: 10.1021/jp201017e.

[59] T. W. Kim, P. W. Chung, and V. S. Y. Lin, “Facile synthesis of monodisperse spherical MCM-48 mesoporous silica nanoparticles with controlled particle size,” *Chem. Mater.*, vol. 22, no. 17, pp. 5093–5104, 2010, doi: 10.1021/cm1017344.

[60] H. I. Meléndez-Ortiz, L. A. García-Cerda, Y. Olivares-Maldonado, G. Castruita, J. A. Mercado-Silva, and Y. A. Perera-Mercado, “Preparation of spherical MCM-41 molecular sieve at room temperature: Influence of the synthesis conditions in the structural properties,” *Ceram. Int.*, vol. 38, no. 8, pp. 6353–6358, 2012, doi: 10.1016/j.ceramint.2012.05.007.

[61] M. Barczak, “Template removal from mesoporous silicas using different methods as a tool for adjusting their properties,” *New J. Chem.*, vol. 42, no. 6, pp. 4182–4191, 2018, doi: 10.1039/c7nj04642a.

# CHAPTER 4: STUDYING DISREGARDED PARAMETERS IN MCM-41-TYPE MSN SYNTHESIS

# 4. STUDYING DISREGARDED PARAMETERS IN MCM-41-TYPE MSN SYNTHESIS

## 4.1. INTRODUCTION

Giving the importance of MSN in a wide range of applications, acquiring a better knowledge about the MSN synthesis mechanism is necessary to know and control their properties. Knowing how each parameter can influence their synthesis is also crucial for tailoring the final properties and structure of the nanoparticles [1][2]. Some of the most commonly studied parameters in the MCM-41-type MSN are the pH value, the silica/surfactant ratio, the reaction time and temperature, the silica precursor used, the concentration of additive alcohols or cosurfactants, etc. Generally, the most observed properties are pore size distribution, mesostructured arrangement (e.g. wormhole-like, dendrimer-like, disordered, hexagonal, lamellar or cubic mesophases), silica condensation degree, particle size (from few nanometres to several microns), morphology (e.g. spheres, hollow spheres, irregular, worm-like, oval or rods) and aggregation [3][4].

Particularly, regarding to MCM-41-type MSN, as it has been mentioned in Chapter 3, the synthesis procedure is quite standardised and based on the conditions employed by Cai et al. in 2001 [5]. Nevertheless, from this starting point, some modifications to this procedure, such as the temperature reaction, pH and time, the surfactant-silica ratio, or the reagents dilution, have been studied in order to introduce variations to some features of the nanoparticles, as it can be read below. However, in spite of the developments and knowledge acquired in the following years, the original protocol remains the most widely used owing to its facile implementation [6], as well as the reasonable quality of the nanoparticles obtained. Yet, this protocol leaves some poorly defined parameters that have been freely interpreted over the last years and whose modification is not always well studied. Variables such as the stirring rate, the magnetic stirrer bar, the container used or the TEOS addition rate among others can be mentioned.

In this work we summarise the influence of the most studied synthesis parameters on MCM-41-type MSN properties. Starting from the state of the art, we present here the study of the effect of some disregarded parameters on the synthesis of MCM-41-type MSN. Therefore, more reproducible, and tailored MCM-41-type MSN can be obtained.

### 4.1.1. Main variables controlling the nanoparticles formation

Some of the most studied and influent factors involved in control of MCM-41-type MSN synthesis are the reaction pH, temperature, and time, as well as the stirring rate and the surfactant/silica precursor ratio.

#### 4.1.1.1. pH

pH is quite determinant in the nanoparticles formation mainly by controlling the charge density of the species involved in the synthesis. This parameter has a great influence on the particles growth step [4]. Charge density of silica increases as pH value moves away from its isoelectric

point (IEP = 2). Hence, higher pH conditions result in an increase in silicate solubility in water, as well as in an increase in the intensity of nucleophilic attack due to the presence of a larger number of hydroxide anions resulting then in higher silica hydrolysis rate [7][8][9][10]. On the other hand, condensation rate reaches the maximum value at neutral pH or softly alkaline (maximum at pH 8.4 [10]), decreasing at acid pH, when silicates are close to the isoelectric point and their density charge decrease, and also decreasing at alkaline pH due to the instability of silica species and the increased repulsions due to their high negative density charge [10]. However, in MSN synthesis, surfactant molecules interact and stabilise the silica precursor at high pH, maintaining relatively high silica condensation rates at pH around 12. This interaction between silica precursor and surfactant is strengthen due to alkaline conditions [3], specifically over pH 11 [4].

Therefore, at higher pH great hydrolysis rates are provoked, but silica condensation is rate-limiting, generating fewer but larger nuclei, which gives as a result the formation of large MSN [10][11][4]. On the contrary, at lower pH, hydrolysis acts as the rate-limiting, and then greater number of nuclei but smaller are formed, since condensation reaction is faster. Then, low hydrolysis rate could lead to long delay time in forming the silica precipitate.[10] Hence, the size of MSN can be tuned modifying the reaction pH, obtaining nanoparticles from few tens of nanometres to almost a micron [3][7][12] [13][14].

Changes in pH also affect the shape of the nanoparticles as well as the ordering of the pores [10][3][7][42]. Particularly, Varache et al. [6] made a detailed study about the effects of changing the pH in the MCM-41-type MSN. Using low NaOH concentrations a worm-like mesostructure highly connected forming aggregates of several hundreds of nanometres was obtained. The structure found was disordered since the condensation rate prevailed over that of the cooperative templating process. Besides, at these conditions the condensation rate was dominant, and therewith, a highly condensed structure was obtained. When the amount of NaOH was increased, reaching a pH around 12, spherical nanoparticles ca. 100 nm with well-defined MCM41 structure were obtained. Some fusions between nanoparticles could be found but not large aggregates. The MCM41 mesostructure could be formed due to the lower condensation degree, which allowed the reorganisation of the hybrid micelles as cylindrical structures and also their hexagonal arrangement. Higher alkaline solutions gave independent and larger nanoparticles with a broad range of sizes. Furthermore, the structure was supermicroporous, with a type 1 isotherm in nitrogen adsorption measurements, due to the shrinkage of pores. The condensation degree is lower due to the low condensation rate at the highest pH.

#### 4.1.1.2. Stirring rate

Stirring rate affects the nanoparticle formation in different ways. Firstly, it modulates the neighbouring silica-surfactant micelles aggregation. At low stirring speed, the formation of large sized nanoparticles is promoted [16][17], meanwhile the increase of stirring speed improves the mixing and thus the contact between silica precursor emulsions and aqueous solution, leading to the formation of smaller nanoparticles [18][19][20][16][21]. On the other hand, a combination of high stirring rate and the presence of ethanol lead to a transformation phase

from hexagonal (2D) to cubic (3D), even at low surfactant concentrations [18][22][23]. In addition, strong stirring rates provokes the deterioration of the morphological regularity due to shearing forces originated [1].

#### 4.1.1.3. Temperature

Temperature of the reaction is related to the solubility of silica and surfactant and to the chemical reaction course (both hydrolysis and condensation) [24][25]. High temperatures facilitate the solubility of silica precursor in aqueous solution, which increases its hydrolysis rate, which is also favoured by temperature. In addition, silica condensation rate is also favoured, boosting the nuclei growth [16][4], rather than producing a higher amount of nuclei. Hence, larger nanoparticles are formed [26][1]. Higher temperatures also favour a better arrangement of mesostructures [1].

In contrast, at low temperatures reaction rate decreases and smaller and more fused nanoparticles are formed. Besides, in these conditions, the mesoporous structure is less ordered, due to the low solubility of silica and surfactant [4]. Furthermore, after calcination there is a great shrinkage due to the low condensation degree and low consistency of the nanoparticles formed. On the other hand, it has also been described how the reaction temperature can determine the structure adopted by the silica-surfactant micelles, such as tubular, lamellar, spherical, hexagonal, etc.[27][28]

#### 4.1.1.4. Time

According to our studies (in Chapter 3) and as some authors reported [4][29], some hours are required to complete the silicate condensation. On the other hand, some studies has been reported that an increase in the reaction time, which is also called aging, produces larger nanoparticles [4][40][56] due to the greater silica oligomers deposition. However, it has been reported that the aging reaction over 4 hours results in the production of smaller nanoparticles [4]. In this sense, Chiang et al. [15] reported that increasing the reaction time in alkaline conditions causes an erosion of silica structure, producing a decrease in the size of the nanoparticles. Nevertheless, size variations reported derived from different reaction times are minor in comparison to those provoked by pH and temperature changes. Conversely, our studies showed that aging barely increase the size of the nanoparticles.

In addition, aging time results in more stable and well-ordered MCM-41 structure [54][57], due to a gradual increase in the degree of condensation, which confers the nanoparticles greater resistance to the shrinkage caused by calcination [18]. These processes can be also associated with a growth of pore wall thickness, and then a decrease in pore size, as it was observed in a synthesis at room temperature [31], although our experiments at 80 degrees suggested that pore wall thickness is not affected.

#### 4.1.1.5. Surfactant/silica precursor ratio

The amount of surfactant used in relation to the silica precursor added is another important variable in the MSN formation. It has been reported that increasing the silica/surfactant ratio results in a larger unit cell framework. This increment is not a consequence of bigger pore size, but thicker pore wall. Then, MSN acquire more stability and endurance. The opposite behaviour is seen when the silica/surfactant ratio is reduced [31].

On the other hand, some textural modifications in the MCM-41-type MSN have been reported. An increase in the surfactant amount from certain value is associated with a mesophase transformation from 2D hexagonal to 3D tubular. In addition, this structural modification is also accompanied by significant morphological and size changes in the nanoparticles obtained, which are irregular in shape and smaller in size [2].

### 4.1.2. Objectives

According to the reviewed information, we focus on the study some disregarded parameters in the synthesis of MCM-41-type MSN such as the synthesis time, the stirring rate, the magnetic stir bar used, the TEOS addition rate and the neutralisation method once nanoparticles are formed.

## 4.2. MATERIALS AND METHODS

### 4.2.1. Chemicals

Tetraethylorthosilicate (TEOS), 1-hexadecyltrimethylammonium bromide (CTAB) and sodium hydroxide (NaOH) were purchased from Sigma-Aldrich. Hydrochloric acid 37% (HCl) was provided by Scharlab.

### 4.2.2. General techniques

Transmission electron microscopy (TEM), $N_2$ adsorption–desorption isotherms, powder X-ray diffraction (PXRD) and dynamic light scattering (DLS), were used in order to characterise the prepared materials. The instruments used were the following: JEOL JEM-1010 microscope for TEM images acquisitions; Bruker D8 Advance diffractometer (Cu Kα radiation) for PXRD measurements; Micromeritics ASAP 2010 automated analyser for recording of $N_2$ adsorption–desorption isotherms, samples were degassed at 120 °C in a vacuum overnight. The specific surface areas were calculated from the adsorption data within the low-pressure range using the BET (Brunauer–Emmett–Teller) model. Pore size was determined following the BJH (Barrett–Joyner–Halenda) method. Particle size were measured by ZetaSizer Nano ZS (Malvern Instruments Ltd.) equipped with a laser of 633 nm and collecting the signal at 173°. All samples were prepared at 1 mg/mL in distilled water and they spun in a centrifuge at 10,000 rpm to remove the large aggregates and sediments before being measured.

### 4.2.3. Synthesis of nanoparticles

Different conditions were used to synthesize MCM-41-type nanoparticles and these are specified in each assay. However, a general protocol was stablished. 1 g of CTAB (2.74 mmol) was mixed with 480 mL of deionised water in a 1L (10.5 cm of outer diameter) cylindrical beaker. The mixture was heated at 50 °C to dissolve the surfactant and stirred with a cylindrical and plain magnetic stir bar (60mm long and 15mm diameter) at 500 rpm. Then, 280 mg of NaOH (7 mmol) dissolved in 3.5 mL of deionised water were added to reach a pH of 12.16, and the temperature solution was adjusted to 80 °C. A watch glass was placed to cover the beaker to minimize the solvent evaporation and therefore to prevent the volume from decreasing during the reaction. When the temperature reached 80 °C, 5 mL of TEOS (25.7 mmol) were added dropwise (5 mL/min), using syringe and needle. Soon after, a white precipitate appeared. The mixture was stirred for 2 h. After this time, the suspension was cooled at room temperature (measured pH 11.75). The solid product was then vacuum filtered with a Buchner over a filter paper (Whatman™ Grade 3MM Chr) and deionised water was added until the suspension reached neutral pH. Finally, the solid was dried under vacuum and grinded to obtain a white powder. After the synthesis, nanoparticles were calcined at 550 °C using an oxidant atmosphere for 5 h in order to remove the surfactant.

### 4.2.4. Image analysis

Transmission electron microscopy was performed to acquire a wide representation of each sample, in order to check size and shape of synthesized nanoparticles, as well as the fusion formed between them. **Size**: At least 100 particles for each sample were counted to obtain a

representative size distribution of the particles. In the case of non-spherical nanoparticles, the size was measured along the longer direction. **Fusions**: Interparticle fusion was studied on at least 200 particles per sample and only those with a clear silica bridge were counted.

## 4.3. RESULTS AND DISCUSSION

### 4.3.1. The importance of the stirring control

The results obtained in Chapter 3 suggest that the stirring plays an important role in the nanoparticles formation, especially in nucleation and growing process. Then, different issues around the stirring were studied.

#### 4.3.1.1. Stirring rate

The influence of the stirring rate in the synthesis reaction of MCM-41-type MSN with respect to the size [16][17] or the morphological changes of the nanoparticles [1] has been studied by other authors, but the analysis of their relationship was superficial. In the following study, we bring out the importance of not only the stirring rate, but also the shape and surface of the magnetic stirrer bar. In addition, stirring is not only related to size and morphology as it has already been reported, but also to the fusion between nanoparticles.

Different samples were prepared modifying the stirring rate (350 rpm, 500 rpm, 900 rpm and 1200 rpm) during the whole reaction on a combined hot-plate magnetic-stirrer device and a plain cylindrical magnetic stir bar. The samples, which were named **MSN-350rpm**, **MSN-500rpm** (corresponding to the standard synthesis), **MSN-900rpm** and **MSN-1200rpm** were characterized by TEM and DLS.

TEM and DLS data were represented in Table 1. According to TEM pictures (Figure 1), the nanoparticles diameter decreased with increasing stirring rates until reaching a minimum value of around 80 nm from 900rpm (**MSN-350rpm** averaged at 112 nm, **MSN-500rpm** at 89 nm, **MSN-900rpm** at 80 nm and **MSN-1200rpm** at 80 nm). The size dispersion in the samples was around a 15% for **MSN-350rpm**, **MSN-500rpm** and **MSN-900rpm** samples, but higher (21%) for the solid obtained at the highest stirring speed (**MSN-1200rpm**). In addition, it is also observable that the nanoparticles morphology is becoming more irregular with the increase of the stirring speed. Thus, **MSN-350rpm** and **MSN-500rpm** tend to have smooth surface and spherical-shape, but at **MSN-900rpm** and especially **MSN-1200rpm** are poorly formed and their surface is rough. We have also used TEM pictures to study the interconnectivity between nanoparticles (ticks on Figure 1). It can be seen that a higher stirring rate leads to a higher number of visible fusions between nanoparticles. In case of **MSN-350rpm**, the population of nanoparticles shows visible silica bridges in ca. 30% of the nanoparticles. This percentage increases to ca. 45% in **MSN-500rpm**, 90% in **MSN-900rpm** and 95% in **MSN-1200rpm**.

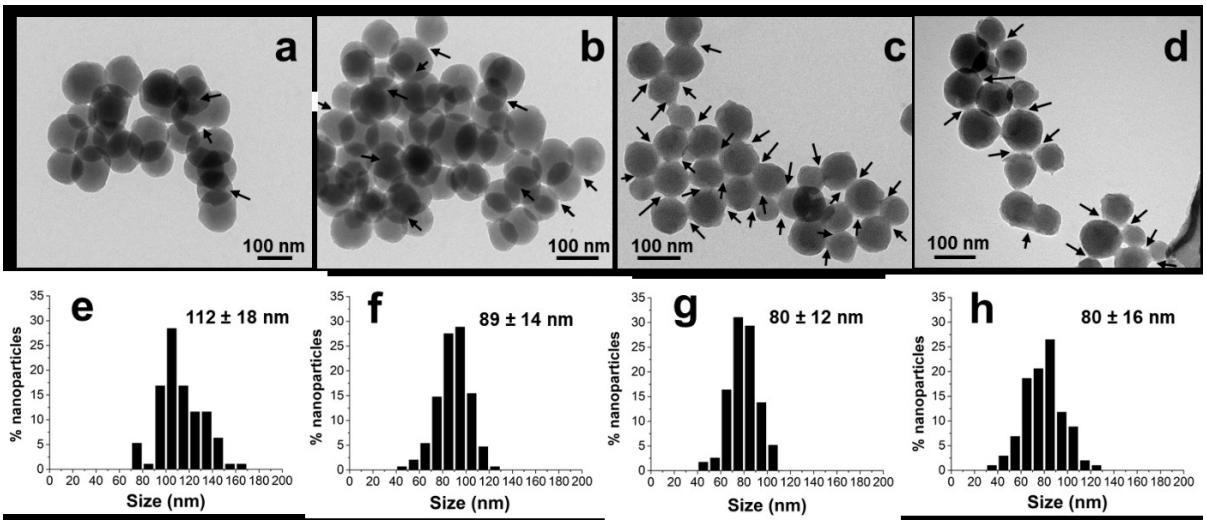


*Figure 1. TEM images and histograms with particle size distribution of **MSN-350rpm** (a, e), **MSN-500rpm** (b, f), **MSN-900rpm** (c, g), and **MSN-1200rpm** (d, h). Arrows indicate the distinguishable fusions.*

*Table 1. TEM and DLS measurement data of samples as a function of the stirring rate.*

| | TEM DATA | | DLS DATA | | |
|---|---|---|---|---|---|
| **SAMPLE** | **SIZE** | **% FUSED NANOPARTICLES** | **HYDRODYNAMIC SIZE (INTENSITY)** | **PDI** | **FWHM** |
| **MSN-350rpm** | 112 ± 18 nm (16%) | 30% | 175 nm | 0.215 | 156 nm |
| **MSN-500rpm** | 89 ± 14 nm (15%) | 45% | 162 nm | 0.203 | 147 nm |
| **MSN-900rpm** | 80 ± 12 nm (15%) | 90% | 147 nm | 0.242 | 166 nm |
| **MSN-1200rpm** | 80 ± 16 nm (21%) | 95% | 168 nm | 0.231 | 234 nm |

DLS measurements were used to obtain the hydrodynamic diameter. All the samples measured were briefly spun in order to remove large aggregates and sediments, whose presence would prevent a quality measurement. The tendency observed in DLS curves (Figure 2) did not exactly match the observations in the TEM pictures. **MSN-350rpm** (175 nm), **MSN-500rpm** (162 nm) and **MSN-900rpm** (147 nm) samples show a decreasing tendency of the hydrodynamic diameter with the increase of the stirring rate, as it happens in TEM images. However, in **MSN-1200rpm** (168 nm) the tendency changes from the one observed in TEM images, and the diameter increases a little bit. This phenomenon may be related to a greater presence of small aggregates in this sample. Additionally, the size dispersion was analysed taking into consideration the width of the DLS curves (FWHM in intensity PSD). Then, from the data in Table 1, it can be seen that the FWHM increased with the stirring rate (**MSN-350rpm** (156 nm), **MSN-500rpm** (147 nm), **MSN-900rpm** (166 nm) and **MSN-1200rpm** (234 nm)). In addition to the increase in dispersion of the size of the nanoparticles, the increase of FWHM of DLS curves with the stirring rate is also caused by an increase in the number of fused nanoparticles that forms dimers, trimers, and larger ones.

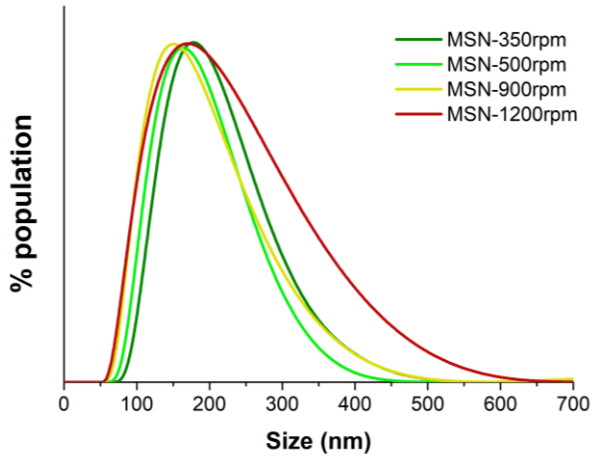


*Figure 2. Size distribution of **MSN-350rpm**, **MSN-500rpm**, **MSN-900rpm**, and **MSN-1200rpm** according to Intensity PSD analysis. Measurements were performed in samples resuspended in distilled water at 1 mg/ml and brief spin pulses were applied to remove the larger aggregates. Note that the x-axis is linear.*

In order to explain the influence of the stirring on the size and morphology of the MSN, it is necessary to understand the mechanism of stirring. In this type of reaction and stirring setup, the axial flow is minimum since the magnetic stirrer bar does not have a propeller configuration. Therefore, the main flow involved in the stirring is the radial flow, which is perpendicular to rotation and follows a uniform angular motion. Radial flow is related to the stirring rate, the longitudinal surface of magnetic stirrer bar and its similarity to a radial impeller or a paddle, i.e., the amount of perpendicular surface to rotation axis, which impose a shear stress to the fluid. Tangential flow is also produced as a result of centrifugal force created by the radial flow. As a consequence of this mixed forces a vortex appears in the centre of the axis, where downward flow domains and tangential flow is almost zero, and which creates a funnel on the surface [32][33]. Figure 3 represents an analysis of simulated flow velocities in cylindrical baker stirred with cylindrical magnetic stir bar. Therefore, an adequate stirring rate is important to obtain MSN with regular morphology, size, and distribution.

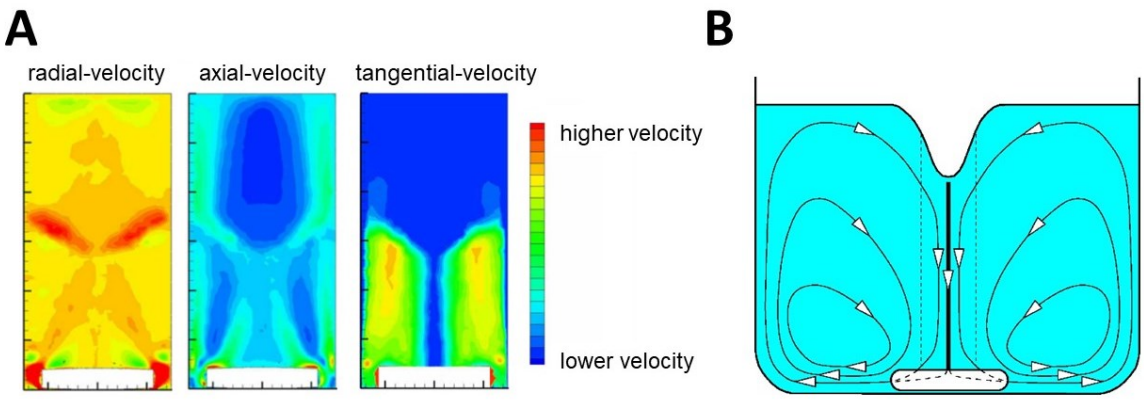


*Figure 3. A) Simulated flow velocities and B) flow patterns in cylindrical baker stirred with cylindrical magnetic stir. A) is adapted from reference* [32]. *Copyright 2015 © IWA publishing. B) is reprinted from reference [33]. Copyright © 2007 American Journal of Physics.*

Hence, the size reduction of nanoparticles due to the increment of the stirring rate could be mainly explained by the influence of the stirring on the hydrolysis and condensation rate. At

higher stirring speeds, the oil-drops of TEOS formed after being added to the aqueous solution are split due to the high radial flow and the shearing forces derived. This provokes an increase of the surface of TEOS oil-drops in contact with water molecules. Additionally, the mixing between both phases (organic and aqueous ones) is higher as the stirring rate increases. As a result of this effect, the amount of TEOS exposed to the solution is increased and thus more TEOS can be hydrolysed. Therewith, it influences in the number of nucleation seeds formed in the initial stages and the nanoparticles size, as is observed in previous chapter.

On the other hand, the increase in fusions between nanoparticles and the deformation of their shape with increasing stirring speed (especially in **MSN-900rpm** and **MSN-1200rpm**) could be the consequence of turbulence and chaotic behaviour from which collisions between cores are more common, the fluid dynamics becomes inhomogeneous and phenomena such as swirling, and cavitation appear. Cavitation can affect mesoporous geometry and order [17]. Besides, high stirring rates can provoke less controllable hydrolysis and condensation steps, and then increase the fusions and irregular nanoparticles growth.

#### 4.3.1.2. Magnetic stirring bar shape

Following this reasoning, the radial flow depends not only on stirring speed, but also on the shape of the magnetic stirrer. A sample called **MSN-egg** was synthesised using an egg-shaped stir bar at 500 rpm (Fig. 4B) and was characterised and compared with **MSN-500rpm** (synthesised with cylindrical-shaped stir bar (Fig. 4A). As can be observed in Figure 4C, the stirring force achieved with the egg-shaped magnetic stirrer is less than with the cylindrical-shaped one.

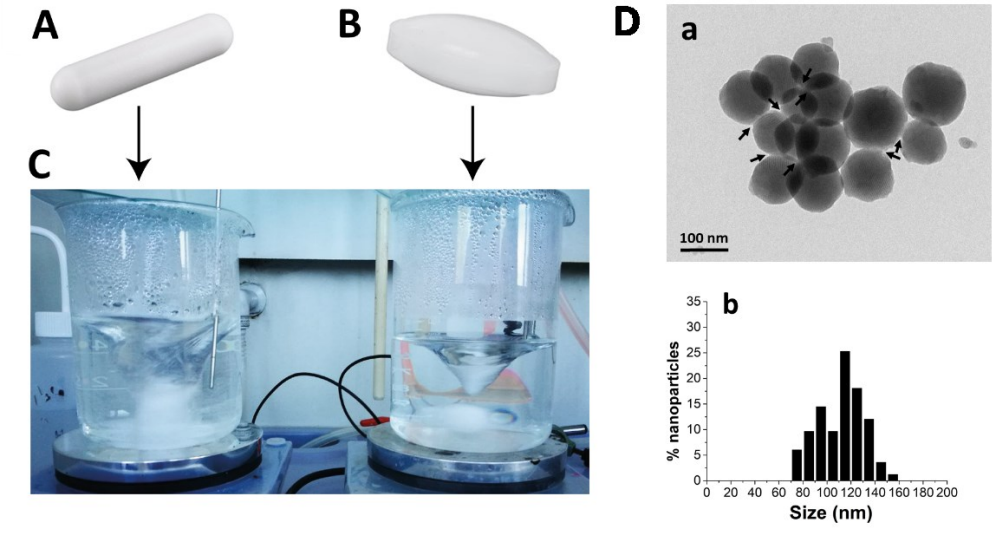


*Figure 4. General set up of MSN synthesis according to the shape of the magnetic stirring bar. (A) Cylindrical-shaped magnetic stir bar. (B) Egg-shaped magnetic stir bar. (C) Comparison of the flow produced by cylindrical-shaped and egg-shaped magnetic stir bars at 500 rpm. (D) TEM image (a) and size distribution histogram (b) of **MSN-egg**.*

As expected, the samples stirred with egg-shaped magnetic stirrer are larger than those stirred with the same speed (**MSN-500rpm**) and like those stirred at lower speed (**MSN-350rpm**) when using a cylindrical stirrer. The average diameter measured for **MSN-egg** using TEM images was 112 ± 19 nm (Fig. 4D), and the hydrodynamic diameter using DLS measurements was 183 nm

(data not shown). Furthermore, the percentage of nanoparticles in which visible silica bridges could be seen was around the 32% of the total nanoparticles. All these values are quite similar to the ones obtained for **MSN-350rpm.**

#### 4.3.1.3. Magnetic stirring bar surface

Another issue studied with respect to the stirring in the synthesis of MCM-41-type MSN was the surface of magnetic stir bar, that is, the roughness or flatness of its surface. A sample named **MSN-rough** was synthesised at 500 rpm with a cylindrical magnetic stirrer bar with pivot ring and burrs (Fig. 5A). The magnetic stir bar had the same dimensions as the cylindrical one. Then, it was characterised with DLS and TEM, and compared with **MSN-500rpm**.

A representative TEM image can be seen in Figure 5B. The average diameter for **MSN-rough** measured using TEM pictures was 100 ± 24 nm, which is slightly higher than the one measured for MSN-500 rpm; and the hydrodynamic diameter using DLS was 167 nm, which is similar to the value obtained for the **MSN-1200rpm** sample. Besides, **MSN-rough** showed in TEM images a higher number of fused particles, even some coalescence, compared to **MSN-500rpm**. Approximately 85% of the nanoparticles in **MSN-rough** are fused together, whose percentage is similar to that of **MSN-900rpm** and **MSN-1200rpm**. Furthermore, the morphology of the nanoparticles is more irregular (less spherical and rougher surface) than that shown by **MSN-500rpm**, being again comparable to the morphology of **MSN-900rpm** and **MSN-1200rpm.**

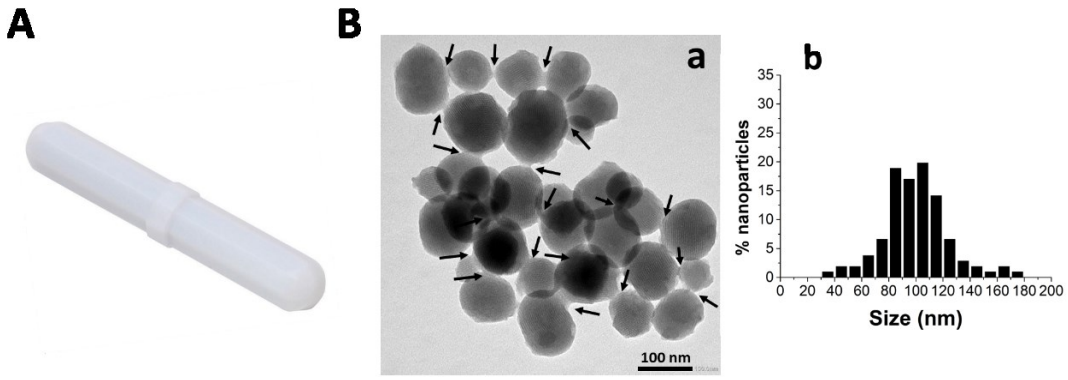


*Figure 5. (A) Cylindrical magnetic stirrer bar with pivot ring and burrs. (B) TEM picture (a) and distribution size histogram (b) of **MSN-rough.***

The different size and morphology of this sample when compared with **MSN-500rpm** (obtained at the same speed but with the smooth cylindrical bar) can be explain with the idea that the irregularities of the stirring bar can provoke the formation of irregular flows. The presence of pivot ring and burrs could form easily chaotic flow, swirling and cavitation, which are related to the fusion and coalescence of nanoparticles. In this context, it is a process similar to that which occurs at high stirring rates.

In summary, it can be pointed out that the control of the stirring during the MCM-41-type MSN synthesis is crucial for the control of the MSN features. On the one hand, the stirring rate affects the MSN formation in fourfold manner: a) changing the nanoparticles size, b) altering the size dispersion of nanoparticles, c) driving to different regularity of their morphology and surface,

and d) modifying the fusion proportion between nanoparticles. On the other hand, the size, shape, and surface of the magnetic stir bar must be taken into account as they influence the stirring force. Depending on the longitudinal surface and the roughness or plainness of the stir bar the shear stress ability and the presence of irregular flows can be modulated and hence, the morphology, the fusion and the size dispersion of nanoparticles can also be controlled. At this point it is important to note that stir bar features or stirring details have not been usually reported despite their proved importance.

### 4.3.2. TEOS addition speed/rate

Some studies have reported a specific addition rate such as 0.1 mL/min [26], 0.25 mL/min [34], 0.38 mL/min [35][9], 0.5 mL/min [15], 1 mL/min [30][6][16][17] or 1.45 mL/min [24] of TEOS, however, they did not take into account the consequences of choosing these specifics rates and they did not explain the criteria to establish this choice. Furthermore, most of the studies do not set a specific TEOS addition rate, but some of them note that TEOS have to be added dropwise or slowly. In fact, Chiang et al. considered the adding rates of TEOS to have a neglected effect on the morphology and structure of MSN [15]. On the contrary, Moongraksathum et al. defend that the rate of TEOS addition, along with the stirring speed and concentration of surfactant, influence on the characteristics of MSN [36]. Oliveira et al. [37] reported a synthesis in which they add the TEOS in two steps, and they test the second addition in controlled dropwise or not controlled. They observed differences when controlling the second addition, such as the formation of a bimodal distribution in particles size, variations in relative surface area and differences concerning agglomeration of nanoparticles. Nevertheless, they did not indicate the TEOS addition rate, and their conclusions are not clear. In other study, even though they did not relate the results and the TEOS addition rate, Lechevallier et al. [34] obtained a quite polydispersed sample (almost a 40% of dispersion), in whose preparation the TEOS is added at 0.25 mL/min. In case of He et al. study [35], they add the TEOS at 0.38 mL/min, and no high dispersion was observed, although the nanoparticles were highly fused and the relative surface area was low (ca. 860 $m^2 g^{-1}$) in comparison with standard synthesis.

In order to improve the understanding of the implications of the TEOS addition rate, we have synthesized samples adding the TEOS at 0.25 mL/min, 1 mL/min, 5 mL/min (corresponding to the standard condition) and also with an instant addition. The samples were named **MSN-0.25**, **MSN-1**, **MSN-5** (standard sample) and **MSN-instant**, respectively. The rest of the parameters were fixed at standard conditions (500 rpm of stirring rate). The samples were characterised by DLS and TEM.

The first noticeable effect was observed directly in the synthesis reaction mixture. In those samples in which TEOS was added slowly (**MSN-0.25** and **MSN-1**) the supernatant of the reaction mixture once filtered or centrifuged was cloudy white (Fig. 6A), and the amount of sediment obtained was quite less than in a standard synthesis. Therefore, some colloidal behaviour is suggested in the reaction mixture obtained in these samples. A couple of hours later, the nanoparticles end up precipitating from the supernatant (Fig. 6B) and can be collected by filtration.

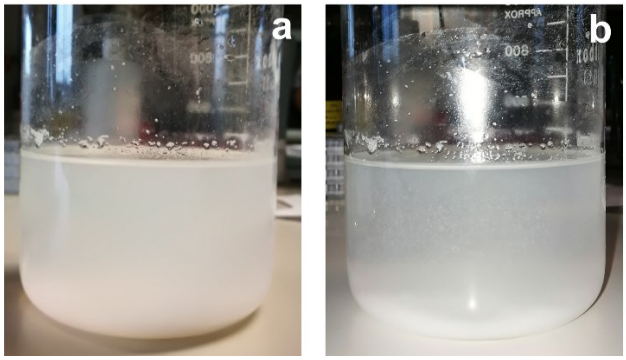


*Figure 6. Photographs of the **MSN-0.25** supernatant after being filtered (a) and two hours after that (b).*

TEM images of the synthesised samples are shown in Figure 7. **MSN-0.25** shows a very broad size distribution for the MSN. Specifically, three differentiable populations of MSN are observed: i) spherical nanoparticles in the range from 70 to 120 nm, being equivalent to the MSN obtained in a standard synthesis; ii) rod-like nanoparticles with the diameter of long axis ranging from 140 nm to 250 nm approximately and the diameter of short axis from 90 nm to 130 nm; and iii) bean-like nanoparticles, which were a kind of bended rods, whose diameters were from 250 nm to more than 400 nm. **MSN-1** shows two different populations: i) spherical nanoparticles from 70 to 120 nm, analogues to the spherical ones in **MSN-0.25**, and ii) rod-like nanoparticles, whose long axis ranges from 140 to 230 nm (a little bit smaller than rods found on **MSN-0.25**), and the diameter of short axis was similar to spherical nanoparticles dimensions (from 90 to 120 nm). In the case of **MSN-5** and **MSN-instant**, only one population of spherical nanoparticles was found, in the range from 60 nm to 130 nm (centred at 94 ± 15 nm) and 50 nm to 120 nm (centred at 85 ± 16 nm), respectively. Besides, **MSN-5** has a more regular and smoother surface than **MSM-instant**, in which some roughness can be seen. All the populations present visible mesoporosity. Considering fusions between nanoparticles, **MSN-0.25** and **MSN-1** materials show fewer visible linkages than the other samples, and **MSM-instant** shows a more and wider silica bridges and coalescing nanoparticles.

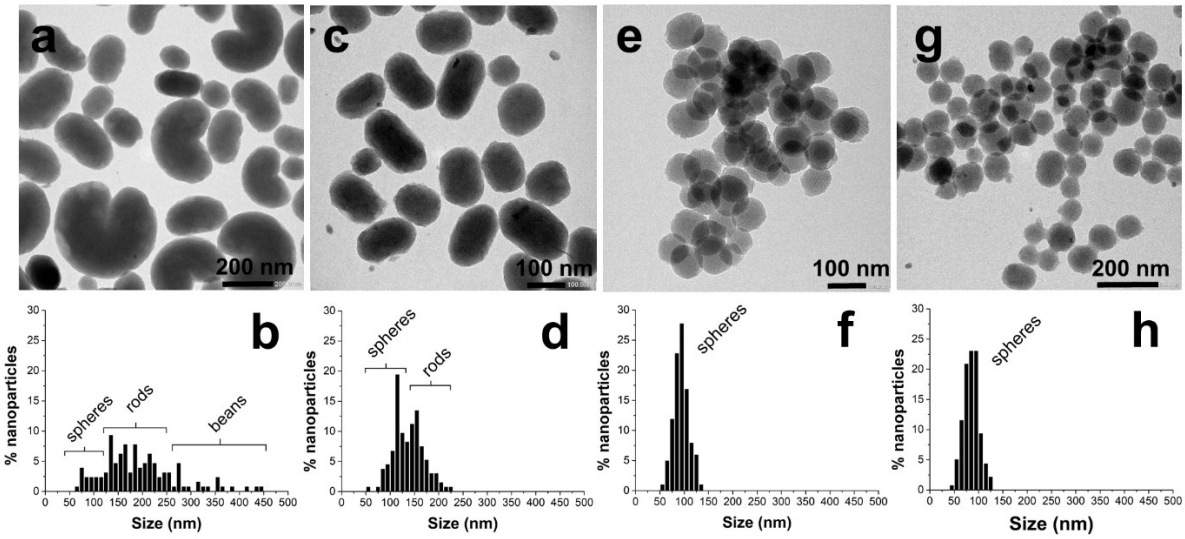


*Figure 7. TEM images of **MSN-0.25** (a), **MSN-1** (c), **MSN-5** (e), and **MSN-intant** (g). In addition, histograms with particle size distribution and MSN morphology indications are showed on (b),(d),(f), and (h), respectively.*

DLS curves were represented in Figure 8. All the samples were measured after a brief spun in order to remove large sediments. **MSN-0.25** shows a unique peak centred at 220 nm, whose distribution is comprised between 100 and 1000 nm, which included the different populations observed in the TEM pictures. Additionally, the DLS peak is centred in the range of rod-like nanoparticles, which is the most abundant population in the sample according to TEM images. **MSN-1** curve includes a unique population of sizes in the range of 60 to 1000 nm (centred at 170 nm). In this case, both spherical and rod-like nanoparticles are abundant, and the size dispersion is broad. **MSN-5** shows a narrower distribution, centred at 165 nm, which comprise a range of sizes from 70 to 500 nm. In this sample, the main population is composed of spherical nanoparticles, and the signal at higher sizes can be due to the presence of small aggregates. Finally, **MSN-instant** presents a broadly dispersed (from 60 nm to 600 nm) peak, which is centred at 166 nm, with some basal signal above 600 nm. This type of curve can be related with the presence of the higher percentage of aggregates in the sample.

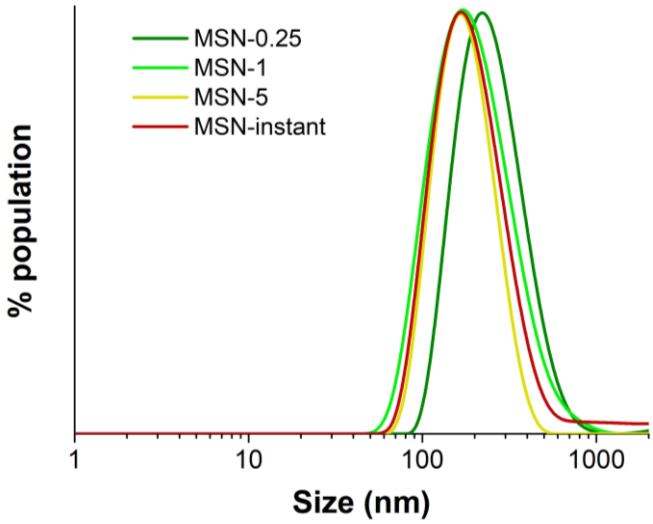


*Figure 8. Size distribution of **MSN-0.25**, **MSN-1**, **MSN-5**, and **MSN-instant** according to Intensity PSD analysis. Measurements were performed in samples resuspended in distilled water at 1 mg/ml and brief spin pulses were applied to remove the larger aggregates.*

As it was discussed in Chapter 3, the TEOS addition rate influences on the hydrolysis and condensation time, and hence on the number of initial seeds formed in the reaction. This has a strong influence in the case of lower addition rates, especially in **MSN-0.25**, in which the three populations observed correspond to three different stages of growth. A similar phenomenon was described in other studies in the case of increasing the amount of TEOS available [25][38]. The mechanism to explain the formation of these populations is suggested as follows. Firstly, spherical nanoparticles are formed as a result of an initial seed formation. Secondly, when spheres are formed and the silica continues depositing over them, the nanoparticles grow mainly in the axis parallel to the channels, forming rod-like nanoparticles. These can be defined as extended spheres, being that the small axis is like the diameter of the spheres and the long axis always coincides with the direction of the CTAB templated channels. In parallel, the aggregation of new surfactant-silica complexes as TEOS is being added leads to a second nucleation step, which forms additional spherical nanoparticles. Thirdly, as the reaction goes by, rod-like nanoparticles coming from previous step can still accumulate more silica and grow. When they reach approximately 250 nm on the long axis, their structure begins to bend, as it is

not strong enough to keep the long axis straight and such an anisotropic morphology. Therewith bean-shaped nanoparticles appear. The sphere nanoparticles formed at second nucleation seed formation can also suffer additional growth and acquire rod morphology. In this latter stage, a third additional formation of seeds takes place being that new silica precursor molecules are added to the suspension. Thus, new spherical nanoparticles are formed.

The mechanism proposed supposes the initiation of three differentiated nucleation cycles, which can be explained according to the Lamer-based growth mechanism [39]. This suggest that a homogenous nucleation takes place when a minimum amount of silica precursor is accumulated in the solution (nucleation threshold). In contrast, when the concentration of silica precursor monomers is below this threshold due to their consumption in the nucleation process silica are preferentially deposited into already existing nuclei, that is, growing process is predominant.

Regarding **MSN-1**, the process can be seen as similar to the one observed in **MSN-0.25**, but the third nucleation does not occur. In this case, the addition rate was faster and the availability of TEOS is higher from the beginning. At initial stages, a greater amount of nucleation seeds is formed and hence, the silica precursor added is not enough to grow bean-shaped nanoparticles. Since most of the TEOS has already been used to grow the higher number of nuclei, this new nucleation cycle does not take place, as nucleation threshold is not reached. MSN-5 and MSN-instant only produce the spherical population as the addition rate of silica precursor is fast enough to form a sufficient number of nucleation seeds to use all the silica available. Since no additional TEOS is added once the nanoparticles are formed, the hydrolysed silica species are distributed homogeneously among the nuclei to form monodisperse nanoparticles.

Bean-shaped nanoparticles formation was also reported by Beltrán-Osuna et al. [17] when they applied very low stirring speed (250 rpm) in their synthesis and a TEOS addition rate of 1 mL $min^{-1}$. In order to check the influence of low stirring speed in the formation of bean-shaped nanoparticles, we synthesised and characterised a standard sample (5 mL $min^{-1}$) but applying 250 rpm (**MSN-250rpm**). Firstly, it has to be mentioned that the suspension obtained once stirred for 2 hours had a colloidal behaviour and a homogeneous milky appearance (Fig. 9A), being impossible to separate the solid from the solvent by filtration or centrifugation, which was similar to the observed in case of **MSN-0.25** and **MSN-1**. TEM and DLS samples were prepared from this suspension. However, when the suspension was left for more than 1 hour, flocs appeared and the solid began to settle (Fig. 9B). Then, it was filtered.

*Figure 9. Photographs of **MSN-250rpm** sample just after being synthesised (a) and two hours after that (b).*

**MSN-250rpm** was observed with TEM (Fig. 10) and measured by DLS (Fig. 11). TEM images of **MSN-250rpm** showed a similar aspect than **MSN-0.25**, namely the presence of three populations: spherical nanoparticles, rod-shaped nanoparticles, and bean-shaped nanoparticles. Nevertheless, in **MSN-250rpm** the corresponding nanoparticles present different proportions and dimensions. Spherical nanoparticles, which were considerably more frequent in this sample, were in the range from 70 to 160 nm. They were slightly larger than spheres in **MSN-0.25**, but equivalent to those found in **MSN-350rpm**. Rod-shaped nanoparticles were also larger than those measured in **MSN-0.25**. They had the diameter of long axis ranging from 170 nm to 300 nm approximately and the diameter of short axis from 120 nm to 180 nm. Bean-shaped nanoparticles were much bigger than previous ones, and their diameters were from 350 nm to more than 600 nm.

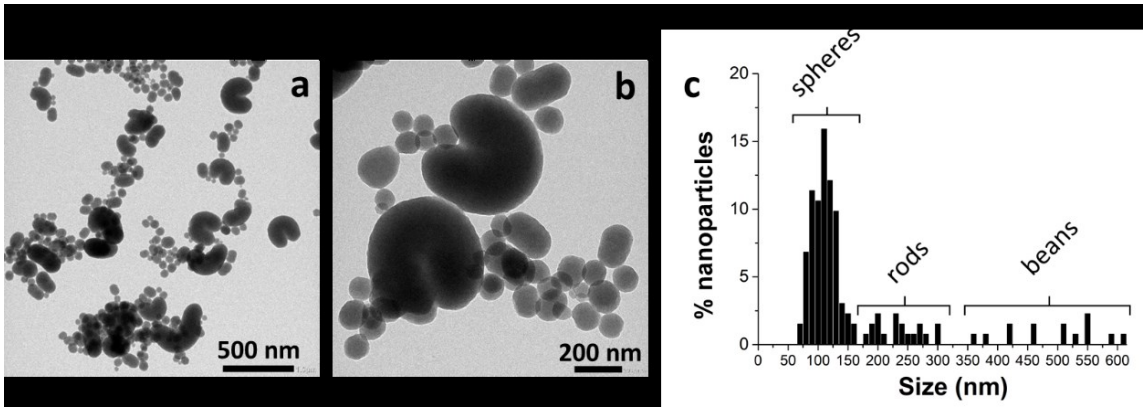


*Figure 10. TEM images at lower and higher magnification of **MSN-250rpm** (a, b), and histogram with particle size distribution and MSN morphology indications (c).*

DLS measurements of **MSN-250rpm** showed a unique but broad population, ranging from 100 nm to 1000 nm (centred at 267 nm) (Fig. 11), which fits with observed on TEM images and is similar to the curve from **MSN-0.25**.

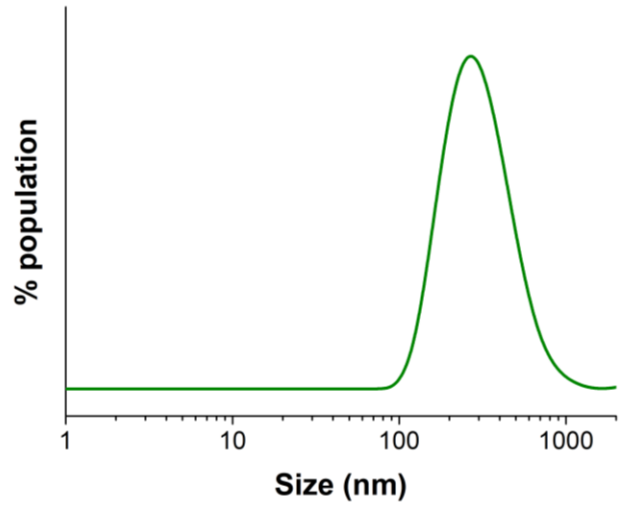


*Figure 11. Size distribution of **MSN-250rpm** according to Intensity PSD analysis. Measurement was performed in the sample resuspended in distilled water at 1 mg/ml and brief spin pulses were applied to remove the larger aggregates.*

Therefore, both stirring rate and TEOS addition rate influence in the amount of TEOS available to be hydrolysed and then in the number of nuclei formed. The formation of few numbers of nuclei in the initial stages leads to the formation of large nanoparticles, but in addition, the progressive emergence of new silica precursor monomers coming from hydrolysed TEOS, both by the slow addition rate of TEOS or the low stirring rate, can provoke new nucleation cycles and then multimodal population of nanoparticles.

### 4.3.3. Influence of synthesis neutralisation

Some authors have reported the neutralization of "as-made MSN" by adding a HCl solution to quench the synthesis reaction in a controlled manner[30][40][41][42] [14][43]. Nevertheless, they did not take into account the consequences on the mesostructure of using this method of stopping the reaction instead of neutralising the synthesis mixture by washing with deionised water, which is most common employed. Hence, we decided to synthesize and characterise samples produced by neutralisation at 2 hours with 7 mL of HCl 1 M, called **MSN-HCl**. The amount of HCl added was chosen to equal the amount of NaOH added previously. The rest of the parameters were fixed at standard conditions (500 rpm of stirring rate, TEOS addition rate of 5 mL/min). These nanoparticles were compared to the standard sample (named in this section as **MSN-$H_2O$**) regarding $N_2$ adsorption-desorption isotherms, PXRD diffractograms, and TEM.

The $N_2$ adsorption and desorption isotherms of both samples were observed and compared (Figure 12A). Both samples showed type IV isotherms, which are typical for mesoporous materials, but had significant differences from each other. On the one hand, the **MSN-HCl** isotherm presents in the monolayer adsorption step (lower $p/p_0$ values, Figure 12A, a) a lower slope than **MSN-$H_2O$**, which indicates that this sample has a smaller relative surface area. Thus, by applying the BET model to calculate the specific surface of these two materials, we have obtained a the BET surface of 1110 ± 30 $m^2\ g^{-1}$ for **MSN-$H_2O$** and 900 ± 60 $m^2\ g^{-1}$ for **MSN-HCl**, which represents a difference between them of more than 200 $m^2\ g^{-1}$. On the other hand, the capillary condensation step (Figure 12A, b) occurred at different at $p/p_0$ values (**MSN-HCl** at 0.21 and **MSN-$H_2O$** at 0.30). This indicates that the pore size in **MSN-HCl** (2.70 ± 0.16 nm) is smaller than **MSN-$H_2O$** (2.26 ± 0.17 nm) (Figure 12B and Table 2, BJH model). Furthermore, the amount of $N_2$ capable to be adsorbed in the central zone of the isotherm (plateau, Figure 23A, c) within the mesopores of both samples was quite contrasting, on the order of 150 $cm^3\ g^{-1}$ lower in **MSN-HCl** mesopores than in those of **MSN-$H_2O$**. This parameter reveals that the pore volume of the **MSN-HCl** material (0.76 ± 0.11 $cm^3\ g^{-1}$) is therefore lower than that of the **MSN-$H_2O$** one (0.98 ± 0.04 $cm^3\ g^{-1}$). Finally, differences were also observed with respect to condensation due to interparticle porosity (Figure 23A, d). In the case of **MSN-$H_2O$**, the value of the interparticle pore volume is 670 ± 70 $cm^3\ g^{-1}$, and in the case of **MSN-HCl** is 400 ± 90 $cm^3\ g^{-1}$.

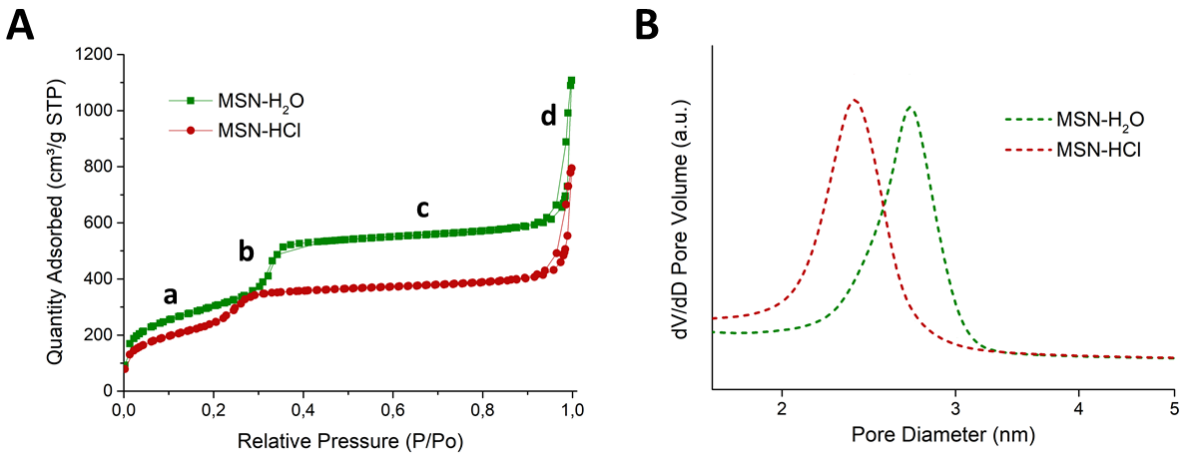


*Figure 12. (A) $N_2$ absorption-desorption isotherm of **MSN-HCl** and **MSN-H₂O**. (a) $N_2$ monolayer adsorption, (b) capillary condensation, (c) plateau region, and (d) interparticle porosity. (B) Pore distribution size of **MSN-HCl** and **MSN-H₂O** according to BJH model.*

*Table 2. Textural properties of samples as a function of the method employed to neutralise them.*

| SAMPLE | BET SURFACE ($m^2\ g^{-1}$) | PORE VOLUME ($cm^3\ g^{-1}$) | PORE SIZE (nm) |
|---|---|---|---|
| **MSN-H₂O** | 1107.85 ± 32.25 | 0.98 ± 0.04 | 2.70 ± 0.16 |
| **MSN-HCl** | 900.24 ± 55.01 | 0.76 ± 0.11 | 2.26 ± 0.17 |

According to the results obtained with the analysis of the $N_2$ adsorption-desorption isotherms, it can be suggested that the nanoparticles in **MSN-HCl** suffered a shrinkage of the structure during the neutralisation process. Thus, a constriction occurs in the pores, reducing their size and volume, and consequently reducing the specific surface area of the material. This shrinkage can be caused by the ion exchange between the $CTA^+$ (from the CTAB) and the $H^+$ (from the HCl), which is considerably smaller than the first. In this context, the nanoparticles newly formed are quite weak and sensitive to changes in the environment and are not strong enough to endure the exchange of the large template molecules for small ions, leading to a great contraction. Hence, the presence of the template molecules is still important in the maintenance of the mesostructured at these stages. This same shrinkage process can occur under other conditions, such as during the addition of ethanol or other organic solvents, which tend to wash off a significant amount of template since the surfactant is more soluble in this type of solvents. In fact, some authors have already reported the weakness of the MSN structure when it is newly synthesised and subjected to external stresses, such as the drying process [29][44].

**MSN-HCl** and **MSN-H₂O,** as-made and calcined, samples were analysed by PXR diffraction (Fig. 13). The diffraction diagram of each sample shows the typical diffractrogram of 2-dimensional hexagonal symmetry (P6mm), the peaks corresponding to the (100), (110), (220) and (210) planes. Nevertheless, both calcined and as-made **MSN-HCl** present their peaks shifted to the right compared to their counterparts in **MSN-H₂O**. This shift, related to the shrinkage observed in the $N_2$ isotherms, did not involve the loss of the hexagonal symmetry of the porous structure. The unit cell calculated for **MSN-HCl** and **MSN-H₂O** (as-made and calcined samples) from the value of the $d_{100}$ distance are included in Table 3. Also in Table 3, unit cell contractions due to the different neutralisation and to the calcination processes are included. It can be observed in

this table that not only a contraction appears when MSN is neutralised with HCl (0.20 nm), but also that the corresponding contraction due to calcination is bigger in the case of **MSN-HCl** (0.79 nm) than in the case of **MSN-$H_2O$** (0.52nm). This different behaviour shows that the structure of **MSN-HCl** is weaker than the standard one, being the mesostructure more affected by calcination process when the as-made material is washed with HCl than just with water. Finally, the differences of unit cell of the final solids (once calcined) is 0.47 nm, which again shows the lower condensation of the mesostructure of the **MSN-HCl** material.

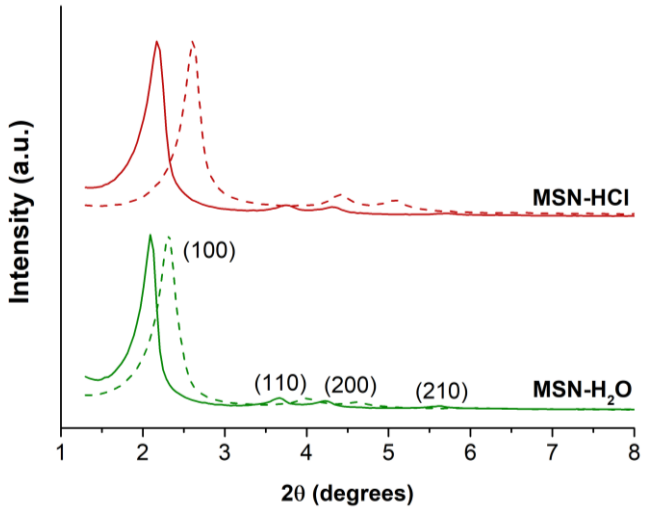


*Figure 13. PRXD patterns of as made (solid lines) and calcined (dashed lines) samples of **MSN-$H_2O$** and **MSN-HCl**.*

*Table 3. PXRD measurements of samples as a function of the method employed to neutralise them.*

| SAMPLE | MSN-$H_2O$ | | MSN-HCl | | |
|---|---|---|---|---|---|
| | Peak [100] (2θ) | Unit cell (nm) | Peak [100] (2θ) | Unit cell (nm) | Unit cell contraction due to HCl neutralisation (nm) |
| **As made** | 2.08 | 4.90 | 2.17 | 4.70 | 0.20 |
| **Calcined** | 2.32 | 4.38 | 2.61 | 3.91 | 0.47 |
| **Unit cell contraction due to calcination (nm)** | - | 0.52 | - | 0.79 | |

According to PXRD and $N_2$ isotherms results, the wall thickness was calculated simply by taking the pore size out of the unit cell value. The value of wall thickness was similar in both samples (1.65 in case of **MSN-HCl** and 1.68 in case of **MSN-$H_2O$**), indicating than the neutralisation did not affect to the wall, and hence, the unit cell decrease in calcined **MSN-HCl** is mostly provoked by a decrease in pore size, which is in accordance with BET analysis.

TEM images of calcined **MSN-HCl** showed standard nanoparticles (Figure 14), namely spherical nanoparticles sized at ca. 90 nm. Nevertheless, they had a rough surface. This phenomenon may be provoked by the shrinkage process, already demonstrated in previous paragraphs. Regarding the literature, other authors which used similar protocols did not see this effect on the nanoparticles [30][45].

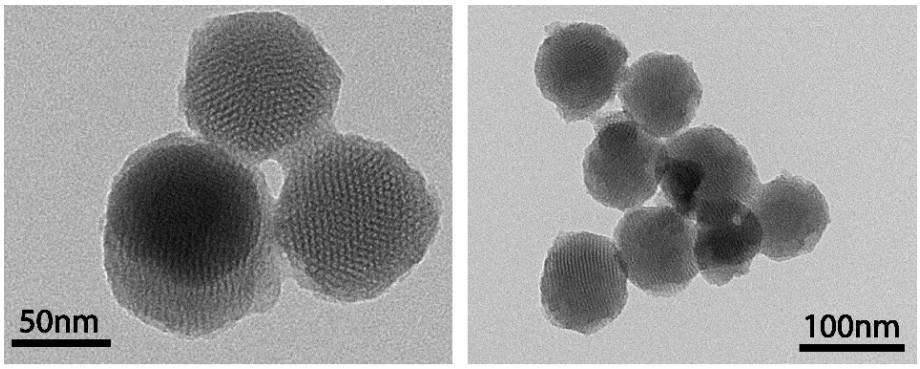


*Figure 14. TEM images at lower and higher magnification of **MSN-HCl**.*

## 4.4. CONCLUSIONS

This chapter presents a solid study of the influence of disregarded synthesis parameters on the MCM-41-type MSN properties.

Taking into account the knowledge acquired in Chapter 3, the stirring rate and dynamics have been correlated with the development and growing of nanoparticles. Then, a relationship has been found between the stirring rate and the size, the shape, and the fusions between nanoparticles. On the first place, the stirring rate influences on the size of nanoparticles by the modulation of hydrolysis rate and nucleation since the mixing of TEOS in the aqueous solution and their contact with water molecules is necessary to be hydrolysed. Hence, low stirring rates lead to large nanoparticles and high stirring rates to smaller ones. In addition, the importance of control the stirring has been indicated not only regarding the stirring speed, but also the magnetic stirrer bar morphology and surface, just as the stirring set up. It has been seen to strongly affect the MSN features, such as the shape of nanoparticles or the fusions among them. In this context, high stirring rates leads to the formation of cavitation phenomenon, strong shearing forces and irregular flows. Similar effects can be found when magnetic stir bars used have burrs and pivot rings. In summary, the control of the stirring during the MCM-41-type MSN synthesis is crucial for the control of the MSN synthesis.

On the other hand, the TEOS addition rate has been found to be quite important in the nanoparticles formation, being possible to modulate the nanoparticles populations both in size and homogeneity. This phenomenon has been found to be related with the availability of silica species, and to affect the rate of hydrolysis and condensation and the formation of nucleation seeds. Furthermore, this behaviour has also been found if extremely low stirring rates are used, even at standard rates of TEOS addition. Therefore, both stirring rate and TEOS addition rate influence in the amount of TEOS available to be hydrolysed and then in the number of nuclei formed.

Finally, it has been demonstrated the weakness and instability of the structure of the MSN when they are just formed, in spite of having been aged four 2 hours. In this sense, it is important to focus on the cooling step, the neutralisation process, and the separation of the solid from the reaction media. On the one hand, the forced neutralisation with HCl 1M affects to the structure and provokes a notable shrinkage of the pores. On the other hand, the control of the stirring rate and the TEOS addition rate allows to observe a transition of the reaction mixture from colloid to floc and sedimentation during the cooling step and shortly after.

On account of the studies performed, more reproducible and controlled MCM-41-type MSN can be produced. This matter has special importance on nanomedicine applications, since size, shape or fusions of the nanoparticles, as well as the polydispersity of the samples strongly affects to the biological properties of the MSN, such as the targeting, biocompatibility, drug release efficiency and clearance [46][37].

## 4.5. REFERENCES


[1] Y. Chen *et al.*, "The complete control for the nanosize of spherical MCM-41," *J. Nanosci. Nanotechnol.*, vol. 12, no. 9, pp. 7239–7249, 2012, doi: 10.1166/jnn.2012.6459.

[2] G. Lelong, S. Bhattacharyya, S. Kline, T. Cacciaguerra, M. A. Gonzalez, and M.-L. L. Saboungi, "Effect of Surfactant Concentration on the Morphology and Texture of MCM-41 Materials," *J. Phys. Chem.*, vol. 112, no. 29, pp. 10674–10680, Jul. 2008, doi: 10.1021/jp800898n.

[3] S. H. Wu and H. P. Lin, "Synthesis of mesoporous silica nanoparticles," *Chem. Soc. Rev.*, vol. 42, no. 9, pp. 3862–3875, 2013, doi: 10.1039/c3cs35405a.

[4] F. Catalano and P. P. Pompa, "Design Rules for Mesoporous Silica toward the Nanosize: A Systematic Study," *ACS Appl. Mater. Interfaces*, vol. 11, no. 50, pp. 47237–47246, 2019, doi: 10.1021/acsami.9b16135.

[5] Q. Cai, Z. S. Luo, W. Q. Pang, Y. W. Fan, X. H. Chen, and F. Z. Cui, "Dilute solution routes to various controllable morphologies of MCM-41 silica with a basic medium," *Chem. Mater.*, vol. 13, no. 2, pp. 258–263, 2001, doi: 10.1021/cm990661z.

[6] M. Varache, I. Bezverkhyy, L. Saviot, F. Bouyer, F. Baras, and F. Bouyer, "Optimization of MCM-41 type silica nanoparticles for biological applications: Control of size and absence of aggregation and cell cytotoxicity," *J. Non. Cryst. Solids*, vol. 408, pp. 87–97, 2015, doi: 10.1016/j.jnoncrysol.2014.10.020.

[7] C. J. Brinker, "Hydrolysis and condensation of silicates: effects on structure," *J. Non. Cryst. Solids*, vol. 100, pp. 31–50, 1988, doi: 10.1016/0022-3093(88)90005-1.

[8] Z. Yi *et al.*, "A New Insight into Growth Mechanism and Kinetics of Mesoporous Silica Nanoparticles by in Situ Small Angle X-ray Scattering," *Langmuir*, vol. 31, no. 30, pp. 8478–8487, 2015, doi: 10.1021/acs.langmuir.5b01637.

[9] Z. A. Qiao, L. Zhang, M. Guo, Y. Liu, and Q. Huo, "Synthesis of mesoporous silica nanoparticles via controlled hydrolysis and condensation of silicon alkoxide," *Chem. Mater.*, vol. 21, no. 16, pp. 3823–3829, 2009, doi: 10.1021/cm901335k.

[10] F. Lu, S. H. Wu, Y. Hung, and C. Y. Mou, "Size effect on cell uptake in well-suspended, uniform mesoporous silica nanoparticles," *Small*, vol. 5, no. 12, pp. 1408–1413, Jun. 2009, doi: 10.1002/smll.200900005.

[11] E. Yamamoto and K. Kuroda, "Colloidal mesoporous silica nanoparticles," *Bull. Chem. Soc. Jpn.*, vol. 89, no. 5, pp. 501–539, 2016, doi: 10.1246/bcsj.20150420.

[12] E. Yamamoto and K. Kuroda, *Preparation and Controllability of Mesoporous Silica Nanoparticles*, 1st ed., vol. 44. Elsevier Inc., 2018.

[13] F. Rizzi *et al.*, "High Surface Area Mesoporous Silica Nanoparticles with Tunable Size in the Sub-Micrometer Regime: Insights on the Size and Porosity Control Mechanisms," *Molecules*, vol. 26, no. 14, p. 4247, Jul. 2021, doi: 10.3390/molecules26144247.

[14] J. Rathousky, M. Zukalova, P. J. Kooyman, and A. Zukal, "Synthesis and characterization of colloidal MCM-41," *Colloids Surfaces A Physicochem. Eng. Asp.*, vol. 241, no. 1–3, pp. 81–86, 2004, doi: 10.1016/j.colsurfa.2004.04.014.

[15] Y. D. Chiang, H. Y. Lian, S. Y. Leo, S. G. Wang, Y. Yamauchi, and K. C. W. Wu, "Controlling particle size and structural properties of mesoporous silica nanoparticles using the

taguchi method," *J. Phys. Chem. C*, vol. 115, no. 27, pp. 13158–13165, 2011, doi: 10.1021/jp201017e.

[16] X. Lv, L. Zhang, F. Xing, and H. Lin, "Controlled synthesis of monodispersed mesoporous silica nanoparticles: Particle size tuning and formation mechanism investigation," *Microporous Mesoporous Mater.*, vol. 225, pp. 238–244, 2016, doi: 10.1016/j.micromeso.2015.12.024.

[17] Á. A. Beltrán-Osuna, J. L. Gómez Ribelles, and J. E. Perilla, "Effects of commonly unreported physicochemical variables on the morphology of mesoporous silica nanoparticles type MCM-41," *J. Nanoparticle Res.*, vol. 19:381, no. 1–14, 2017, doi: 10.1007/s11051-017-4077-2.

[18] T. W. Kim, P. W. Chung, and V. S. Y. Lin, "Facile synthesis of monodisperse spherical MCM-48 mesoporous silica nanoparticles with controlled particle size," *Chem. Mater.*, vol. 22, no. 17, pp. 5093–5104, 2010, doi: 10.1021/cm1017344.

[19] T. Yokoi, T. Karouji, S. Ohta, J. N. Kondo, and T. Tatsumi, "Synthesis of mesoporous silica nanospheres promoted by basic amino acids and their catalytic application," *Chem. Mater.*, vol. 22, no. 13, pp. 3900–3908, Jul. 2010, doi: 10.1021/cm9037846.

[20] W. Y. Sang and O. P. Ching, "Tailoring MCM-41 mesoporous silica particles through modified sol-gel process for gas separation," in *AIP Conference Proceedings*, Oct. 2017, vol. 1891, no. 1, p. 020147, doi: 10.1063/1.5005480.

[21] T. Yokoi *et al.*, "Mechanism of formation of uniform-sized silica nanospheres catalyzed by basic amino acids," *Chem. Mater.*, vol. 21, no. 15, pp. 3719–3729, Aug. 2009, doi: 10.1021/cm900993b.

[22] S. M. Mousavi Elyerdi, M. N. Sarvi, and A. J. O'Connor, "Synthesis of ultra small nanoparticles (< 50 nm) of mesoporous MCM-48 for bio-adsorption," *J. Porous Mater.*, vol. 26, no. 3, pp. 839–846, Jun. 2019, doi: 10.1007/s10934-018-0650-z.

[23] L. Luo, Y. Liang, E. S. Erichsen, and R. Anwander, "Monodisperse mesoporous silica nanoparticles of distinct topology," *J. Colloid Interface Sci.*, vol. 495, pp. 84–93, 2017, doi: 10.1016/j.jcis.2017.01.107.

[24] M. Yu *et al.*, "A simple approach to prepare monodisperse mesoporous silica nanospheres with adjustable sizes," *J. Colloid Interface Sci.*, vol. 376, no. 1, pp. 67–75, 2012, doi: 10.1016/j.jcis.2012.03.014.

[25] N. A. Zainal, S. R. A. Shukor, H. A. A. Wab, and K. A. Razak, "Study on the effect of synthesis parameters of silica nanoparticles entrapped with rifampicin," *Chem. Eng. Trans.*, vol. 32, pp. 2245–2250, 2013, doi: 10.3303/CET1332375.

[26] P. Khodaee, N. Najmoddin, and S. Shahrad, "The effect of ethanol and temperature on the structural properties of mesoporous silica synthesized by the sol-gel method," *J. Tissues Mater.*, vol. 1, no. 1, pp. 10–17, 2018, doi: 10.22034/JTM.2018.67254.

[27] L. Li, J. Song, J. Wang, and W. Fan, "Controllable synthesis of mesoporous silica with hierarchical architecture," *Mater. Express*, vol. 7, no. 4, pp. 283–290, Aug. 2017, doi: 10.1166/mex.2017.1381.

[28] S. Ma, Y. Wang, and Y. Zhu, "A simple room temperature synthesis of mesoporous silica nanoparticles for drug storage and pressure pulsed delivery," *J. Porous Mater.*, vol. 18, no. 2, pp. 233–239, Apr. 2011, doi: 10.1007/s10934-010-9375-3.

[29] J. Zhang, Z. Luz, and D. Goldfarb, “EPR Studies of the Formation Mechanism of the Mesoporous Materials MCM-41 and MCM-50,” *J. Phys. Chem. B*, vol. 101, no. 36, pp. 7087–7094, Sep. 1997, doi: 10.1021/jp9709621.

[30] M. Varache, I. Bezverkhyy, F. Bouyer, R. Chassagnon, F. Baras, and F. Bouyer, “Improving structural stability of water-dispersed MCM-41 silica nanoparticles through post-synthesis pH aging process,” *J. Nanoparticle Res.*, vol. 17, no. 9, 2015, doi: 10.1007/s11051-015-3147-6.

[31] H. I. Meléndez-Ortiz, L. A. García-Cerda, Y. Olivares-Maldonado, G. Castruita, J. A. Mercado-Silva, and Y. A. Perera-Mercado, “Preparation of spherical MCM-41 molecular sieve at room temperature: Influence of the synthesis conditions in the structural properties,” *Ceram. Int.*, vol. 38, no. 8, pp. 6353–6358, 2012, doi: 10.1016/j.ceramint.2012.05.007.

[32] J. Li, B. Deng, B. Zhang, X. Shen, and C. N. Kim, “CFD simulation of an unbaffled stirred tank reactor driven by a magnetic rod: Assessment of turbulence models,” *Water Sci. Technol.*, vol. 72, no. 8, pp. 1308–1318, 2015, doi: 10.2166/wst.2015.314.

[33] G. Halász, B. Gyüre, I. M. Jánosi, K. G. Szabó, and T. Tél, “Vortex flow generated by a magnetic stirrer,” *Am. J. Phys.*, vol. 75, no. 12, pp. 1092–1098, 2007, doi: 10.1119/1.2772287.

[34] S. Lechevallier *et al.*, “Luminescence Properties of Mesoporous Silica Nanoparticles Encapsulating Different Europium Complexes: Application for Biolabelling,” *J. Nanomater.*, vol. 2013, p. 11, 2013, doi: 10.1155/2013/918369.

[35] Q. He *et al.*, “The effect of PEGylation of mesoporous silica nanoparticles on nonspecific binding of serum proteins and cellular responses,” *Biomaterials*, vol. 31, no. 6, pp. 1085–1092, Feb. 2010, doi: 10.1016/j.biomaterials.2009.10.046.

[36] B. Moongraksathum and Y. W. Chen, “Synthesis and size control of uniform, spherically shaped hexagonal mesoporous silica,” *J. Porous Mater.*, vol. 26, no. 1, pp. 51–58, Feb. 2019, doi: 10.1007/s10934-018-0609-0.

[37] D. M. Oliveira and A. S. Andrada, “Synthesis of ordered mesoporous silica MCM-41 with controlled morphology for potential application in controlled drug delivery systems,” *Cerâmica*, vol. 65, no. 374, pp. 170–179, Jun. 2019, doi: 10.1590/0366-69132019653742509.

[38] J. W. Kim, L. U. Kim, and C. K. Kim, “Size Control of Silica Nanoparticles and Their Surface Treatment for Fabrication of Dental Nanocomposites,” 2007, doi: 10.1021/bm060560b.

[39] P. P. Ghimire and M. Jaroniec, “Renaissance of Stöber method for synthesis of colloidal particles: New developments and opportunities,” *J. Colloid Interface Sci.*, vol. 584, pp. 838–865, 2021, doi: 10.1016/j.jcis.2020.10.014.

[40] K. J. Edler, “Current understanding of formation mechanisms in surfactant-templated materials,” *Aust. J. Chem.*, vol. 58, no. 9, pp. 627–643, 2005, doi: 10.1071/CH05141.

[41] C. E. Fowler, D. Khushalani, B. Lebeau, and S. Mann, “Nanoscale Materials with Mesostructured Interiors,” *Adv. Mater.*, vol. 13, no. 9, pp. 649–652, May 2001, doi: 10.1002/1521-4095(200105)13:9<649::AID-ADMA649>3.0.CO;2-G.

[42] S. Sadasivan, C. E. Fowler, D. Khushalani, and S. Mann, “Nucleation of MCM-41 nanoparticles by internal reorganization of disordered and nematic-like silica -

Surfactant clusters," *Angew. Chemie - Int. Ed.*, vol. 41, no. 12, pp. 2151–2153, 2002, doi: 10.1002/1521-3773(20020617)41:12<2151::AID-ANIE2151>3.0.CO;2-U.

[43] S. Sadasivan, D. Khushalani, and S. Mann, "Synthesis and shape modification of organo-functionalised silica nanoparticles with ordered mesostructured interiors," *J. Mater. Chem.*, vol. 13, no. 5, pp. 1023–1029, May 2003, doi: 10.1039/b300851g.

[44] I. Mukherjee *et al.*, "Effect of nonsurfactant template content on the particle size and surface area of monodisperse mesoporous silica nanospheres," *Microporous Mesoporous Mater.*, vol. 122, no. 1–3, pp. 168–174, Jun. 2009, doi: 10.1016/j.micromeso.2009.02.030.

[45] M. Varache *et al.*, "Loading of Cisplatin into Mesoporous Silica Nanoparticles: Effect of Surface Functionalization," 2019, doi: 10.1021/acs.langmuir.9b00954.

[46] L.-P. Wu, D. Wang, and Z. Li, "Grand challenges in nanomedicine," *Mater. Sci. Eng. C*, vol. 106, p. 110302, Jan. 2020, doi: 10.1016/j.msec.2019.110302.

# CHAPTER 5: THE OBTAINING OF COLLOIDAL MCM-41-TYPE MSN

# 5. THE OBTAINING OF COLLOIDAL MCM-41-TYPE MSN

## 5.1. INTRODUCTION

Obtaining discrete, monodisperse and colloidal MSN, along with controllable particle and pore size, is highly attractive to researchers due to promising applications in fields such as chromatography, cosmetics, catalysis and adsorption [1]. Specifically, colloidal MSN preparation is especially important in biomedical applications, such as drug and gene delivery or biosensors [2], because of the need to control the physical, hydrodynamic, and chemical properties of the nanodevices. This is because the use of non-colloidal nanoparticles may provoke toxicity, vascular and lymphatic blocking [3], and the worsening of the efficacy of cellular uptake and other pharmacokinetic processes, such as the blood circulation time and biodistribution, which are related to the capture by reticuloendothelial system (RES) [4]. In addition, achieving colloidal properties in nanoparticles is helpful to fine control the functionalisation and drug loading and release [5]. Thus, the suspendability of MSN has been pursued by a plenty of research groups.

In this context, the goal is not only to obtain discrete MSN, but also to form stable colloidal suspensions in aqueous and, more important, in physiological media. This remains as a great challenge, due to the ionic interactions among the particles in the nanoscale [6][7], as well as the presence of salts and proteins in the physiological fluids [8], which both tend to aggregate the MSN.

The aim of this work is to improve the knowledge about the obtaining, characterisation, and manipulation of colloidal MCM-41-type MSN. For this purpose, in this work we start from a critical review of the studies that report the obtaining of colloidal, well-suspended or discrete MSN, especially MCM-41-type ones. Considering the state of the art and the knowledge obtained in the previous chapters, the colloidal behaviour of several nanoparticles under different conditions is studied and compared. In addition, we present a methodology to characterise the colloidal stability of MSN. Finally, applying the colloidal physics theory, the knowledge reported in the literature, as well as our own research, a conceptual and operational framework is developed. It is made up of considerations in terms of understanding not only the principles governing the colloidal stability of MSN, but also some rules for reducing the nanoparticles aggregation and sedimentation, and for manipulating and characterizing the colloidal MSN.

### 5.1.1. Colloidal suspensions

#### 5.1.1.1. Introduction to colloids

A colloidal suspension or colloid is defined as an intrinsically complex system or mixture which contains microscopically dispersed insoluble particles (ranging from 1 to 1000 nm in diameter) suspended and evenly distributed throughout another substance, which is called solvent and it is formed by smaller molecules (generally, in atomic dimensions) [9][10][11]. There are several types of colloid mixtures, depending on the nature and state (solid, liquid or gas) of the dispersed

molecule and the solution. The colloidal systems most common are sol (solid particles in a liquid phase), emulsion (liquid dispersed in other liquid phase), foam (gas dispersed in a liquid or solid phase), and aerosol (liquid or solid particles in a gas phase). In the context of colloidal mesoporous silica nanoparticles, we refer to a sol mixture.

It has to be remarked that colloids, unlike solutions, do not constitute a dissolved solute in a solvent. Then colloidal properties differ from solutions properties. Colloids have a heterogeneous nature since they are formed by two differentiable phases. However, they have a homogeneous appearance, being that they appear as a homogeneous solution and suspended particles are so tiny that are not visible to the naked eye.

For a mixture to be classified as a colloid, its suspended particles must not settle down, i.e., the suspension must be stable over the time. This stability is largely associated with the continuous motion of particles in the suspension, called Brownian movement, which opposes the gravitational force. This movement is based on the intrinsic fluctuations of particles due to temperature and the collisions between them [12], which provokes a random zigzag movement. Stability of a suspension is compromised when particles tend to aggregate and sediment, which can be a reversible phenomenon, or they can irreversibly coagulate or flocculate [9] (Scheme 1).

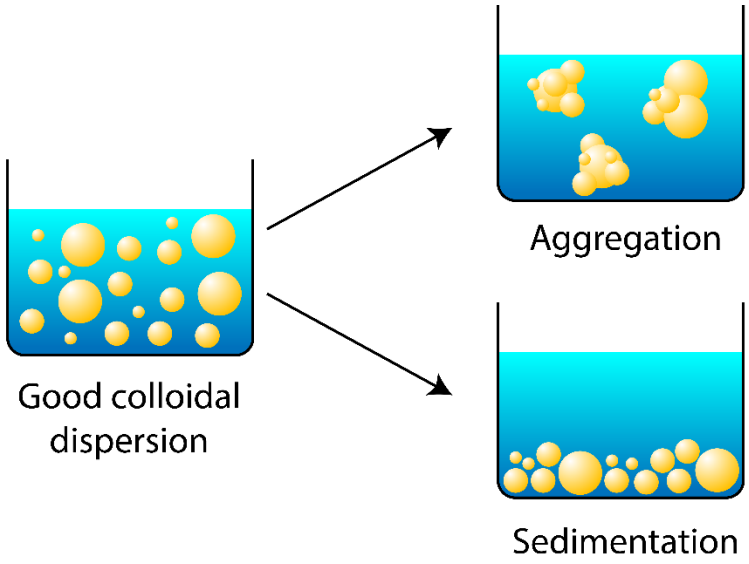


*Scheme 1. Schematic representation of stable colloids and different behaviours of unstable colloids.*

#### 5.1.1.2. Colloids properties

Therefore, due to the stability of a colloidal suspension and the minute size of particles, phases cannot be separated by ordinary filtering or centrifugation. For this purpose, ultracentrifugation and ultrafiltration have to be used. However, another method such as dialysis can be used to separate the colloidal suspensions, being that the membrane used has very small pores. Since dialysis is a slow process, it can be improved by applying electrical force, resulting in the method known as electrodialysis.

Secondly, colloidal suspensions exhibit specific optical properties. The main property that they show is the scattering or dispersion of light, whose typology depends on the size of the particles

(Figure 1) [13]. On the one hand, when the colloids are in the same size order or slightly larger than the wavelength of the incident light, the interaction between the light and the colloidal particles follows the Tyndall scattering. The intensity of light scattered due to Tyndall effect strongly depends on the size of the particles, but it is independent of the light wavelength. As a result of the Tyndall effect, when a laser passes through a colloidal suspension, an illuminated path called Tyndall cone is formed. It has to be noted that solutions do not exhibit Tyndall effect and hence, the formation of this cone can be used as experimental manner to distinguish them. Additionally, for colloidal suspensions formed by homogeneous spheres in the range of the light wavelength Mie theory can be applied to mathematically describe the Tyndall scattering and then, it is called Mie scattering [14]. The intensity of light scattered by Mie scattering depends strongly on the light wavelength and on the size of the nanoparticles, and for this reason is mainly applicable to homogeneous colloids. Finally, in case of suspensions of the smallest colloids the dispersed light is described by the Rayleigh scattering. This last type is highly dependent on the wavelength of the incident light, being more intense at higher electromagnetic radiation frequency. Besides, the intensity of the light scattered by Rayleigh model is much less intense than Tyndall scattering or Mie scattering [13].

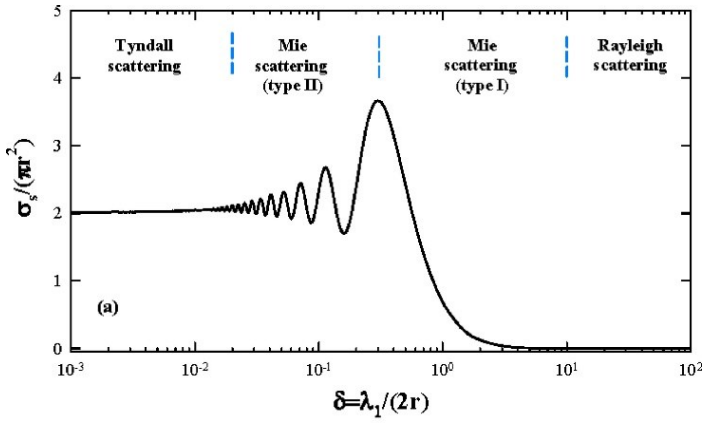


*Figure 1. Calculated curve of the relative scattering cross section against the parameter δ. The parameter δ represents a ratio between the wavelength and the nanoparticle size. The wavelength is fixed at 500 nm. The sample studied consisted of polystyrene microspheres in water. The Tyndall scattering is assigned to larger particles, the Mie scattering to intermediate sizes and Rayleigh scattering to smaller nanoparticles. Reprinted with permission from reference* [13]. *Copyright © 2009 American Institute of Physics.*

#### 5.1.1.3. Physics of colloids

According to the physical principles of colloids, their behaviour depends on the **thermodynamics** of the system, including the enthalpic and entropic contributions to the total free or potential energy [15]. The tendency of any system is to minimise this energy if there is no external force acting. The free energy in a colloidal suspension depends on the sum of the total interaction forces that are present in the suspension [11][16].

First, the **Brownian force** is the main inner force in a colloid. It is caused by the thermal agitation and the consequent bombardment by the surrounding fluid molecules, which act as a randomising effect. Such as is mentioned above, colloids particles are in the range of a few nanometres up to a few micrometres. These particles are called Brownian particles, being that the Brownian motion has a notable effect over them. The distribution of Brownian particles is

described by diffusion motion. Colloidal particles possess an upper size limit, from which Brownian motion is not strong enough to move the particles in an erratic manner. These particles are known as non-Brownian particles, which are passive entities acted only by external forces or flows to drive their dynamics. Apart from non-Brownian particles, Brownian motion is small or negligible when particles are moving in an imposed flow (inertial force), or they are active swimmers or sedimenting colloids. In general, the **gravitational force,** opposite to Brownian motion, is precisely the force that tends to sediment non-Brownian particles.

Other different external forces can be found acting in a colloid. For example, the colloidal particles experience internal dipole fluctuations, which give rise to formal charges and then, relative weak attraction forces, also known as **van der Waals interactions** or dispersion forces. These interactions are always attractive, producing colloidal aggregation if they prevail. Dispersion forces can be strong at short distances and high contact surface, but they decrease dramatically with distance (in a quadratic manner) and slightly with increasing salt level.

**Double layer or ionic interactions** are also important in the colloidal behaviour. This effect is caused by the existence of permanent charges in the colloidal particles. In case of colloids with identical particles, these interactions are always repulsive, because they possess the same charge with the same sign. In case with different populations of particles, interactions can be repulsive or attractive depending on the sign of the charge. Ionic interactions increase with the charge densities per unit area of particles but decrease mainly with the dielectric permittivity of solvent and the presence of salts, since these screen the ionic interaction between colloids. In addition, double layer forces decrease exponentially with the distance between particles.

As mentioned above, other force implied in the colloids dynamics is the **inertial force**, which is caused by the movement of the fluid in which the colloidal particles are suspended. Nevertheless, the colloidal dispersion studied in this context occurs at low Reynolds numbers, namely at rest conditions or low laminar flow. Then, particles are quasi-inertia-free and viscous forces dominate over inertial ones. **Viscous force**, which depends on the solvent and the presence of solutes, hinder the movement of the colloids, and then decrease the number of collisions and the aggregation in a colloidal dispersion.

Despite the variety of forces that interact in a colloidal system, for Brownian particles the free energy can be approximated simply by taking and adding the Van der Waals interactions, acting as the main attractive force, and the double layer interactions, resulting from electric charges, which act as the main repulsive force. The Figure 2 shows the **energy evolution** in a homogeneous colloidal suspension of Brownian particles as a function of the distance among the particles. At shorter distances, there is a deep attractive well, in which Van der Waals forces dominate. This well is referred to as the primary minimum and is related to the aggregation between particles. At in-between distances, the energy profile rises to a maximum, where double layer force dominates. Subsequently there is a secondary minimum, in which Van der Waals forces prevail again. This secondary minimum is not generally associated with the aggregation kinetics, but in larger particles it can be relatively deep and makes it easier to overcome the primary minimum.

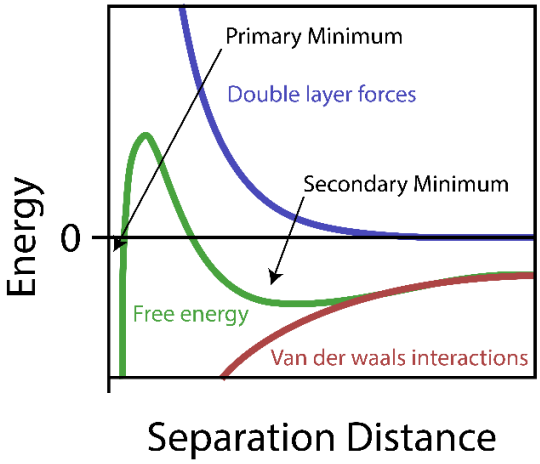


*Figure 2. Representation of the potential energy of a colloidal suspension (green), which is mainly calculated from the contributions of van der Waals (red) and double layer (blue) interactions.*

In this context, it can be inferred that the concentration of the colloidal suspension influences on their stability, since the concentrated suspensions will have a greater **tendency to sediment** because their particles are closer to each other, and vice versa. On the other hand, the concentration of salts in the solvent also influences on the interactions forces between particles. At high salt levels and high ionic charges, van der Waals forces prevail over ionic forces, being that the screening caused by ions in solution affects the surface charge to a greater extent. At low salt levels and low ionic charges, the double layer contribution dominates, because in absence of high screening ionic forces are higher than dispersion ones. Finally, surface charge densities are involved in the evolution of the energy curve too. At high surface charge densities, the repulsion between nanoparticles increases and then the double layer force dominates; meanwhile at lower surface charge densities, the ionic force decreases and van der Waals interactions become pervasive. In this context, small changes in composition can drastically affect the stability and properties of colloids.

The **aggregation** of particles in a colloidal dispersion corresponds to the deep primary energy minimum. Generally, particles experience diffusional motion in the fluid. Within this stochastic movement, the particles can come close enough and stick to each other, forming aggregates if they overcome the energy barrier caused by double layer force, either because the electrostatic repulsion is weak or because inertial force is high due to a strong stirring causing more and stronger collisions between particles. Initially, when particles aggregate, they form dimers and trimers and other oligomers; as the aggregation proceeds, they can form larger flocs or clusters. Once particles are aggregated, they could sometimes be resuspended by adding external forces, but this process hardly occurs spontaneously.

The **aggregation rate** can be studied and determined by analysing some variables. This parameter is increased by increasing the temperature, the concentration of colloids, the salinity, and the valence of salts (the ionic strength); and it is decreased with a major viscosity of samples and higher surface charge density. When the conditions of the suspension are favourable to aggregation, the aggregation rate is constant and fast, and the sample follows a behaviour called diffusion-controlled aggregation, namely, aggregation is driven by the inner diffusion of particles. In those cases in which colloidal suspension is stable, the aggregation rate is slowed

down, since particles needs to cross the energy barrier, in a similar way to the activation energy in a chemical reaction. This behaviour is named reaction-controlled aggregation. The transition between a behaviour to another is relatively sharp and is known as critical coagulation concentration. This point is important and characteristic of the aggregation process in each colloidal system. In this context, this provides a stability threshold of the colloidal dispersion [17][18][19].

**Sedimentation** can occur when Van der Waals or attractive forces dominate the system and tend to aggregate the nanoparticles, forming large flocs unable to have colloidal stability. Moreover, in presence of already non-Brownian particles, the Brownian motion is negligible and then, they tend to sediment [16]. Generally, in a colloidal suspension sedimentation is partially hindered as the downward flow of descending particles move a volume of fluid that must be compensated for by a back flow of fluid. Nevertheless, once sedimentation starts, it is favoured by intrinsic convection if the void left by moving fluid is filled by other sedimenting particles. Therefore, the sedimentation velocity is larger in the case of neutral spheres, due to the attractive pair potential contributions, and lower in charge-stabilised spheres, owing to the longer-range electric repulsion to each other. In essence, sedimentation occurs because it reduces the interfacial tension between the colloidal particles and the solvent.

In order to **guarantee the stability** of the colloidal suspensions, they can be provided with stabilisers, whose approaches most employed are charge and steric stabilisation. Therefore, colloidal nanoparticles can be functionalised with ionisable chemical groups on their surface or with self-avoiding polymer chains, respectively. The interactions among the nanoparticles can be also altered by modifying the dispersive solvent. For example, the addition of salts screens the electrostatic repulsions and tends to agglomerate the nanoparticles. Nevertheless, the presence of non-adsorbing polymer reduces the attractive forces. In addition, the interactions can be modified by applying external energy such as electric or magnetic fields, heat source, movement, ultrasounds, gravity, etc.

### 5.1.2. Dynamic light scattering (DLS)

Such as it was described in the general introduction, **dynamic light scattering** (DLS) is used to calculate the size of the particles and molecules in a sample. DLS registers over the time the fluctuations of the particles and compounds in a sample that follow the Brownian motion.

Therefore, working with stable colloidal suspensions or dissolutions is a requirement for the proper operation of DLS measurements. In case of MSN preparations, large agglomerates, sediments, and particles that settling down do not follow the Brownian motion. This provokes irregular and complex shifts in the speckle pattern and correlation data that cannot be fitted with the different mathematical approaches the technic uses. Another limitation the method can encounter is the high polydispersity in a MSN sample. The measurement of this type of samples results in the formation of a mix of speckle patterns belonging to different sizes of nanoparticles that sometimes cannot be isolated from each other and therewith, they are fitted as a wide range of size populations or are unable to be measured.

Usually, DLS analysis will try to give us a result, but it is not always reliable. In this context, it is useful to have a deep knowledge about the DLS functioning in order to analyse and interpret the data obtained when a DLS sample is measured, and to discriminate the quality and reliability of results.

#### 5.1.2.1. Count rate

The count rate shows the number of photons detected per time. This data can give us a first approach to determine the sample quality and concentration. A proper count rate function exhibits stable peaks and valleys, with similar amplitude and height (Fig. 3A, a). On the other hand, if sharp and wider spikes are observed at the same time, it means there is dust or aggregates in the sample. These aggregates can also provoke a decreasing and increasing in the count rate, which modifies the height of peaks (Fig. 3A, b). Other phenomenon such as wild fluctuations in count rate could be found due to thermal gradients (Fig. 3A, c). Additionally, if count rate is too high or too low may be due to inadequate sample concentrations, presence of absorbance or fluorescence, the instability of sample during the measurement and the presence of large aggregates.

In this context, the use of the derived count rate (DCR), which is a value calculated from count rate function, can be a sensitive tool to study the stability and sedimentation of MSN over time. If the DCR of a sample remains constant over time, their scattering is constant too and it can be assumed their stability. On the contrary, if the DCR decreased over time, it can be suggested that the sample is decanting [20].

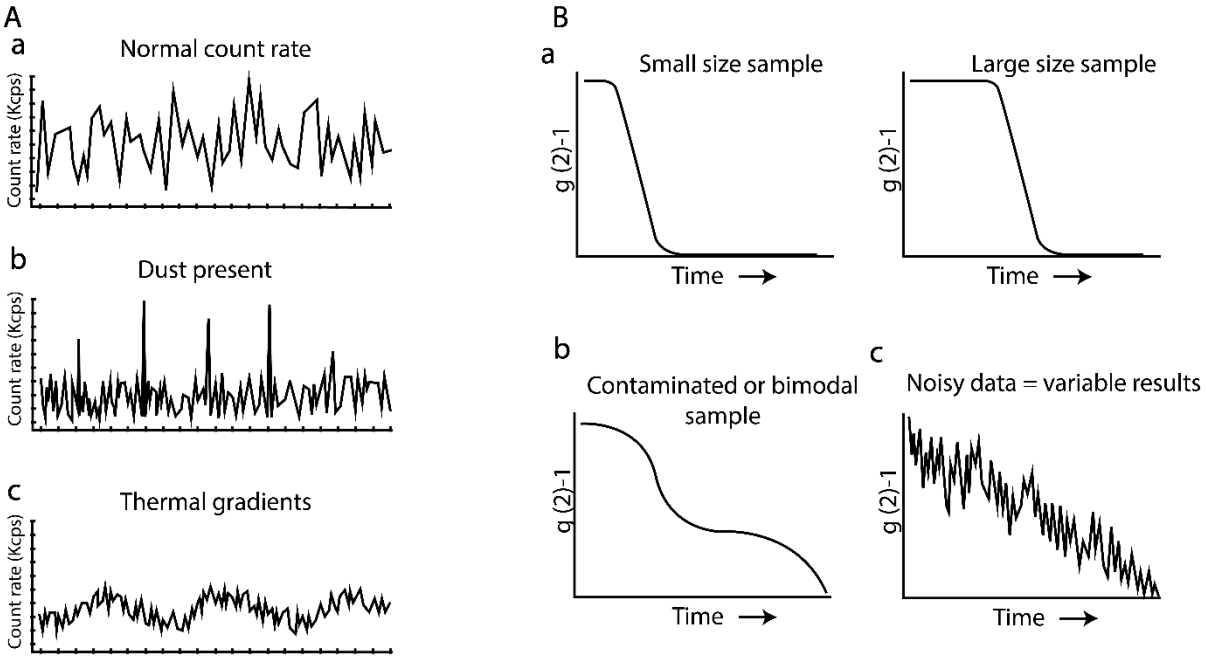


*Figure 3. (A) Examples of count rates display in case of (a) stable suspension, (b) presence of dust or large aggregates, and (c) thermal gradients. (B) Examples of correlation function display in case of (a) monomodal, (b) bimodal and (c) unstable suspension.*

#### 5.1.2.2. Correlation function

The correlation function is one of the outputs the technic shows us when a measurement is performed, and through which size distribution is calculated. This function is useful to interpret some problems in the sample or measurement [21]. On the one hand, the y-intercept of correlation function can be used to evaluate the signal-to-noise ratio in a sample. This must be between 0.85 and 0.95. Lower values mean we are measuring a weak scattering sample or a turbid sample, which have a high background scattering. Higher values occur when count rate of sample fluctuate wildly and background is not stable, for example, in sample with high content of dust. When correlation function y-intercept is out of range, it can also mean that sample is too concentrated or too diluted, or that absorbance and/or fluorescence are present. If the y-intercept values are out of the range, the results obtained are not invalid, but the results are less robust and reliable.

Regarding the correlation curve, it must be able to be fitted to a smooth n-modal curve (Fig. 3B, a,b). In the presence of agglomerates or impurities, non-smooth and irregular curves are obtained, which cannot be reliably fitted (Fig. 3B, c). Finally, correlation function must be fitted to a single exponential decay in a single-size MSN dispersion. For n-size samples, the curve will be n-modal, namely, the sum of exponential decays. However, this technique is not always able to fit this type of samples. Besides, the measurement of highly polydispersed samples or the presence of agglomerates do not exhibit a smooth and exponential decay and cannot be fitted as such.

Therefore, the quality of the correlation function, following the criteria discussed, is directly related to the reliability of the measurement performed.

#### 5.1.2.3. Attenuator

The intensity of scattered and collected light must be within a range in which the detector operates successfully. Then, DLS instruments use an attenuator, which automatically controls the light intensity emitted by the laser. Attenuator values are set from 1 to 11, corresponding a setting of 1 to a maximum attenuation, and 11 to no attenuation. Hence, more concentrated samples correspond to lower attenuator values and diluted sample to higher ones. In case of MSN dispersions, proper measurements are usually those that have an attenuator from 6 to 9, since the corresponding samples are found more stable. Therefore, samples set to lower attenuator than 6 are too concentrated, which can lead to a great aggregation and sedimentation of nanoparticles and disturb the measurement. On the other hand, those samples in which the attenuator is higher than 9 can be too diluted. In the case of MSN with an attenuation of 10, errors and noise in the correlation function tend to lead to unreliable results.

#### 5.1.2.4. Cumulants and distribution analysis

DLS method can analyse the correlation function considering two methods: cumulants and distribution analysis. The data obtained by means of both methods can be used if a good fitting of the correlation function is observed for each one.

#### 5.1.2.4.1. Cumulants analysis

Cumulants analysis is the simplest method to analyse the correlation function, based on fitting the logarithm of the correlation function to a polynomial function, and then, giving the size dispersion as a simple Gaussian distribution. The mean of this Gaussian is known as Z-average and the width as Polydispersion index (PDI).

Z-average: is the most reliable and stable number produced by the technique and is used for quality control purposes provided some quality criteria are met. These requirements are: i) the sample must be monomodal, ii) the particles must be spherical, and iii) the samples must have a narrow distribution size (PDI below or slightly greater than 0.1). For broader distributions, it starts to be unwise to rely on the Z-average mean. Furthermore, Z-average can only be used to compare results obtained in the same dispersant. This number is intensity-based value, so it is very sensitive to small changes in the sample or the presence of small populations of aggregates.

Polydispersion index (PDI): indicates the broadness of the size distribution in the calculated Gaussian function. PDI is a dimensionless number, which goes from 0 to 1. For homogeneous samples, such as MSN suspensions, the smaller the value of the PDI parameter, the narrower the size distribution, and then, the greater the reliability of the results obtained. It is rare to find smaller PDI values than 0.05 in other samples than high monodisperse standards, and much less in MSN dispersions. On the other side, MSN suspensions with PDI values as of 0.5-0.7 indicate a too broad size distribution or a high presence of sediments and aggregates and, therefore, the sample is not suitable to be measured by DLS. PDI values from 0.1 to 0.3 indicate an acceptable MSN suspension.

#### 5.1.2.4.2. Distribution analysis

Distribution analysis is based on considering the function as the sum of different contribution from different particle sizes and is therefore also called particle size distribution (PSD) analysis. Therefore, this method is more appropriate for those samples with broader distribution size or with different populations. Regarding this method, several data can be obtained: intensity PSD, volume PSD and number PSD.

The intensity PSD is the fundamental size distribution generated by DLS and is related to the amount of light scattered by the populations in the sample. In that context, intensity distribution can be somewhat misleading, as smaller populations of aggregated or large particles result in high signals because the larger particles scatter at a sixth power their size. The intensity of light scattered can be calculated by the Rayleigh approximation equation (Equation 1).

$$I = I_0 \frac{1+cos^2\theta}{2R^2}\left(\frac{2\pi}{\lambda}\right)\left(\frac{n^2-1}{n^2+2}\right)^2\left(\frac{d}{2}\right)^6 \quad (1)$$

The intensity data can be converted using Mie theory to the volume distribution or the number distribution. The volume PSD represents the total volume of each population of particles, and the number PSD shows the number of particles in each population. Intensity to volume and number conversions are valid if the sample meets the following requirements: the particles are spherical and homogeneous, the optical properties of particles are known, and there is no error in the intensity distribution. The last requisite is important, because small errors in the intensity distribution are over-amplified in the volume and number distributions. Then, volume and

number PSD are generally used for comparative and estimative purposes and not for absolute values consideration.

Therefore, distributions calculated in terms of intensity, volume and number are often quite different. On the one hand, intensity distributions emphasise the larger populations, and on the other hand, number distribution emphasise the smaller ones. It is explained by the different contribution of each size population to the whole distribution, as the equations 2-4 shows, where *a* and *b* are the sizes of two nanoparticles populations.

$$\% N_a = \frac{N_a}{N_a + N_b} \cdot 100 \quad (2)$$

$$\% V_a = \frac{N_a \cdot a^3}{N_a \cdot a^3 + N_b \cdot b^3} \cdot 100 \quad (3)$$

$$\% I_a = \frac{N_a \cdot a^6}{N_a \cdot a^6 + N_b \cdot b^6} \cdot 100 \quad (4)$$

## 5.2. THE OBTAINING OF COLLOIDAL MSN: A CRITICAL REVIEW

Getting colloidal MSN suppose a step forward in nanomaterials and nanomedicine fields. To date, there are quite studies that report the obtaining of discrete and colloidal MSN, although most of these results are still far from being reproducible or scaled, and they are also inadequate to be applied in nanomedicine. In addition, only a few of them talk about MCM-41-type MSN. The synthesis of suspendable MSN is indeed a challenge, as some authors stated in 2018 [22]. Proof of this is that even when researchers are still working on it, the synthesis reported by Cai et al. in 2001 [23] is one of the most widely used procedures for obtaining of MCM-41-type MSN, and it has not been replaced by any other improved protocol in most studies. Then, a critical review of the literature about obtaining discrete and colloidal mesoporous silica nanoparticles is developed below.

### 5.2.1. MCM-41-type MSN

In case of MCM-41-type MSN the number of reported studies about the obtaining of discrete and colloidal suspensions are scarce.

One of the works in this context was carried out by Lu et al. in 2009, in which the obtaining of well-suspended and uniform MCM-41-type MSN [24] was reported for the first time. These MSN were prepared by a two-step method, namely separating nucleation step from growth step. For this reason, they used diluted conditions for TEOS and surfactant. The catalyser used was $NH_4OH$, which has less alkaline strength than NaOH. They obtained nanoparticles with high surface area (ca. 1000-1300 $m^2\ g^{-1}$) and pore volume values of ca. 0.9-1.1 $cm^3\ g^{-1}$. However, the TEM images show clear interparticle aggregation in most of samples, even though they indicate that the particles did not aggregate. Therefore, the presence of these clear bridges between nanoparticles contrast with the DLS results, which show just a slight increase in particles diameter compared with TEM measurements.

Other work described by Begum et al. in 2010 affirmed that the preparation of monodisperse and stable colloidal MCM-41-type MSN by using a bioinspired route, which was based on polyamine-catalysed silicification and the use of mild conditions [25]. They used polyallylamine or poly(L-lysine) as co-surfactant and basic catalyser. The synthesis was performed in citrate buffer solution and silicic acid was used as the silica precursor, which was added to a mixture of CTAB, citrate and polyamine. The nanoparticles obtained have suitable parameters for biomedical and drug delivery applications, since they have a size of 40 to 250 nm, have a surface area ca. 700-1000 $m^2\ g^{-1}$ and pore volume ca. 0.6-0.9 $cm^3\ g^{-1}$. Besides, DLS assays showed a narrow distribution size. Nevertheless, TEM images showed fusions between nanoparticles in most samples. In addition, DLS assays were performed with as-made nanoparticles directly taken from the reaction suspension. In this way, the measured samples contained an excess of CTAB, which usually acts as nanoparticles dispersant [26][27].

Lechevallier et al. [28] also claimed to obtain spherical shape and non-agglomerated MCM-41-type nanoparticles. They followed the standard synthesis established by Cai et al. including some modifications, such as setting the TEOS addition in a slower rate (0.25 mL/min); allowing the reaction to stir for 20 hours, instead of 2 hours; and calcining the sample at 500 degrees, rather

than 550 degrees. They managed to prepare nanoparticles with high surface area (1018 $m^2 g^{-1}$) and high pore volume (1.397 $cm^3 g^{-1}$). Nevertheless, TEM pictures showed nanoparticles with a broad size dispersion, being the average of Feret's diameter 116 nm with a standard deviation of 45 nm (almost a 40%). Moreover, some fusions between nanoparticles can be observed in the images. No further assays were performed in this study to check the colloidal behaviour, such as DLS or colloidal appearance in different solvents.

Some studies suggest that the aggregation and formation of mesoporous bridges between nanoparticles might be owing to the presence of carbonates and ethanol in the reaction mixture, which are formed as side-products during the synthesis reaction. Carbonates are derived from carbonation of the NaOH in contact with the atmospheric $CO_2$ and ethanol from the hydrolysis of TEOS. Varache and coworkers [29] studied the effect of both compounds and reported the synthesis of stable colloidal MCM-41 nanoparticles. On the one hand, they verified the obtaining of highly fused MCM-41-type nanoparticles when the MSN were prepared using a NaOH solution aged several days in ambient air that, therefore, was greatly carbonated. The authors explained this behaviour because the interactions of carbonate anions with the surfactant micelles enhance the silica polymerisation rate, as was previously described [30], and interfere the mesophase arrangement. Nevertheless, in this assay extreme conditions were used such as leaving the NaOH solution aging for a few days and reaching a 41% of carbonation. Generally, MSN synthesis use fresh NaOH solutions, which are prepared just before being added to the CTAB solution and do not show significant carbonation. On the other hand, they asserted that the higher presence of ethanol tended to aggregate slightly the nanoparticles. They compared the standard synthesis and one in which the presence of ethanol is reduced and observed that the standard nanoparticles had larger hydrodynamic sizes but without an increase in the nanoparticle size, identifying a greater aggregation in it. The authors argue that the presence of ethanol increase the miscibility of TEOS oil droplets in water, which in turn increases the rates of hydrolysis and condensation, making the reaction faster and presumably less controllable. In addition, ethanol facilitates the matter transfer between the nuclei during the formation of nanoparticles, which could generate bonds between them. Nevertheless, this reasoning clash with previous knowledge, which asserts that the use of ethanol as co-solvent helps to the formation of circular and discrete nanoparticles, as is extensively reported in the Stöber method and derived protocols [31][32]–[35][36]. As a result, Varache et al. claim to have obtained non-aggregated and stable nanoparticles by using inert atmosphere with $N_2$ flow. This not only would protect the NaOH from carbonation, but also would reduce the formation of ethanol during the MSN synthesis. The results were validated with TEM analysis and DLS measurements. However, no representative TEM images are shown at the work. In addition, DLS analysis were performed on as-made nanoparticles directly taken from the reaction suspension.

Carbonaro et al. described the preparation of stable colloidal MCM-41-type MSN doped with a dye for imaging applications [37]. The synthesis was performed at room temperature and using TEOS as silica precursor, CTAB as surfactant, $NH_4OH$ as catalytic base, ethyl acetate as growth inhibitor or co-surfactant, and water as solvent. The samples prepared, such as MCM-41-type MSN, had a high surface area (1268 $m^2 g^{-1}$) and high pore volume (ca. 1 $cm^3 g^{-1}$) once surfactant was removed. The nanoparticles obtained showed the appearance of stable dispersions in water over time for months. Nevertheless, these measurements were performed on as-made samples, which will not be used in a realistic context. In addition, TEM images let observe some fusions

between nanoparticles and, therefore, the nanoparticles are not discrete. On the other hand, DLS measurements were not performed to ensure the colloidal stability of the samples.

### 5.2.2. Other MSN frameworks

In the literature, studies that report obtaining of well-suspended or colloidal MSN with other frameworks are quite common. They can be classified according to the method or approach used for this purpose.

#### 5.2.2.1. Stöber-like synthesis

One of the most common approach to prepare monodisperse particles is the **Stöber-like synthesis**, where ethanol is included as co-solvent and the catalytic base used is ammonium hydroxide. Nevertheless, studies reporting the obtaining of effective non-aggregated-monodispersed mesoporous silica materials following a Stöber-like procedure give spheres in the micron and sub-micron scale, mostly above 300 nm. It could be said that there is a compromise between the synthesis of monodisperse particles and reducing their size to nanoscale.

Some studies follow this strategy, such as those led by professor Golubev [38][39][40][41][42]. Other authors, such as Tao [43] and Baliś [44], follow similar procedures. Nonetheless, most of these works do not carry out suspension stability assays, far less in physiological conditions.

Sun et al. synthesised monodisperse and colloidal stable silicate "nanoscintillators" on a large-scale for their application in photodynamic therapy [45]. These nanoscintillators were prepared with MSN synthesised through a Stöber-like synthesis (ethanol as co-solvent and $NH_4OH$ as catalyser), doped with different metals and whose surface was functionalised with targeting agents. These nanoparticles had uniform size, with a diameter of 80.8 ± 3.5 nm calculated using TEM images and hydrodynamic diameter of 101.2 ± 2.7 nm measured by DLS. In addition, nanoparticles obtained had excellent colloidal stability in water, PBS (pH 7.4), 10% FBS and DMEM over two weeks, being one of the few studies that measure the suspendibility properties in physiological media. However, although they claim to have synthesised mesoporous silica nanoparticles, in their work there is not information or characterisation on porosity, surface area, pore volume or size.

Paula et al. broadly studied the colloidal stability of different samples of MSN as a function of their topology and functionalisation in the presence of several physiological-like medium (BSA or alginate in PBS, human blood plasma) [6]. The synthesis performed was derived from the Stöber method combined with co-condensation in order to add different organosilanes. Two types of nanoparticles were synthesised, spherical ones and irregular ones. Both were functionalised either with amino-groups or phosponate-groups. The spherical samples showed surface area ca. 700 $m^2\ g^{-1}$ and a pore volume ca. 1 $cm^3\ g^{-1}$. Meanwhile, irregular samples had higher surface area (ca. 930 $m^2\ g^{-1}$) and pore volume (ca. 2 $cm^3\ g^{-1}$). Both samples are considered to be suitable for cargo delivery. The nanoparticles obtained were observed by TEM, showing they were highly aggregated. Therefore, even though the diameter measured in TEM images is

ranged from 40 to 80 nm, DLS assays showed quite larger diameters in all the samples. In fact, it was not possible to perform DLS measurements in PBS since the suspensions were unstable and settled down. In the case of DLS analyses performed in deionized water, diameters measured were around 120 nm (PDI = 0.1), between two and three times the diameter obtained by TEM. These results seem to indicate that the nanoparticles are effectively fused and agglomerated. In addition, the presence of biomolecules (BSA or alginate) provokes, on the one hand, that some samples multiply by twice their average size (diameters in the ranging from 200 to 300 nm) and, on the other hand, that the suspensions become unstable and sediment. Authors claimed that all the MSN samples were colloidal stabilised in human blood plasma (55%), however, they did not show DLS or stability assays.

#### 5.2.2.2. High dilution method

High dilution method is based on diluting the silica precursor in the synthesis by means of increasing the amount of solvent or decreasing the amount of precursor, in order to keep the particles formed separately [7]. In fact, dilution method was the strategy chosen by Cai et al. [23], Fowler et al. [46], Nooney et al. [47] and Rathousky et al. [48] in the first studies performed to synthesise mesoporous silica nanoparticles from microparticles synthesis protocols. None of these methods obtained non-aggregated and colloidal nanoparticles. Cai et al. did not report that the nanoparticles synthesised were stable colloidal or monodisperse. In the case of Fowler and co-workers, they asserted the obtaining of colloidal suspensions of MSN. Nevertheless, the suspensions obtained were a mix of two differentiable populations (10 nm and 100 nm), which are difficult to separate from each other. Besides, the authors did not show DLS measurements or proved the colloidal behaviour of surfactant removed samples. Nooney and co-workers reported that they had obtained colloidal nanoparticles ca. 60 nm and 190 nm using a derived Stöber synthesis, but it is unclear whether the observations were made on as-made or calcined nanoparticles and which was the solvent used to suspend them. No DLS assays were reported. Synthesis made by Rathousky et al. obtained highly fused nanoparticles.

Furthermore, there are some major limitations around this method. Collecting and isolating the MSNs from a highly diluted solution requires considerable time and energy and has a low yield [46][29][49][7]. In addition, these samples are often difficult to be scaled to larger quantities [7].

#### 5.2.2.3. Binary surfactant mixture

The use of binary surfactant mixture is based on the addition of a steric stabiliser as a secondary surfactant, which remains in the external side of micelles, where silicate groups are polymerising. This procedure makes possible to control the growth of nanoparticles and to reduce the contact between silanol groups of different micelles, since the secondary surfactant hinder the micelles from fusing with each other. Some of steric stabiliser used are Pluronic F127 [50], PEG [51], triethanolamine (TEA) [7] or l-lysine [52].

In spite of the extended use of this method, most of the reported nanomaterials synthesised by binary surfactant mixture have important limitations in the obtaining of discrete, monodisperse

and colloidal MSN. In some cases, the surface area decreases considerably, obtaining non-suitable nanoparticles for drug delivery applications. For example, Pan et al. [53] used TEA to prepared nanoparticles that possessed a surface area of 390−560 $m^2$ $g^{-1}$. Sun et al. [54] synthesised monodisperse MSN by biphase stratification approach. In this system, an aqueous phase contains the surfactant template and the stabiliser (TEA), meanwhile an organic phase is prepared with the silica precursor which is released progressively to the aqueous phase with the stirring. The authors obtained samples highly monodispersed and stable MSN ca. 100 nm in a TRIS derived buffer for 24 hours, obtaining a polydispersity index below 0.1. Nevertheless, the BET surface area calculated was 262.4 $m^2$ $g^{-1}$. In other cases, such as in the studies developed by professor Imai [46][47], the addition of a co-surfactant causes the structure of the nanoparticles to be poorly formed or the nanoparticles be highly fused.

Undoubtedly, TEA is the most widely used stabiliser in binary surfactant mixture protocols. This molecule possesses chelating properties for silicate species that influence the hydrolysis and condensation rate, that limits the growth and aggregation of seeds or silica-surfactant nuclei, especially when high dilution conditions are not used. Therefore, TEA acts as a hydrolysis-retarding agent, leading to better control of nucleation, growth, and formation of nanoparticles. In addition, TEA can act as basic catalyser in some cases, replacing NaOH or $NH_4OH$, due to its alkaline nature. When TEA is used as a base, the synthesis is conducted at lower pH (ca. 8.5-10) due to its lower basic strength. In this context, it has been reported that the substitution of other alkaline agents for TEA is critical to obtain well-dispersed nanoparticles [7][57].

The use of TEA as a complementary surfactant and catalytic agent for the obtaining of monodisperse and non-aggregated MSN was broadly studied by Kuroda and co-workers. In 2012, they reported the preparation of colloidal MSN [58] with diameter from 20 to 80 nm by using TEA as catalyser and co-surfactant. The size of nanoparticles was verified by TEM and DLS. The nanoparticles had a BET surface area ca. 900 $m^2$ $g^{-1}$ and a colloidal appearance at naked eye. In 2015, they used TEA as catalyser in a seed-growth method with the hydrolysis rate variation method (SH method) to obtain colloidal MSN [59]. This method is based on the fine control and separation of nucleation and particle growth, which allows to control the nanoparticles size and to reduce the fusions between the nanoparticles. This control was achieved by dosing the addition of silica precursor, the use of different silica precursor concentrations and types and the use of a moderate alkaline pH. The particles obtained were in the range of 40 to 150 nm, have a BET surface area ca. 900 $m^2$ $g^{-1}$ and have a colloidal appearance at naked eye. Nevertheless, in both studies, TEM images showed some fusions between nanoparticles and a mixture of different populations. Besides, DLS measurement were only performed in as-made nanoparticles. Just several months later, they published the obtaining of colloidal MSN by using similar protocols but adding different trialkylbenzenes as pore size modulators [60]. The nanoparticles obtained show a colloidal appearance. DLS measurements performed in as-made and dialysed samples showed colloidal and stable behaviour. However, according to supplementary data, DLS results contrast with the high number of fusions among nanoparticles observed in TEM images. In addition, there was not any information reported about the surface obtained or pore volume.

In addition to limitations indicated above, studies developed by Kuroda and co-workers are time-consuming procedures (the whole synthesis took almost a week, including the surfactant extraction, since the dialysis is a very slow process).

The group of professor Bein also performed several studies including TEA as a co-surfactant and alkaline agent as an approach to synthesise colloidal MSN. In 2006, they reported to obtain colloidal suspensions of MSN ca. 100 nm, which were functionalised by co-condensation with mercapto groups [61]. Thus, they combine the binary surfactant method with the surface modification in order to avoid the fusion and aggregation between nanoparticles. The synthesis performed followed a biphase stratification approach as other authors reported in the case of binary surfactant systems. In 2007, they published the obtaining of colloidal bare MSN [7]. The synthesis was performed using the seed-based mechanism. In 2008, they described the obtaining of colloidal suspensions of particles between 40 and 150 nm functionalised by co-condensation with different organotriethoxysilanes, which introduced different functional groups [62]. In 2010, they published other study using TEA as catalyser and combining with co-condensation method to obtain colloidal MSN [63]. Generally, in all these studies, the nanoparticles prepared showed a high surface area in the range of 900 to 1200 $m^2 g^{-1}$, which is suitable for delivery applications. They obtained colloidal solutions stable in ethanol, even over several months or a year. DLS measurements in ethanol or water showed narrow size distributions, in some case with a PDI ca. 0.1. Nevertheless, in each of these works interparticle fusions, and even coalescence, are observable. These aggregations were confirmed by analysing DLS assays, since the size calculated is two or three times that observed in TEM images. In 2010, professor Bein and co-workers also reported a study similar to the previous ones, in which the organosilane was added through delayed co-condensation approach [64]. Organosilane added was attached to a PEG tail, conferring the nanoparticles suspension stability. Although the nanoparticles obtained have a high surface area (ca. 1440 $m^2 g^{-1}$) when they are uncapped, this value is reduced to a range between 750 and 1000 $m^2 g^{-1}$ when PEG is added. In addition, the presence PEG hinders the cargo loading, being that pores entrance are not available. Unfortunately, DLS measurements showed that capped nanoparticles are well dispersed, but uncapped nanoparticles tend to aggregate. On the other hand, nanoparticles observed in TEM images are highly fused, coalesced and not well formed.

None of the studies reported by Bein and co-workers performed DLS assays in physiological media or derived one, being one of the most restrictive assays regarding the colloidal stability. In addition, the fact that these particles do not have highly ordered mesopores prevents a fine control of compound loading and release behaviour, an important limitation in control release applications [29].

Yu and co-workers used $TEAH_3$ as soft base catalyst instead of TEA, in a binary surfactant mixture synthesis. They reported the obtaining of reproducible, facile, large-scale, monodisperse and colloidal MSN samples [1]. They synthesised MSN using dendritic-like pore using CTATos as surfactant, and Pluronic F127 as non-ionic co-surfactant and inhibitor of particle growth, in some cases, or imidazolium ionic liquids as co-surfactant, in others. They obtain nanoparticles from 40 to 300 nm, with a low surface area (values from 300 to 450 $m^2 g^{-1}$) and an averaged pore volume (from 0.6 to 0.9 $cm^3 g^{-1}$), which are much less efficient than MCM-41-type for delivery application. Although dendritic pores allow loading larger cargos due to a bigger pore size, this

fact makes difficult to block the pores to achieve the control of the release. TEM images do not allow in most cases to distinguish fusions between neighbouring nanoparticles, although some fusions are observed. On the other hand, they did not show any other stability or colloidal assays, such as DLS.

Finally, professor Kleitz, professor Fortin and co-workers reported the development of a synthesis protocol to obtain well-dispersed and colloidal MCM-48 type MSN. They used a binary surfactant mixture, formed by CTAB and Pluronic F127, in combination with Stöber-like procedure (water and EtOH as solvent and co-solvent, and $NH_4OH$ as alkaline catalyser) and the silica precursor used was TEOS. The reaction was performed at room temperature, and it was only stirred for 1 min, and then aged during 24 h under static conditions. The first study of this group related to this issue was developed in 2011 [65], where MCM-48 and MCM-41 types MSN were synthesised. Nevertheless, in this study they reported some limitations. On the one hand, clear fusions between nanoparticles can be seen in the TEM images. On the other hand, DLS measurements were performed with suspensions previously centrifuged at low force (500 rfc for 10 min), in order to remove the aggregates and sediments. In spite of limitations observed in this initial study, other publications of Kleitz and Fortin group were able to reproduce the production of colloidal and stable MCM-48 type MSN [66] [57][58][59][69], with similar features concerning the nanoparticles size, the surface area and pore volume, among others. However, some limitations are detected in most of these studies, either some aggregations or fusions are observed on TEM pictures, no representative or distinguishable pictures were showed, or DLS measurements were only performed in water. However, some solid results can be remarked in the study performed in 2016 [57], where they reported the obtaining of different spherical nanoparticles in the range of 45 to 500 nm, including 90 and 150 nm. The samples possessed high surface area (ca. 1200 $m^2\ g^{-1}$) and large total pore volume (ca. 1 $cm^3\ g^{-1}$). TEM images do not have sufficient magnification to distinguish the presence of fusions, but there is no visible evidence of them. DLS monitoring shows narrow hydrodynamic particle size distributions (PDI between 0.02 and 0.15), slightly larger than sizes observed by TEM, as it is expected in non-aggregated nanoparticles. During the measurements, performed in water and saline solutions, no aggregates or flocculates were detected. Furthermore, the suspensions prepared were stable at least a week. The authors remarked that these assays were performed with nanoparticles after drying and calcination, which are normally bottlenecks found in other works. Considering these reported evidences, it is confirmed the excellent colloidal stability of these nanoparticles.

In addition, this procedure has been repeated or modified by other groups, especially in the last years. Some of the publications have been able to adequately reproduce properly the same characteristics in terms of colloidal stability, mesoporosity and size. However, in most cases the DLS studies or other assays to check the colloidal stability were not so complete and detailed, and then, some information useful to validate them is missed [70][71][72][73][74][75]. In this context, in some studies the nanoparticles obtained are quite fused or with a tendency to agglomerate, and there is not information about DLS assays [76][77][78].

#### 5.2.2.4. Synthesis without surfactant

Other studies were developed using a non-surfactant method, but other organic molecule was used as templating agent in order to synthesise non-aggregated MSN.

Mukherjee et al. [79] described a synthesis in which surfactants were not used as a template, but monosaccharides. They claimed to obtain monodisperse and colloidal mesoporous silica nanospheres. Hence, using different conditions and templates, they obtain particles from 50 to 1000 nm. Nevertheless, the nanoparticles prepared below 200 nm barely achieve 400 $m^2 g^{-1}$ of surface area. In addition, DLS measurements were performed directly from the reaction mixture, including ethanol, monosaccharides' excess and mildly alkaline pH. These conditions are mentioned to facilitate the suspension of MSN and far from physiological ones.

Qiao et al. reported in 2018 a synthesis of monodispersed and colloidal stable nanometric organosilica particles [22]. The authors employed a surfactant-free method to obtain the nanoparticles using the so-called waterborne sol-gel process. In the study, L-arginine was used as alkaline catalyser and γ-MPS as organo-silane source and template agent. A liquid-liquid biphase was formed by organic compounds (TEOS and γ-MPS) and aqueous solution (water and L-arginine), where organic precursor is delivered to the latter. DLS assays showed sizes slightly larger than TEM images, in the range of 30 to 800 nm, and the PDI values are lower than 0.1, which support the colloidal stability of samples. Nevertheless, the samples had a low surface area, which was calculated in the range of 475 to 680 $m^2 g^{-1}$ and whose pore volume corresponded to 0.1 to 0.3 $cm^3 g^{-1}$.

Hartlen et al. reported a similar synthesis of highly monodisperse and colloidal small silica spheres [80]. They separated the seed step from the growth process. In the first one, they used as co-solvents cyclohexane and water, and L-arginine as template agent and soft base catalyser. The first growth step is based on diluting the seeds and adding the same compounds to the dilution. The second growth step was based on Stöber method. They reported the obtaining of nanoparticles ranging 15 to 200 nm. TEM images showed monodispersed and arranged nanoparticles, and no fusions between them were visible. Nevertheless, they did not reported information about the nanoparticles mesoporosity and surface area, nor the colloidal stability.

Yokoi and his co-workers reported some studies about the obtaining of colloidal MSN employing lysine as template and soft base catalyser [52][81]. The nanoparticles were obtained in the range of 10 to 50 nm. Nevertheless, TEM images were not clear enough to distinguish if the nanoparticles were not aggregated. Furthermore, the authors did not perform any assay to confirm the colloidal stability. In addition, the surface area obtained was very low (ca. 230 $m^2 g^{-1}$).

#### 5.2.2.5. Other approaches

Yu et al. reported the synthesis of uniform, spherical shape, monodisperse and non-aggregated MSN by using a sodium acetate solution like a weak base [49]. They obtained MSN in the range of 50 to 110 nm, adjusting the size using different temperatures. They performed a post-synthesis thermal treatment in acidic or basic conditions to increase the surface area and pore volume. TEM images showed non-aggregated nanoparticles and DLS measurements indicated a narrow size dispersion and stable solution. Nevertheless, DLS measurements gave smaller

diameter values than those calculated from TEM images, which is controversial. This result suggests the inconsistence of DLS results being that hydrodynamic diameter must be a bit larger than nanoparticle diameter. Besides, DLS assays were carried out in ethanol solutions, which is not representative of the colloidal behaviour in aqueous or physiological conditions. On the other hand, the surface area and pore volume obtained were very low, with values around 200 $m^2 g^{-1}$ and 0.2 $cm^3 g^{-1}$ respectively, which were increased to ca. 500 $m^2 g^{-1}$ and 0.5 $cm^3 g^{-1}$ after thermal treatment. However, it seems that thermal treatment was associated with the appearance of fusion between some nanoparticles.

### 5.2.3. Conclusions and outlook

In general, to the best of our knowledge it can be concluded that regardless of the method employed to synthesise the nanoparticles, they have a constant propensity to fuse, agglomerate, or sediment, at least in physiological conditions. In addition, there seems to be a compromise between obtaining colloidal nanoparticles and, on the one hand, achieving sizes in the nanoscale, that is, below 200-300 nm; and, on the other hand, maintaining the appropriate mesoporosity, such as high surface area and high pore volume. However, it must be mentioned the step forward developed by the Kleitz and Fortin group, who have achieved the production and characterisation of quite reproducible MSN with high stability and colloidal behaviour, even in quasi-physiological conditions.

## 5.3. MATERIALS AND METHODS

### 5.3.1. Chemicals

Tetraethylorthosilicate (TEOS), 1-hexadecyltrimethylammonium bromide (CTAB), sodium hydroxide (NaOH), 3-mercaptopropyltrimetoxysilane (MPTMS), (3-aminopropyl)triethoxysilane (APTES), (3-isocyanatopropyl)triethoxysilane (IPTES), 2,2'-Dipyridyl disulphide, methoxypolyethylene glycol thiol average Mn 800 (SH-PEG), methoxypolyethylene glycol amine average Mn 750 ($NH_2$-PEG), triethylamine (TEA), Dulbecco's Modified Eagle Medium (DMEM), Fetal Bovine Serum (FBS) and Dulbecco's Phosphate Buffered Saline (PBS) were purchased from Sigma-Aldrich. Hydrochloric acid 37% (HCl), dichloromethane (DCM) and acetonitrile (ACN) were provided by Scharlab. Succinic anhydride, 1-(3-Dimethylaminopropyl)-3-ethylcarbodiimide hydrochloride (EDC) and N-hydroxysuccinimide (NHS) were purchased from Thermo Fisher Scientific.

### 5.3.2. General techniques

Transmission electron microscopy (TEM), $N_2$ adsorption–desorption isotherms, powder X-ray diffraction (PXRD), dynamic light scattering (DLS), nanoparticle tracking analysis (NTA) and UV-Visible spectrophotometry were used in order to characterise the prepared materials. The instruments used were the following: JEOL JEM-1010 microscope for TEM images acquisitions; Bruker D8 Advance diffractometer (Cu Kα radiation) for PXRD measurements; Micromeritics ASAP 2010 automated analyser for recording of $N_2$ adsorption–desorption isotherms, samples were degassed at 120 °C in a vacuum overnight. The specific surface areas were calculated from the adsorption data within the low-pressure range using the BET (Brunauer–Emmett–Teller) model. Pore size was determined following the BJH (Barrett–Joyner–Halenda) method. Particle size and ʒ potential in solution were measured by ZetaSizer Nano ZS (Malvern Instruments Ltd.) equipped with a laser of 633 nm and collecting the signal at 173°. The NTA were performed in Nanosight NS300 (Malvern Instruments Ltd.). UV-Visible measurements were recorded with a JASCO V-650 Spectrophotometer.

### 5.3.3. Synthesis of nanoparticles

Different conditions were used to synthesise MCM-41-type nanoparticles. A standard protocol was stablished. 1 g of CTAB (2.74 mmol) was mixed with 480 mL of deionised water in a 1L (10.5 cm of outer diameter) cylindrical beaker. The mixture was heated at 50 °C to dissolve the surfactant and stirred with a cylindrical and plain magnetic stir bar (60mm long and 15mm diameter) at 500 rpm. Then, 280 mg of NaOH (7 mmol) dissolved in 3.5 mL of deionised water were added, and the solution temperature was adjusted to 80 °C. A watch glass was placed to cover the beaker to minimise the solvent evaporation and therefore to avoid the volume from decreasing during the reaction. When the temperature reached (80 °C), 5 mL of TEOS (25.7 mmol) were added dropwise (5 ml $min^{-1}$), using syringe and needle. Soon after, a white precipitate appeared. The mixture was stirred for 2 h. After this time, the suspension was cooled at room temperature, and the solid product was vacuum filtered on Buchner on a filter paper (Whatman™ Grade 3MM Chr, pore size of 6 µm) and deionised water was added until neutralise the suspension. Then, the solid was dried under vacuum and grinded to obtain a white powder.

After the synthesis, nanoparticles were calcined at 550 °C using an oxidant atmosphere for 5 h in order to remove the surfactant.

Some parameters were tuned one by one, such as the stirring rate (350 rpm, 500 rpm, 900 rpm and 1200 rpm), the magnetic stir bar morphology (plain or with pivots and ring), the reaction time (5 min, 20 min, 1 hour, 2 hours or 4 hours), the TEOS addition rate (0.25, 1 or 5 ml $min^{-1}$ or instant addition) or the neutralisation step (neutralisation with water or with HCl 0.1M before the filtration of solid product).

### 5.3.4. Functionalisation of nanoparticles

Nanoparticles were functionalised with MPTMS, APTES and IPTES, posteriorly PEGylated. Briefly, 150 mg of standard calcined samples were suspended in 15 mL of ACN and they were generously sonicated. They were divided in three vials, adding 5 mL to each one (50 mg of nanoparticles). 47 µL of MPTMS were added to the first suspension, 53 µL of APTES were added to the second suspension and 59 µL of IPTES were added to the third one. The suspensions were stirred for 5.5 hours at room temperature. After that, the solids were centrifuged and washed three times with ACN and dried under vacuum. Then, **MSN-SH**, **MSN-$NH_2$** and **MSN-NCO** were obtained respectively.

In order to PEGylate each solid, the next steps were followed.

30 mg of **MSN-SH** were suspended in 3 mL of ACN and sonicated generously. 66 mg of 2,2'-dipyridyl disulphide were added to the suspension and the mixture was stirred overnight at room temperature. The suspension became yellowish some minutes after the addition of the disulphide. Next day, the yellowish solid was centrifuged and washed with ACN several times until obtaining an uncoloured solid and then, it was dried under vacuum. 25 mg of resulting solid were suspended in 3mL of ACN and sonicated generously. 60 mg of SH-PEG were added to the suspension and the mixture was stirred overnight at room temperature. After that, the solid was centrifuged and washed with ACN five times and dried under vacuum. The solid obtained was called **MSN-SH-PEG**.

30 mg of **MSN-$NH_2$** were suspended in 3 mL of DCM and sonicated briefly. 15 mg of succinic anhydride and 15 µL of TEA were added to the mixture and the mixture was stirred overnight. After that, the solid was centrifuged and washed twice with DCM and twice with ACN and dried under vacuum. 15 mg of the resultant solid (MSN-COOH) were suspended in 3 mL of MES Buffer (1M at pH 6) and sonicated generously. 10 mg of EDC and 10 mg of NHS were added to the suspension. The mixture was stirred 30 minutes and then, the solid was centrifuged and washed three times with PBS. The activated solid was suspended in 3 mL of PBS and briefly sonicated. 30 mg of $NH_2$-PEG were added to the suspension and stirred overnight at room temperature. Then, the solid was centrifuged and washed five times with distilled water and dried under vacuum.

30 mg of **MSN-NCO** were suspended in 3 mL of ACN and sonicated generously. 60 mg of $NH_2$-PEG and 11.15 µL of TEA (1 eq.) were added to the suspension. The mixture was stirred overnight at room temperature. After that, the solid was centrifuged and washed five times with ACN and dried under vacuum. The solid obtained was called **MSN-NCO-PEG**.

### 5.3.5. Spin pulses

The centrifuge employed had a radius of 6.026 cm. The equation 5 can be used to convert rpm with a known radius *r* to relative centrifugal force (rcf).

$$rcf = 1.118 \cdot 10^{-5} \cdot r \cdot rpm^2 \quad (5)$$

## 5.4. METHODOLOGY OF CHARACTERISATION OF COLLOIDAL PROPERTIES IN MSN SUSPENSIONS

Before addressing the obtaining of discrete and colloidal MSN, an evaluation and characterisation methodology must be developed in this field. Hence, several methods were studied, tested, and developed in order to study the colloidal stability of the evaluated nanoparticles. These methods are described down below.

### 5.4.1. Colloidal appearance

The appearance of a concentrated colloidal suspension formed by MSN has a homogeneous and milky appearance, that is, no sediments or flocs should be observed in it. Therefore, the observation at a naked eye of particles or specks in a suspension is illustrative of the presence of large aggregates, being that the entities in the nanoparticle range cannot be distinguished. In this context, the milky and homogeneous appearance must be sustained over time in an MSN suspension to be considered as a stable colloid.

Considering this, some suspensions were observed and analysed. Similar observations were reported in other studies [29][82][83][84], although they were not focused on the detection of small specks in the suspension. Some examples are showed in Figure 4. In Fig. 4A the different aliquots obtained in Chapter 3 called DA were showed. It can be observed that samples **DA2**, **DA3** and **DA4** (Fig. 4A, c,d,e) showed a colloidal appearance, namely milky and homogeneous. Nevertheless, **DA5** (Fig. 4A, f) showed the formation of flocs, the most likely cause being the aggregation between the nanoparticles. In Figure 4B, it is captured the evolution of just synthesised **MSN-250rpm**, which were described in Chapter 4. The suspension obtained just after the synthesis of **MSN-250rpm** presented colloidal appearance (Fig. 4B a), but with time it began to flocculate and sediment (Fig 4B, b,c). In Figure 4C two suspensions of MSN were compared. Fig. 4C.a corresponds to a suspension of **MSN-$NH_2$-PEG** at 5 mg/ml after being generously sonicated and briefly spun to remove the presence of aggregates. It can be observed that the suspension does not show any speck or particle and is completely homogeneous, confirming its colloidal appearance. Fig. 4C.b represents the suspension of bare standard MSN at 5 mg/ml prepared following the same procedure. In this second sample, the presence of aggregates which exceed the nanoscale is fairly visible. When the light pathway inside the suspension is large, the high turbidity does not allow correctly seeing the suspended objects. However, by decreasing the light pathway (see inset in Figure 4C) the aggregates can be discovered. Additionally, shaking this kind of suspension can facilitate the observation of the aggregates.

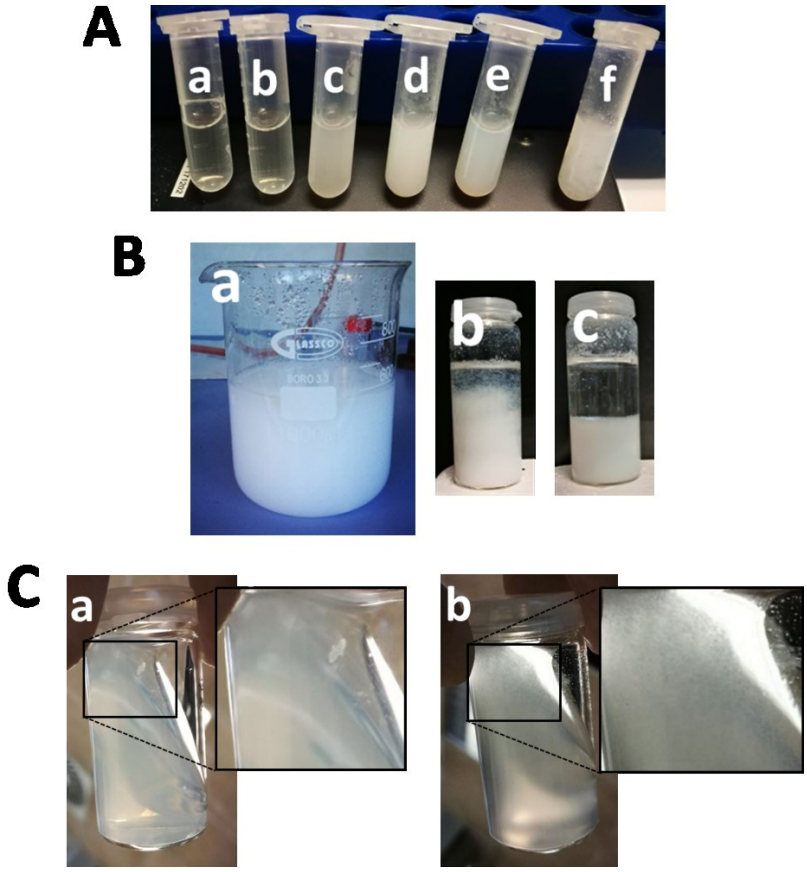


*Figure 421. Colloidal appearance of different MSN samples. A) Photograph of (a) **A0** and (b-f) **DA** (1-5) samples from Chapter 3. B) Photograph of **MSN-250rpm** sample (a) just synthesised, (b) after 2 hours and (c) after 4 hours. C) Photograph of (a) sonicated and spun **MSN-$NH_2$-PEG** preparation and (b) sonicated and spun bare **MSN** preparation.*

### 5.4.2. Decantation and fraction weighing

Continuing with a similar reasoning to previous section, a step forward was quantifying the percentage of nanoparticles that remained suspended and the percentage which sedimented over time, when a suspension was left settling down. For this purpose, the pellet resulting from the decantation process was collect and weighed after being dried.

Thus, the method was implemented with a standard sample of MCM-41-type MSN suspended in distilled $H_2O$ (5 mg/mL) and sonicated during 1 hour prior to the assays. The suspensions were left to stand, and the supernatants were collected at different times (1, 5, 12, 24, 48 and 72 hours). The pellets left in the vials were dried in an oven at 70 degrees and weighed.

The results are represented in Figure 5. It can be observed a sharp decrease in the percentage of nanoparticles suspended (from 100% to 35%) at the first minutes and hours (up to 5 hours), which posteriorly (from 5 hours to 72 hours) are stabilised at ca. 30%. Therefore, it can be suggested that the decantation process is faster at first stages, where larger aggregates of nanoparticles, which behaves as non-Brownian entities, sediment quickly due to the predominance of gravity on them. After the sedimentation of these large entities, which seem to correspond to the 70% in weight of the MSN suspension, the nanoparticles that remain

suspended are stabilised and the sedimentation rate considerably decrease. It can be suggested that the suspension remaining is stable for a couple of days.

With regard to this method employed to measure the colloidal stability, it has to be signalled that a considerable variability was observed between the different assays, which was in the order of a 20% of relative deviation.

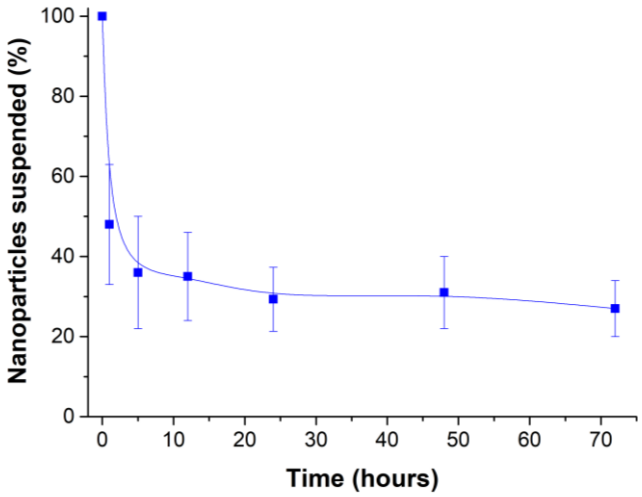


*Figure 5. Decantation and fraction weighing of standard MSN sample (5 mg/ml in distilled water, sonicated 1 hour). The percentage of nanoparticles is measured by weighting the pellet decanted.*

In summary, the main limitation of this method is the considerable experimental mistake related with the difficult separation between the decanted and suspended MSN. Namely, when the suspended nanoparticles are collected, it is possible to also take a decanted portion of nanoparticles and collect them. In addition, in order to minimise the error in the weight of pellets, the technic requires the use of relatively high amounts of MSN (15 mg per vial). Finally, to obtain useful results, the time required to decant the samples and dry the pellets is usually over one day. Therefore, it is not and immediate technic to determine the stability of the colloid.

### 5.4.3. Dynamic light scattering

Dynamic light scattering is a standard technic to characterise MSN, resulting in the hydrodynamic diameter of the nanoparticles. Nevertheless, a common sample of bare MSN is usually integrated by large aggregations of nanoparticles that tend to sediment both in water and in other aqueous solutions such as PBS. The presence of these big aggregates and sediments precludes to obtain good quality measurements, since these large entities do not follow the Brownian motion and, therefore, disturb the acquisition of correlated speckling patterns of dispersed light.

Given that context and according to our observations and the procedures applied in some studies [65][85], it is considered that decanting (overnight, 24 hours or 48 hours) or briefly spinning the samples in a centrifuge are possible methods to remove the large aggregates and sediments. Needless to say that the aliquot collected from the suspended fraction will not correspond to the entire sample, but it will at least facilitate to measure the hydrodynamic

diameter of the basic and single entities, that is, the hydrodynamic diameter of the individual nanoparticles. Therefore, these measurements should be closer to the size obtained by measuring the nanoparticles using TEM images.

Both methods to prepare the samples were used (decantation and centrifugation), but it is considered that pulse centrifugation had advantages over decantation, being that it allowed controlling and tuning the strength applied to the samples, which made more reproducible and comparable assays. In addition, this methodology is faster, in contrast to decantation, which takes at least one day.

In order to check the procedure, DLS measurements were performed from a standard sample of MCM-41-type MSN at 1 mg/ml, previously sonicated, subjected to spin pulses of increasing strength (at 0 rpm, 2500 rpm, 5000 rpm, 7500 rpm, 10000 rpm, 12000 rpm and 13500 rpm) (Figure 6). When the sample were not spun or spun at 2500 rpm it contained large sediments and the DLS measurements did not meet good quality criteria. The sample spun at 5000 rpm showed three peaks centred at 135 nm, 850 nm, and 5300 nm. The rest of the samples presented only two populations. The main population was found at 180 nm, 167 nm, 180 nm, and 158 nm when the sample was spun at 7500 rpm, 10000 rpm, 12000 rpm and 13500 rpm, respectively. In all these samples a secondary peak corresponding to large particles, from 3000 to 6000 nm (centred at 3500 nm), was obtained, but it always represented a small proportion in comparison to the main peak.

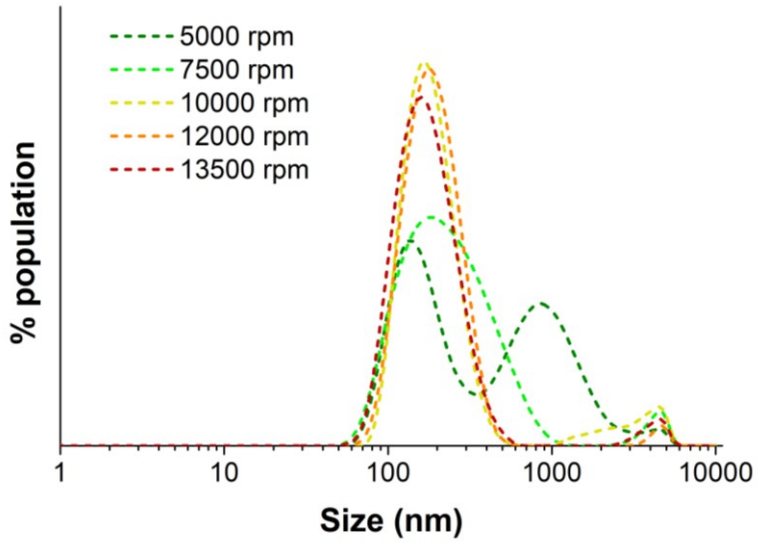


*Figure 6. Size distribution of standard MSN sample (1 mg/ml in distilled water and sonicated 1 hour) according to Intensity PSD analysis, when it is subjected to increasing spin pulses (5000 rpm, 7500 rpm, 10000 rpm, 12000 rpm and 13500 rpm). Non-spun and sample spun at 2500 rpm did not meet good quality criteria due to the presence of large aggregates.*

The tendency observed was that the populations corresponding to large aggregates were decreasing in the sample as the strength of the spin pulse increases, as expected. The main peak observed in all the samples, which was centred at ca. 180 nm, corresponded to the populations with the smallest sizes. This peak was defining and narrowing with the increase of spin pulses strength. In this sense, the main peak of the sample spun at 7500 rpm showed a size distribution

from 60 nm to 1000 nm, but when the samples were spun at 10000 rpm, 12000 rpm and 13500 rpm, the distribution was in the range of approximately 60 to 500 nm.

On the other hand, the expected size for individual nanoparticles in DLS measurements must be some larger (few tens of nanometres) than the value of the size for single MSN measured in the TEM images (from 50 to 130 nm), considering DLS measures the hydrodynamic diameter. Nevertheless, it cannot explain the main peak includes populations up to 600 nm. Accordingly, it is undeniable that the main population also contained dimers, trimers, and other oligomers. In this sense, it can be said that these small and aggregated entities had a colloidal behaviour similar to that of the individual nanoparticles under the conditions studied since they remain suspended once high spin pulses were applied.

Furthermore, it is observable that the peak maximum of the main population had moderated variations from one sample to the other (± 45 nm). Then, it is hypothesised that depending on the strength of pulse spins the presence of small oligomers changes and the peak maximum is shifted. It can be also explained considering the measurement of a polydispersed sample, in which small and large aggregates are present, moderately disturbs the speckle pattern and therewith the mathematical calculations involved in the analysis. Therefore, the preparation of the MSN samples to be measured in DLS is quite important in order to obtain precise results.

Finally, it must be remarked that although larger populations were observed in the DLS curves regardless the strength of the spin pulse, their real proportion in the samples were quite small. The size distribution was analysed by Intensity PSD, which is a more reliable approach, but it overestimates the larger size populations. Considering the Rayleigh approximation equation (eq. 1), which relate the number of particles of a specific size and the intensity of light scattered, the larger size populations, those observed above 3000 nm in Figure 6, could be neglected.

### 5.4.4. UV light attenuation

DLS measurements presents some advantages in the characterisation of the colloidal behaviour, such as the determination of the existent populations and the dispersion of their sizes, as well as the high sensitivity to the presence of aggregates and sedimentation. Nevertheless, the DLS technique is not the most suitable to quantify the concentration of the samples and each of their populations.

Therefore, another method has been used to quantify the amount of MSN suspended in a sample according to the light scattered by the sample, measured with the UV spectrophotometer. Previously, Khlebtsov et al. reported the quantification of silica nanoparticles on spectrophotometer by using the technique called spectroturbidimetry (STT) [86]. As Khlebtsov and He [13] propose, the scattering cross section, which is the intrinsic parameter of turbidity for a determined particle, is related to the size and shape of the scattering bodies. Then, turbidity is proportional through the scattering cross section to the concentration of nanoparticles. In addition, larger particles disperse higher amounts of light, just as it is expressed in the Rayleigh equation showed previously. Furthermore, the scattering cross section is also dependent on the wavelength used. Other authors also used the UV-Visible absorption to quantify the amount of MSN in a suspension [87][88].

In our case, the characterization of the colloidal properties of the samples was carried out by measuring the attenuation that can be described as the loss of light between the light source and the detector due to both scattering and absorption. For bare MSN samples, this attenuation can be attributed just to the light dispersion as the absorption phenomenon can be neglected in the range studied (300-800 nm) [89][90][91]. Hence, a 5 mg/ml MSN suspension in distilled water was prepared and generously sonicated (1 hour) and its attenuation from 300 to 800 nm was studied at different spin pulses. The clear dependence of the attenuation spectrum with the nanoparticles size and the wavelength used was observed (Figure 7). The spectra analysed were normalised regarding their maximum at 300 nm. The spectra measurements showed that the non-spun sample attenuated the light approximately a 60% at 800 nm as compared to the attenuation at 300 nm. In contrast, when the sample was briefly spun, the difference between the attenuation at 300 nm and that at higher wavelengths was much wider. As the strength of the spin pulse applied increased, the attenuation at 800 nm decay to ca. 25% when the sample was spun at 2500 rpm, ca. 15% in case of spinning at 5000 rpm and in the range of 9 to 13% at 7500, 1000 and 12500 rpm.

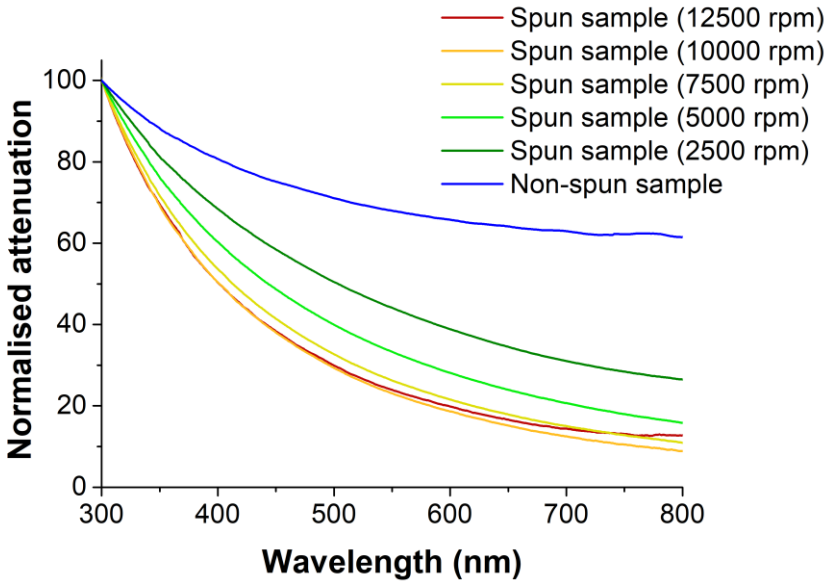


*Figure 7. UV light attenuation spectra behaviour of standard MSN sample (5 mg/ml, in distilled water, sonicated 1 hour) when it is subjected to increasing spin pulses. The attenuation is normalised form the value at 300 nm in each sample.*

Therefore, the standard and non-spun sample, which consists of a mixture of large and small aggregates, oligomers, and individual nanoparticles according to DLS results (Figure 6), showed large relative attenuation at higher wavelengths. In this sense, the presence of some particles above 500 nm increases sharply the relative light attenuation at wavelengths above 300 nm [13][92], and therewith, an spectrum with a lower decay was observed. On the other hand, the spun samples, in which the percentage of oligomers and individual nanoparticles is progressively predominating over the larger aggregates as the strength of the spin pulse increases, present a steep decay in the attenuation at higher wavelengths. Besides, the decay is steeper with the increasing strength of the spin pulse, indicating the reduction of aggregated populations.

Taking into account these reasoning, according to the attenuation spectra and DLS results (Fig. 6 and Fig. 7), when the sample is non-spun, spun at 2500 rpm or 5000 rpm, the presence of large

aggregates (over 500 nm) is still quite significant. Nevertheless, from 7500 rpm this presence is highly reduced, finding nanoparticles mainly up to 500 nm.

Despite the dependence of the attenuation on the presence of populations of nanoparticles of different sizes, in terms of simplify the calculations some approximations were applied in the performed UV light attenuation assays. It was considered that the scattering cross section in MSN suspensions was constant at 800 nm regardless the presence of aggregates, and then the attenuation only depends on the concentration of the suspended nanoparticles. Hence, some sub-estimation in the concentration calculation of spun samples could occur. In this context, it was quantified the amount of suspended MSN when different pulse spins where applied, by measuring the attenuation at 800nm (Figure 8). A similar method was developed by Paula and co-workers [6], where they evaluated the colloidal stability by quantify the MSN suspended regarding the measured light absorption after centrifuge the samples at different centrifugal forces. Figure 8 showed how the percentage of suspended nanoparticles, from the total amount of nanoparticles prepared, decreased with the increasing pulse spin strength. Then, at 1200 rpm, the suspended nanoparticles represented around the 56% of total sample, and decrease to the 37%, 21%, 12%, 9% and 7% when it was applied 2500 rpm, 5000 rpm, 7500 rpm, 10000 rpm and 12500 rpm, respectively. The decay can be fitted to an exponential equation.

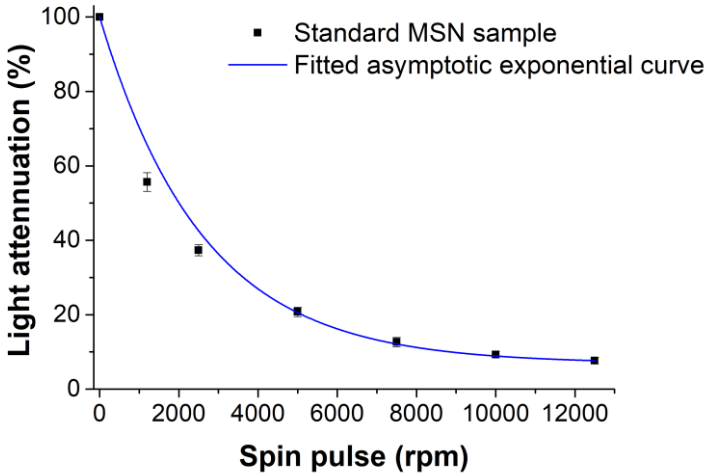


*Figure 8. UV light attenuation at 800 nm of standard MSN sample (5 mg/ml, in distilled water, sonicated 1 hour) when it is subjected to increasing spin pulses. The percentage of suspended nanoparticles against the spin pulse strength was fitted to an asymptotic exponential decay.*

In this sense, it was established a rapid and simple method to quantify the number of suspended nanoparticles, by means of their light attenuation, in a sample that is exposed to different conditions in comparison to the original sample. The variability of results between the assays performed was quite small, considering the methodology got considerable reproducibility, especially if it is compared with the decantation and weighting process. Moreover, the procedure was quite rapid, obtaining the results after some minutes.

### 5.4.5. Nanoparticles tracking analysis

Like DLS, nanoparticle tracking analysis (NTA) is a technique highly sensitive to each population found in the sample, including the presence of some aggregates, and therefore, it can be used to study the colloidal stability of the MSN samples. In spite to that, it has to be noted that the analysis software usually removes from the analysis the signals coming from larger populations and artefacts through several thresholds [93]. In the case of MSN analysis, the particles above 500 nm are usually removed, and then, some of the information on the presence of aggregates is lost. Bearing in mind this, different MSN samples were prepared to be analysed in NTA (Figure 9). The nanoparticles used were **MSN-SH-PEG**, in order to minimise a priori predominant populations of large aggregates.

First, the distilled water in the laboratory was measured as a control sample (Fig. 9a). Some particles were detected in this sample in the range from 50 to 500 nm, indicating the presence of artefacts like dust or other contaminants, although their concentration was low ($1.04 \cdot 10^7$ particles/ml). Then, several samples of untreated **MSN-SH-PEG** were measured, in which no centrifugation, decantation or filtration was applied. The optimal concentration found to analyse by NTA this type of sample was 10 µg/ml, and the representative tendency can be seen in Fig. 9b. The size dispersion graph shows different populations ranging from 50 to 400 nm, although most of them were located up to 250 nm. Several maximums and peaks were observed from 100 to 200 nm. Then, Figure 9c and Figure 9d show the NTA analysis of a sample containing 1 mg/ml of **MSN-SH-PEG** that has been filtered using 0.45 and 0.22 µm pore size filters, respectively. In these cases, it can be observed that when the samples were filtered, the size distribution of nanoparticles measured became narrower and a single predominant population centred at ca. 145 nm can be identified. In the case of the filtration with 0.45 µm pore size filter, the number of nanoparticles which cross the filter are higher ($1.20 \cdot 10^9$ particles/ml) and then the noise due to artefacts is reduced. In contrast, when the sample is filtered using a pore of 0.22 µm, the population able to cross the filter is an order of magnitude lower ($1.28 \cdot 10^8$ particles/ml). As a result of that, the peak corresponding to the main population is less defined and some noise is observed. Finally, another 1 mg/ml sample of **MSN-SH-PEG** was decanted for 24 hours. After that, the resulting supernatant was diluted 100, 40 and 10 times and measured in NTA, and the results are shown in Fig. 9e, Fig. 9f and Fig. 9g, respectively. These samples showed a size distribution ranging from 50 to 400 nm, but a predominant population is clearly visible at ca. 145 nm. In addition, as seen in Figure 9c and 9d, the measurement of more concentrated samples showed less noise and better definition of the main population peak.

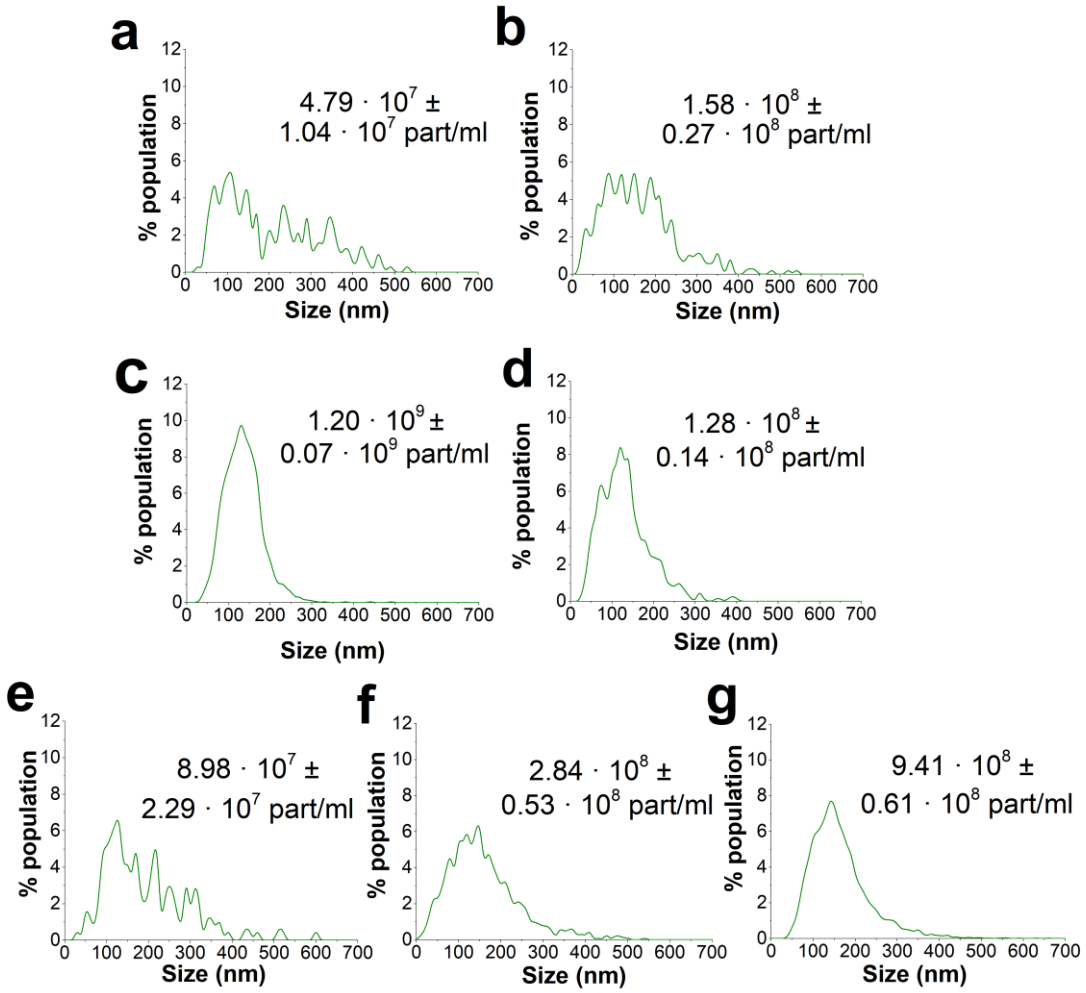


*Figure 9. NTA measurements of (a) distilled water, (b) untreated **MSN-SH-PEG** at 10 µg/ml, (c) filtered **MSN-SH-PEG** using 0.45 µm pore size, (d) filtered **MSN-SH-PEG** using 0.22 µm pore size, and decanted **MSN-SH-PEG** and diluted (e) 100, (f) 40, and (g) 10 times.*

Additionally, some frames of the videos recorded during the NTA are shown in Figure 10. The images were taken in a 3-d chamber, and then, the sizes of nanoparticles are different, depending on their position in z-axis. In the control sample (distilled water) (Fig. 10a) some particles corresponding to artefacts can be observed. In the case of the untreated sample large flashes of light can be observed corresponding to the presence of aggregates (Fig. 10b). Finally, the samples corresponding to filtered (Fig. 10c) and decanted preparations (Fig. 10d) showed the presence of mostly single nanoparticles.

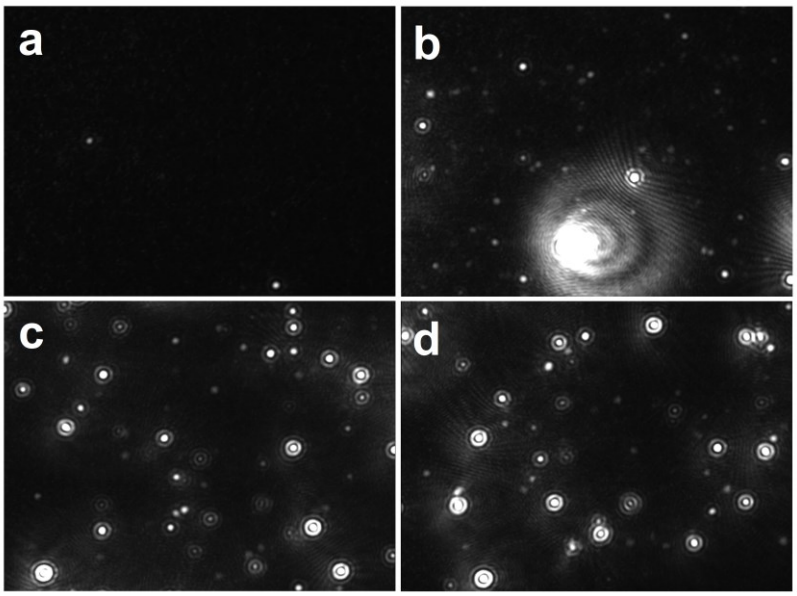


*Figure 10. NTA video frames of (a) distilled water, (b) untreated sample, (c) sample filtered at 0.45 µm, and (d) sample decanted and diluted 10 times.*

According to the results obtained in NTA, a hydrodynamic size of ca. 145 nm was precisely and repeatedly obtained for **MSN-SH-PEG** sample. Nevertheless, the technique showed some limitations. On the one hand, the range of concentration in which it worked was quite narrow, and highly diluted samples had to be prepared. On the other hand, the sensitivity of the technique towards small aggregates and artefacts required the use of filtration or decantation to obtain narrow dispersions that showed a clear value corresponding to the individual nanoparticles.

### 5.4.6. Conclusions and outlook

After reviewing the methods that can be used to determine the colloidal stability of nanoparticles suspensions some remarks can be done. First, the UV light attenuation is a quantitative method in contrast to DLS and colloidal appearance. Additionally, UV light attenuation has not restrictions in terms of the amount MSN needed to perform the measurements. In case of decantation and fraction weighing method, the samples should start from high amounts of nanoparticles in order to minimise the error when the pellet is weighted. For NTA, the concentration range in which the technique works is too limiting, and many artefacts can be detected at low concentrations, as it also happens in DLS measurements. Finally, UV light attenuation it is a simple, rapid, and cost-effective method, which does not require specialised personnel. Consequently, the UV light attenuation technique is method chosen in combination with the application of increasing spin pulses to determine the colloidal stability of our MSN samples, although other complementary assays and methods will be also performed.

## 5.5. RESULTS AND DISCUSSION

### 5.5.1. Transition from colloidal to agglomerated samples

In both Fig. 4A and Fig. 4B in the colloidal appearance section, it is possible to see a transition from colloidal to agglomerated MSN suspension. This transition was also observed in previous chapters, in both aliquots and parameters tuning assays, which was produced from some minutes to few hours after the MSN synthesis.

These changes in the colloidal properties of MSN were also studied by DLS measurements, observing the correlation function and Intensity PSD analysis. A standard synthesised sample of MSN was measured both directly from the reaction just after being synthesised (**MSN-direct**) and then after being filtered and dried (**MSN-dried**). No spin pulses were applied in order to measure the whole sample and detect the presence of aggregates. The correlation function and Intensity PSD analysis are shown in Figure 11. It can be observed that the correlation function of **MSN-direct** is mono-modal and presents a clear and smooth exponential decay (Fig. 11A, top). Therefore, the correlogram can be fitted precisely according to cumulant and distribution analysis. In this case, the Intensity PSD curve shows a single peak with a narrow distribution, which is centred at 123.3 nm and presents a PDI value of 0.062 (Fig. 11A, bottom). In contrast, the **MSN-dried** shows a floundering decay (Fig. 11B, top), which cannot be properly fitted in terms of performing either cumulant or distribution analysis. The result is the obtaining of an unreliable Intensity PSD curve, which shows two main populations around 50 nm and 190 nm (Fig. 11B, bottom). Both measurements are representative of the data normally obtained.

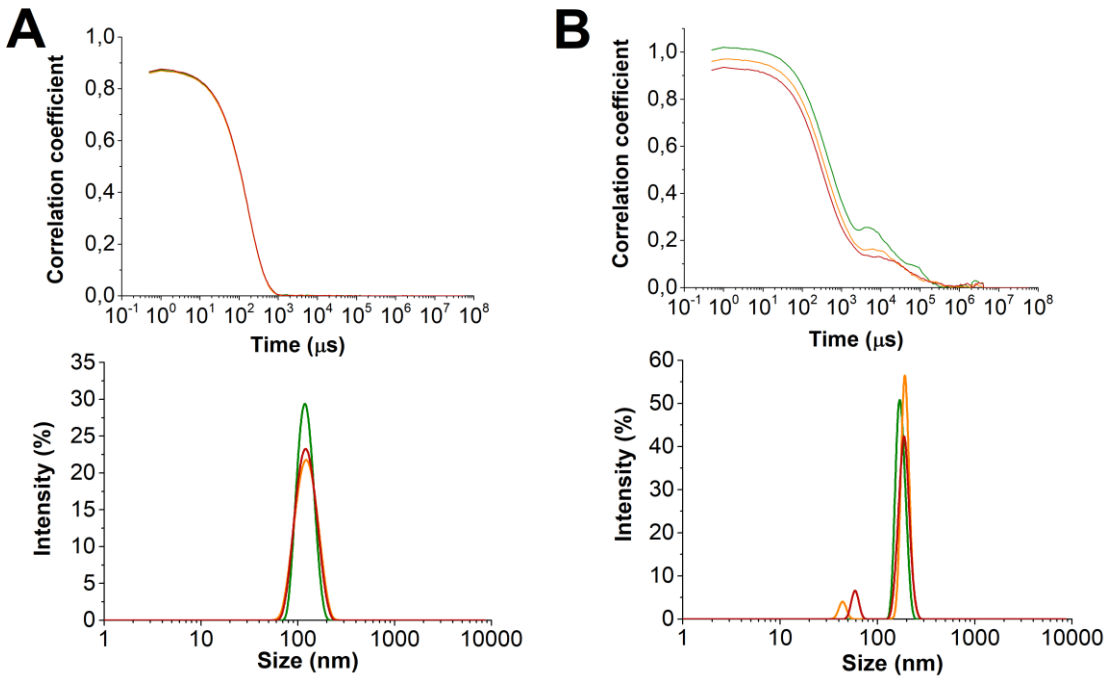


*Figure 11. DLS data of **MSN-direct** (A) and **MSN-dried** (B). Correlation function (top) and size distribution according to Intensity PSD analysis (bottom) were shown.*

The drying of MSN has been reported to be involved in the aggregation of the sample [20][51][57][94] [95]. It has been described that this can occur either by the large surface tension and capillarity of the aqueous solutions [15], the formation of Si–O–Si bonds [2], the collapse of

silica-surfactant structures and silica rearrangement [96][97][98], or the attractive forces due to the proximity of nanoparticles [99] during the drying process.

Furthermore, it has been suggested that the transition from colloidal to agglomerated MSN is partially irreversible, since a colloidal suspension of MSN can only be obtained later by sonicating and then decanting, filtering or spinning the MSN suspension, in order to remove the large amount of aggregates.

### 5.5.2. Tuning synthesis parameters and their influence on colloidal stability

The effect of tuning different parameters on MCM41-type MSN synthesis has been also studied regarding the colloidal stability. In this context, the nanoparticles used were those synthesised in the Chapter 4, in accordance with the reaction time, stirring rate or magnetic stir bar used, TEOS addition rate or neutralisation step. The behaviour of different MSN suspensions when they are spun at increasing spin pulses are shown in Figure 12. All the samples follow the tendency of an exponential asymptotic curve when the percentage of light attenuation are represented as a function of spin pulse strength. The percentage of light attenuation can be considered as the percentage of suspended nanoparticles after the spin pulse, and then, describes their colloidal stability, as it was proposed in the previous section (3.4.).

According to the reaction time (Fig. 12A), **MSN-2hours** sample, which corresponds to the standard synthesis, presents the best colloidal stability throughout the different spin pulses. In case of **MSN-5min**, **MSN-20min, MSN-1hour** and **MSN-4hours** the percentage of nanoparticles suspended after the spin pulses are worsened. Nevertheless, the differences between them reach a 10% at most. On the other hand, in relation with the variation of the stirring rate and magnetic stir bar (Fig. 12B), the better stability is registered for lower stirring rates (**MSN-350rpm** and **MSN-500rpm**), but the differences with the rest of samples (**MSN-900rpm** and **MSN-1200rpm**) do not reach the 10%. Regarding the sample **MSN-rough**, it showed worse stability than **MSN-500rpm**, in spite of using the same stirring rate in both samples, but the differences are minor too. On the other hand, what regards to the TEOS addition rate (Fig. 12C), the results show that the nanoparticles present more sedimentation or decantation when the TEOS is added quicker (**MSN-5** and **MSN-quick**), and then, **MSN-0.25** and **MSN-1** are more stable. Finally, concerning the neutralisation step (Fig. 12D), larger differences can be observed when comparing the **MSN-HCl** sample with the standard one (**MSN-$H_2O$**). The **MSN-HCl** sample reaches a stability improvement of ca. 15% at low and intermediate spin pulses and over a 5% at high pulses.

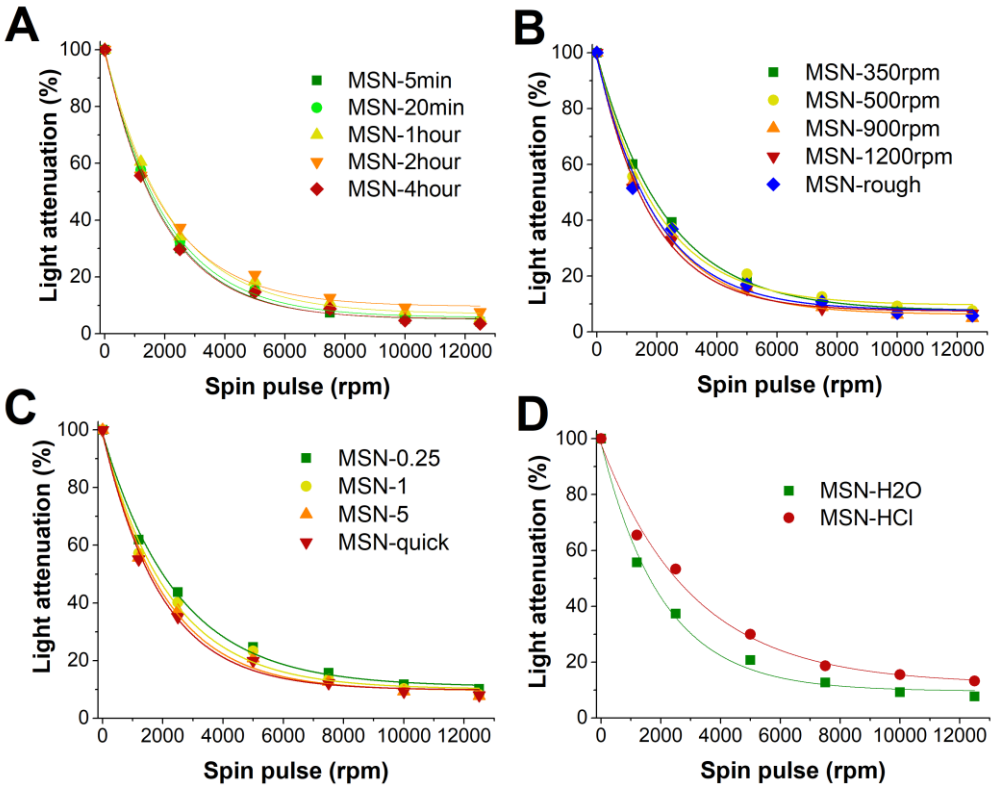


*Figure 12. UV light attenuation at 800 nm of different MSN samples synthesised in Chapter 4 when they are subjected to increasing spin pulses. They were prepared at 5 mg/ml, in distilled water and sonicated for 1 hour. A) Samples as a function of the reaction time (**MSN-5min**, **MSN-20min**, **MSN-1hour**, **MSN-2hours** and **MSN-4hours**). B) Samples as a function of the stirring method (**MSN-350rpm**, **MSN-500rpm**, **MSN-900rpm**, **MSN-1200rpm** and **MSN-rough**). C) Samples as a function of the TEOS addition rate (**MSN-0.25**, **MSN-1**, **MSN-5** and **MSN-quick**). D) Samples as a function of the neutralisation step (**MSN-HCl** and **MSN-$H_2O$**). The percentage of suspended nanoparticles against the spin pulse strength was fitted to an asymptotic exponential decay.*

It should be noted that the differences observed in the colloidal stability of MSN suspensions in compared to the one obtained at standard conditions were not very large for the parameters studied: reaction time, stirring rate and TEOS addition rate. The difference observed is as high as a 10% at low and intermediate spin pulses, but around the 5% or less at high spin pulses, where the percentage of suspended nanoparticles tended to be similar. These values are slightly increased in case of the neutralisation with HCl, which led to differences up to 15% and over 5% respectively. In this sense, it should be remarked that the conditions used in the study (high nanoparticles concentration, bare MSN, distilled water as dispersant fluid) can be very restrictive in terms of colloidal stability and this fact can reduce the differences that can be observed.

However, a clear trend can be determined in each assay with respect to colloidal stability and parameters fit. Firstly, it can be affirmed that stirring during 2 hours are the optimal reaction time in the MCM-41-type MSN synthesis, since shorter or longer times lead to worse stability, such as it was described by Catalano et al. [100] and firstly reported by Cai et al. [23]. Secondly, the use of high stirring rates leads to less stable samples, such as it was expected according to TEM observations in Chapter 4. Thus, the optimal stirring rate can be adjusted between 350 and 500 rpm. Besides, the presence of burs and pivot in the magnetic stirring bar worsens the suspendability, in accordance with the fusions observed on TEM images at Chapter 4 too. Thirdly, it is observed that the instability of nanoparticles increases with the TEOS addition rate.

However, this observation can be an artefact produced by the large differences regarding the nanoparticles size, which strongly affects to the light attenuation at longest wavelengths. Finally, the neutralisation with HCl offers a better colloidal stability.

### 5.5.3. The effect of MSN preparation

The preparation of MSN suspensions was analysed by using this decantation and fraction weighting technique. Three samples were prepared according to the different process employed to suspend the MSN: a) sonicating briefly (few tens of seconds) to disperse the large aggregates seen at naked eye, b) sonicating 1 hour and c) sonicating 1 hour and stirring 1 hour.

Figure 13 shows how the nanoparticles settled over time for the three preparations. Fig. 13A displays pictures of the samples taken at different times and represents visually the behaviour of the three MSN suspensions. Fig. 13B shows the quantification of the percentage of suspended nanoparticles as a function of the weighting of decanted pellet. These results indicate that the sample that was only briefly sonicated mostly sediment in one hour. The pictures taken of this sample (a) show as the cloudy suspension turns mostly clear at few hours and almost all the nanoparticles are settled down in the bottom of vial. In contrast, when the nanoparticles were sonicated during 1 hour or sonicated and stirred during 1 hour, the sedimentation of MSN was reduced and around a 30% of nanoparticles remained suspended after 72 h. The pictures of these samples (b and c) show the cloudy suspension remain even at 72 hours and the pellet formed is smaller. This fact means that prolonged sonication achieved a difference greater than 30% respect to nanoparticles in suspension. On the other hand, no significant differences were observed between the samples b) and c). Thus, the stirring process during 1 hour did not improve the stability of MSN suspension after being generously sonicated.

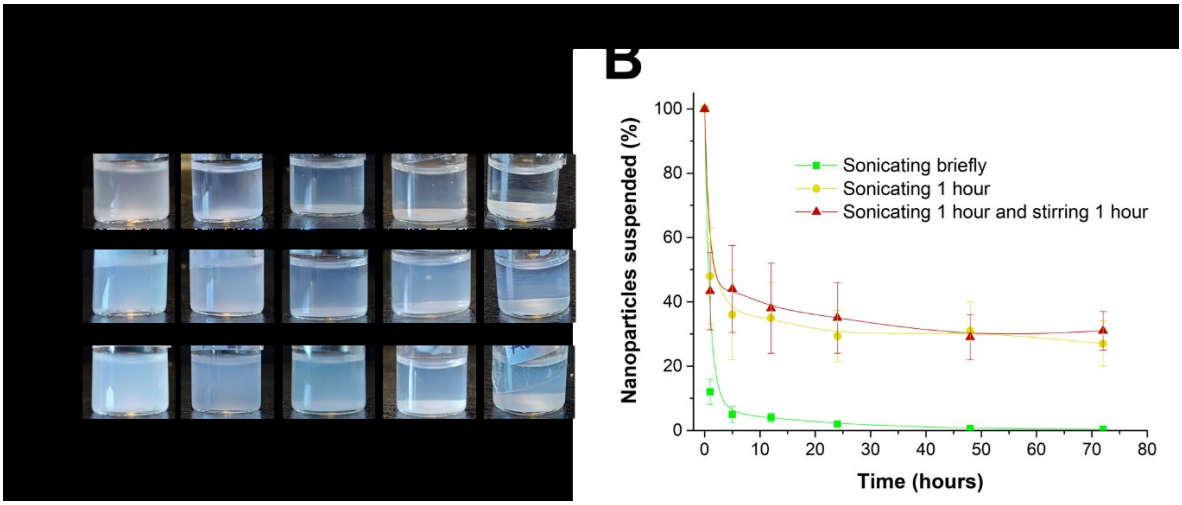


*Figure 13. A) Photographs of decanting standard MSN samples (5 mg/ml in distilled water) a) sonicated briefly, b) sonicated during 1 hour and c) sonicated during 1 hour and stirred during 1 hour. Pictures were taken at 0, 1, 5, 24 and 72 hours. B) Decantation and fraction weighing of the previous standard MSN samples preparations. The percentage of nanoparticles is measured by weighting the pellet decanted.*

According to the results, the importance of sonicating generously a MSN suspension is evident and necessary to obtain a moderately stable suspension. It is considered that the sonication is involved in the disagglomeration of nanoparticles bound by physic interactions. In the early

stages of the sonication, the larger aggregates, most of them visible at naked eye, are broken apart. Nevertheless, further time is required to disagglomerate the nanoparticles below the micron range, which is required to obtain Brownian entities. Besides, the sonication during 1 hour causes the temperature to rise to 40-45˚C, which can also contribute to the disagglomeration process. However, about a 60% of nanoparticles in a naked MSN suspension in distilled water sediment up to 5 hours and the 70% at 72 hours. This can be produced due to the presence of intermediate and large aggregates bound chemically, and the slow but continuous reagglomeration of nanoparticles in the suspension. Finally, the stirring process does not provide additional dispersibility in the nanoparticles after being generously sonicated. In this sense, it is considered a less aggressive process compared to sonication.

Additionally, the effect of the sonicating time, in combination with the application of spin pulses, was also analysed by UV light attenuation (Figure 14). As it was expected, the sample sonicated during 1 hour shows higher attenuation and then a higher amount of nanoparticles suspended than the sample only briefly sonicated. The improvement remained above the 5% of suspended nanoparticles regardless the strength of spin pulse applied, and it reached the 10% at intermediate spin pulses.

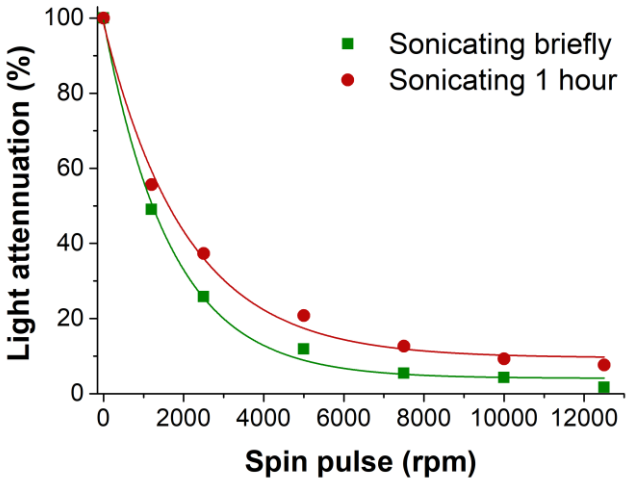


*Figure 14. UV light attenuation at 800 nm of a standard MSN sample (5 mg/ml, in distilled water) when it is sonicated briefly or sonicated during 1 hour and subjected to increasing spin pulses. The samples were fitted to asymptotic exponential curve.*

### 5.5.4. The influence of solvent in colloidal stability

The influence of the dispersant medium was studied using UV light attenuation methodology. Therefore, MSN were suspended in distilled water, PBS and supplemented DMEM, and were subjected to different spin pulses (Figure 15). In comparison with the distilled water, the dispersion of MSN in PBS reduces the stability, especially al low pulse spins. For example, there is a 10% reduction of nanoparticles suspended at 1200 rpm in PBS compared to distilled $H_2O$. However, at higher spin pulses the percentage of suspended nanoparticles levels off in both cases. In case of nanoparticles suspended in DMEM, their stability is higher, especially at

intermediate spin pulses. The sample suspended in DMEM shows an increase of between 5 to 10% of nanoparticles suspended compared to those suspended in distilled in water.

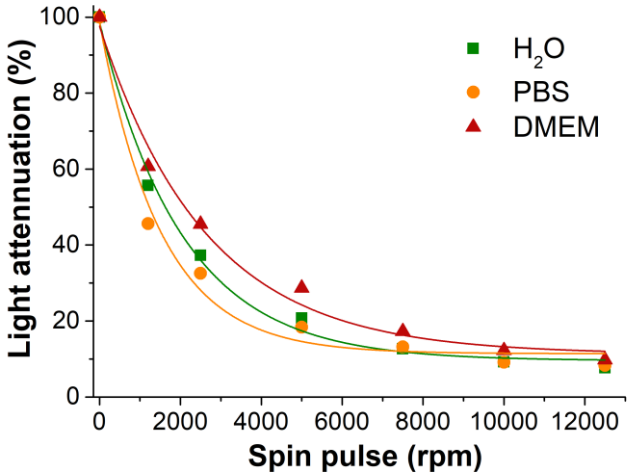


*Figure 15. UV light attenuation at 800 nm of standard MSN sample (5 mg/ml, sonicated 1 hour) when is suspended in different media (distilled water, PBS or DMEM) and subjected to increasing spin pulses. The samples were fitted to asymptotic exponential curve.*

The behaviour of MSN suspensions can be explained according to the colloidal physics theory. The presence of salts coming from PBS buffer worsen the colloidal stability of MSN. The reduction of stability is explained since the ionic strength, which is related with the presence of salts, screens the electrostatic repulsions between bare MSN, which are essential to the dispersion of nanoparticles. Nevertheless, at high spin pulses this effect becomes less relevant. On the other hand, the composition of supplemented DMEM seems to improve the colloidal stability of MSN. This can occur because the proteins and other compounds in the medium form a protein crown that sterically hinders the agglomeration and sedimentation of the nanoparticles. This effect can counteract the shielding of electrostatic repulsions provoked by the presence of large amount of salts in the medium.

On the other hand, the influence of different solvents in the behaviour of the suspension was also analysed by the decanting and fraction weighting method. The solvents chosen were the most used in terms of synthesis and functionalisation of MSN (ACN and EtOH), and the aqueous media used in the in vitro assays ($H_2O$ and PBS). The pellets were weighed after overnight decantation. The results obtained are shown in Figure 16. The amount of suspended nanoparticles was about the 38% in the case of the suspension in water, which fits quite well with the behaviour observed in the previous assay after 1 hour sonication and 15 hours settling (Fig. 13B). The percentage of nanoparticles suspended was reduced in the rest of the solvents. In PBS was around 20%, in ACN below 20% and close to 25% in the case of EtOH.

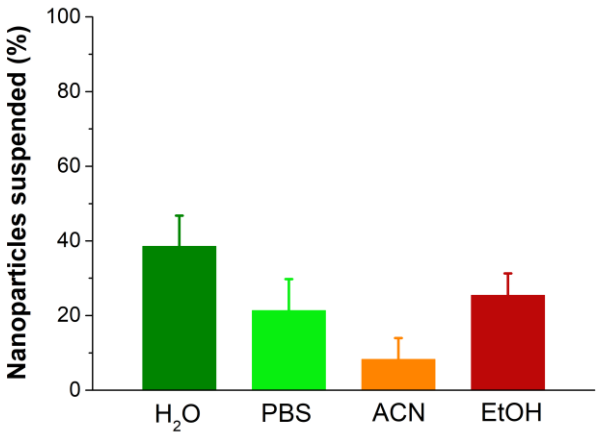


*Figure 16. Decantation and fraction weighing method applied on standard MSN samples suspended in different media (distilled water, PBS, ACN and EtOH). Pellets were collected after settling during 15 hours.*

The results show the expected tendency, in accordance to previous results and colloids physical theory. On the one hand, the sedimentation in PBS sample is higher than the one obtained in distilled water. However, apart from to the effect of ionic strength on the destabilization of the suspension, the method employed could overestimate the amount of decanted nanoparticles when using PBS (10 mg/ml of salts) since some amount of salts can be weighed along with the MSN in the pellet. On the other hand, the influence of organic solvents is variable. Although ACN is quite hydrophilic solvent, the stability of MSN in ACN is quite impaired. This is explained by the fact that the ACN is an aprotic solvent, which cannot form hydrogen bonds with the silanol groups on the MSN surface [99]. In contrast, the stability of MSN suspended in EtOH is greater precisely due to the ability of EtOH to form these bonds, even though the polarity of EtOH is lower than that of ACN.

### 5.5.5. The influence of MSN concentration in colloidal stability

Another assay was performed to determine the effect of the concentration of MSN suspensions on their stability. Hence, four different concentrations were prepared (0.1 mg/ml, 0.5 mg/ml, 1 mg/ml and 5 mg/ml) and their stability analysed as a function of the intensity of the spin pulse applied (Figure 17). As it can be observed in Fig. 17, the concentration of MSN suspensions strongly affects their colloidal stability. The more diluted the suspension, the more stability was found. The difference between the most diluted (0.1 mg/ml) and most concentrated (5 mg/ml) sample was greater than the 20% in low and intermediate spin pulses, but it was reduced in high ones.

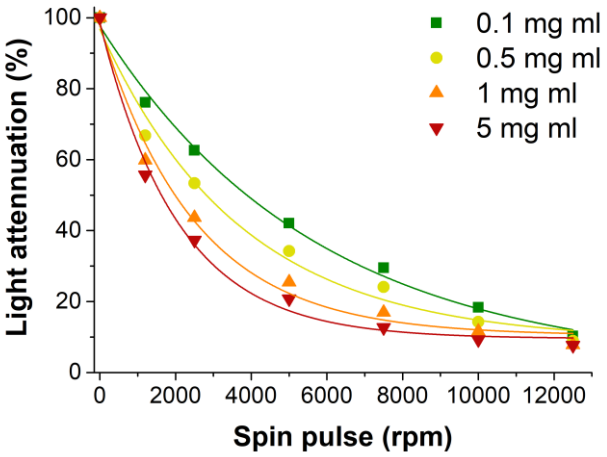


*Figure 17. UV light attenuation at 800 nm of standard MSN sample (in distilled water, sonicated 1 hour) for suspensions prepared at different concentrations (0.1 mg/ml, 0.5 mg/ml, 1 mg/ml and 5 mg/ml) and subjected to increasing spin pulses. The samples were fitted to asymptotic exponential curve.*

Therefore, the concentration of MSN preparations can be suggested as highly influent on the nanoparticles stability. The higher amount nanoparticles in a suspension implies higher number of collisions and agglomeration between them, leading to sedimentation. This effect is greater at low spin pulses, but at higher ones, the concentration effect becomes less relevant, since the centrifugal force tends to agglomerate the nanoparticles regardless the concentration.

### 5.5.6. Functionalisation and its implications on colloidal stability

Finally, the implications of functionalising the nanoparticles in terms of colloidal behaviour were studied. According to the literature, the MSN functionalisation can either avoid or promote their agglomeration. Hoang Thi et al. reported that the synthesis of functionalised MSN, especially on an industrial scale, is limited inter alia due to their potential aggregation [101]. Paula et al. described that functionalisation with amine groups promotes the sedimentation of MSN, but other types of functionalisation such as phosphonate groups stabilise nanoparticles suspensions in the long term [6]. Bagwe et al. reported the effect of functionalising with different groups and their effect on MSN aggregation, suggesting a similar behaviour to that of Paula's study [102]. Many other studies reported the improvement of colloidal stability of MSN after their PEGylation [64][83][103][104][105].

In our study, bare MSN have been functionalised with different groups in order to characterise the effect on their colloidal stability. The functional groups chosen are some of the most used in the functionalisation of MSN for biological applications: amino ($-NH_2$), thiol (-SH) and isocyanate (-NCO). Thus, the samples obtained were called **MSN-$NH_2$**, **MSN-SH** and **MSN-NCO**, respectively. In addition, all the samples have been PEGlyated to compare the effect of this additional functionalization on different nanoparticles, obtaining the samples **MSN-$NH_2$-PEG**, **MSN-SH-PEG** and **MSN-NCO-PEG**. The UV light attenuation was measured for each of these samples after the application of different spin pulses.

The results obtained are shown in Figure 18. It can be seen in this figure that the functionalisation with thiol groups (**MSN-SH**) (Fig. 18A) has a negative effect on dispersibility of MSN both at low and high spin pulses. A constant 10% reduction of suspended nanoparticles can be observed with respect to bare MSN. Nevertheless, when these nanoparticles were PEGylated (**MSN-SH-PEG**) their suspendability is fairly improved, especially at low and intermediate spin pulse strengths. In this sense, the percentage of nanoparticles suspended at 1200 rpm and 2500 rpm is 96% and 78%, respectively. This means up to a 45% improvement of suspended nanoparticles compared to the non-functionalised sample. However, as spin pulses increase, the difference is reduced reaching almost equal values when using a 12500 rpm pulse. The functionalisation with amine groups (**MSN-$NH_2$**) (Fig. 18B) tends to stabilise the MSN suspension, although this stabilization only occurs for low spin pulses, overcoming a 25% of suspended nanoparticles in comparison with bare MSN. In contrast, at high spin pulses, the colloidal stability is strongly reduced, even reaching values below bare MSN (around a 10%). The PEGylation of these nanoparticles (**MSN-$NH_2$-PEG**) largely stabilises the MSN suspension, reaching high values of nanoparticles in suspension at low spin pulses. For example, at 1200 rpm and 2500 rpm, we have measured a 97% and 87% of suspended nanoparticles, respectively. Besides, at high spin pulses the stabilisation remained at least a 10% improved with respect to bare MSN. Finally, the functionalisation with isocyanate groups (**MSN-NCO**) (Fig. 18C) had a similar effect to that of thiol groups, that is, to lead to greater sedimentation regardless the strength of spin pulses. The percentage of suspended nanoparticles was reduced by at least a 10% compared to bare MSN. In addition, the PEGylation of **MSN-NCO** (**MSN-NCO-PEG**) induced an improved stability in the same vein that **MSN-SH-PEG**. This means that we have obtained huge differences in dispersibility at low spin pulses (about a 40%), but the amount of suspended nanoparticles tends to be equal to, and even lower, than bare MSN at high spin pulses.

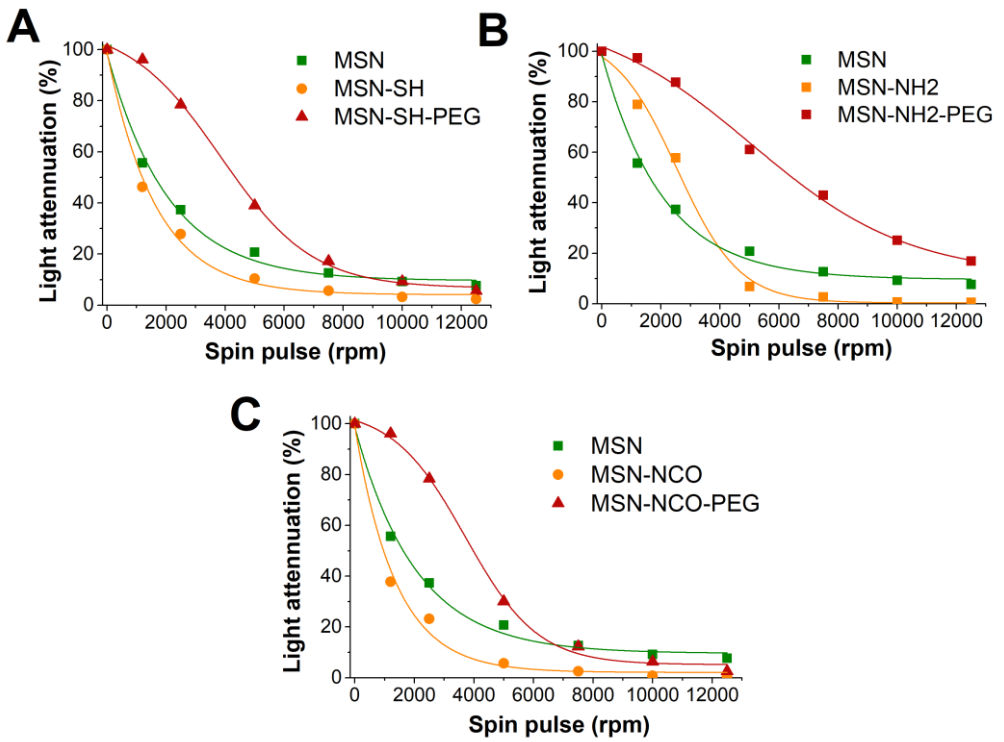


*Figure 18. UV light attenuation at 800 nm for functionalised MSN samples (5 mg/ml, in distilled water, sonicated 1 hour) when they are subjected to increasing spin pulses: A) **MSN-SH** and **MSN-SH-PEG**, B) **MSN-NH₂** and **MSN-NH₂-PEG** and C) **MSN-NCO** and **MSN-NCO-PEG**. PEGylated and aminated MSN behaviour were fitted to sigmoid curve, the rest of samples were fitted to asymptotic exponential curve.*

According to these results, it can be considered that generally the functionalisation of MSN with trialkoxysilanes worsens the suspensability of nanoparticles. It is hypothesised to be caused by three main reasons. First, the functionalisation with some trialkoxysilanes (i.e. MPTMS and IPTES) leads to the reduction of the charge on the nanoparticles surface, since the silanol/silanolate groups are substituted by the organic ones. Second, the substitution of silanols by organic moieties can increase the attraction between nanoparticles and their aggregation and sedimentation. This can be produced either by the reduction of the polarity of nanoparticles surface, as in the case of propyl chain, which worsens the solvation of nanoparticles, which prefer to stablish dispersion bonds to each other instead of be close to water molecules; or by the inclusion of chemical groups which can be attracted to each other by hydrogen or polar bonds (-NCO, -$NH_2$, -SH, -OH, -CHO, etc.). Third, the functionalisation process is an additional step in which interparticle covalent bonds can be easily formed (Scheme 2). This fact can result in the irreversible aggregation of nanoparticles, forming clusters from tens to hundreds of nanoparticles (from oligomers to large aggregates). Exceptionally, some of these considerations are not valid for **MSN-$NH_2$**, which shows at low spin pulses an improved suspendability. This phenomenon is explained because the amine groups confer high positive charge density to the MSN (working at neutral or slightly acidic pH). Then, the positive charge on the surface of **MSN-$NH_2$** produces electrostatic repulsion between the nanoparticles. This effect is only seen at low spin pulses values, where the repulsion between ammonium groups is able to counteract the aggregation effects produced by chemical properties (surface polarity and charge) and interparticle bonds formation. At high spin pulses, the repulsion provoked by charged amine groups becomes less relevant.

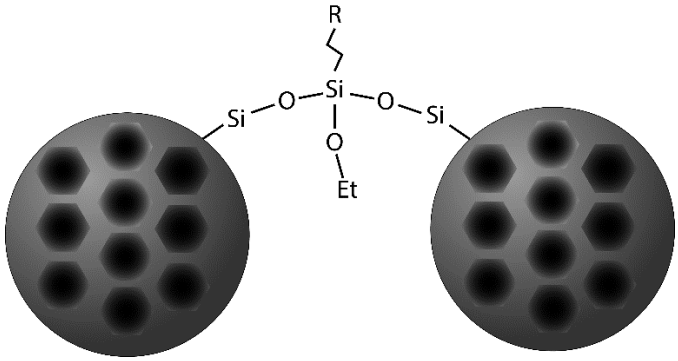


*Scheme 2. Schematic representation of the formation of interparticle bonds in the MSN functionalisation process.*

As widely reported, our assays have also demonstrated the effect of PEGylation, which acts as colloidal stabiliser and improves the percentage of suspended nanoparticles when different spin pulses are applied. This effect is found even though the previous step (addition of trialkoxysilanes) provokes the formation of irreversible aggregates. Then, the PEGylation of MSN can confer colloidal stability to oligomers and nanoparticles aggregates, which in the non-PEGylated state would decant. Nevertheless, at high spin pulses the stabilisation effect is reduced, even suppressed in case of **MSN-SH-PEG** and **MSN-NCO-PEG**. Therefore, we suggested that the colloidal behaviour of nanoparticles that is stabilised through steric (PEGylation) or electrostatic (-$NH_2$) hindrance can be fitted to a sigmoid function, namely, this behaviour describes a significant stabilisation at low spin pulses, which is strongly affected above a certain threshold of centrifugal force. For most of these samples the stabilisation threshold was around 5,000 rpm.

According to the results obtained, it can be concluded that the PEGylation step is crucial in order to obtain a final preparation with stable colloidal properties. Moreover, even the application of spin pulses to PEGylated MSN allows some larger aggregates to be removed without losing large amounts of nanoparticles, which is useful for some applications, such as biomedicine.

## 5.6. CONCEPTUAL AND OPERATIONAL FRAMEWORK OF MSN SUSPENDABILITY

As a result of mesoporous silica nanoparticles synthesis, a mixture of products is obtained (Scheme 3). The mixture is formed by a) isolated and discrete nanoparticles, b) agglomerated nanoparticles by physical interactions and c) fused nanoparticles by chemical bonds. In this context, the entities found in a MSN sample are large aggregates, from hundreds of nanometres to several microns; small aggregates or oligomers, in the nanoscale range, such as dimers and trimers; and single or isolated nanoparticles. Regardless the modifications made in the synthesis or the protocol used, all three components are obtained to a greater or lesser extent. However, the percentage of each population can be adjusted by optimising the MSN synthesis and manipulation.

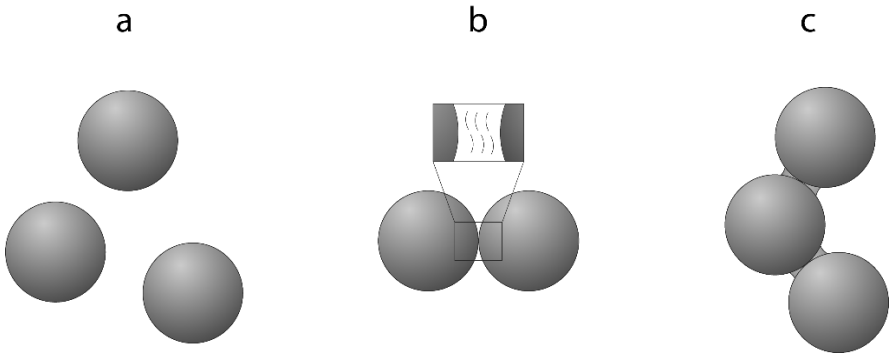


*Scheme 3. Schematic representation of the existent populations in a MSN sample. A) Isolated and discrete nanoparticles, B) agglomerated nanoparticles by physical interactions and C) aggregated nanoparticles by chemical bonds.*

### 5.6.1. Aggregation by means of chemical bonding

During the synthesis process, it is common that nanoparticles tend to form aggregates as a result of particle or seeds coalescence during the formation of the nanoparticles, fusion of formed nanoparticles or covalent bonding of chemical groups on the MSN surface, that is form Si–O–Si bridging bonds between nanoparticles.

#### 5.6.1.1. Coalescence

The most severe irreversible aggregation type is **coalescence** [25], which consists in the collapse of two premature nanoparticles (Figure 19). According to the observations obtained in the previous chapters and in the literature [50], this phenomenon is probably caused by high and hard collisions between forming nanoparticles when the stirring conditions lead to turbulent flow. Furthermore, it can be related to the presence of heterogeneous nucleation conditions due to the presence of dust, burs or solid contaminants in the synthesis reaction medium. Then, controlled stirring conditions, and the use of plain magnetic stir bar and clean materials, are necessary to avoid or limit the coalescence.

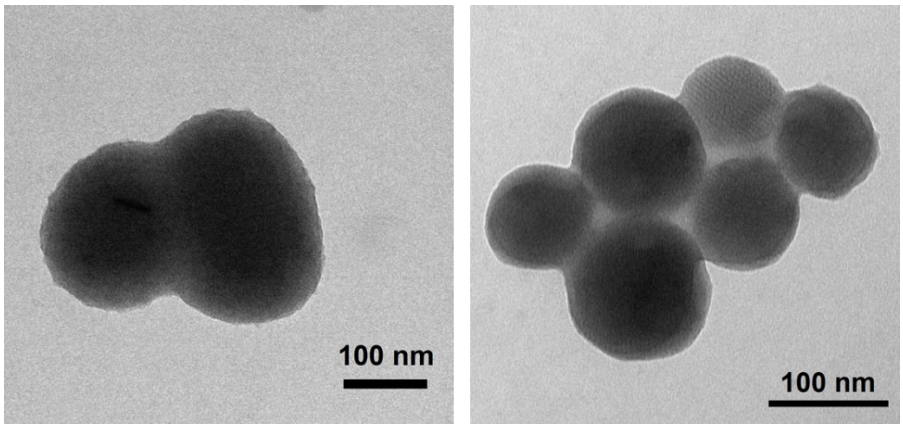


*Figure 19. TEM pictures of coalesced nanoparticles.*

#### 5.6.1.2. Silica bridges

The formation of silica **bridges or necks** between nanoparticles is also very common [7][29]. It is the result of the extension of condensation process through adjacent nanoparticles once they are almost formed (Figure 20). These bridges can appear as an elongation of silica-surfactant mesostructures between nanoparticles. They can also be caused by the dissolution and reprecipitation of silica species, because the solubility of silica on the surface of a spherical particle with a positive curvature is greater than the solubility of a neck region with negative curvature. Thus, during the nanoparticles formation, it can take place a net migration of silica towards the bridges between nanoparticles, where silica tends to condensate [49].

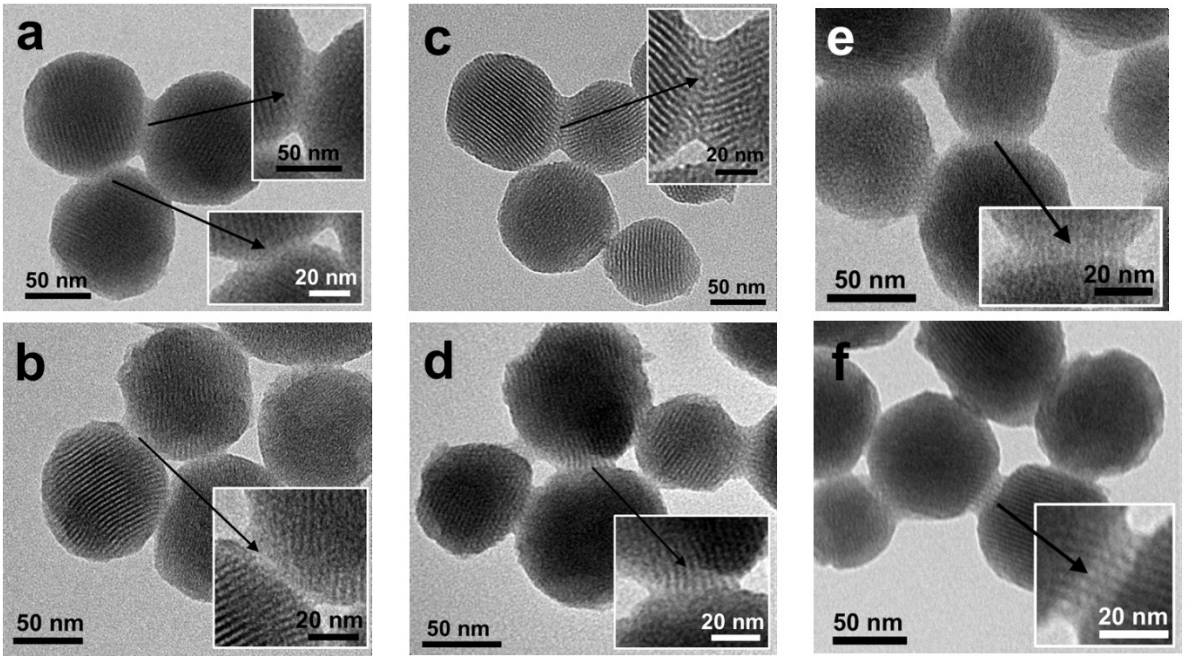


*Figure 20. Different TEM pictures of silica necks. Amorphous silica neck (a, b), templated silica neck (c, d), templated silica neck parallel to pores of both adjacent nanoparticles (e, f). Arrows point the silica necks under consideration.*

These interpretations justify that the formation of both bridges and coalescence between nanoparticles take place during the synthesis reaction. In addition, it is remarkable that they are

observable from samples taken directly from the reaction process by TEM characterisation. Therefore, these phenomena seem to be independent from the surfactant removal process, the storage and even the drying process.

As mentioned, the presence of coalesced or silica-necked nanoparticles is observable in TEM images, being that a continuous matter of condensed silica network can be distinguished that connects nanoparticles to each other. In addition, occasionally the silica bridge can be formed by templated silica (with observable channels or pores), and even formed by channels that connect two nanoparticles (Fig. 20).

The development of silica bridges is less avoidable than coalescence since they are produced by softer conditions and intrinsic features of system, such as solubility of silica, stochastic collisions due to Brownian motion and van der Waals interactions between nanoparticles. According to the literature, there are some resources to avoid or minimise this aggregation between nanoparticles. Most of the reported studies are based on **preventing the direct contact** between nanoparticles [2] such as high dilution method, binary surfactant method, and modification of silanol surface by co-condensation synthesis, among others, just as it is described in the review.

On the other hand, it has been reported the importance of understanding and **controlling both nucleation and growth steps**. Some studies propose to separate and control these two steps to improve the production of discrete, size-controlled and uniform nanoparticles, being that the production of controlled and dispersed seeds or nuclei is crucial for the obtaining of discrete MSN [24][106][107]. In fact, it has been observed that nanoparticles which are synthesised with an initial core of metal has a narrower size distribution and less aggregation [2][108][109][110]. Some authors developed the so called seed-growth method that monitors the nucleation and growth of nanoparticles by controlled attenuation of the reaction [59]. It is based, for instance, on adding small portions of TEOS successively, and therewith, the silica hydrolysis rate is regulated by changing the reaction environment.

However, as we showed in the previous review, most of the methods employed are not able to eliminate in a significant way the formation of silica necks, being almost idiosyncratic in MSN samples, especially for MCM-41-type MSN.

Finally, in order to minimise the formation of silica bridges it is possible to focus on **optimising the standard conditions** for the synthesis of MSN. For example, Catalano et al. [100] studied the influence of temperature, pH and reaction time in MCM-41-type MSN synthesis. They describe that optimal temperature in the MSN synthesis for obtaining the best morphological and mesoporosity properties and good dispersion in aqueous solution is 80 °C, the same as it was previously reported by Cai et al. [23]. In fact, in relation with the reported effect by which higher reaction temperature achieves less aggregation compared to low temperatures [7][111], it has been found that the use of lower temperatures (60 or 70 °C) results in more aggregated nanoparticles. Regarding the pH, Cai et al. used NaOH to produce a theoretical pH of ca. 12.2. According to Catalano studies, this pH has been found to be the optimum value in the case of MCM-41-type MSN to obtain well-formed nanoparticles in terms of size and dispersion. Lower pH leads to smaller, less formed and more fused nanoparticles. Higher pH values produce larger nanoparticles not so suitable for biomedical applications. About the reaction time, according to Cai and Catalano, a value between 1 and 2 hours is optimal in terms of mesoporosity,

nanoparticle size distribution and good dispersion properties. Our experiments in Chapter 3 showed that the optimal reaction time was 2 hours. Finally, what concerns to stirring rate, as we observed and suggested above, extremely fast stirring speeds are related to particle aggregation [50], finding an optimal stirring rate between 350 rpm and 500 rpm. Smaller stirring rates lead to too low hydrolysis reaction and then large size and bean-shaped nanoparticles are formed.

#### 5.6.1.3. Covalent bonds

Other type of irreversible aggregation that the nanoparticles can suffer is the formation of **covalent bonds** between them once they are completely formed, namely, the formation of siloxane bonds due to the condensation of silanol groups of different nanoparticles (Scheme 4). These bonds are not observable by TEM characterisation and then, they are not distinguishable from nanoparticles aggregated by physic interactions. It can be caused in the last stages of nanoparticles synthesis reaction, but especially during the template removal, the subsequent manipulation steps, and even during the storage in dried conditions. Then, measures to avoid them are necessary both in synthesis reaction and in post-synthesis conditions. For all these reasons, this type of aggregation is the most difficult one to evade and monitor.

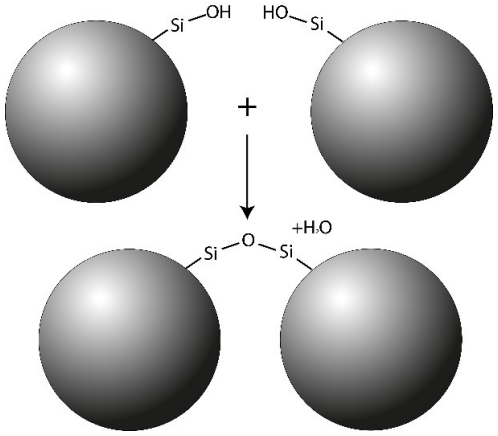


*Scheme 4. Schematic representation of the formation of interparticle siloxane bonds.*

The formation of any type of irreversible aggregation can be observed indirectly in the $N_2$ adsorption-desorption isotherms. At high $p/p_0$ values, the condensation due to the interparticle porosity associated with the aggregation between nanoparticles can be observed. Thus, the height of the sharp rise at these values is closely related to the aggregation. However, in dried conditions, this value is also related with the disposition of nanoparticles to each other and the space they create among them.

Concerning the precautions and resources for avoiding interparticle covalent bonds, they should be the same as the ones used in the reaction synthesis for avoiding silica bridges. Nevertheless, it must be taken into account that covalent bonds can be formed after the synthesis reaction. Then, it is important to heed the conditions used in the subsequent steps, such as cooling down process, pH neutralisation, isolation method (centrifugation, filtration, precipitation, or evaporation) and drying approach (evaporation of water by high temperatures, vacuum, room atmosphere or avoiding the nanoparticles drying). As we have suggested, during the mentioned processes there is an irreversible transition from colloidal to agglomerated suspension and

sedimentation, being the most probable cause of this transformation the formation of covalent bonds between nanoparticles. Unfortunately, most of these steps are not well studied, tend to be less standardised and are quite difficult to be controlled.

On the other hand, surfactant removal is considered to be a crucial step in the aggregation of nanoparticles [49], particularly those related to the formation of covalent bonds between silanols. For instance, calcination process is reported to lead to non-suspendible and aggregated nanoparticles due to interparticle silanol groups condensation [24][2][112]. Even the solvent extraction method is reported to affect to the colloidal stability of MSN, since the increase of surfactant in the solvent can counteract the electrostatic repulsion between nanoparticles and provoke their aggregation [20].

Finally, storage approach is also important for the preservation of unbound nanoparticles. Several authors have described the importance of keeping the MSN samples always in a liquid suspension and not drying them [61][113], being that the drying process facilitate the aggregation of particles, maybe by the formation of interparticle siloxane bonds.

### 5.6.2. Sedimentation by physical agglomeration

Apart from the formation of irreversible or quasi-irreversible aggregates by chemical bonds, MSN suspensions can also tend to agglomerate and sediment due to the formation of physical and, a priori, reversible agglomerations. As it was described in the introduction, the agglomeration between MSN depend on the forces acting over them, mainly the double layer force, as a repulsive interaction, and the Van der Waals interactions, as an attractive one. Other secondary forces can be found. For example, steric impediments act as repulsive forces, and electrostatic forces can also produce attractive interaction in the case of opposite sign charges. In addition, other attractive forces such as specific molecular affinity or molecular bridging can be found [15]. In essence, the nanoparticles suspension systems will tend to minimise the potential energy, and thus, going to an energy minimum. Depending on the parameters of the corresponding MSN sample, the graph which describes their behaviour will be closer to aggregated state (Figure 21A) or colloidal state (Figure 21B).

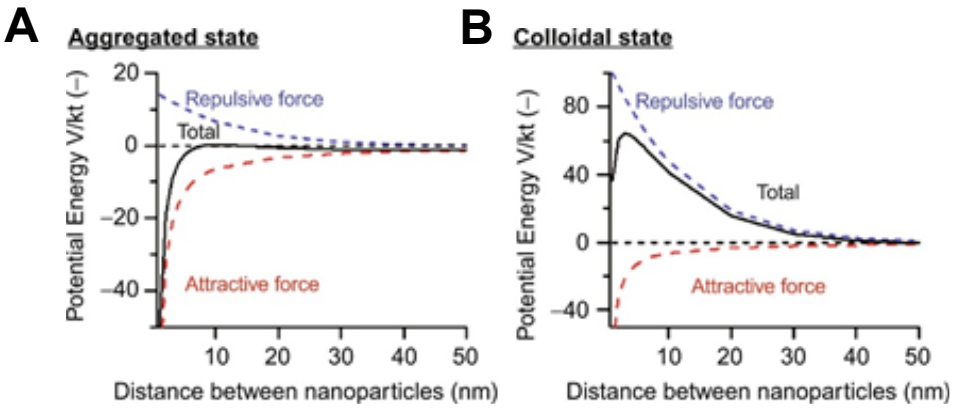


*Figure 21. Potential energy calculations for different MSN samples in the (A) aggregated and (B) colloidal states as a function of the attractive and repulsive forces acting over them. Adapted from reference* [114]. *Copyright © 2018 Elsevier.*

The stability of a MSN suspension can also be expressed as the difference between the energy resulting from the contact between the nanoparticles and the solvent (in Fig. 21, larger distance between nanoparticles), and the energy when the nanoparticles are in close contact (in Fig. 21, distance between nanoparticles below 1 nm) [5][99]. This difference is associated with various parameters, such as the size of the nanoparticles, their surface and surface charge and the solvent employed [9]. It should be noted that some systems which have a maximum similar to the one in the colloidal state graph but lower (Figure 21B), in some conditions can surpassed it due to external forces and fall into the primary minimum, leading to the agglomeration of nanoparticles.

It has to be noted that the bulk density of MCM-41-type MSN is 0.34 g/mL, according to some suppliers (i.e. Sigma Aldrich). Therefore, the initial premise is that the MSN should not sink in water or aqueous solutions and thus, their propensity should be to float, or at least not sink. Nevertheless, the Archimedes principle is violated at the nanoscale, where in addition to the difference in density, other parameters intervene in the suspendability of the particles, such as Brownian motion, the size and morphology of the particles and the interactions with the fluid [11][115][116].

#### 5.6.2.1. Nanoparticles size

Regarding size of the nanoparticles, the smaller particle size gives rise to in more intense attractive interactions between particles (van der Waals) and therefore, when the size of the particles decreases, the agglomeration of particles is promoted [3]. In this context, some authors report that small particles have a tendency to aggregate and form larger nanoparticles if their size is smaller than 50 nm, resulting in polydispersed samples [117].

In this context, it seems to be clear that the obtaining of discrete and colloidal MSN in the micron and sub-micron scale is more common, for example, using Stöber-like synthesis protocols. Nevertheless, it has to be remarked that particles over micron range are not usually Brownian particles, and therewith, they tend to sediment.

#### 5.6.2.2. Dispersant medium

The medium in which the MSN are suspended plays an important role in their physicochemical behaviour and, therefore, in their colloidal stability. The fluid determines the pH, the ionic strength, and the possible presence of molecules that can interact with the nanoparticles.

In this sense, the increase of the amount of salts, and then, the increase of the ionic strength in a MSN suspension tends to shield the electrostatic repulsion between nanoparticles, and then favour the aggregation among them.

The presence of small molecules, proteins or polymers can affect in the same vein [6] or facilitate the dispersion. Therefore, the suspendibility of nanoparticles in physiological media should be studied taking into account these multifactorial implications.

In case of organic solvents, we observe that is quite influent the presence of proton donors to form hydrogen bonds with the nanoparticles. Then, aprotic solvents will suspended much worst the MSN than protic ones. In this sense, some functionalisation with hydrophobic organosilanes must to be done to stabilise a MSN suspension in nonprotic solvents [118].

#### 5.6.2.3. Nanoparticles surface

Among the characteristics of the surface of nanoparticles that influence in their stability it can be included the charge, the topography and the presence of steric hindrance on the surface.

The surface charge is the main repulsive force that keeps the nanoparticles dispersed. Some authors report that nanoparticles must have a highly negative or positive ζ potential (< -30 mV or > +30 mV) to be stable [119][120]. Nevertheless, the precise value depends on the size of the nanoparticles and the medium in which the nanoparticles are going to be suspended. In this context, one of the parameters that influences on the zeta potential is the pH. At acidic pH the ζ potential of MSN shifts towards positive values and at alkaline pH towards negative values. At a certain pH value, the ζ potential becomes neutral (isoelectric point) and corresponds to the conditions in which the nanoparticles are less stable. In consequence, neutral, and especially hydrophobic surfaces on MSN result in very unstable suspensions if they are suspended in polar or aqueous solvents. In the case of bare MSN, below pH 5 they will be mostly neutral, and therefore more oriented to aggregate and sediment (Figure 22). In this sense, it should be noted that the physiological pH varies from 4 to 7.5, in which range the bare MSN present a ζ potential from neutral to moderately negative (with a maximum of ca. -25 mV). In addition, distilled and deionised water usually present a pH around 5-6, since the dissolution of atmospheric $CO_2$ produces a slight acidification. Therefore, bare MSN tend to be only slightly dispersible at these conditions. The functionalisation with charged groups can shift the ζ potential to higher values, either negatives or positives. For example, the functionalisation with amine groups confers to the ζ potential of the MSN higher values than +40 mV at pH 6, but it is sharply reduced above pH 7. The functionalisation with carboxylate groups provides values lower than -30 mV above pH 5 [121]. On the other hand, as-made MSN possess a positive ζ potential in distilled water ca. 40 mV, and for this reason, they can be more stable in suspension. This fact is observed in bibliography, where DLS measurements of as-made MSN usually indicate the colloidal behaviour of samples.

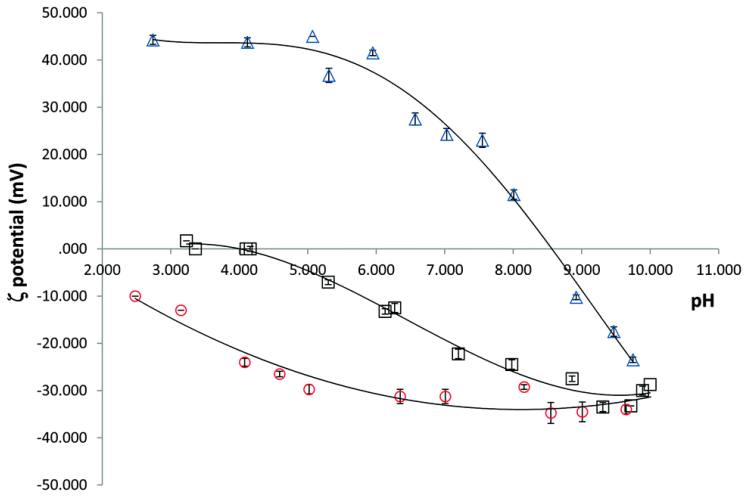


*Figure 22. ζ potential curves as a function of pH at constant ionic strength of MSN (black squares), amino-MSN (blue triangles) and carboxy-MSN (red circles). Reprinted from reference* [121]. *Copyright © 2015 Royal Society of Chemistry.*

Regarding the topography of MSN surface, it can be smoother or rougher. In case of a rough surface, the interaction between the nanoparticles can be reduced and therefore, the Van der Waals forces will also decrease, increasing the stability of the suspension. However, accordingly to the observations reported by Paula et al. [6] this influence is variable, and depends on many other parameters.

Additionally, the presence of steric hindrance provided by polymers such as PEG or entities as lipid bilayer confers to the MSN suspensions greater stability. This is the result of the obstruction the polymers provoke, which reduce the interaction between the nanoparticles [122]. In addition, these steric agents are usually highly solvated with a considerable thick layer of water, which acts as a hindrance too. Our experimental assays in this chapter support this fact.

#### 5.6.2.4. Nanoparticles concentration

The amount of MSN in a suspension determines the number of collisions and the distance between them. Thus, higher concentrations lead to a higher amount of collisions and shorter distances. According to the potential energy graph, at very short distances (below 5 nm) the energy is minimised in the so called primary minimum, which provokes the aggregation of nanoparticles. Similarly, the increase of collisions causes the agglomeration between them. We observed the same tendency experimentally.

Therefore, limiting the concentration of nanoparticles in the different steps of synthesis and functionalisation can be recommended to avoid their agglomeration, the formation of interparticle bonds, etc.

#### 5.6.2.5. Characterisation

The physical agglomeration of MSN can be characterised by several methods [15] but it is not always easy to be distinguished from the chemical aggregation.

Throughout this chapter we have developed some methodologies to determine the colloidal stability of the nanoparticles in suspension, as well as the presence of aggregates. In the literature we can find some of them and many others, such as dynamic light scattering, nanoparticles tracking analysis or conventional light scattering [123], as well as small-angle scattering of light, neutrons, or X-rays. Even some studies propose the use of atomic force microscopy (AFM) for the characterisation of the aggregation of nanoparticles. The advantage of these methods is that they are compatible with suspended samples, and it is not necessary to isolate or dry the sample.

On the other hand, electron microscopy, particularly transmission method, is a widely reported technique as used for that purpose. Nevertheless, some limitations can be found, such as obtaining 2D-images of 3D-objects, so the information is not complete. In this context, the agglomerated but not fused nanoparticles can be sometimes distinguished in TEM images due to the presence of perceptible silica bridges. However, agglomerated nanoparticles cannot be discriminated from particles attached by covalent bonds. Another limitation of the methodology is that nanoparticles suspensions must be dried in order to be observed in electron microscopy, which can induce additional aggregation due to capillary forces.

### 5.6.3. From physical interactions to chemical aggregation

It must be mentioned that, in general, colloidal suspensions can suffer a transition from physical interactions to chemical aggregation, also known as **sintering** [15]. Thus, both interaction types cannot be treated as two perfectly separated and isolated pockets. In this sense, albeit the formation of interparticle covalent bonds over the life of MSN can be common, this process is promoted if the van der Waals and other attractive interactions dominate, being that there is an increased contact between the nanoparticles, in both dried and suspended ones.

In addition, this process can explain the transition from colloidal to agglomerated nanoparticles, which is especially observed after nanoparticles synthesis, where flocs are formed, or after drying step, in which abundant populations of large aggregates appear.

### 5.6.4. Colloidal MSN manipulation

In relationship with the previously mentioned issues, the obtaining of colloidal and stable MSN leads to the appearance of other obstacles associated with their manipulation. There are mainly two processes associated with this, the isolation and collection of the nanoparticles from the suspension, and the storage and stability of the suspension.

#### 5.6.4.1. Colloidal MSN isolation

It must be understood that through the MSN synthesis and functionalisation steps some washing steps or solvents changes are needed. Thus, the isolation of nanoparticles from their dispersant is required. Taking into account that colloidal suspensions cannot be filtrated or centrifuged by conventional methods, some alternatives must be found.

In case of centrifugation, high centrifugal forces must be applied, being that a low centrifugation will only decant the most unstable particles of the suspension. Some authors described the application of relative centrifugal force above 40,000 to decant colloidal MSN [7][49][63], for which ultracentrifugation equipment is needed. However, common MSN samples can be pellet just applying relatively low relative centrifugal force (around 10,000 rcf), since their colloidal stability is not so strong. In those cases, the fraction of perfectly stable and dispersed particles present in MSN suspension will remain in the supernatant if sufficient centrifugal force is not applied to make them decant. Indeed, this fact produces that, in the progressive steps of synthesis and functionalisation of MSN, the more stable and dispersed nanoparticles population is washed and thrown with the supernatant.

In case of filtration, other obstacles can appear. First, the filter must have a small enough pore to retain the nanoparticles on it (generally below micron scale); otherwise, the nanoparticles will cross the filter and be lost in the supernatant or cannot be separated from the dispersant. Secondly, considering that the pores of the filters must be below the micron range, it is quite probable that the suspension seals the filter by accumulation of the sample on the filtering matrix. This phenomenon is intensified with the presence of small aggregates or artefacts, such as dust or salt crystals. Some filters used in this context are membrane circles with a pore size 0.2 or 0.45 µm of different materials (nylon, PTFE, etc.) [79]; filtering paper nº 5, which a slightly larger pore size, around 2.5 µm [58]; or fritted filter funnels nº5, with pore sizes in the range from 1 to 1.6 µm.

On the other hand, alternative isolation methods have been reported. Yamada et al. [60] described that they dried the sample by heating the colloidal MSN at 120 °C for 12 h, that is, by evaporating the solvent. Nevertheless, as it was mentioned throughout the text, the drying process has been suggested to be associated with the aggregation of MSN. In this context, some studies are focused on finding alternative drying methods to reduce their effect on the MSN stability and structure, such as freeze-drying [15][20][58].

In summary, the centrifugation, filtration or evaporation processes can provoke the loss of colloidal stability, either by sintering (meaning, the formation of irreversible bonds between nanoparticles) or due to the changes in the dispersant conditions, in terms of pH, salt and molecules composition, temperature, etc. In this sense, the more aggressive conditions used for the nanoparticles isolation, the more possibility to lose the colloidal properties.

#### 5.6.4.2. Colloidal MSN storage

An additional important step to focus on in this context is the storage of MSN, either at short-term and long-term. In terms of avoiding the loss of colloidal behaviour derived from drying the MSN, some of authors described the storage of colloidal MSN in ethanolic suspension [6][63][99]. It has to be remarked that the suspension of MSN in ethanolic suspension is limited to the storage of bare MSN or those MSN whose functionalisation is compatible with ethanol dispersion. In case of the systems prepared to operate in aqueous solution, such as the molecular gates or targeting agents, a conformational change can occur in the presence of ethanol. Thus, they can unspecifically release the cargo inside the pores over time, or simply, inactivate the function of the present organic molecules. This is especially problematic in case

of the functionalisation with biomolecules, which are highly employed in biomedical applications and are usually incompatible with ethanol or other organic solvents.

Other authors suggest storing the nanoparticles in suspension by adding repulsive or steric stabilisers, and only dry them after that [15]. For example, Schneid et al. [20] proposed the use of BSA to protect the MSN during the drying process and guarantee the redispersibility of MSN after that.

In contrast, the protocol used by Bouchoucha and co-workers [57] and derived studies, can produce robust colloidal MSN avoiding the storage of the nanoparticles in suspension. They reported the colloidal behaviour of their nanoparticles suspensions even after drying and calcination of the samples. Therefore, the implications of drying the nanoparticles are not very clear, and can be fairly influenced by the nanoparticles type.

## 5.7. CONCLUSIONS

The obtaining of colloidal MSN is highly sought after by researches, especially for biomedical applications. However, despite the efforts made in this regard, the state of the art is still far from preparing discrete, monodisperse, colloidal, reproducible and scalable synthesis of MSN, necessary requirements for conducting clinical trials.

We can affirm that every step in the synthesis and manipulation of nanoparticles influences the obtaining of discrete and colloidal nanoparticles. On the one hand, it can be necessary to achieve a fine control of the synthesis processes, such as the silica-surfactant templating, the nucleation and the nanoparticle growth. Generally, these processes are related to large fusions and coalescence. The literature is full of studies to optimise these processes, but they are not always effective. On the other hand, other steps that normally are not on the focus have been demonstrated to reasonably influence in this issue. Some of these steps are the manner to stop the reaction synthesis (diluting or washing with distilled water, adding acid to neutralise the pH), the way to separate de solid from the reaction media (filtration, centrifugation, evaporation), the drying method applied (heat, vacuum or avoiding drying the nanoparticles), and the storage employed (in dry, ethanol suspension, dried atmosphere). Particularly, they can be involved in the formation of interparticle covalent bonds and physic agglomeration, which could be related to the transition from colloidal to agglomerated samples. Furthermore, functionalisation is liable to cause aggregation of nanoparticles and loss of colloidal properties or, on the contrary, improve the colloidal stability, mainly through the addition of steric and electrostatic hindrance, especially in case of PEGylation. Finally, the sample preparation (grinding and sonication), the properties of the suspension media (the ionic strength, the presence of stabilising molecules, the presence of H to form hydrogen bonds, the polarity, etc.) and the concentration of nanoparticles have been found to have a crucial role in the colloidal stability of MSN, even greater than synthesis modifications.

With all of that in mind, one of the approaches to deal with the obtaining of colloidal MSN is following the maxima “keep it simple”. According to the literature and the experimental and theoretical observations, the use of complex protocols, the addition of co-surfactants, the ageing, the high dilution and other resources do not suppose important improvements in the obtaining of colloidal MSN. The limitations in the nanoscale materials manufacturing, the silica chemistry, and especially, the scalable and cost-effective production, are barriers hardly to overcome if the strategy consists in find the perfect protocol to prepare stable, colloidal and monodisperse MSN. On the contrary, the approach to go on the safe side is to know the limitations the MSN employed and starting from them to find the way to reduce them or deal with them. In this sense, drawing from the standard synthesis of MCM-41-type MSN [23] final preparations of colloidal suspensions of functionalised nanoparticles can be obtained. The more efficient action is based on optimising the functionalisation in terms of surface charge or steric hindrance to limit the agglomeration and sedimentation of nanoparticles, as well as applying centrifuge pulses or decantation processes to remove from the sample those large sediments and aggregates formed in each step of the MSN synthesis and functionalisation. Additionally, some studied parameters (dispersant medium, nanoparticles concentration and sonication time) are quite important in terms of working with stable suspensions of MSN, either in case of their functionalisation or their use in biological applications. They do not require an

overexertion, neither they are cost-effective nor time-consuming, becoming simple measures to work with suspended nanoparticles. Finally, bearing in mind this strategy, it is reasonably that the final and colloidal suspensions obtained will include not only single nanoparticles, but also dimers, trimers and other small oligomers, which achieve similar behaviour than single ones in terms of colloidal properties.

## 5.8. REFERENCES


[1] Y. J. Yu *et al.*, "Facile synthesis of size controllable dendritic mesoporous silica nanoparticles," *ACS Appl. Mater. Interfaces*, vol. 6, no. 24, pp. 22655–22665, Dec. 2014, doi: 10.1021/am506653n.

[2] S. H. Wu and H. P. Lin, "Synthesis of mesoporous silica nanoparticles," *Chem. Soc. Rev.*, vol. 42, no. 9, pp. 3862–3875, 2013, doi: 10.1039/c3cs35405a.

[3] D. M. Oliveira and A. S. Andrada, "Synthesis of ordered mesoporous silica MCM-41 with controlled morphology for potential application in controlled drug delivery systems (Síntese de sílica mesoporosa ordenada tipo MCM-41 com controle morfológico para potencial aplicação em sistemas de libe," *Cerâmica*, vol. 65, pp. 170–179, 2019, doi: 10.1590/0366-69132019653742509.

[4] M. Varache, I. Bezverkhyy, F. Bouyer, R. Chassagnon, F. Baras, and F. Bouyer, "Improving structural stability of water-dispersed MCM-41 silica nanoparticles through post-synthesis pH aging process," *J. Nanoparticle Res.*, vol. 17, no. 9, 2015, doi: 10.1007/s11051-015-3147-6.

[5] W. H. Fu, Y. Guan, Y. M. Wang, and M. Y. He, "A facile synthesis of monodispersed mesoporous silica nanospheres with Pm3n structure," *Microporous Mesoporous Mater.*, vol. 220, pp. 168–174, 2016, doi: 10.1016/j.micromeso.2015.09.004.

[6] A. J. Paula *et al.*, "Topography-driven bionano-interactions on colloidal silica nanoparticles," 2014, doi: 10.1021/am405594q.

[7] K. Möller, J. Kobler, and T. Bein, "Colloidal suspensions of nanometer-sized mesoporous silica," *Adv. Funct. Mater.*, vol. 17, no. 4, pp. 605–612, Mar. 2007, doi: 10.1002/adfm.200600578.

[8] F. Tang, L. Li, and D. Chen, "Mesoporous silica nanoparticles: Synthesis, biocompatibility and drug delivery," *Adv. Mater.*, vol. 24, no. 12, pp. 1504–1534, 2012, doi: 10.1002/adma.201104763.

[9] L. Belloni, "Colloidal interactions," *J. Phys. Condens. Matter*, vol. 12, no. 46, 2000, doi: 10.1088/0953-8984/12/46/201.

[10] "General chemistry : principles and modern applications / Ralph H. Petrucci - Trove." https://trove.nla.gov.au/work/9799296 (accessed Oct. 09, 2020).

[11] I. D. I. Fisica, S. Internazionale, and D. I. Fisica, *Fisica dei colloidi complessi 2013* `. 2013.

[12] "The Feynman Lectures on Physics Vol. I Ch. 41: The Brownian Movement." https://www.feynmanlectures.caltech.edu/I_41.html (accessed Oct. 09, 2020).

[13] G. S. He, H. Y. Qin, and Q. Zheng, "Rayleigh, Mie, and Tyndall scatterings of polystyrene microspheres in water: Wavelength, size, and angle dependences," *J. Appl. Phys.*, vol. 105, no. 2, p. 023110, Jan. 2009, doi: 10.1063/1.3068473.

[14] Á. G. U. Helmut H. Telle, *Laser Spectroscopy and Laser Imaging: An Introduction*. Series in Optics and Optoelectronics, 2018.

[15] A.-C. Genix and J. Oberdisse, "Nanoparticle self-assembly: from interactions in suspension to polymer nanocomposites," *Soft Matter*, vol. 14, p. 5161, 2018, doi: 10.1039/c8sm00430g.

[16] W. B. Russel, D. A. Saville, and W. R. Schowalter, *Colloidal Dispersions*. Cambridge

University Press, 1989.

[17] M. Elimelech; J. Gregory; X. Jia, *Particle Deposition and Aggregation - 1st Edition*. Butterworth-Heinemann, 1995.

[18] H. Holthoff *et al.*, "Measurement of absolute coagulation rate constants for colloidal particles: Comparison of single and multiparticle light scattering techniques," *J. Colloid Interface Sci.*, vol. 192, no. 2, pp. 463–470, Aug. 1997, doi: 10.1006/jcis.1997.5022.

[19] G. Trefalt, I. Szilagyi, and M. Borkovec, "Measuring particle aggregation rates by light scattering," 2013. Accessed: Oct. 27, 2020. [Online]. Available: www.colloid.ch/aggregation.

[20] A. da C. Schneid, C. P. Silveira, F. E. Galdino, L. F. Ferreira, K. Bouchmella, and M. B. Cardoso, "Colloidal Stability and Redispersibility of Mesoporous Silica Nanoparticles in Biological Media," *Langmuir*, vol. 36, no. 39, pp. 11442–11449, Oct. 2020, doi: 10.1021/acs.langmuir.0c01571.

[21] E. H. M. Sakho, E. Allahyari, O. S. Oluwafemi, S. Thomas, and N. Kalarikkal, "Dynamic Light Scattering (DLS)," *Therm. Rheol. Meas. Tech. Nanomater. Charact.*, vol. 3, pp. 37–49, 2017, doi: 10.1016/B978-0-323-46139-9.00002-5.

[22] X. G. Qiao, P. Y. Dugas, L. Veyre, and E. Bourgeat-Lami, "L -Arginine-Catalyzed Synthesis of Nanometric Organosilica Particles through a Waterborne Sol-Gel Process and Their Porous Structure Analysis," *Langmuir*, vol. 34, no. 23, pp. 6784–6796, Jun. 2018, doi: 10.1021/acs.langmuir.8b00042.

[23] Q. Cai, Z. S. Luo, W. Q. Pang, Y. W. Fan, X. H. Chen, and F. Z. Cui, "Dilute solution routes to various controllable morphologies of MCM-41 silica with a basic medium," *Chem. Mater.*, vol. 13, no. 2, pp. 258–263, 2001, doi: 10.1021/cm990661z.

[24] F. Lu, S. H. Wu, Y. Hung, and C. Y. Mou, "Size effect on cell uptake in well-suspended, uniform mesoporous silica nanoparticles," *Small*, vol. 5, no. 12, pp. 1408–1413, Jun. 2009, doi: 10.1002/smll.200900005.

[25] G. Begum, R. K. Rana, S. Singh, and L. Satyanarayana, "Bioinspired Silicification of Functional Materials: Fluorescent Monodisperse Mesostructure Silica Nanospheres," *Chem. Mater.*, vol. 22, no. 2, pp. 551–556, Jan. 2010, doi: 10.1021/cm9031013.

[26] T. Suteewong *et al.*, "Ordered mesoporous silica nanoparticles with and without embedded iron oxide nanoparticles: Structure evolution during synthesis," *J. Mater. Chem.*, vol. 20, no. 36, pp. 7807–7814, Sep. 2010, doi: 10.1039/c0jm01002b.

[27] A. B. Albeladi, S. A. AL-Thabaiti, and Z. Khan, "Effect of CTAB on the surface resonance plasmon intensity of silver nanoparticles: Stability and oxidative dissolution," *J. Mol. Liq.*, vol. 302, p. 112565, Mar. 2020, doi: 10.1016/j.molliq.2020.112565.

[28] S. Lechevallier *et al.*, "Luminescence Properties of Mesoporous Silica Nanoparticles Encapsulating Different Europium Complexes: Application for Biolabelling," *J. Nanomater.*, vol. 2013, p. 11, 2013, doi: 10.1155/2013/918369.

[29] M. Varache, I. Bezverkhyy, L. Saviot, F. Bouyer, F. Baras, and F. Bouyer, "Optimization of MCM-41 type silica nanoparticles for biological applications: Control of size and absence of aggregation and cell cytotoxicity," *J. Non. Cryst. Solids*, vol. 408, pp. 87–97, 2015, doi: 10.1016/j.jnoncrysol.2014.10.020.

[30] Y. Du *et al.*, "The search of promoters for silica condensation and rational synthesis of

hydrothermally stable and well ordered mesoporous silica materials with high degree of silica condensation at conventional temperature," *Microporous Mesoporous Mater.*, vol. 112, no. 1–3, pp. 225–234, Jul. 2008, doi: 10.1016/j.micromeso.2007.09.033.

[31] L. Luo, Y. Liang, E. S. Erichsen, and R. Anwander, "Monodisperse mesoporous silica nanoparticles of distinct topology," *J. Colloid Interface Sci.*, vol. 495, pp. 84–93, 2017, doi: 10.1016/j.jcis.2017.01.107.

[32] S. Liu *et al.*, "The Influence of the Alcohol Concentration on the Structural Ordering of Mesoporous Silica: Cosurfactant versus Cosolvent," *J. Phys. Chem. B*, vol. 107, no. 38, pp. 10405–10411, 2003, doi: 10.1021/jp034410w.

[33] S. Kachbouri, N. Mnasri, E. Elaloui, and Y. Moussaoui, "Tuning particle morphology of mesoporous silica nanoparticles for adsorption of dyes from aqueous solution," *J. Saudi Chem. Soc.*, vol. 22, no. 4, pp. 405–415, 2018, doi: 10.1016/j.jscs.2017.08.005.

[34] K. S. Rao, K. El-Hami, T. Kodaki, K. Matsushige, and K. Makino, "A novel method for synthesis of silica nanoparticles," *J. Colloid Interface Sci.*, vol. 289, no. 1, pp. 125–131, 2005, doi: 10.1016/j.jcis.2005.02.019.

[35] L. M. Rossi, L. Shi, F. H. Quina, and Z. Rosenzweig, "Stöber synthesis of monodispersed luminescent silica nanoparticles for bioanalytical assays," *Langmuir*, vol. 21, no. 10, pp. 4277–4280, 2005, doi: 10.1021/la0504098.

[36] P. Khodaee, N. Najmoddin, and S. Shahrad, "The effect of ethanol and temperature on the structural properties of mesoporous silica synthesized by the sol-gel method," in *2018 25th Iranian Conference on Biomedical Engineering and 2018 3rd International Iranian Conference on Biomedical Engineering, ICBME 2018*, Jul. 2018, doi: 10.1109/ICBME.2018.8703594.

[37] C. M. Carbonaro *et al.*, "High efficient fluorescent stable colloidal sealed dye-doped mesostructured silica nanoparticles," *Microporous Mesoporous Mater.*, vol. 225, pp. 432–439, May 2016, doi: 10.1016/j.micromeso.2016.01.028.

[38] E. Y. Trofimova, D. A. Kurdyukov, Y. A. Kukushkina, M. A. Yagovkina, and V. G. Golubev, "Synthesis of monodispersed mesoporous spheres of submicron size amorphous silica," *Glas. Phys. Chem.*, vol. 37, no. 4, pp. 378–384, Aug. 2011, doi: 10.1134/S108765961104016X.

[39] E. Yu Trofimova *et al.*, "Monodisperse spherical mesoporous silica particles: fast synthesis procedure and fabrication of photonic-crystal films," *Nanotechnology*, vol. 24, no. 15, p. 155601, Apr. 2013, doi: 10.1088/0957-4484/24/15/155601.

[40] E. Y. Stovpiaga, D. A. Kurdyukov, Y. A. Kukushkina, V. V. Sokolov, and M. A. Yagovkina, "Monodisperse spherical silica particles with controlled-varied diameter of micro- and mesopores," *Glas. Phys. Chem.*, vol. 41, no. 3, pp. 316–323, May 2015, doi: 10.1134/S1087659615030153.

[41] D. A. Kurdyukov *et al.*, "High-surface area spherical micro-mesoporous silica particles," *Microporous Mesoporous Mater.*, vol. 223, pp. 225–229, Mar. 2016, doi: 10.1016/j.micromeso.2015.11.018.

[42] S. V Shmakov, V. V Klimenko, S. V Konyakhin, D. A. Eurov, D. A. Kurdyukov, and V. G. Golubev, "Investigation of Toxic Effect and Penetration into Cells of Monodisperse Spherical Composite Particles Based on Mesoporous Silica," *Tech. Phys.*, vol. 63, no. 9, pp. 1316–1322, Sep. 2018, doi: 10.1134/S1063784218090190.

[43] J. Tao *et al.*, “Facile synthesis of yolk–shell structured monodisperse mesoporous organosilica nanoparticles by a mild alkalescent etching approach,” *J. Colloid Interface Sci.*, vol. 527, pp. 33–39, Oct. 2018, doi: 10.1016/j.jcis.2018.05.024.

[44] A. Baliś and S. Zapotoczny, “Tailored Synthesis of Core-Shell Mesoporous Silica Particles—Optimization of Dye Sorption Properties,” *Nanomaterials*, vol. 8, no. 4, p. 230, Apr. 2018, doi: 10.3390/nano8040230.

[45] W. Sun *et al.*, “Monodisperse and Uniform Mesoporous Silicate Nanosensitizers Achieve Low-Dose X-Ray-Induced Deep-Penetrating Photodynamic Therapy,” *Adv. Mater.*, vol. 31, no. 16, p. 1808024, Apr. 2019, doi: 10.1002/adma.201808024.

[46] C. E. Fowler, D. Khushalani, B. Lebeau, and S. Mann, “Nanoscale Materials with Mesostructured Interiors,” *Adv. Mater.*, vol. 13, no. 9, pp. 649–652, May 2001, doi: 10.1002/1521-4095(200105)13:9<649::AID-ADMA649>3.0.CO;2-G.

[47] R. I. Nooney, D. Thirunavukkarasu, Y. Chen, R. Josephs, and A. E. Ostafin, “Synthesis of Nanoscale Mesoporous Silica Spheres with Controlled Particle Size,” *Nature*, 2002, doi: 10.1021/cm0204371.

[48] J. Rathousky, M. Zukalova, P. J. Kooyman, and A. Zukal, “Synthesis and characterization of colloidal MCM-41,” *Colloids Surfaces A Physicochem. Eng. Asp.*, vol. 241, no. 1–3, pp. 81–86, 2004, doi: 10.1016/j.colsurfa.2004.04.014.

[49] M. Yu *et al.*, “A simple approach to prepare monodisperse mesoporous silica nanospheres with adjustable sizes,” *J. Colloid Interface Sci.*, vol. 376, no. 1, pp. 67–75, 2012, doi: 10.1016/j.jcis.2012.03.014.

[50] T. W. Kim, P. W. Chung, and V. S. Y. Lin, “Facile synthesis of monodisperse spherical MCM-48 mesoporous silica nanoparticles with controlled particle size,” *Chem. Mater.*, vol. 22, no. 17, pp. 5093–5104, Sep. 2010, doi: 10.1021/cm1017344.

[51] Y. S. Lin and C. L. Haynes, “Synthesis and characterization of biocompatible and size-tunable multifunctional porous silica nanoparticles,” *Chem. Mater.*, vol. 21, no. 17, pp. 3979–3986, 2009, doi: 10.1021/cm901259n.

[52] T. Yokoi, Y. Sakamoto, O. Terasaki, Y. Kubota, T. Okubo, and T. Tatsumi, “Periodic arrangement of silica nanospheres assisted by amino acids,” *J. Am. Chem. Soc.*, vol. 128, no. 42, pp. 13664–13665, 2006, doi: 10.1021/ja065071y.

[53] L. Pan *et al.*, “Nuclear-Targeted Drug Delivery of TAT Peptide-Conjugated Monodisperse Mesoporous Silica Nanoparticles,” *J. Am. Chem. Soc.*, vol. 134, no. 13, pp. 5722–5725, Apr. 2012, doi: 10.1021/ja211035w.

[54] P. Sun *et al.*, “Biopebble Containers: DNA-Directed Surface Assembly of Mesoporous Silica Nanoparticles for Cell Studies,” *Small*, vol. 15, no. 20, p. 1900083, May 2019, doi: 10.1002/smll.201900083.

[55] K. Ikari, K. Suzuki, and H. Imai, “Structural control of mesoporous silica nanoparticles in a binary surfactant system,” *Langmuir*, vol. 22, no. 2, pp. 802–806, 2006, doi: 10.1021/la0525527.

[56] K. Suzuki, K. Ikari, and H. Imai, “Synthesis of Silica Nanoparticles Having a Well-Ordered Mesostructure Using a Double Surfactant System,” *J. Am. Chem. Soc.*, vol. 126, no. 2, pp. 462–463, Jan. 2004, doi: 10.1021/ja038250d.

[57] M. Bouchoucha, M.-F. Côté, R. C.-Gaudreault, M.-A. Fortin, and F. Kleitz, “Size-

Controlled Functionalized Mesoporous Silica Nanoparticles for Tunable Drug Release and Enhanced Anti-Tumoral Activity," *Chem. Mater.*, vol. 28, no. 12, pp. 4243–4258, Jun. 2016, doi: 10.1021/acs.chemmater.6b00877.

[58] H. Yamada, C. Urata, Y. Aoyama, S. Osada, Y. Yamauchi, and K. Kuroda, "Preparation of colloidal mesoporous silica nanoparticles with different diameters and their unique degradation behavior in static aqueous systems," *Chem. Mater.*, vol. 24, no. 8, pp. 1462–1471, Apr. 2012, doi: 10.1021/cm3001688.

[59] H. Yamada, C. Urata, E. Yamamoto, S. Higashitamori, Y. Yamauchi, and K. Kuroda, "Effective Use of Alkoxysilanes with Different Hydrolysis Rates for Particle Size Control of Aqueous Colloidal Mesostructured and Mesoporous Silica Nanoparticles by the Seed-Growth Method," *ChemNanoMat*, vol. 1, no. 3, pp. 194–202, Jul. 2015, doi: 10.1002/cnma.201500010.

[60] H. Yamada, H. Ujiie, C. Urata, E. Yamamoto, Y. Yamauchi, and K. Kuroda, "A multifunctional role of trialkylbenzenes for the preparation of aqueous colloidal mesostructured/mesoporous silica nanoparticles with controlled pore size, particle diameter, and morphology," *Nanoscale*, vol. 7, no. 46, pp. 19557–19567, 2015, doi: 10.1039/C5NR04465K.

[61] K. Möller, J. Kobler, and T. Bein, "Colloidal suspensions of mercapto-functionalized nanosized mesoporous silica," *J. Mater. Chem.*, vol. 17, no. 7, pp. 624–631, 2007, doi: 10.1039/B611931J.

[62] J. Kobler, K. Möller, and T. Bein, "Colloidal Suspensions of Functionalized Mesoporous Silica Nanoparticles," *ACS Nano*, vol. 2, no. 4, pp. 791–799, Apr. 2008, doi: 10.1021/nn700008s.

[63] V. Cauda, C. Argyo, A. Schlossbauer, and T. Bein, "Controlling the delivery kinetics from colloidal mesoporous silica nanoparticles with pH-sensitive gates," *J. Mater. Chem.*, vol. 20, no. 21, p. 4305, 2010, doi: 10.1039/b918590a.

[64] V. Cauda, C. Argyo, and T. Bein, "Impact of different PEGylation patterns on the long-term bio-stability of colloidal mesoporous silica nanoparticles," *J. Mater. Chem.*, vol. 20, no. 39, pp. 8693–8699, Oct. 2010, doi: 10.1039/c0jm01390k.

[65] R. Guillet-Nicolas, J.-L. Bridot, Y. Seo, M.-A. Fortin, and F. Kleitz, "Enhanced Relaxometric Properties of MRI 'Positive' Contrast Agents Confined in Three-Dimensional Cubic Mesoporous Silica Nanoparticles," *Adv. Funct. Mater.*, vol. 21, no. 24, pp. 4653–4662, Dec. 2011, doi: 10.1002/adfm.201101766.

[66] M. Bouchoucha, É. Béliveau, F. Kleitz, F. Calon, and M.-A. Fortin, "Antibody-conjugated mesoporous silica nanoparticles for brain microvessel endothelial cell targeting," *J. Mater. Chem. B*, vol. 5, no. 37, pp. 7721–7735, Sep. 2017, doi: 10.1039/C7TB01385J.

[67] E. Juère *et al.*, "In Vitro Dissolution, Cellular Membrane Permeability, and Anti-Inflammatory Response of Resveratrol-Encapsulated Mesoporous Silica Nanoparticles," *Mol. Pharm.*, vol. 14, no. 12, pp. 4431–4441, Dec. 2017, doi: 10.1021/acs.molpharmaceut.7b00529.

[68] M. Bouchoucha, R. B. Van Heeswijk, Y. Gossuin, F. Kleitz, and M. A. Fortin, "Fluorinated mesoporous silica nanoparticles for binuclear probes in 1H and 19F Magnetic Resonance Imaging," *Langmuir*, vol. 33, no. 40, pp. 10531–10542, Oct. 2017, doi: 10.1021/acs.langmuir.7b01792.

[69] S. Sarkis, F. Silencieux, K. E. Markwick, M.-A. Andréfortin, and C. A. Hoesli, “Magnetic Resonance Imaging of Alginate Beads Containing Pancreatic Beta Cells and Paramagnetic Nanoparticles,” 2017, doi: 10.1021/acsbiomaterials.7b00404.

[70] Z. Chaudhary *et al.*, “Efficient photoacoustic imaging using indocyanine green (ICG) loaded functionalized mesoporous silica nanoparticles,” *Biomater. Sci.*, vol. 7, no. 12, pp. 5002–5015, Dec. 2019, doi: 10.1039/C9BM00822E.

[71] J. Wang, M. Xu, K. Wang, and Z. Chen, “Stable mesoporous silica nanoparticles incorporated with MoS2 and AIE for targeted fluorescence imaging and photothermal therapy of cancer cells,” *Colloids Surfaces B Biointerfaces*, vol. 174, pp. 324–332, Feb. 2019, doi: 10.1016/j.colsurfb.2018.11.030.

[72] C.-Y. Lin, C.-M. Yang, and M. Lindén, “Influence of serum concentration and surface functionalization on the protein adsorption to mesoporous silica nanoparticles,” *RSC Adv.*, vol. 9, no. 58, pp. 33912–33921, Oct. 2019, doi: 10.1039/C9RA05585A.

[73] J. Zhuang, J. Zhang, M. Wu, and Y. Zhang, “A Dynamic 3D Tumor Spheroid Chip Enables More Accurate Nanomedicine Uptake Evaluation,” *Adv. Sci.*, vol. 6, no. 22, p. 1901462, Nov. 2019, doi: 10.1002/advs.201901462.

[74] E. Juère *et al.*, “Gastro-protective protein-silica nanoparticles formulation for oral drug delivery: In vitro release, cytotoxicity and mitochondrial activity,” *Eur. J. Pharm. Biopharm.*, vol. 151, pp. 171–180, Jun. 2020, doi: 10.1016/j.ejpb.2020.03.015.

[75] D.-J. Koo, J. Choi, M. Ahn, B. H. Ahn, D.-H. Min, and S.-Y. Kim, “Large-Scale 3D Optical Mapping and Quantitative Analysis of Nanoparticle Distribution in Tumor Vascular Microenvironment,” *Bioconjug. Chem.*, vol. 31, no. 7, pp. 1784–1794, Jul. 2020, doi: 10.1021/acs.bioconjchem.0c00263.

[76] M. Deaconu *et al.*, “Norfloxacin delivery systems based on MCM-type silica carriers designed for the treatment of severe infections,” *Mater. Chem. Phys.*, vol. 238, p. 121886, Dec. 2019, doi: 10.1016/j.matchemphys.2019.121886.

[77] F. Mirante, N. Gomes, M. C. Corvo, S. Gago, and S. S. Balula, “Polyoxomolybdate based ionic-liquids as active catalysts for oxidative desulfurization of simulated diesel,” *Polyhedron*, vol. 170, pp. 762–770, Sep. 2019, doi: 10.1016/j.poly.2019.06.019.

[78] F. Mirante *et al.*, “Mesoporous nanosilica-supported polyoxomolybdate as catalysts for sustainable desulfurization,” *Microporous Mesoporous Mater.*, vol. 275, pp. 163–171, Feb. 2019, doi: 10.1016/j.micromeso.2018.07.036.

[79] I. Mukherjee *et al.*, “Effect of nonsurfactant template content on the particle size and surface area of monodisperse mesoporous silica nanospheres,” *Microporous Mesoporous Mater.*, vol. 122, no. 1–3, pp. 168–174, Jun. 2009, doi: 10.1016/j.micromeso.2009.02.030.

[80] K. D. Hartlen, A. P. T. Athanasopoulos, and V. Kitaev, “Facile preparation of highly monodisperse small silica spheres (15 to >200 nm) suitable for colloidal templating and formation of ordered arrays,” *Langmuir*, vol. 24, no. 5, pp. 1714–1720, Mar. 2008, doi: 10.1021/la7025285.

[81] T. Yokoi *et al.*, “Mechanism of formation of uniform-sized silica nanospheres catalyzed by basic amino acids,” *Chem. Mater.*, vol. 21, no. 15, pp. 3719–3729, Aug. 2009, doi: 10.1021/cm900993b.

[82] Q. Zhao *et al.*, “Dual-stimuli responsive hyaluronic acid-conjugated mesoporous silica

for targeted delivery to CD44-overexpressing cancer cells," *Acta Biomater.*, vol. 23, pp. 147–156, 2015, doi: 10.1016/j.actbio.2015.05.010.

[83] L. S. Wang *et al.*, "Biofunctionalized phospholipid-capped mesoporous silica nanoshuttles for targeted drug delivery: Improved water suspensibility and decreased nonspecific protein binding," *ACS Nano*, vol. 4, no. 8, pp. 4371–4379, 2010, doi: 10.1021/nn901376h.

[84] A. Yildirim, G. B. Demirel, R. Erdem, B. Senturk, T. Tekinay, and M. Bayindir, "Pluronic polymer capped biocompatible mesoporous silica nanocarriers," *Chem. Commun.*, vol. 49, no. 84, pp. 9782–9784, 2013, doi: 10.1039/c3cc45967e.

[85] J. D. Robertson *et al.*, "Purification of Nanoparticles by Size and Shape," *Sci. Rep.*, vol. 6, pp. 1–9, 2016, doi: 10.1038/srep27494.

[86] B. N. Khlebtsov, V. A. Khanadeev, and N. G. Khlebtsov, "Determination of the Size, Concentration, and Refractive Index of Silica Nanoparticles from Turbidity Spectra," *Langmuir*, vol. 24, no. 16, pp. 8964–8970, Aug. 2008, doi: 10.1021/la8010053.

[87] W. Zhao, W. Ji, Y. Zhang, L. Du, and S. Wang, "A competitive fluorescence quenching-based immunoassay for bisphenol A employing functionalized silica nanoparticles and nanogold," *RSC Adv.*, vol. 6, no. 45, pp. 38950–38956, Apr. 2016, doi: 10.1039/C5RA26366B.

[88] J. Verma, "Analysis on Synthesis of Silica Nanoparticles and its Effect on Growth of T. Harzianum & Rhizoctonia Species," *Biomed. J. Sci. Tech. Res.*, vol. 10, no. 4, Oct. 2018, doi: 10.26717/BJSTR.2018.10.001972.

[89] V. Balakrishnan, H. Azwana, A. Wab, K. A. Razak, and S. Shamsuddin, "Vitro Evaluation of Cytotoxicity of Colloidal Amorphous Silica Nanoparticles Designed for Drug Delivery on Human Cell Lines," *J. Nanomater.*, vol. 2013, 2013, doi: 10.1155/2013/729306.

[90] W. Zhao, W. Ji, Y. Zhang, L. Du, and S. Wang, "A competitive fluorescence quenching-based immunoassay for bisphenol A employing functionalized silica nanoparticles and nanogold †," 2016, doi: 10.1039/c5ra26366b.

[91] I. A. Rahman, P. Vejayakumaran, C. S. Sipaut, J. Ismail, and C. K. Chee, "Size-dependent physicochemical and optical properties of silica nanoparticles," *Mater. Chem. Phys.*, vol. 114, no. 1, pp. 328–332, Mar. 2009, doi: 10.1016/J.MATCHEMPHYS.2008.09.068.

[92] B. N. Khlebtsov, V. A. Khanadeev, and N. G. Khlebtsov, "Determination of the Size, Concentration, and Refractive Index of Silica Nanoparticles from Turbidity Spectra," *Langmuir*, vol. 24, no. 16, pp. 8964–8970, Aug. 2008, doi: 10.1021/la8010053.

[93] X. Lu and R. M. Murphy, "Nanoparticle tracking for protein aggregation research," in *Methods in Molecular Biology*, vol. 1777, Humana Press Inc., 2018, pp. 145–158.

[94] W. Y. Sang and O. P. Ching, "Tailoring MCM-41 mesoporous silica particles through modified sol-gel process for gas separation," in *AIP Conference Proceedings*, Oct. 2017, vol. 1891, no. 1, p. 020147, doi: 10.1063/1.5005480.

[95] Z. Zhang, A. Mayoral, and I. Melián-Cabrera, "Protocol optimization for the mild detemplation of mesoporous silica nanoparticles resulting in enhanced texture and colloidal stability," *Microporous Mesoporous Mater.*, vol. 220, pp. 110–119, Jan. 2016, doi: 10.1016/j.micromeso.2015.08.026.

[96] K. J. Edler, "Current understanding of formation mechanisms in surfactant-templated

materials," *Aust. J. Chem.*, vol. 58, no. 9, pp. 627–643, 2005, doi: 10.1071/CH05141.

[97] M. J. Hollamby, D. Borisova, P. Brown, J. Eastoe, I. Grillo, and D. Shchukin, "Growth of mesoporous silica nanoparticles monitored by time-resolved small-angle neutron scattering," *Langmuir*, vol. 28, no. 9, pp. 4425–4433, 2012, doi: 10.1021/la203097x.

[98] R. Deshpande, D.-W. Hua, D. M. Smith, and C. J. Brinker, "Pore structure evolution in silica gel during aging/drying. III. Effects of surface tension," *J. Non. Cryst. Solids*, vol. 144, no. C, pp. 32–44, Jan. 1992, doi: 10.1016/S0022-3093(05)80380-1.

[99] J. Kecht and T. Bein, "Functionalization of Colloidal Mesoporous Silica by Metalorganic Reagents," *Langmuir*, vol. 24, no. 24, pp. 14209–14214, Dec. 2008, doi: 10.1021/la802115n.

[100] F. Catalano and P. P. Pompa, "Design Rules for Mesoporous Silica toward the Nanosize: A Systematic Study," *ACS Appl. Mater. Interfaces*, vol. 11, no. 50, pp. 47237–47246, 2019, doi: 10.1021/acsami.9b16135.

[101] T. T. Hoang Thi, V. Du Cao, T. N. Q. Nguyen, D. T. Hoang, V. C. Ngo, and D. H. Nguyen, "Functionalized mesoporous silica nanoparticles and biomedical applications," *Mater. Sci. Eng. C*, vol. 99, no. November 2017, pp. 631–656, 2019, doi: 10.1016/j.msec.2019.01.129.

[102] R. P. Bagwe, L. R. Hilliard, and W. Tan, "Surface Modification of Silica Nanoparticles to Reduce Aggregation and Nonspecific Binding," *Langmuir*, vol. 22, no. 9, pp. 4357–4362, Apr. 2006, doi: 10.1021/la052797j.

[103] T. Asefa and Z. Tao, "Biocompatibility of Mesoporous Silica Nanoparticles," 2012, doi: 10.1021/tx300166u.

[104] M. Varache *et al.*, "Loading of Cisplatin into Mesoporous Silica Nanoparticles: Effect of Surface Functionalization," 2019, doi: 10.1021/acs.langmuir.9b00954.

[105] F. Lu *et al.*, "A General Strategy to Encapsulate Semiconducting Polymers within PEGylated Mesoporous Silica Nanoparticles for Optical Imaging and Drug Delivery," *Part. Part. Syst. Charact.*, vol. 37, no. 6, p. 1900483, Jun. 2020, doi: 10.1002/ppsc.201900483.

[106] J. Gu, J. Liu, Y. Li, W. Zhao, and J. Shi, "One-pot synthesis of mesoporous silica nanocarriers with tunable particle sizes and pendent carboxylic groups for cisplatin delivery," *Langmuir*, vol. 29, no. 1, pp. 403–410, Jan. 2013, doi: 10.1021/la3036264.

[107] E. Yamamoto, M. Kitahara, T. Tsumura, and K. Kuroda, "Preparation of size-controlled monodisperse colloidal mesoporous silica nanoparticles and fabrication of colloidal crystals," *Chem. Mater.*, vol. 26, no. 9, pp. 2927–2933, 2014, doi: 10.1021/cm500619p.

[108] S. Liu and M. Han, "Synthesis, functionalization, and bioconjugation of monodisperse, silica-coated gold nanoparticles: Robust bioprobes," *Adv. Funct. Mater.*, vol. 15, no. 6, pp. 961–967, Jun. 2005, doi: 10.1002/adfm.200400427.

[109] J. Chen, R. Zhang, L. Han, B. Tu, and D. Zhao, "One-pot synthesis of thermally stable gold@mesoporous silica core-shell nanospheres with catalytic activity," *Nano Res.*, vol. 6, no. 12, pp. 871–879, Sep. 2013, doi: 10.1007/s12274-013-0363-1.

[110] I. B. da C. J. Meireles, M. F. Cipreste, P. L. Gastelois, W. A. de A. Macedo, D. A. Gomes, and E. M. B. de Sousa, "Synthesis and characterization of gold nanorods coated by mesoporous silica MCM-41 as a platform for bioapplication in photohyperthermia,"

*Nanotechnology*, vol. 32, no. 50, p. 505720, Dec. 2021, doi: 10.1088/1361-6528/ac28db.

[111] N. A. Zainal, S. R. A. Shukor, H. A. A. Wab, and K. A. Razak, "Study on the effect of synthesis parameters of silica nanoparticles entrapped with rifampicin," *Chem. Eng. Trans.*, vol. 32, pp. 2245–2250, 2013, doi: 10.3303/CET1332375.

[112] V. Cauda, C. Argyo, D. G. Piercey, and T. Bein, "'Liquid-phase calcination' of colloidal mesoporous silica nanoparticles in high-boiling solvents," *J. Am. Chem. Soc.*, vol. 133, no. 17, pp. 6484–6486, May 2011, doi: 10.1021/ja1067492.

[113] H. Yamada, C. Urata, E. Yamamoto, S. Higashitamori, Y. Yamauchi, and K. Kuroda, "Effective Use of Alkoxysilanes with Different Hydrolysis Rates for Particle Size Control of Aqueous Colloidal Mesostructured and Mesoporous Silica Nanoparticles by the Seed-Growth Method," *ChemNanoMat*, vol. 1, no. 3, pp. 194–202, Jul. 2015, doi: 10.1002/cnma.201500010.

[114] E. Yamamoto and K. Kuroda, *Preparation and Controllability of Mesoporous Silica Nanoparticles*, 1st ed., vol. 44. Elsevier Inc., 2018. doi: 10.1016/bs.enz.2018.09.001

[115] A. Parola, S. Buzzaccaro, E. Secchi, and R. Piazza, "Sedimentation equilibrium and the generalized Archimedes' principle," *J. Chem. Phys*, vol. 138, p. 114907, 2013, doi: 10.1063/1.4795427.

[116] Y. Zimmels, "Generalized buoyancy forces in dispersions," *J. Appl. Phys.*, vol. 68, no. 5, pp. 2007–2012, Sep. 1990, doi: 10.1063/1.346550.

[117] X. Lv, L. Zhang, F. Xing, and H. Lin, "Controlled synthesis of monodispersed mesoporous silica nanoparticles: Particle size tuning and formation mechanism investigation," *Microporous Mesoporous Mater.*, vol. 225, pp. 238–244, 2016, doi: 10.1016/j.micromeso.2015.12.024.

[118] E. Yamamoto, A. Shimojima, H. Wada, and K. Kuroda, "Mesoporous Silica Nanoparticles with Dispersibility in Organic Solvents and Their Versatile Surface Modification," *Langmuir*, vol. 36, no. 20, pp. 5571–5578, May 2020, doi: 10.1021/acs.langmuir.0c00729.

[119] R. Rajagopalan and J. V. Yakhmi, *Chapter 8 - Nanotechnological approaches toward cancer chemotherapy*. Elsevier Inc., 2017.

[120] E. Piktel, K. Niemirowicz, M. Watek, T. Wollny, P. Deptuła, and R. Bucki, "Recent insights in nanotechnology-based drugs and formulations designed for effective anti-cancer therapy," *J. Nanobiotechnology*, vol. 14, no. 1, pp. 1–23, 2016, doi: 10.1186/s12951-016-0193-x.

[121] G. E. Musso, E. Bottinelli, L. Celi, G. Magnacca, and G. Berlier, "Influence of surface functionalization on the hydrophilic character of mesoporous silica nanoparticles," *Phys. Chem. Chem. Phys.*, vol. 17, no. 21, pp. 13882–13894, 2015, doi: 10.1039/C5CP00552C.

[122] D. Tarn, C. E. Ashley, M. Xue, E. C. Carnes, J. I. Zink, and C. Jeffrey Brinker, "Mesoporous Silica Nanoparticle Nanocarriers-Biofunctionality and Biocompatibility," *Acc Chem Res*, vol. 46, no. 3, pp. 792–801, 2013, doi: 10.1021/ar3000986.

[123] M. Kaasalainen *et al.*, "Size, Stability, and Porosity of Mesoporous Nanoparticles Characterized with Light Scattering," *Nanoscale Res. Lett.*, vol. 12, no. 1, p. 74, Dec. 2017, doi: 10.1186/s11671-017-1853-y.

# CHAPTER 6: THE IMPLICATIONS OF CALCINATION AND EXTRACTION OF THE SURFACTANT IN MCM-41-TYPE MSN

# 6. THE IMPLICATIONS OF CALCINATION AND EXTRACTION OF THE SURFACTANT IN MCM-41-TYPE MSN

## 6.1. INTRODUCTION

### 6.1.1. Surfactant removal of MSN

Surfactant is an essential agent to synthesise MSN by a template-directed method. Nevertheless, once MSN are formed, the elimination of the surfactant from the pores is mandatory in almost all the cases. In this sense, the pores must be emptied to host inside them other compounds, such as active pharmaceutical ingredients or dyes. On the other hand, the presence of surfactant can cause cytotoxicity when the particles are used in biomedical applications. In case of CTAB, which is the main surfactant used in the synthesis of MCM-41-type MSN, their toxicity is found even at residual concentrations [1][2][3].

In the last decades, different methods to eliminate the surfactant have been developed, such as calcination, extraction, or dialysis. Regarding the procedure employed, the properties of the nanoparticles can be strongly affected. Some parameters influenced by the elimination procedure are the surfactant elimination efficiency [4][3], the silica condensation degree [5], the mesoporosity [4][6] and the aggregation between nanoparticles [7][8][9]. Therefore, the removal of the surfactant plays an important role in the preparation of MSN, whose implications must be studied in a systematic manner.

According to that, the elimination of surfactant is not a trivial issue and presents some limitations. In this context, even some groups decided to use of non-surfactant templates in the synthesis of MSN [10].

#### 6.1.1.1. Calcination

Calcination is the most frequently applied method to remove the surfactant, due to its simplicity and effectivity [11]. It is based on the thermal treatment of samples in order to provoke the combustion and oxidation of the organic compounds. The temperature and time required to eliminate the surfactant depends on the surfactant employed. In case of non-ionic co-polymer surfactants, the temperature employed is in the range of 300 to 350 °C [5][12]. However, the cationic surfactants, such as the CTAB, are more difficult to be removed due to the strong interactions between the silica framework and the surfactant molecules. Hence, higher temperatures in the range of 450 °C to 600 °C are required, as lower ones lead to incomplete decomposition [3][10][12]. The most frequently reported calcination temperature to remove the CTAB in MSN is 550 °C ([13][14][15][16][17]). Additionally, during the calcination process, the silicate framework is consolidated via thermal condensation of non-bound silanol groups and elimination of structural defects [11][18]. This consolidation gives rise to strengthened and more stable materials [5].

Nevertheless, the calcination and the derived consolidation of the framework has also negative implications, as an strong condensation of the silanols on the surface [5][19], which reduces the

number of silanol groups compared to the as-made samples [11]. This reduction affects to the reactivity of MSN surface, since its functionalisation capacity is minimised [5]. Besides, the calcination process is incompatible with the co-condensation synthesis method or the functionalisation prior to the surfactant elimination [11].

Furthermore, high condensation of silanols provokes significant network shrinkage, which can impair the mesostructured framework of MSN [5][20][21]. Apart from this, it is also reported that calcination induces significant agglomeration of nanoparticles due to the formation of interparticle bonds [7][8][9][11][19].

In this context, some authors reported the application of calcination at lower temperatures [5], such as 500 °C [22][23][24][25], but they did not explain the implications in the silica framework with respect to the temperature chosen. In fact, most of them belong to the first studies on mesoporous materials in the 90s.

#### 6.1.1.2. Solvent extraction

The solvent extraction procedure was developed to avoid the disadvantages the calcination presents [26]. It consists of the elimination of surfactant by washing it with specific solutions. The solutions employed must be able to weaken the bonds between the silica surface and the surfactant. Generally, the process is facilitated using refluxing conditions. In case of ionic surfactants, ionic exchange is required to replace the electrostatic bonds between the silica and the surfactant. For this purpose, the solutions prepared to wash the CTAB include a cation by which the cation $CTA^+$ is substituted. Some examples are the use of HCl [2][3][27][28][29][30], NaCl [31][32] or $NH_4NO_3$ [33][34][1]. On the other hand, the solubilisation of the surfactant is important in this process, so the solvents used are those in which the CTAB is strongly soluble. The most commonly used are ethanol [35] and methanol [27][34], but other solvents can be used, such as 1,4-dioxane [29]. Regarding the effectiveness of complete template removal, some studies report the extraction with $NH_4NO_3$ or HCl remove completely the FTIR bands associated to $CTA^+$ [3][14][34][36][37], although other studies differ [2][29].

In the case of the use of an extraction method, the silanol condensation is much lower than that provoked by calcination [9]. Consequently, the amount of silanol groups on the surface is higher, obtaining suitable materials to be functionalised. In this sense, extraction is a less aggressive method that provokes less shrinkage in the network. In addition, the method is compatible with co-condensed materials and its prior functionalisation [11]. Although, as a counterpart, extracted materials are less consolidated and lack of hydrothermal stability [18].

Another advantage found in the reported extraction procedures is its compatibility with the suspendability of nanoparticles. When extraction procedures are used the suspended nanoparticles do not need to be dried, and that is the reason why this method can be transferable to colloidal MSN [19]. Additionally, the use of extraction method is also reported to be involved in the dissociation of interparticle silanol bonds [11].

Nevertheless, the main limitation that can be found in extraction method is that some template usually remains in the inside of the mesopores due to strong electrostatic or hydrogen bonding interactions [2][4] [11][18], which can be associated with the materials cytotoxicity [6]. In

addition, the template elimination by solvent extraction is usually time consuming, it requires large volume of solvents, which, in spite of the possibility of being recycled, present difficulties in the scalability of the process and environmental implications [10][11][18]. It is also reported that the repeated exposure to organic solvents during extraction may result in possible accumulation of free radicals in the MSN and unexpected negative consequences toward cells [6].

#### 6.1.1.3. Other methods

Alternative methods have been developed in order to find suitable surfactant removal procedures according to the applications of the materials. For example, some authors have applied dialysis to remove the template. This procedure is mainly based on the same principles as solvent extraction. However, it uses a dialysis membrane to retain the nanoparticles and facilitate the sequential renewal of the solvent in order to shift the equilibrium and force the exchange and removal of the surfactant. The solution most commonly employed is acetic acid in ethanol [38][39][40][41], but other salts such as NaCl [42] or solvents such as 2-propanol [43] are also used. The method is reported to be effective in the complete elimination of surfactant [39][44][45]. Other advantages of using this method are that the silica framework barely varies after being dialysed and the silanol condensation is quite limited [40], although the main benefit is its compatible use with colloidal and disperse MSN, since it avoids the dry-resuspension cycles and the sharp changes in solvent or solutions [9][41][44][46]. Nevertheless, the dialysis process is steeply time-consuming, in the range of several days to weeks. Moreover, it requires a large amount of solvents, which provokes limitations in the field of natural environment and costs for a scalable production [34].

The treatment of MSN with hydrogen peroxide was also developed to remove polymeric templates [11][47]. It is based on advanced oxidation process, via reactive oxygen species (such as $OH^{\cdot}$), which are able to completely degrade the organic compounds into $CO_2$ and $H_2O$. Compared to calcination and extraction methods, the shrinkage is reduced, and high relative surface and pore volumes are obtained. Additionally, the number of silanol groups in the surface are large. Nevertheless, the procedure is time consuming and requires the use of an iron catalyst, which can lead to the presence of iron residues.

Other less common methods have been developed, such as ether cleavage [11], pyrolysis in $N_2$ flow [12], methanol-enhanced supercritical $CO_2$ extraction [48], non-thermal plasma oxidation [20][49] and methods derived from calcination, such as rapid calcination or microwave-assisted calcination [11] or liquid-phase calcination [7].

### 6.1.2. Silanol groups in MSN

The proportion of silanol groups in the MSN is closely related to the method employed for the surfactant removal. These silanol groups play an important role in some properties of the MSN such as their surface reactivity [6]. Also, the surface charge is associated with the presence of the silanol groups since they can be deprotonated to form silanolates, which are negatively

charged. The negative charge that the surface of the MSN acquires can be determinant in the formation of electrostatic repulsive forces that hinder the aggregation and sedimentation of particles. Furthermore, the silanol groups give the surface of the nanoparticles certain polarity and ability to form hydrogen bonds with aqueous or protic solvents. The siloxane bonds on the surface can lead to increased hydrophobicity and reduced negative charge on the surface, for example [47]. In this sense, the chemistry of the MSN surface, determined mainly by the presence of silanol groups, influences the adsorption capacity of some molecules, such as gases [50], as well as the interaction with specific molecules, such as drugs, dyes or other active pharmaceutical ingredients [6][51]. Even, it has be reported the relation between the amount of silanol groups and the toxicity or haemolytic activity of nanoparticles [52][53].

The silanol groups found in MSN can be classified into different types according to their position in the nanoparticle, their connectivity with silica tetrahedron and the proximity to each other [50][54]. In Figure 1 a schematic representation of the types of silanol groups are shown. On the one hand, regarding their position in the nanoparticles, they can be found in the external surface, the mesopores surface or the internal framework of the nanoparticles. In this sense, it is estimated that the external silanol groups represent only the 6% of the total silanol groups in a particle [55]. On the other hand, in respect of their connectivity with silica atoms, they can be isolated silanol groups when silicon is $Q_3$ type (≡Si-OH), or geminal silanol groups in case of $Q_2$ silicon (=Si-$(OH)_2$), namely, a silicon atom that is bonded to two "OH" groups. Finally, with regard to their proximity to each other, they can be isolated or vicinal, that is, if they are close enough to interact and form hydrogen bonds among them. By contrast, if silanol groups are condensed and they form siloxane bonds, the silicon state is $Q_4$ (≡Si-O-Si≡).

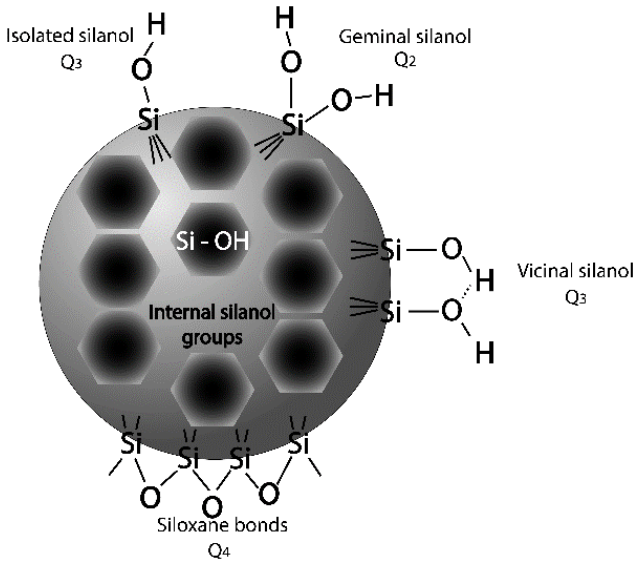


*Figure 1. Schematic representation of silanols types in MSN. Adapted from reference* [50]. *Copyright © 2005 Springer.*

The formation of silanol groups usually occurs during the course of MSN synthesis, due to the incomplete condensation of the silica obtained from the hydrolysed precursor molecules. This can be because the silanol groups are not close enough to react and/or the reaction is not thermodynamically or cinematically favoured due to temperature, pH, or time conditions. It should be noted that hydrolysis and condensation of silica occur in a dynamic equilibrium during

the MSN synthesis. On the other hand, the silanol groups can also be formed through rehydroxylation of condensed siloxane groups in favourable conditions (acidic or alkaline pH, high temperature, aqueous solutions) [50]. For example, this can be produced by solvent extraction method or hydrothermal treatments [11].

### 6.1.3. Biodegradation of MSN

The presence of silanol groups and, ultimately, the silica polymerisation degree of MSN is closely related to their ability to be degraded in determined conditions. This is particularly relevant within the biomedical applications, in which the MSN must be biodegraded in physiological fluids and in an *in vivo* context. Therefore, many researchers in the field of nanomaterials and nanomedicine have focused on this topic in recent years.

In order to develop safe nanomaterials and achieve clinical trials, MSN must be eliminated from the body. The organism has excretion systems that are able to remove soluble molecules and very small particles (< 5 nm) mainly by renal clearance. To that end, MSN must be degraded into orthosilicic acid, $Si(OH)_4$, or derived silica oligomers, which are solubilised in aqueous solutions [6]. This degradation process consists of the breakage, through the hydrolysis, of siloxane bonds (Si-O-Si) by the nucleophilic attack of $H_2O$ molecules, but specially $OH^-$ anions [56][57].

Therefore, two challenges appear in the development of safe and effective MSN in the biomedical context. On the one hand, the obtaining of stable MSN for a period of time that allows the efficient drug loading and functionalisation, as well as their distribution in the organism, the reach to the target organs and the effective release in them [58]. On the other hand, these nanomaterials must be degraded and cleared after their biomedical mission, and they must not accumulate in the body in the long term.

In several *in vitro* and *in vivo* assays MSN have been demonstrated to be biodegradable materials in physiological conditions [56][59]. Nevertheless, they tend to accumulate in the reticuloendothelial (RES)-related organs, such as liver and spleen, where their clearance can take several weeks or even months due to their low degradation rate [60][61][62]. In fact, some toxicity associated with the long-term accumulation has been found [63][64][65]. In this sense, the mechanism and kinetics of MSN degradation are complex processes that depend on the specific properties of the nanoparticles themselves and the surrounding environment [66].

#### 6.1.3.1. Parameters which influence the degradation rate

The rate of silica dissolution or degradation depends on different parameters, such as the concentration of nanoparticles, their structure and surface, the functionalisation, and the degree of condensation of the silica.

The concentration of nanoparticles has been considered very influent on their degradation, since the dissolution of silica, via formation of $Si(OH)_4$, is limited to its solubility constant. Hence, over determined silica concentration, the solubilisation of $Si(OH)_4$ molecules is saturated and the degradation rate is hindered. Consequently, huge differences in degradation rates have

been observed when low or high MSN concentrations are compared [59][67]. In this context, the diffusion of the nanoparticles throughout an organism may help to their degradation, while the concentration in specific organs in higher concentrations may provoke the opposite effect.

On the other hand, some authors demonstrated that the degradation of MSN is independent of the nanoparticles size, but it is highly dependent of the specific surface area and porosity [40][67][68][69]. In particular, the degradation rate can be associated with the amount of surface which is in contact with water molecules. Hence, it has been also observed that colloidal MSN had higher degradation behaviour than aggregated ones, whose surface was partially impeded [40].

As it was mentioned, the silica condensation degree and the presence of silanol groups are also quite influent on the nanoparticles degradation rate [56][70]. In fact, it has been reported that the silanol groups are the initial point for the silica degradation when MSN are suspended in biological fluids [71]. The condensation of silica framework can be determined by the synthesis method, and especially, the surfactant removal procedure. Some synthesis approaches such as low temperature sol-gel synthesis [56], biphasic stratification [64] or free-surfactant method [72] have been used to reduce the silica condensation degree and favour the degradation. Regarding the surfactant elimination method, calcined samples are highly consolidated, and therewith, tend to show remarkably low degradation percentages [67][73][59][74] in comparison with extracted MSN, which present low structural consolidation [75]. However, Bhavsar et al. [76] reported the complete degradation of MSN calcined at 540 °C, in both *in vitro* and *in vivo* studies in less than a week. On the other hand, dialysed MSN presents very low consolidation, similar to extracted ones, which leads to the obtaining of highly degradable MSN [40][77].

The surface functionalisation of MSN has also been demonstrated to promote their hydration and hydrolysis progress, as the functional groups can act as sites to initiate the hydrolysis of the silica [77].

Finally, the surrounding media and environment are also involved in the biodegradation of nanoparticles. The presence of ions in the fluid, such as in the physiological one, favours the degradation process [66] . The pH of the solution can facilitate or slow down the degradation, due to the dependence of the hydrolysis rate with the pH, being higher at alkaline and acidic pH [9]. In this context, the media that generally are used for *in vitro* assays try to simulate the physiological conditions in terms of pH and saline composition and hence, should facilitate the degradation of the nanoparticles. Some media used are PBS at pH 5 and 7.4, simulated buffer fluid (SBF) or cell culture media (like DMEM). Additionally, some complementary components such as foetal bovine serum (FBS) or glutathione reduced (GSH) can be added. The temperature is also influent in the kinetics of the degradation [78] and it has to be set at a physiological value (37 °C).

#### 6.1.3.2. Strategies for promoting the degradation rate

Some effective strategies to improve the MSN degradation have been attempted in the last years [56]. These approaches include modifying the nanoparticles composition or surface as well as including stimuli-responsive bonds within the silica framework [79].

On the one hand, there are many studies that report the improvement of degradation behaviour from doping with metal oxides. The coordination bonds the metals stablish inside the silica network facilitates its degradability in the physiological fluids [32]. In this context, degradability has been successfully achieved with the introduction of metals like calcium [74][80], iron [81], copper [82][83], magnesium and zinc [84], and manganese [32].

On the other hand, the incorporation of organo-bridged alkoxysilanes can help the degradation of MSN framework under specific and controlled conditions, as they can be formed by different organic functional groups [85][62]. They can be prepared by adding organosilanes during the MSN synthesis, which intercalate within the silica framework. Thus, both diselenide [86] and disulphide [64] bridges have been added to MSN in order to promote the degradation through the bio-reducing cellular environment. Carbon dots have also been incorporated into MSN, conferring them swelling and hydrolysable Si-C bonds [87].

### 6.1.4. Conclusions and outlook

In this context, the objective we have set for the present work has been to carry out a systematic study on the implications of the use of different surfactant removal procedures on standard MCM-41-type MSN. The methods tested have been the calcination at different temperatures (400, 450, 500 and 550 °C) and the solvent extraction by using HCl-ethanol and $NH_4NO_3$-ethanol mixtures. Then, some physicochemical properties of the calcined and extracted samples such as the surfactant presence after the elimination step, the silica condensation degree, the mesostructured framework, the colloidal stability, and the surface reactivity, were analysed. In addition, the biocompatibility of nanoparticles was tested, as well as their degradation in a simulated physiological environment, to validate their use in biomedical applications.

## 6.2. MATERIALS AND METHODS

### 6.2.1. Chemicals

The compounds tetraethylorthosilicate (TEOS), 1-hexadecyltrimethylammonium bromide (CTAB), sodium hydroxide (NaOH), Dulbecco's Phosphate Buffered Saline (PBS), ammonium nitrate ($NH_4NO_3$), (3-aminopropyl)triethoxysilane (APTES) and (3-isocyanatopropyl)triethoxysilane (IPTES) were purchased from Sigma-Aldrich. Hydrochloric acid 37% (HCl), acetonitrile, and absolute ethanol were purchased from Scharlab.

### 6.2.2. General techniques

Transmission electron microscopy (TEM), $N_2$ adsorption–desorption isotherms, powder X-ray diffraction (PXRD), Fourier transform infrared spectroscopy (FTIR), solid-state nuclear magnetic resonance (NMR), thermogravimetric analysis (TGA), dynamic light scattering (DLS), electrophoretic light scattering (ELS) and UV-Visible spectroscopy were used in order to characterize the prepared materials. The instruments used were the following: JEOL JEM-1010 microscope for TEM images acquisitions; Bruker D8 Advance diffractometer (Cu Kα radiation) for PXRD measurements; Micromeritics ASAP 2010 automated analyser for recording of $N_2$ adsorption–desorption isotherms, samples were degassed at 120 °C in vacuum overnight. The specific surface areas were calculated from the adsorption data within the low-pressure range using the BET (Brunauer–Emmett–Teller) model. Pore size distribution was determined following the BJH (Barrett–Joyner–Halenda) method. A Bruker Tensor 27 instrument was used to record infrared spectra. ss-NMR were performed in Bruker Avance III 400 WB spectrophotometer. Particle size and ʒ potential in solution were measured by ZetaSizer Nano ZS (Malvern Instruments Ltd.) equipped with a laser of 633 nm and collecting the signal at 173°. FTIR measurements were taken by Bruker Tensor 27 spectrometer. UV-visible measurements were recorded with a JASCO V-650 Spectrophotometer.

### 6.2.3. Synthesis of nanoparticles

1 g of CTAB (2.74 mmol) was mixed with 480 mL of deionised water in a 1L (10.5 cm of outer diameter) cylindrical beaker. The mixture was heated at 50 °C and stirred with a cylindrical and plain magnetic stir bar (60mm long and 15mm diameter) at 500 rpm to dissolve the surfactant. Then, 280 mg of NaOH (7 mmol) dissolved in 3.5 mL of deionised water were added, and the temperature solution was adjusted to 80 °C. A watch glass was placed to cover the beaker to minimize the evaporation solvent and therefore to avoid the volume decreasing during the reaction. When the temperature reached 80 °C, 5 mL of TEOS (25.7 mmol) were added dropwise, using syringe and needle. Soon after, a white precipitate appeared. The mixture was stirred for 2 h. After this time, the suspension was cooled at room temperature, and the solid product was vacuum filtered in a Buchner filtering device over a filter paper (Whatman™ Grade 3MM Chr) and deionised water was added until neutralising the suspension. Then, the solid was dried under vacuum and grinded to obtain a white powder, named **MSN-as made.**

### 6.2.4. Surfactant removal

After the synthesis, different methods were employed to remove the surfactant. Calcination: **MSN-as made** was calcined in an oxidant atmosphere for 5 hours at 400, 450, 500 and 550 °C,

to obtain respectively **MSN-400**, **MSN-450**, **MSN-500** and **MSN-550**. Extraction: the solid was extracted using different solvents. First, 300 mg of the **MSN-as made solid** were suspended and briefly sonicated in 6 ml of fuming HCl in 100 ml ethanol. The suspension was refluxed for 2 hours and washed with ethanol three times. Three cycles of refluxing-washing were performed. The solid was dried during 24 hours at 37°C and finally ground. The obtained material was called **MSN-extHCl**. A similar procedure was followed for the surfactant extraction with ammonium nitrate, but the extracting solution was prepared with 2 mg of $NH_4NO_3$ in 100 ml of ethanol. The solid obtained was called **MSN-ext$NH_4NO_3$**.

### 6.2.5. DLS measurements

DLS samples were prepared suspending and sonicating generously the nanoparticles in distilled water (1 mg NP/ml) and spinning them briefly (at 10,000 rpm) to remove the presence of large aggregates or sedimentation and get quality measurements. ELS samples were prepared suspending and sonicating generously the nanoparticles in distilled water (10 mg NP/ml) and spinning them briefly (at 10,000 rpm) to remove the presence of large aggregates or sedimentation, which would have disturbed the electrophoretic movement measurements.

### 6.2.6. Suspendability assays

The nanoparticles were suspended at 5 mg/ml concentration in distilled water and sonicated for 1 hour. The samples were subjected to increasing spin pulses (at 1200, 2500, 5000, 7500, 10000 and 12500 rpm) and the UV light attenuation at 800 nm was measured. The procedure is developed in Chapter 2.

### 6.2.7. MSN functionalisation

Calcined samples were functionalised with APTES and IPTES. 100 mg of each sample (**MSN-temp**) were suspended and briefly sonicated in 6 mL of acetonitrile. Every sample was split in two vials (3 mL per vial) and 53 µL of APTES or 59 µL IPTES were respectively added to each suspension. The mixtures were stirred for 5.5 hours at room temperature. Then, the samples were centrifuged and washed with acetonitrile three times. Finally, the solids were dried at 70 °C. The solids obtained were called **MSN-temp-$NH_2$** and **MSN-temp-NCO**, where 'temp' corresponded to the calcination temperature of each sample.

### 6.2.8. Biocompatibility assays

The *in vitro* cytotoxicity assays were performed on human brain glioblastoma cells (LN-18). Cell culture was incubated in Dulbecco's Modified Eagle Medium (DMEM) high glucose supplemented (Sigma-Aldrich) with 10% of serum foetal bovine (SFB) (Sigma-Aldrich) and in 5% $CO_2$ at 37 °C and underwent passage twice a week. The nanoparticles used to treat the cells were suspended and generously sonicated in DMEM-SFB. Cells were treated for 4 hours and incubated with fresh media. At 72 hours, 10 µL of WST-1 reagent (Roche Applied Science) were added to each well (in a 96-well microtiter plate) and were incubated for 1 hour at 37 °C. The absorbance, directly related with cell activity, was read at 440 nm. Cell viability measurements were taken in a Wallac 1420 Victor2 Microplate Reader (Perkin Elmer).

### 6.2.9. Degradation assays

Nanoparticles were suspended at 1 mg/mL concentration in PBS and generously sonicated. Then, the suspension was stirred with a magnetic stirrer for 2 weeks at room temperature. Small aliquots (50μL) were collected after 1, 4, 7 and 14 days, and studied by transmission electron microscopy. After collecting each aliquot, the nanoparticles suspension was centrifuged and then resuspended in fresh PBS to avoid saturation on silicic acid of the media and facilitate the degradation process.

### 6.2.10. Image analysis

TEM images were used to analyse the properties of MSN, such as their size or mesoporosity. At least 200 particles for each sample were counted to obtain the diameter data and the percentage of nanoparticles with mesoporosity. Nanoparticles were considered to possess mesoporosity only if clear hexagonal ordering of the pores or parallel channels could be observed.

## 6.3. RESULTS AND DISCUSSION

### 6.3.1. Synthesis and surfactant removal

The MCM-41-type MSN were synthesised according to the protocol described in the experimental section. After that, 1.85 g of the as-made solid (**MSN-as made**) were obtained. **MSN-as made** was characterised by PDXR before the surfactant was removed. 50 mg of **MSN-as made** were kept for posterior comparison with the modified samples using ELS, TGA and cytotoxicity techniques. The remaining material was divided into six vials (300 mg each one) and a different method were used on each one to remove the surfactant. Then, the nanoparticles of four of the vials were calcined using different temperatures (400 °C, 450 °C, 500 °C and 550 °C) and then **MSN-400**, **MSN-450**, **MSN-500** and **MSN-550** samples were respectively obtained. Additionally, the nanoparticles of the two remaining vials were suspended in the corresponding extraction solutions, ethanol:HCl and ethanol:$NH_4NO_3$, leading to **MSN-extHCl** and **MSN-ext$NH_4NO_3$** samples, accordingly. All the obtained samples were characterised using the mentioned procedures.

The calcination temperatures employed were chosen in order to compare the standard calcination (at 550 °C) with less aggressive temperatures, in terms of studying the differences in their biodegradation and condensation degree, among other. The lower limit was set at 400 °C according to the reported temperature in which the $CTA^+$, when acting as a template, appears to be mostly calcined [88][89][90][91][51] as has been stablished by DSC, DTA or TGA assays.

At naked eye, some differences were observable between the samples (Figure 2). On the one hand, the solid calcined at 400 °C (**MSN-400**) showed a beige colour, indicating the presence of some thermal decomposition products from $CTA^+$. All the samples calcined at temperatures above 400 °C were obtained in the form of a white powder. However, a small percentage of **MSN-450** also showed a light beige appearance (not observed on Figure 2). This effect could be produced by a heterogeneous distribution of temperature inside the oven. On the other hand, both extracted solids (**MSN-extHCl** and **MSN-ext$NH_4NO_3$**) were also obtained in the form of a white powder, and these powders were finer than the ones obtained by calcination (not showed).

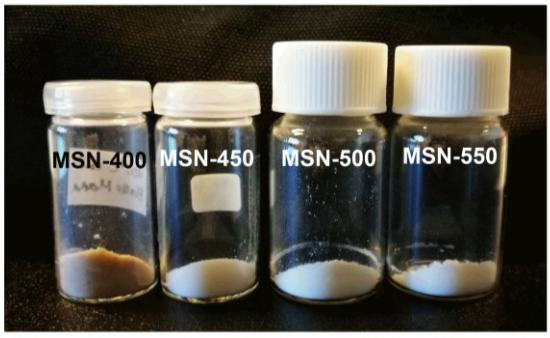


*Figure 2. Photograph of calcined samples.*

### 6.3.2. Surfactant removal efficiency

First, the different methods to remove the surfactant template were compared in terms of their efficiency. For this purpose, both thermogravimetric analysis (TGA) and Fourier-transform infrared spectroscopy (FTIR) were used. The analysis comprised the samples calcined at different temperatures (**MSN-400**, **MSN-450**, **MSN-500** and **MSN-550**) and the solids whose surfactant was eliminated by extraction (**MSN-extHCl** and **MSN-ext$NH_4NO_3$**).

The TGA curves (Figure 3A) and FTIR spectra (Figure 3B) of calcined solids are represented in comparison with the **MSN-as made**. The TGA results (Fig. 3A) are shown according to the percentage of the dry solid (removing from the initial weight the contribution of moisture and other solvents) as a function of temperature, according to considerations previously reported [92][93]. Therefore, the loss of weight observed is associated with the sum of the decomposition of organic matter and the silanol condensation. **MSN-as made** had a weight loss of 45.9%. The tendency observed in the curve was a sharp drop from 180 °C to 360 °C (Fig. 3A, dashed lines), which is roughly the region where $CTA^+$ has been reported to decompose [94][95][31]. This decay represents a weight loss of 39%. After that, a second weight loss is observed with a less steep slope from 360 °C to 550 °C, which represents the 4.5% of weight and that can be associated with the combustion of $CTA^+$ residues and the condensation of first silanol groups. Finally, above 550 °C (until 1000 °C) the weight loss is much less pronounced, in which only a reduction of the 2.5% of weight that can be attributed to silanol condensation. In contrast, the percentage of weight loss in the calcined samples is highly reduced, and this percentage decreases with calcination temperature. Hence, calcined samples showed a total weight loss of 5.6%, 4.1%, 3.8% and 3.4%, in the case of **MSN-400**, **MSN-450**, **MSN-500** and **MSN-550**, respectively, which are in the range reported in the literature [90][92]. The difference between the three latter samples (**MSN-450**, **MSN-500** and **MSN-550**) is below 1% and their curves are barely distinguishable in the Figure 3A (yellow, orange, and red lines, respectively). In the case of **MSN-400**, the difference is higher (a 1.5% compared to **MSN-450**) and its curve is more visible (Figure 3A, light green line). Additionally, **MSN-400** presents a decay more pronounced in the interval from 360 °C to 550 °C, from which the curve separates from the rest.

FTIR spectroscopy of **MSN-as made** was used to check the presence of bands associated with the $CTA^+$ molecules (Fig 3B, dotted lines). According to the literature and our observations in **MSN-as made** spectra, these bands are located approximately at 2959, 2918 and 2850 $cm^{-1}$ (stretching bands from methylene (-$CH_2$-) and methyl groups (-$CH_3$)), 1470 and 1400 $cm^{-1}$ (bending bands from -$CH_2$- and -$CH_3$) and 724 $cm^{-1}$ (rocking band from -$CH_2$-) [96]. Only alkane related peaks of $CTA^+$ can be observed in FTIR spectroscopy, as tertiary amines lack of signal. In the case of the calcined samples (**MSN-400**, **MSN-450**, **MSN-500** and **MSN-550**), their spectra only show the bands associated with the silica matrix and no bands related to the $CTA^+$ molecules are appreciated, regardless of the calcination temperature used.

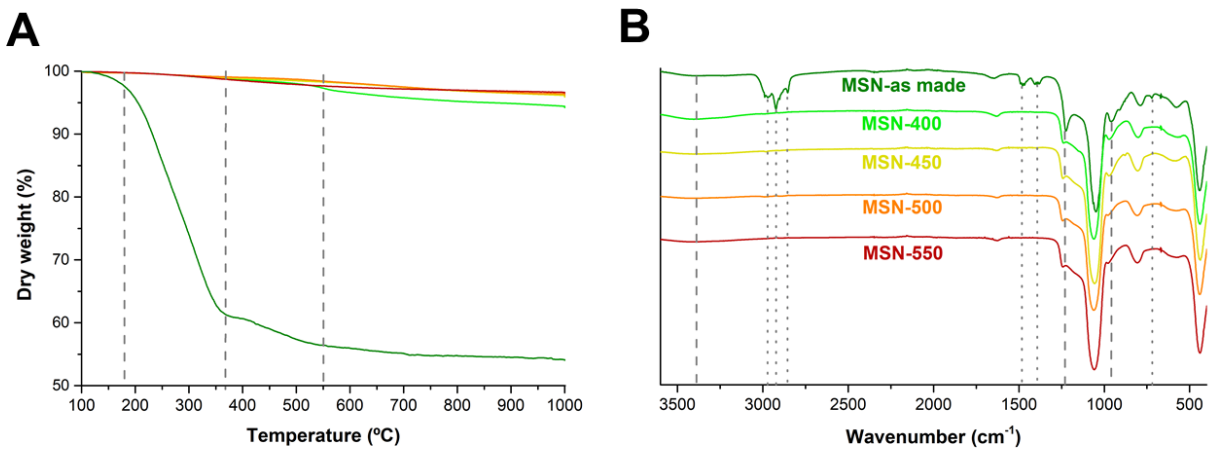


*Figure 3. Surfactant removal efficiency of calcination at different temperatures. (A) TGA curves of calcined and as-made samples. Dashed lines indicate the three differentiable stages in weight loss. The values of weight were expressed according to the percentage of the dry solid (removing from the initial weight the contribution of moisture and other solvents). (B) FTIR spectra of calcined and as-made samples. Dotted lines indicate the $CTA^+$ associated FTIR bands. Dashed lines indicate the Si-OH and flexibility associated lines. The colors used in both graphs are correlated.*

According to the observations made at naked eye, in which the beige appearance of **MSN-400**, and **MSN-450** to a lesser extent, the presence of some $CTA^+$ residues is proposed. Nevertheless, FTIR results showed the disappearance of signals associated with $CTA^+$ in the four calcined samples. We hypothesise, then, that the residues remaining in **MSN-400** and **MSN-450** are coke residues, whose FTIR signals are negligible and therefore, their presence is compatible with the experimental observations [97][98]. Coke residues are reported to remain in the MSN when the calcination process is not complete [10][24][99], and the presence of even 1% in weight of coke residues may explain the colour found in **MSN-400** and **MSN-450** solids. Hence, we can only claim to totally eliminate the $CTA^+$ and their residues as of 500 °C. In this context, there is not consensus about the minimum temperature necessary to remove completely the $CTA^+$ from the mesopores in the literature, which varies from 350 °C to 600 °C [12][100][101][102].

For their part, TGA curves show a progressive decrease of weight loss with increasing calcination temperature. This can be produced by a double phenomenon when calcination temperature increase. On the one hand, the elimination of coke residues, which are still present when samples are calcined at 400 °C to 450 °C. On the other hand, the progressive condensation of silanols, which is reported to occur even from 400 °C by some authors [5][20]. In this context, Potapov et al. [50] analysed the silanol condensation as a function of the temperature applied on precipitated amorphous silica, and reported silanol condensation at even lower temperatures. They described that silanol condensation occurs in three stages depending on the type of the silanols involved, their location inside the silica framework and the proximity between them: 1) from 190 to 400 °C the vicinal and geminal -OH groups are decomposed, 2) from 400 to 780 °C the main contribution is due to condensation of free nearby individual -OH groups and 3) above 780 °C the condensation is limited to the widely spaced -OH groups. In this respect, the weight loss values of calcined samples are in the range of the reported values for silanol condensation (about the 5% [93]). In fact, the amount of silanols in MSN prior to surfactant extraction has been reported to be quite high, in accordance with the percentage of $Q_2$ and $Q_3$ [14] silicon centres.

Considering that the standard calcination temperature (550 °C) totally removes the surfactant, the percentage of weight decrease in **MSN-550** (3.4%) is associated with the presence of silanol groups. The rest of the samples, **MSN-400**, **MSN-450** and **MSN-500**, exceed the weight loss of the standard sample in a 2.2%, 0.7% and 0.4% in weight lost, respectively. These percentages can be assumed to correspond to the presence of additional silanol groups in these samples in comparison with **MSN-550**, in addition to some coke residues in case of **MSN-450**, and specially, **MSN-400**.

In summary, it can be concluded the efficiency of surfactant removal is optimal calcining above 500 °C, since some coke residues can remain in MCM-41-type MSN at conditions studied (calcination for 5 hours at oxidant atmosphere). In addition, a progressive condensation of silanols is supposed to take place above 400 °C, according to the observations and the reported literature. Nevertheless, further assays such as the determination of silica condensation degree, elemental analysis and cytotoxicity must be done to validate these results.

On the other hand, the TGA curves (Figure 4A) and FTIR spectra (Figure 4B) of extracted solids (**MSN-extHCl** and **MSN-ext$NH_4NO_3$**) were also studied in comparison with the **MSN-as made**.

The TGA results (Fig. 4A) showed a weight loss of 13.1% for **MSN-extHCl** and a 12.6% for **MSN-ext$NH_4NO_3$**. Even though these percentages are quite lower than those observed for the **MSN-as made**, they are higher than those measured for the calcined samples. Similar behaviours were observed in other studies, which reported a weight loss of 10% in TGA curves for extracted MSN with $NH_4NO_3$, NaCl or HCl in ethanol or methanol [1][31][36]. The TGA curves for both extracted samples show the most significant weight reduction in the range from 420 °C to 570 °C. In this region (Fig. 4A, dotted lines), both extracted solids lose around a 7% of matter.

Regarding the FTIR spectra (Fig. 4B), both extracted samples, **MSN-extHCl** and **MSN-ext$NH_4NO_3$**, showed the disappearance of most of the $CTA^+$ associated FTIR bands (Fig. 4B, dotted bands), such as the signals at 720, 1470, 2850 and 2918 $cm^{-1}$. Nevertheless, the bands at 1400 $cm^{-1}$ (bending bands from -$CH_2$- and -$CH_3$) of and 2959 $cm^{-1}$ (stretching bands from -$CH_2$- and -$CH_3$) were present in both samples. In addition, other peaks in the 3000 $cm^{-1}$ region appears, such as those at 2918 and 2850 $cm^{-1}$.

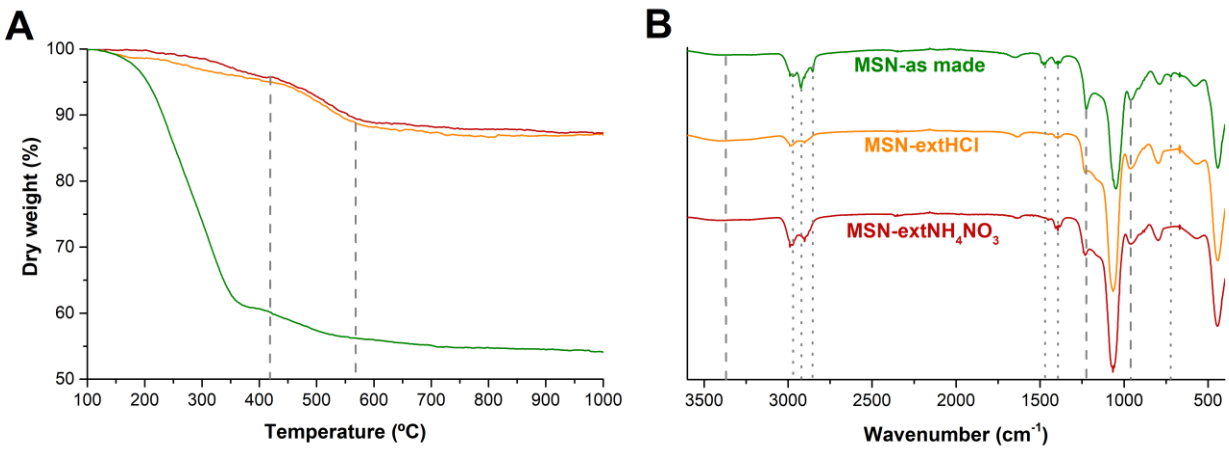


*Figure 4. Surfactant removal efficiency of extraction methods. (A) TGA curves of extracted and as-made samples. Dashed lines indicate the region in which the thermal decomposition is greater in extracted samples. The values of weight were expressed according to the percentage of the dry solid (removing from the initial weight the contribution of moisture and other solvents). (B) FTIR spectra of extracted and as-made samples. Dotted lines*

*indicate the $CTA^+$ associated FTIR bands. Dashed lines indicate the Si-OH and flexibility associated lines. The colors used in both graphs are correlated.*

TGA curves seem to suggest that the weight loss observed over 425 °C is not mainly due to surfactant presence, since the surfactant elimination is principally found at lower temperatures (since 180 °C). On the other hand, the high percentage of weight loss (above 10%) cannot be produced only by the higher amount of silanol groups remaining in extracted samples, since the reported weight of silanol groups in as-made samples is close to the 5% of the nanoparticles weight [93]. This suggests the presence of other residues in the extracted samples.

These considerations fit also with the FTIR spectra. FTIR bands found in extracted samples cannot correspond to $CTA^+$, as some of its associated bands are not present in the spectra and other peaks do not fit exactly in wavenumber. In concert with that, it can be hypothesised that the observed bands may be better assigned to ethanol traces (whose bands appear at 1384 and 2980 $cm^{-1}$). However, this cannot explain the main weight decrease found in TGA, since their evaporation is located even below 100 °C. Thus, it is suggested that the bands at 2980 $cm^{-1}$, 2900 $cm^{-1}$ and 1400 $cm^{-1}$ can be attributed to the presence of ethoxy groups, which are formed during the solvent extraction by esterification of some silanol groups [11][19], which can be produced in acidic ethanol suspension at refluxing conditions [103].

Consequently, it can be suggested that the extraction methods employed remove completely the $CTA^+$ from MSN. Nevertheless, both extraction with HCl/ethanol and $NH_4NO_3$/ethanol lead to the obtaining of nanoparticles with ethoxy groups attached to the surface.

### 6.3.3. Condensation degree and Si-OH on surface

The condensation degree was evaluated in order to know the effect on the condensation degree of the silica matrix of the different methods applied to remove the surfactant. For this purpose, FTIR spectra above mentioned were again analysed focusing on the bands related to the silica framework. Additionally, $Si^{29}$-ss-NMR measurements (Table 1) were performed to study the silica connectivity. Third, ELS measurements were analysed to study the ζ potential of samples (Table 1), considering that the negative charge of MSN comes from the deprotonated silanols (silanolates, $Si\text{-}O^-$) on the surface.

Starting with the FTIR spectra, the bands of interest in relation to the condensation degree of the MSN silica matrix are those associated with Si-OH group (stretching wide band at 3400 $cm^{-1}$ of O-H bond and bending band at 954 $cm^{-1}$ of Si-OH bond) and the one associated with Si-O-Si bonds (the shoulder at 1217 $cm^{-1}$ due to bending vibrations) (Fig. 3B and 4B, dashed lines) [12][104][105]. In the case of the calcined samples, it can be observed (Fig. 3B, dashed lines) that the bands associated with the Si-OH bonds (at 3400 and 954 $cm^{-1}$) decrease progressively as the calcination temperature increases compared with **MSN-as made**, especially above 500 °C. On the same vein, the shoulder at 1217 $cm^{-1}$, which is quite sharp in **MSN-as made**, is highly reduced in all the calcined samples. This decrease in the intensity of the shoulder at 1217 $cm^{-1}$ can be related with the condensation increase of MSN provoked by the calcination that must produce an increment of the framework rigidity, which interferes in the stretching and bending Si-O-Si vibrations. On the other hand, the extracted samples were analysed on the same vein. The FTIR spectra (Fig. 4B, dashed lines) revealed that the bands associated with the Si-OH and

O-H vibrations (3400 $cm^{-1}$, 954 $cm^{-1}$) were not so reduced in comparison with calcined samples, neither the stretching nor bending Si-O-Si vibrations (1217 $cm^{-1}$).

On the other hand, NMR spectroscopy was used to quantify the connectivity of silica, namely the percentage of the $Q_2$, $Q_3$ and $Q_4$ signals in each spectrum since these signals are closely related to the silica condensation degree. In this sense, the measured spectra showed a correlation between the temperature of calcination and the increase of silica condensation degree (Table 1), with exception of the samples **MSN-400** and **MSN-450**, which showed spectra with narrow and unresolved bands, which did not allow to fit them to a Gaussian function and, therefore, no consistent data were obtained for these samples. For this reason, these samples were not included in the analysis. In case of **MSN-500** and **MSN-550**, their $Q_2$ signal is reduced from 10.2% in **MSN-as made** to 5.1% and 4.2% respectively. The same can be applied to the $Q_3$ signal (48.6% > 43.5% > 28.5%). Oppositely, the calcination process increases progressively the value of $Q_4$ signal in the samples (41.2 < 51.4 < 67.3). In summary, the degree of condensation (DK) (Table 1), calculated according to the equation reported by Barczak [11] (equation 1 from Chapter 3), increased with the calcination temperature (84.5 < 86.6 < 90.8 in **MSN-as made**, **MSN-500** and **MSN-550**, respectively). The results were consistent with the data previously reported [5][11][24][47][106]. In the same way, the NMR spectra of extracted samples showed a decrease of the intensity of the $Q_2$ band from 10.2% in the **MSN-as made** to 5.9% and 6.8% in **MSN-extHCl** and **MSN-ext$NH_4NO_3$,** accordingly, a slight decrease of the $Q_3$ band from 48.6% to 43.1% and 43.6%, respectively, and a relatively low increase of the $Q_4$ band from 41.2% to 51% and 49.6% were experimentally found. Following these tendencies, the calculated DK of **MSN-extHCl** and **MSN-ext$NH_4NO_3$** was 86.3 and 85.7, respectively, a little bit higher than the one of the as-made sample.

*Table 1. Data related with the silica condensation degree (ζ potential and percentage of the $Q_2$, $Q_3$, $Q_4$ peaks respect to the total ss-NMR signal) for the samples obtained using different surfactant removal methods.*

| SAMPLE | ζ POTENTIAL (mV) | $Si^{29}$-ss-NMR | | | |
|---|---|---|---|---|---|
| | | % $Q_2$ | % $Q_3$ | % $Q_4$ | Degree of condensation (DK) |
| **MSN-400** | - 33.8 ± 1.4 | - | - | - | - |
| **MSN-450** | - 35.5 ± 2.4 | - | - | - | - |
| **MSN-500** | - 36.8 ± 1.5 | 5.1 | 43.5 | 51.4 | 86.6 |
| **MSN-550** | - 32.9 ± 1.7 | 4.2 | 28.5 | 67.4 | 90.8 |
| **MSN-extHCl** | - 38.1 ± 0.9 | 5.9 | 43.1 | 51.0 | 86.3 |
| **MSN-ext$NH_4NO_3$** | - 37.6 ± 1.2 | 6.8 | 43.6 | 49.6 | 85.7 |
| **MSN-as made** | + 33.5 ± 3.2 | 10.2 | 48.6 | 41.2 | 84.5 |

Regarding the ζ potential (Table 1), it can be observed that the negative charge increases when increasing the calcination temperature from 400 to 500 °C (- 33.8 < - 35.5 < - 37.6 mV) but decreases at 550 °C (- 35.8 mV). It can be explained due to the sum of two variables. On the one hand, the presence of surfactant residues (coke) in the nanoparticles may soften the negative charge that **MSN-400** and **MSN-450** should have due to silanol/silanolate groups. On the other hand, raising the calcination temperature increases the condensation of silanol/silanolate groups and, therefore, the negative charge is reduced. Then, only over 500 °C it can be observed

the ζ potential reduction due to silanol condensation. For their part, the ζ potential values for extracted samples were -38.1 and -37.3 mV for **MSN-extHCl** and **MSN-extNH$_4$NO$_3$**, respectively. These values were more negative than any calcined sample, indicating the higher number of silanol/silanolate groups, at least compared with **MSN-550** and **MSN-500**.

According to the data obtained in FTIR, $Si^{29}$-ss-NMR and ELS it can be said that the use of increasing calcination temperatures leads to the increase of the silica condensation degree and to the reduction of silanol groups. In addition, the extraction method produces a lower condensation degree compared with calcination, and their framework flexibility is less affected by extraction procedures than calcination ones. Hence, the use of extraction methods is much less aggressive than the use of calcination even at low temperatures. Nevertheless, further assays must be done in order to obtain more consistent results in $Si^{29}$-ss-NMR spectra.

### 6.3.4. Mesostructured framework shrinkage

The framework shrinkage was also mentioned as one of the more affected parameters in relation with the surfactant removal method. Hence, the porosity of calcined and extracted samples was studied.

First, PXRD was performed and analysed (Figure 5 and Table 2). The diffraction pattern of both calcined and extracted samples (Fig. 5) present the peaks observed in typical MCM-41 material, corresponding to crystallographic planes (100), (110), (200) and (210), though the peak that can be assigned to the (210) planes is not always visible in the patterns due to its small intensity and the loss of long-range order after surfactant removal. Focusing on the main peak (100), the interplanar distance $d_{100}$ was calculated by applying the Bragg's law (equation 4 from the Chapter 1), and the unit cell for a hexagonal structure was also calculated (equation 6 from the Chapter 1) (Table 2). A considerable reduction in $d_{100}$ when nanoparticles are calcined can be calculated. **MSN-as made** presents a $d_{100}$ of ca. 4.23 nm, while in calcined samples the $d_{100}$ value is in the range from 3.68 to 3.82. No clear correlation was found between the calcination temperature and the peak shift. Similar observation was reported by Basso et al. [5]. In contrast, in extracted samples the $d_{100}$ value barely change from as-made sample, being 4.19 and 4.10 nm in **MSN-extHCl** and **MSN-extNH$_4$NO$_3$**, respectively. To make easier the comparison between the structural shrinkage suffered for the different samples, the unit cell contraction has been calculated and a clear different behaviour can be observed. Calcined samples present a contraction in the range of 0.4-0.5 nm and extracted samples 0.05-0.15 nm.

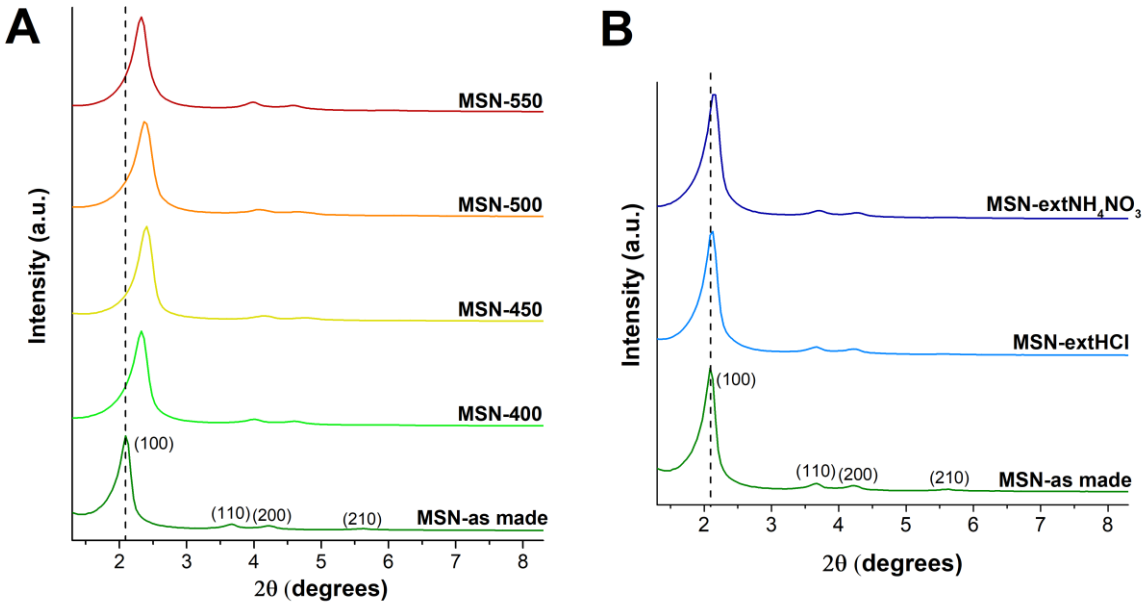


*Figure 5. PRXD patterns of calcined (A) and extracted (B) samples in comparison to as-made sample. Dotted lines indicate the position of (100) in **MSN-as made**. Miller index of symmetry planes are indicated in parenthesis.*

On the other hand, the FWHM of peak (100) ($FWHM_{100}$) was calculated for each sample, as well as the FWHM ratio as the width of the (100) peak in calcined and extracted samples related to the width of this same peak in the as-made sample (Table 2). The data show an increase of the $FWHM_{100}$ after the surfactant removal, regardless the extraction method employed. Nevertheless, the $FWHM_{100}$ ratio was higher in the case of the calcined samples (ranging from 1.23 to 1.41) than in the extracted ones (ranging from 1.14 to 1.18).

*Table 2. Crystallography data of samples obtained with the different surfactant removal methods. (FWHM ratio: width of the (100) peak in calcined and extracted samples related to the width of this same peak in the as-made sample).*

| SAMPLE | Peak (100) (2θ) | $d_{100}$ (nm) | Unit cell (nm) | Unit cell contraction (nm) | $FWHM_{100}$ | $FWHM_{100}$ ratio |
|---|---|---|---|---|---|---|
| **MSN-As made** | 2.09 | 4.23 | 4.88 | - | 0.22 | - |
| **MSN-400** | 2.31 | 3.82 | 4.41 | 0.47 | 0.28 | 1.27 |
| **MSN-450** | 2.40 | 3.68 | 4.25 | 0.63 | 0.27 | 1.23 |
| **MSN-500** | 2.38 | 3.71 | 4.28 | 0.60 | 0.31 | 1.41 |
| **MSN-550** | 2.34 | 3.77 | 4.35 | 0.53 | 0.28 | 1.27 |
| **MSN-ExtHCl** | 2.11 | 4.19 | 4.84 | 0.04 | 0.25 | 1.14 |
| **MSN-Ext$NH_4NO_3$** | 2.15 | 4.10 | 4.74 | 0.14 | 0.26 | 1.18 |

According to these results, it can be suggested that the structure shrinkage is more pronounced in calcined samples than in extracted ones, even at lower calcination temperatures, as it has been widely reported [11][19][20]. Therefore, the use of temperatures above 400 °C affects the silica framework to a greater extent than the exposure to an organic solvent and refluxing temperatures (ca. 80 °C), in case of **MSN-ext$NH_4NO_3$** sample, or even to additional highly acidic

conditions, in case of **MSN-extHCl**. This phenomenon is also observed in the increment of the structure disturbance and symmetry defects, which can be also found in the literature [107] and is indicated by the value of the $FWHM_{100}$. This was found to be greater in calcined samples than in extracted ones, although the difference between them was less pronounced.

The $N_2$ absorption-desorption isotherms were also employed to study the mesoporosity of calcined and extracted samples. The results are shown on Figure 6 and Table 3. In the Figure 6A the isotherms of calcined samples are shown. Both showed the typical isotherm of MCM-41 material. It is observable how the slope of the isotherms in the interval of the $N_2$ monolayer formation, which is related to the BET surface area, increases slightly as higher calcination temperatures are used. The capillary condensation, which represents the filling of the pores, is found at the same pressure in all the cases ($p/p_o$ = 0.31). Nevertheless, the quantity of $N_2$ adsorbed at average pressures increases progressively with the rise of the calcination temperature, which suggest an increase in pore volumes. In the Figure 6B the isotherms of extracted samples are shown in comparison to standard calcined sample (calcined at 550 °C). The extracted samples show quite similar isotherms. They show lower slope in $N_2$ monolayer adsorption region and lower amount of $N_2$ adsorbed at average pressures than the standard calcined sample. In the case of the capillary condensation, the extracted samples show the jump slightly shifted to higher pressures ($p/p_o$ = 0.32). The calculated data from the isotherms according to BET and BJH methods are shown in Table 3.

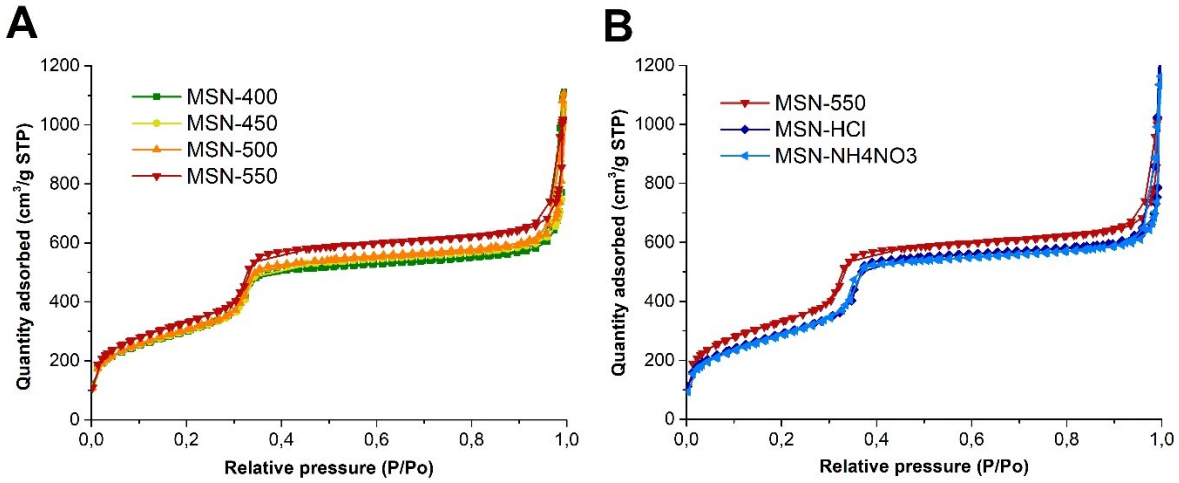


*Figure 6. $N_2$ absorption-desorption isotherms of A) calcined samples and B) extracted samples compared to **MSN-550**.*

The specific surface area of calcined samples is slightly higher with increasing the calcination temperature (1096 < 1097 < 1115 < 1208 $m^2/g$), as it is also the pore volume (0.97 < 1.00 < 1.01 < 1.09 $cm^3/g$). In contrast, the pore size remains similar in the calcined samples (in the range from 2.83 to 2.85 nm), and no correlation was found between the calcination temperature and the shrinkage extent, as shown by PXRD data. Therefore, the increase in specific surface area appears to be related to the increase in pore volume, rather than to the increase of the pore size. Regarding the extracted samples, the surface area is smaller than the one of the calcined ones, 1079 and 1086 $m^2/g$ for **MSN-extHCl** and **MSN-extNH$_4$NO$_3$**, respectively, just as is the pore volume (lower than 1.00 $cm^3/g$ in both cases). The pore size is similar to the one of calcined ones (in the range from 2.80 to 2.86 nm).

*Table 3. Mesoporosity of samples as a function of surfactant removal method.*

| SAMPLE | BET surface ($m^2/g$) | Pore size (nm) | Pore volume ($cm^3/g$) | Wall thickness (nm) |
|---|---|---|---|---|
| **MSN-400** | 1096 | 2.83 | 0.97 | 1.58 |
| **MSN-450** | 1097 | 2.85 | 1.00 | 1.40 |
| **MSN-500** | 1115 | 2.83 | 1.01 | 1.45 |
| **MSN-550** | 1208 | 2.84 | 1.09 | 1.51 |
| **MSN-ExtHCl** | 1079 | 2.86 | 0.99 | 1.98 |
| **MSN-Ext$NH_4NO_3$** | 1086 | 2.80 | 0.97 | 1.94 |

The wall thickness was also calculated according to the equation 7 in the Chapter 1. In case of calcined samples, this value ranges from 1.40 to 1.58 nm. There was not a clear correlation between the wall thickness and the calcination temperature. In the case of extracted samples, the calculated wall thickness is quite bigger (in the range from 1.94 to 1.98 nm).

In order to analyse the results, it must be considered that mesoporosity, especially the pore volume value, depends on two parameters: the lattice shrinkage and the removal efficiency. In other words, the pore volume can be reduced not only by shrinkage process, but also by the presence of surfactant residues, or even, the presence of residues derived from the template removal method chosen. Nevertheless, no agreement is found in the literature with respect to the effect of surfactant removal in mesostructured framework. There are previous studies that applied different calcination temperatures in KIT-6 and SBA-15 materials and they reported that the specific surface area and pore volume were optimised at intermediate temperatures, where the surfactant was completely removed, but the shrinkage was less pronounced [5]. On the other hand, other studies reported that the calcination process lead to smaller pore size and volume in comparison with extraction method, due to the sharp shrinkage provoked by calcination [11][19][108]. Conversely, He et al. [35] reported the obtaining of a specific surface area ca. 863 $m^2/g$, which is quite low, in MCM-41-type MSN extracted with ethanol and HCl reflux. In this case, it can be hypothesised that the surface reduction is not provoked by the extraction method by itself but to the application of the ethanol washing immediately after the formation of the nanoparticles. We suggest that because, based on our observations, silica framework is still weak just after their synthesis. This is especially true before the formed solid is dried, from which is assumed that a considerable fraction of silanol groups are condensed, and the framework is consolidated. Considering that, the ethanol washing can dissolve a part of the $CTA^+$ molecules that are inside the pores and provoke a strong shrinkage of the unconsolidated silica framework. In another study, Hudon et al. [3] reported that the extraction with ethanol-HCl leads to lower surface area in comparison with calcined sample, but they did not justify these results.

According to the results obtained some considerations can be suggested. On the one hand, there is a progressive elimination of surfactant as the calcination temperature increases that is emptying the pores, and therefore, provokes that the pore volume and BET surface increase also progressively. Nevertheless, the average pore size remains constant since its measurement is not affected by the small amount of residues present in the pores, which can be located in the inner part of them. In case of extracted samples, the presence of some residues, such as alkoxy

groups in the mesopores can also provoke the obtaining of smaller pore volumes and specific surface areas. On the other hand, the shrinkage observed in PRXD data in calcined samples compared with those extracted, which hardly suffer this phenomenon, is not mainly due to differences in pore size, which is similar in all samples, but rather to differences in wall thickness. In fact, the differences in wall thickness between extracted and calcined samples and the differences in unit cell contraction are in the same range (close to 0.5 nm). Therefore, the shrinkage of calcined samples is not produced by a pore size contraction, in contrast to the effect observed when the aging of the nanoparticles is studied (Chapter 4), but by a decrease in the thickness of the wall if we compare with that of extracted samples. This decrease in pore wall thickness can be provoked by the increase of silica connectivity and structure sintering due to calcination conditions.

### 6.3.5. Colloidal behaviour

The influence of surfactant removal method was analysed according to the UV light attenuation when increasing spin pulses were applied (method developed in Chapter 5) (Figure 7).

The behaviour of calcined samples is shown in Figure 7A. The curves in this picture show a better colloidal behaviour when lower calcination temperatures are applied (**MSN-400** > **MSN-450** > **MSN-500** > **MSN-550**). The difference between the samples is not very wide, ranging between 10 and 15% of nanoparticles in suspension for lower spin pulses. However, the curves equalise when the spin pulses exceed 7,500 rpm. On the other hand, the behaviour of extracted samples is shown in Figure 7B. The colloidal stability of both extracted samples at low spin pulses are quite improved in comparison to the standard calcined sample (**MSN-550**). At 1,200 rpm, the percentage of suspended nanoparticles reaches the 80%, being more than a 25% higher than **MSN-550** and a 15% over the more suspendable calcined sample (**MSN-400**).

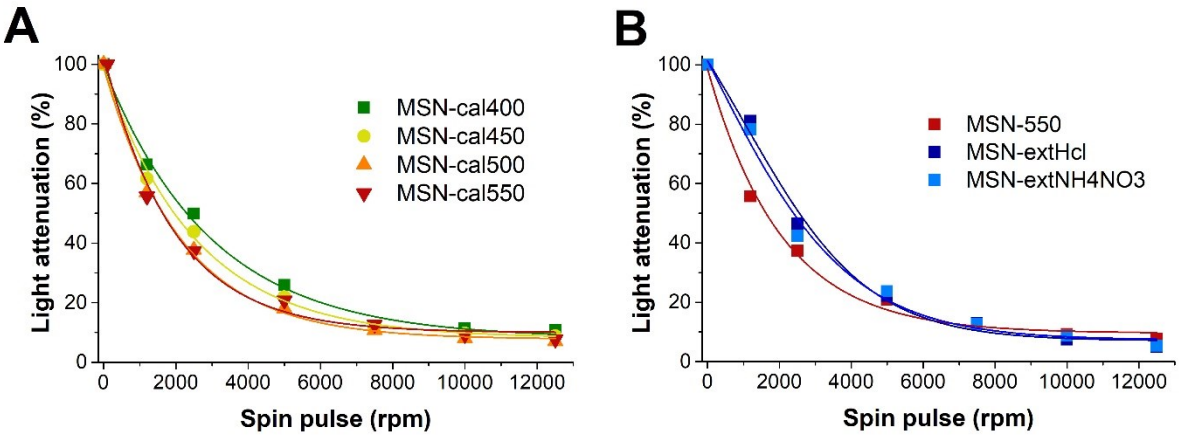


*Figure 7. UV light attenuation at 800 nm of (A) calcined and (B) extracted samples (compared to standard calcination) when they are spun at different pulses strength. The nanoparticles were suspended at 5 mg/ml concentration in distilled water and sonicated during 1 hour before the colloidal stability assay.*

According to the data, our hypothesis is that the improvement of colloidal stability in both, calcined samples at lower temperatures and extracted samples, are mainly caused by the higher amount of silanol groups in the surface. In case of calcined samples, the percentage of

suspended nanoparticles is not directly correlated by the ζ potential value. Nevertheless, as it was suggested previously, although the ζ potential of **MSN-400** and **MSN-450** is less negative than the one of **MSN-500**, due to the supposed presence of decomposition residues of surfactant, it can be assured that the amount of silanolate groups, and therewith, the repulsion between nanoparticles, decrease as the temperature of calcination increase. Consequently, the stability of nanoparticles suspensions decreases with the calcination temperature. In this sense, both extracted samples, which presented a more negative ζ potential value and a demonstrated higher percentage of silanols groups on the surface, reasonably show higher stability in suspension.

Nevertheless, the differences observed in relation to the colloidal stability of the different samples are not so great compared those observed in case of functionalisation or sample preparation (in Chapter 5). In this sense, the similarities in the curves of calcined and extracted samples question the negative effect of standard calcination in the suspendability of MSN by formation of interparticle bonds or fusions [7][9][26][109]. On the contrary, this effect seems to be produced after nanoparticles synthesis and during the drying process, such as it was mentioned in Chapter 5, in the section "transition from colloidal to agglomerated samples". These conclusions could provide new insights in the study of calcination or extraction implications in the suspendability of MSN.

### 6.3.6. Functionalisation effectiveness

The functionalisation effectiveness was evaluated given its relationship with the silica condensation degree and the amount of available silanols, and therefore, the surfactant removal method [6][110]. For this purpose, the calcined samples (**MSN-400**, **MSN-450**, **MSN-500** and **MSN-550**) were functionalised with APTES and IPTES, obtaining the solids **MSN-temp-$NH_2$** and **MSN-temp-NCO**.

The samples were characterised by TGA, and the decomposition curves are shown in Figure 8. The solids **MSN-temp-$NH_2$** (Fig. 8A) showed a sharp decrease of weight in the temperature range from 300 to 600 °C, in which the APTES has been described to decompose when is attached to MSN [111][112]. The percentage of weight loss in **MSN-400-$NH_2$**, **MSN-450-$NH_2$**, **MSN-500-$NH_2$** and **MSN-550-$NH_2$** were respectively 17.6, 18.3, 19.9 and 16.1%. In the case of **MSN-temp-NCO** (Fig. 8B), the TGA curves showed a weight decrease more gradual and sustained, but also can be observed a higher weight loss in the range from 300 to 600 °C. The percentages of weight loss found in **MSN-temp-NCO** samples were quite smaller than those observed in **MSN-temp-$NH_2$**. The values measured were 10.1, 9.6, 9.1 and 8.2% in **MSN-400-NCO**, **MSN-450-NCO**, **MSN-500-NCO,** and **MSN-550-NCO,** respectively.

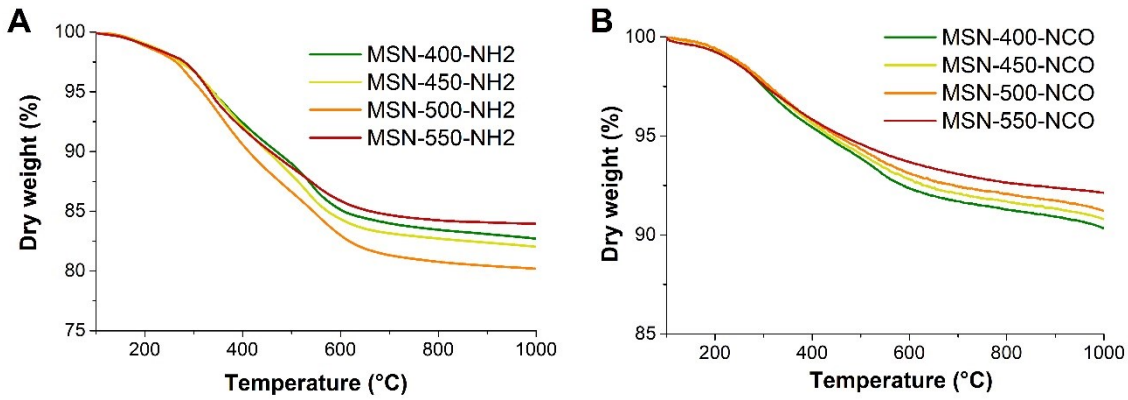


*Figure 8. TGA curves of (A) MSN-temp-$NH_2$ and (B) MSN-temp-NCO samples. The values of weight were expressed according to the percentage of the dry solid (removing from the initial weight the contribution of moisture and other solvents).*

It is assumable that the observed decomposed matter mainly corresponds with the organosilane groups attached to the nanoparticles surface, and to a lesser extent, some silanol groups which still remain in the nanoparticles, or even coke residues in case of functionalised **MSN-400** (whose appearance remained beige) and **MSN-450**. According to these results, the functionalisation with APTES tends to be much greater than the functionalisation with IPTES. This can be explained by the alkaline nature of APTES, which acts as their own reaction catalyser, giving that the hydrolysis rate of ethoxy groups is promoted at alkaline pH. Moreover, in these conditions, a multilayer functionalisation can be produced due to horizontal and vertical polymerisation of APTES [113]. In the case of the functionalisation with IPTES, it can be supposed that the reaction of silanisation is more controlled, and it leads to mostly a monolayer, due to the main horizontal polymerisation of the organosilane.

Regarding the tendency of the functionalisation effectiveness observed in **MSN-temp-$NH_2$** it does not correlate perfectly with the calcination temperature, finding more functionalisation in **MSN-500-$NH_2$** than in **MSN-400-$NH_2$** and **MSN-450-$NH_2$**. This can be explained because the samples calcined at lower temperatures possess less relative surface area and pore volume to be functionalised, such as the $N_2$ isotherms showed, due to the presence of surfactant residues, which limit the functionalisation. In the case of **MSN-550-$NH_2$**, a lower functionalisation than in the samples calcined at lower temperatures is observed, which suggest that both **MSN-500-$NH_2$** and **MSN-550-$NH_2$** have their surface practically clean and the main difference among them is the loss of silanol groups due to condensation from 500 to 550 °C during the calcination. Nevertheless, the nanoparticles functionalised with IPTES (**MSN-temp-NCO**) did show a correlation between the calcination temperature and the functionalisation effectiveness. This can be explained because of the small differences in the weight loss between this samples (e.g., a 1% between **MSN-400-$NH_2$** and **MSN-500-$NH_2$**) can be considerably affected by experimental variability.

In this sense, the modulation of surface reactivity is studied by adjusting the calcination temperature. The heat employed in the calcination process influences not only on the amount of silanol groups available in the surface to form siloxane bonds with organosilanes, but also on the surface cleaning and its availability to be silanised considering the presence or absence of surfactant residues.

### 6.3.7. Biocompatibility of NPs

The biocompatibility of synthesised samples was tested in vitro. Some studies in the literature reported similar studies with different calcined or extracted MSN samples.

To the best of our knowledge, there are not reported studies in which the biocompatibility of bare MSN calcined at lower temperatures than the one of the standard synthesis has been tested. Concerning the bare MSN extracted, the literature shows some examples. Some of them showed that the extracted MSN presented cytotoxicity in viability assays. For example, He et al. [2] as one of the first studies in which the extraction was applied to MSN, reported a high toxicity in their preparations. Nevertheless, the method employed was unable to totally remove the surfactant. For their part, Yildirim et al. [1] described low cytotoxicity at high nanoparticles concentrations. In the same vein, Hudon et al. [3] reported some cytotoxicity in extracted nanoparticles, especially at high concentrations over 100 µg/ml, in spite of showing a complete removal of surfactant. Oppositely, most of the studies with extracted samples, especially in the last years, showed no toxicity due to an improved surfactant removal efficiency, such as the ones in references [14][35].

In this context, cytotoxicity assays dose-response curves were performed (Figure 9). In this figure it can be observed that none of the samples calcined or extracted presented cytotoxicity, even at high concentrations, up to 250 µg/ml. Only **MSN-as made** sample provoked toxicity over the cells, even at the lowest MSN concentration (10 µg/ml). This data demonstrates the high toxicity of $CTA^+$, even at low concentrations.

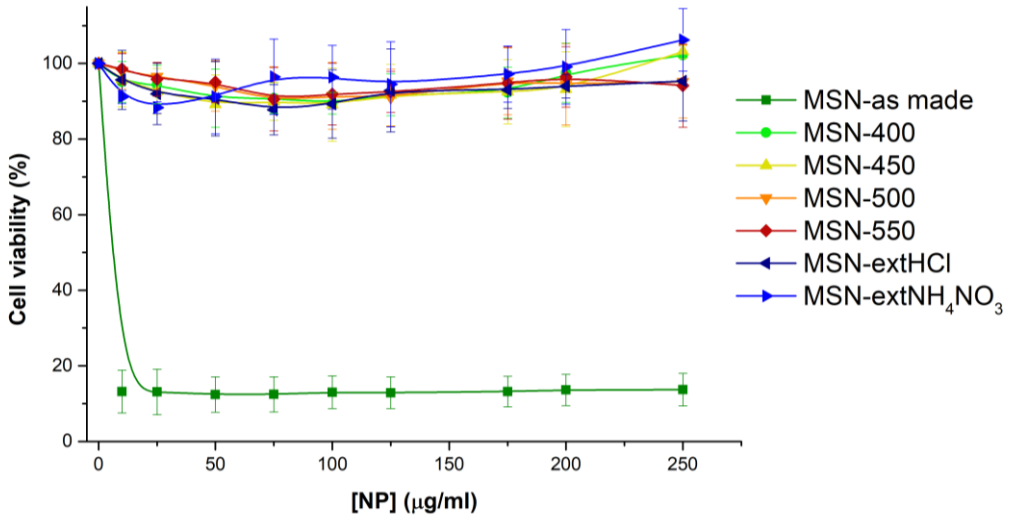


*Figure 9. Cell viability assay. Dose-response curves of LN-18 cells treated with different concentrations of calcined and extracted samples. Cell viability was measured with WST-1 reagent after 72 hours of the addition of nanoparticles.*

These results reinforce the idea that the elimination of surfactant by calcination and extraction employed methods has been complete, or that the presence of some $CTA^+$ residues are non-cytotoxic. Regarding the last reasoning it can be hypothesised that the decomposition residues are not toxic in the concentrations they are present; or that they are strongly attached to the

inner pores surface and therewith, they cannot achieve their biological target to produce the toxic effects.

### 6.3.8. Biodegradability of calcined and extracted samples

The degradability of some of the synthesised solids, particularly **MSN-400**, **MSN-500**, **MSN-550** and **MSN-extHCl**, was studied. For this purpose, they were suspended on PBS at pH 7.4 in terms of simulating a physiological fluid, at 1 mg/ml. The solids were stirred for two weeks at room temperature, and the aliquots were taken at different times (0, 1, 4, 7 and 14 days). The aliquots were characterised by TEM and DLS.

TEM images are shown in Figure 10. All the samples present evidence of progressive degradation over time. On the one hand, the degradation was more remarkable as lower temperatures were used for calcination, and therefore, **MSN-400** presents the highest degradation level among the calcined samples. **MSN-550** shows high stability and low degradation in the time recorded. On the other hand, the extracted sample (**MSN-extHCl**) shows signs of degradation even greater than **MSN-400**.

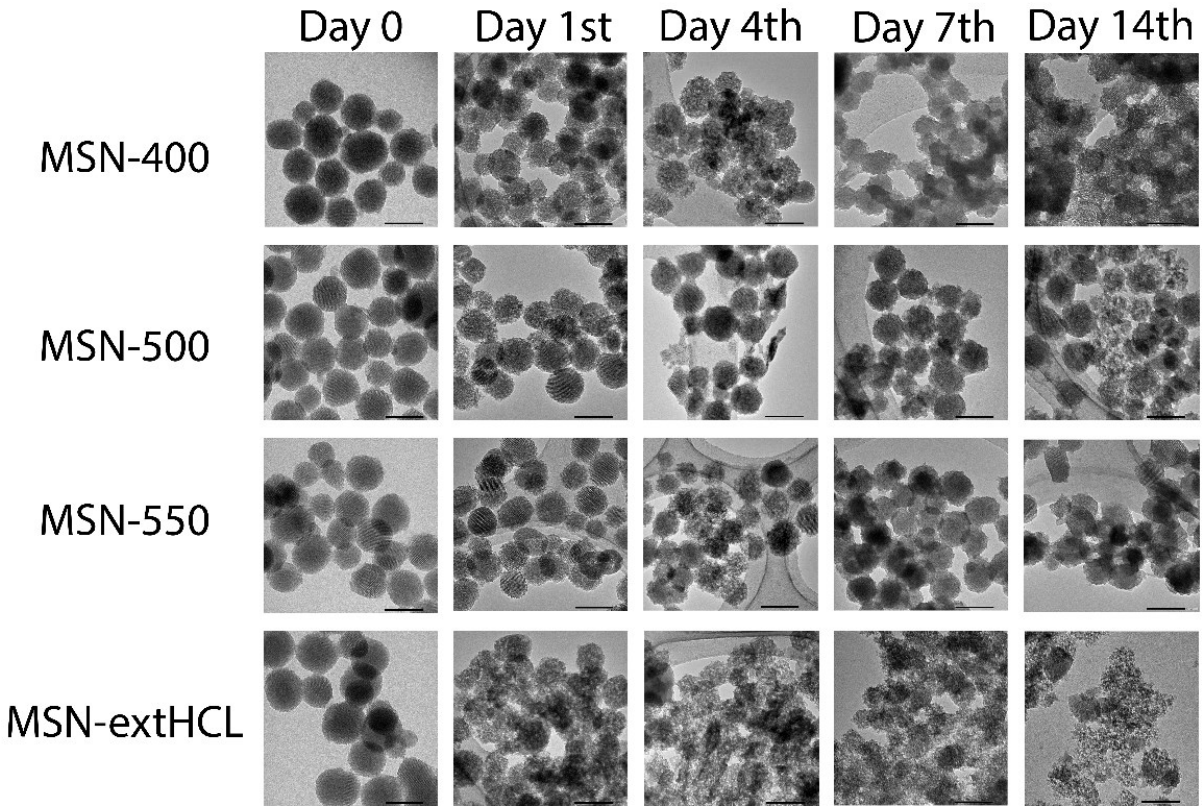


*Figure 10. Biodegradability assay. TEM images of **MSN-400**, **MSN-500**, **MSN-500** and **MSN-extHCl** over time (0, 1, 4, 7 and 14 days). Nanoparticles were prepared at 1 mg/mL concentration in PBS and generously sonicated before start the biodegradation assay. The*

As a consequence of degradation, several processes were observable. First, the nanoparticles surface becomes very rough even from the initial stages. This is provoked by the hydrolysis of silica starting at the surface and progressing towards the centre of the nanoparticle [68]. Consequently, a decrease in the size of the nanoparticles was observed by TEM measurements,

whose average was represented in Figure 11. In this, it can be seen that the nanoparticles size decreases for all samples, even after the first day of assay. In fact, nanoparticles size tends to be degraded faster in the first day and slower after that. This behaviour is compatible with that described by He et al. [67] and other authors [75], in which the degradation is faster during the first hours but then stabilises. The downsizing in **MSN-550** nanoparticles is lower than the one in other samples (from 89 nm to ca. 71 nm after 14 days). In the case of **MSN-500**, the decrease in nanoparticles size is slightly higher, reaching 66 nm at 14 days. On the other hand, a greater size reduction in the case of **MSN-400** and **MSN-extHCl** was observed, but the formation of amorphous and aggregated mass after 1 and 4 days, respectively, difficult to distinguish the nanoparticles, and thus, their measurement.

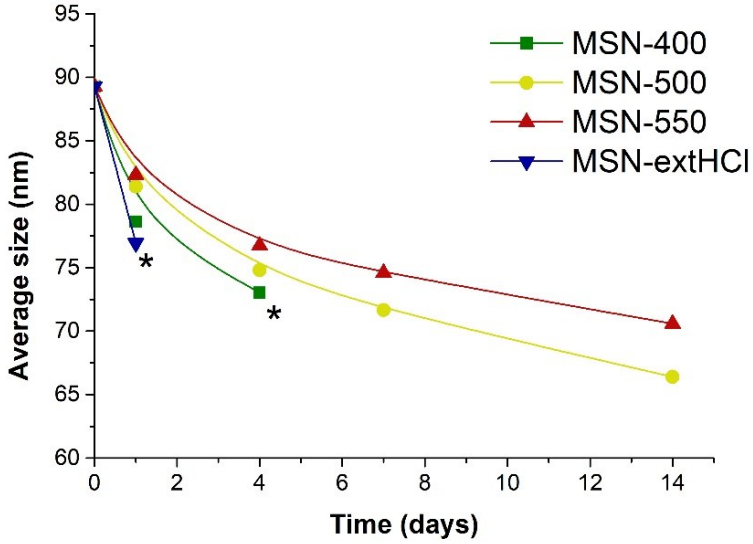


*Figure 11. Biodegradability assay. Evolution of nanoparticles (**MSN-400**, **MSN-500**, **MSN-550** and **MSN-extHCl**) average size over time (0, 1, 4, 7 and 14 days). * From this day the nanoparticles cannot be distinguished properly and their size cannot be measured.*

The size evolution was also monitored by DLS measurements (Figure 12). The data show that size distribution over time did not show a decrease in the mean size, but rather an increase and, more important, a widening of the size distribution curves. This effect has also been observed in other studies [32], and it has been hypothesised to be related to the increase of fusion degree between nanoparticles as the degradation process progresses. In this context, the samples **MSN-550** and **MSN-500** showed less changes in DLS curves over time and less formation of aggregates due to particle fusion. In contrast, **MSN-400** and **MSN-extHCl** showed a shift in their distribution size to larger sizes, due to the formation of a high number of fused clusters of nanoparticles, which were also observed in the TEM images, especially in **MSN-extHCl** material.

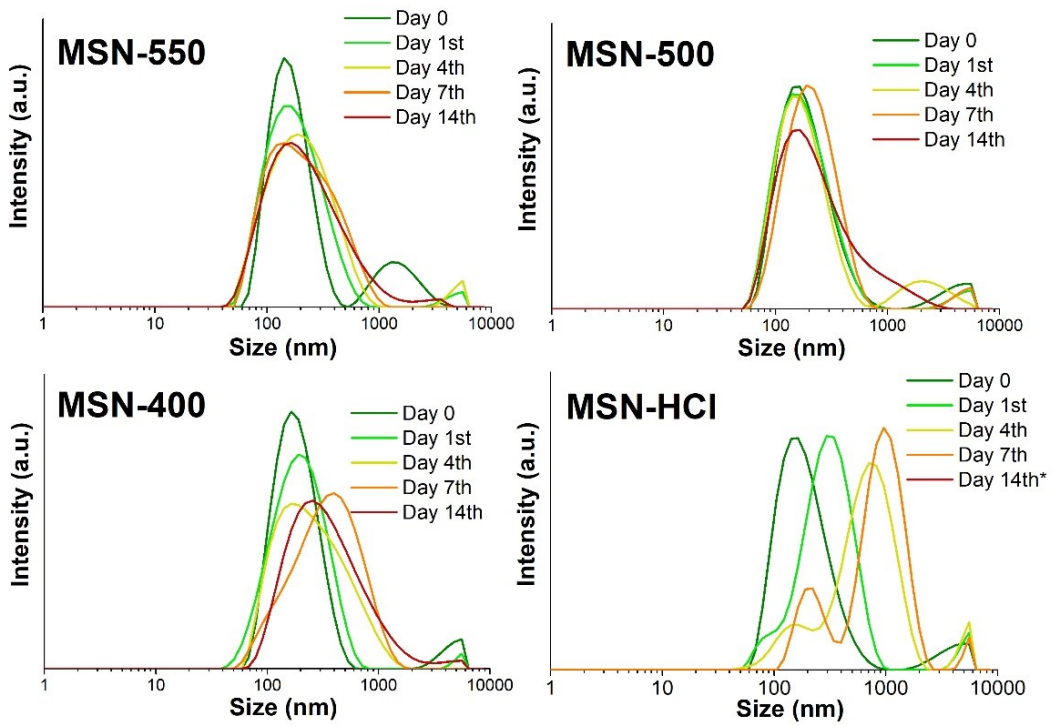


*Figure 12. Biodegradability assay. DLS curves, by Intensity PSD analysis, over time. *The curve of the sample **MSN-extHCl** is not showed since it did not meet the quality criteria due to the high number of large aggregates.*

Regarding the degradation phenomena, Table 4 summarise the qualitative state of each MSN sample over time according to the appearance of nanoparticles, namely, the regularity of shape, the mesostructured silica framework and the formation of fusions between nanoparticles.

*Table 4. Nanoparticles appearance as a function of removal surfactant method over time.*

| SAMPLE | MSN-400 | MSN-500 | MSN-550 | MSN-ExtHCl |
|---|---|---|---|---|
| **Day 0** | ++ | ++ | ++ | ++ |
| **Day 1** | ++ | ++ | ++ | + |
| **Day 4** | + | + | ++ | - |
| **Day 7** | - | + | ++ | - |
| **Day 14** | - | + | + | - |

++ Mostly spherical-shaped MSN, surface distinguishable from each other.

+ Mostly spherical-shaped and highly fused MSN, surfaces not clearly distinguishable from each other.

- Highly aggregated MSN, formation of amorphous mass, difficult to distinguish them.

Another visible phenomenon associated with the nanoparticles degradation was the loss of ordered mesoporosity, which has been widely reported [59][75]. Although changes in the mesoporosity can be analysed by $N_2$ adsorption-desorption isotherms, large amounts of MSN are required for using this technique and therefore, the mesoporous structure was qualitatively analysed and based on the observation of TEM images (Figure 9). According to that, the percentage of nanoparticles which possess visible and ordered mesoporosity (parallel channels

or hexagonally arranged pores) was quantified (Table 5). No results were extracted from samples that form amorphous silica and in which nanoparticles cannot be distinguished (-). The percentage of nanoparticles which presented ordered mesoporosity over time decreases in all the samples. In the extracted sample (**MSN-extHCl**) the process was extremely fast, and only less than 20% of nanoparticles preserve the ordered mesoporosity after the first day. In the following days, the nanoparticles cannot be distinguished from each other. Conversely, calcined samples show great toughness, and the percentages fell slower. The robustness of mesostructure followed the same tendency than that observed throughout the chapter, namely, the higher the calcination temperature, the greater the robustness. In this sense, after two weeks, the percentage of nanoparticles which remains with their ordered mesoporosity is ca. 70% in **MSN-550** and ca. 40% in **MSN-500**. In the case of **MSN-400** this percentage is ca. 60% after 4 only days and, after that, their nanoparticles cannot be distinguished any more.

*Table 5. Percentage of nanoparticles showing ordered mesoporosity over time as a function of the method employed to remove the surfactant.*

| SAMPLE | MSN-400 | MSN-500 | MSN-550 | MSN-ExtHCl |
|---|---|---|---|---|
| **Day 0** | 100% | 100% | 100% | 100% |
| **Day 1** | 87% | 92% | 96% | 17% |
| **Day 4** | 62% | 75% | 84% | - |
| **Day 7** | - | 46% | 81% | - |
| **Day 14** | - | 38% | 73% | - |

According to the results obtained, it can be suggested that both the calcined and the extracted samples showed evidence of degradation at the conditions used. In this vein, the degradation rate was higher as the condensation degree of silica framework was smaller, such as it is observable in **MSN-400** and **MSN-ExtHCl**. Therefore, the degradation rate is correlated with the surfactant removal method and the calcination temperature, being for example, lower in **MSN-500** and **MSN-550**. Furthermore, the degradation process is associated with several effects over the nanoparticles: 1) the nanoparticles surface becomes rough; 2) the nanoparticles size decreases over the days, especially at the beginning during the first day; 3) the nanoparticles are fusing and form aggregated clusters; 4) amorphous silica agglomerates appears and the ordered mesoporosity of remaining nanoparticles decreases. In this sense, we suggest that the fusions, the loss of mesoporositiy and the precipitation of amorhopus silica are provoked because the hydrolysis process is accompanied by condensation reactions that in the absence of the template produces the breakdown of the mesoporous structure [114].

## 6.4. CONCLUSIONS

In this chapter, we present a systematic study of the implications of the surfactant removal method in MCM-41-type MSN. In particular, different calcined and extracted samples are compared, using calcination at different temperatures (400, 450, 500 and 550 °C) and two different mixtures for the extraction of the surfactant (HCl-ethanol and $NH_4NO_3$-ethanol).

The template removal efficiency has been studied by FTIR spectroscopy and TGA curves. In the case of calcination method, we observed that only from 500 °C the surfactant and their coke residues are completely eliminated. Coke residues cannot be identified in FTIR spectra because their main bond is single C-C, although the beige appearance of MSN calcined at 400 and 450 °C suggest their presence. For their part, the extraction method used showed the complete elimination of $CTA^+$ as their associated FTIR bands disappear in extracted samples and their appearance is white. However, in these cases the presence of some organic compound such as ethoxy- groups, in addition to silanol ones, may be present in the extracted samples as some ethoxy-specific bands are distinguishable in FTIR spectra and TGA curves showed a high decrease (greater to 10%) of weight over 400 °C. We presume that these ethoxy- groups are formed mainly during the extraction process by esterification of silanol groups in acidic and ethanolic environment under reflux.

The silica condensation degree, which has been reported to be closely associated with the method employed to remove the surfactant, has also been studied by FTIR spectroscopy, NMR and ELS. All calcined samples significantly increase their silica condensation degree compared with the as-made sample. This can be observed in the decrease the bands associated with Si-OH bonds in the FTIR spectra. Additionally, the increase in condensation and the reduction of silanol groups with calcination temperature and can also be observed in the NMR spectra (DK values9. However, the extracted samples suffer a lesser decrease of this signals in comparison with calcined samples regardless the temperature, and therefore, they show a lower condensation degree of silica, as can be seen by comparing the intensity of the Si-OH bands in FTIR and the DK values. In addition, the calcination consolidates the silica framework, increasing its rigidity to a greater extent than extraction, since Si-O-Si bending vibrations are mainly disturbed in calcined FTIR spectra.

Another parameter that can be correlated with the silica condensation is the ζ potential measured in ELS technic, as this parameter is related with the surface charge of the nanoparticles, which depends, among other things, on the amount of silanol/silanolate in the nanoparticles surface. However, we have not been able to correlate the ζ potential with the calcination temperature as this parameter can also be influenced by the presence of $CTA^+$ residues, such as coke residues, which can counteract the negative charges. In the case of the extraction method, nanoparticles with lower ζ potential were produced due to the absence of $CTA^+$ residues and the high amount of silanol groups on their surface.

The effect over the silica framework was studied by PXRD and $N_2$ absorption-desorption. It has been demonstrated that the surfactant removal is associated with the shrinkage of the silica framework. Calcined samples present a stronger shrinkage than extracted samples, which is observed in the higher unit cell contraction. In this context, conversely to the expected results, the higher shrinkage in calcination process is not provoked by an extra reduction of the pore

size, but a decrease in pore wall thickness in comparison with the extracted solids. Additionally, according to the $FWHM_{100}$ values we can see that calcined samples showed greater disorder of the silica framework.

On the other hand, the specific surface area and pore volume increased with increasing calcination temperature, which suggests the progressive removal of surfactant residues as calcination temperature increases. In the case of extraction, samples with smaller surface area and pore volumes are obtained, which supports the presence of organic compounds, as ethoxy groups, in the surface of the extracted nanoparticles.

Colloidal stability was analysed by measuring the attenuation light of samples when they were spun at different strength pulses. We observed an improved colloidal stability in samples calcined at lower temperatures and in those extracted. This behaviour can be understood as that the gentler removal methods allow an extra negative charge on the MSN due to the presence of a greater quantity of silanol groups, which gives rise to higher repulsive forces that stabilise the nanoparticles in suspension.

The reactivity of nanoparticles surface was studied in TGA curves after the functionalisation of calcined samples with diverse organosilanes, since the degree of functionalisation is supposed to be related with the amount of silanol groups on the nanoparticles surface. First, the functionalisation with APTES was greater than the functionalisation with IPTES, due to horizontal and vertical polymerisation provoked by the alkaline behaviour of the APTES itself. Concerning the reactivity of nanoparticles that have been calcined at different temperatures, two different tendencies were observed. On the one hand, the nanoparticles functionalised with APTES did not show a higher reactivity when calcination temperatures were lower (at 400 or 450 °C). This was explained by the presence of coke residues when nanoparticles are calcined below 500 °C, which can impede the complete functionalisation of the surface. The optimal temperature was found to be 500 °C, when the surface was clean of residues and the amount of silanol groups is still greater than that in the sample calcined at 550 °C. By contrast, the nanoparticles functionalised with IPTES showed a correlation between the reactivity and the calcination temperature. Nevertheless, the differences between the samples are quite small and may be affected by experimental variability.

In addition, the samples were studied regarding their compatibility in biomedical applications. On the one hand, all prepared nanoparticles showed no cytotoxicity in cell cultures, in spite of the presence of coke residues or ethoxy groups. Then, all calcined and extracted samples, including their variations, seemed to be compatible within biomedical context, or at least, in *in vitro* assays. On the other hand, the degradation of prepared samples was studied simulating physiological conditions. Although all studied samples show signs of degradation after 14 days, the degradability is higher for samples calcined at lower temperatures, and especially high in extracted samples. Then, the degradation rate is clearly related to the silica condensation degree. In addition, different phenomena associated with nanoparticles degradation have been stablished, such as the emergence of surface roughness, the nanoparticles size decrease, the fusion between nanoparticles, the formation of aggregated clusters, and the appearing of amorphous silica agglomerates and the decreasing of mesoporosity in remaining nanoparticles.

On account of the performed studies, it can be affirmed that the method employed to remove the surfactant is quite influent on the physicochemical properties of MSN, and therefore, on

their use in the chemical and biomedical field. In this context, we can suggest that the use of calcination method at 500 °C can be better than the standard calcination at 550 °C in terms of functionalisation effectiveness, colloidal stability and biodegradability. In the same vein, the use of extracted samples can be an interesting alternative regarding the same features. Nevertheless, if the concrete application of MSN requires long-term use, higher calcination temperatures can be more suitable considering the longer lifetime which confers the higher silica condensation degree.

## 6.5. REFERENCES


[1] A. Yildirim, M. Turkaydin, B. Garipcan, and M. Bayindir, "Cytotoxicity of multifunctional surfactant containing capped mesoporous silica nanoparticles," *RSC Adv.*, vol. 6, no. 38, pp. 32060–32069, Mar. 2016, doi: 10.1039/C5RA21722A.

[2] Q. He, Z. Zhang, Y. Gao, J. Shi, and Y. Li, "Intracellular Localization and Cytotoxicity of Spherical Mesoporous Silica Nano- and Microparticles," *Small*, vol. 5, no. 23, pp. 2722–2729, Dec. 2009, doi: 10.1002/smll.200900923.

[3] S. P. Hudson, R. F. Padera, R. Langer, and D. S. Kohane, "The biocompatibility of mesoporous silicates," *Biomaterials*, vol. 29, no. 30, pp. 4045–4055, Oct. 2008, doi: 10.1016/j.biomaterials.2008.07.007.

[4] M. Barczak, "Template removal from mesoporous silicas using different methods as a tool for adjusting their properties," *New J. Chem.*, vol. 42, no. 6, pp. 4182–4191, 2018, doi: 10.1039/C7NJ04642A.

[5] A. M. Basso, B. P. Nicola, K. Bernardo-Gusmão, and S. B. C. Pergher, "Tunable effect of the calcination of the silanol groups of KIT-6 and SBA-15 mesoporous materials," *Appl. Sci.*, vol. 10, no. 3, pp. 1–16, 2020, doi: 10.3390/app10030970.

[6] T. Asefa and Z. Tao, "Biocompatibility of Mesoporous Silica Nanoparticles," 2012, doi: 10.1021/tx300166u.

[7] V. Cauda, C. Argyo, D. G. Piercey, and T. Bein, "'Liquid-phase calcination' of colloidal mesoporous silica nanoparticles in high-boiling solvents," *J. Am. Chem. Soc.*, vol. 133, no. 17, pp. 6484–6486, May 2011, doi: 10.1021/ja1067492.

[8] F. Lu, S. H. Wu, Y. Hung, and C. Y. Mou, "Size effect on cell uptake in well-suspended, uniform mesoporous silica nanoparticles," *Small*, vol. 5, no. 12, pp. 1408–1413, Jun. 2009, doi: 10.1002/smll.200900005.

[9] S. H. Wu and H. P. Lin, "Synthesis of mesoporous silica nanoparticles," *Chem. Soc. Rev.*, vol. 42, no. 9, pp. 3862–3875, 2013, doi: 10.1039/c3cs35405a.

[10] I. Mukherjee *et al.*, "Effect of nonsurfactant template content on the particle size and surface area of monodisperse mesoporous silica nanospheres," *Microporous Mesoporous Mater.*, vol. 122, no. 1–3, pp. 168–174, Jun. 2009, doi: 10.1016/j.micromeso.2009.02.030.

[11] M. Barczak, "Template removal from mesoporous silicas using different methods as a tool for adjusting their properties," *New J. Chem.*, vol. 42, no. 6, pp. 4182–4191, 2018, doi: 10.1039/c7nj04642a.

[12] L. Mahoney and R. T. Koodali, "Versatility of Evaporation-Induced Self-Assembly (EISA) method for preparation of mesoporous TiO2 for energy and environmental applications," *Materials*, vol. 7, no. 4. MDPI AG, pp. 2697–2746, 2014, doi: 10.3390/ma7042697.

[13] Q. Cai, Z. S. Luo, W. Q. Pang, Y. W. Fan, X. H. Chen, and F. Z. Cui, "Dilute solution routes to various controllable morphologies of MCM-41 silica with a basic medium," *Chem. Mater.*, vol. 13, no. 2, pp. 258–263, 2001, doi: 10.1021/cm990661z.

[14] M. Varache, I. Bezverkhyy, L. Saviot, F. Bouyer, F. Baras, and F. Bouyer, "Optimization of MCM-41 type silica nanoparticles for biological applications: Control of size and absence of aggregation and cell cytotoxicity," *J. Non. Cryst. Solids*, vol. 408, pp. 87–97,

2015, doi: 10.1016/j.jnoncrysol.2014.10.020.

[15] S. Bhattacharyya, G. Lelong, and M. L. Saboungi, “Recent progress in the synthesis and selected applications of MCM-41: A short review,” *J. Exp. Nanosci.*, vol. 1, no. 3, pp. 375–395, 2006, doi: 10.1080/17458080600812757.

[16] Y. Chen *et al.*, “The complete control for the nanosize of spherical MCM-41,” *J. Nanosci. Nanotechnol.*, vol. 12, no. 9, pp. 7239–7249, 2012, doi: 10.1166/jnn.2012.6459.

[17] P. Khodaee, N. Najmoddin, and S. Shahrad, “The effect of ethanol and temperature on the structural properties of mesoporous silica synthesized by the sol-gel method,” *J. Tissues Mater.*, vol. 1, no. 1, pp. 10–17, 2018, doi: 10.22034/JTM.2018.67254.

[18] R. Kumar, H. T. Chen, J. L. V. Escoto, V. S. Y. Lin, and M. Pruski, “Template removal and thermal stability of organically functionalized mesoporous silica nanoparticles,” *Chem. Mater.*, vol. 18, no. 18, pp. 4319–4327, Sep. 2006, doi: 10.1021/cm060598v.

[19] J. Kecht and T. Bein, “Functionalization of Colloidal Mesoporous Silica by Metalorganic Reagents,” *Langmuir*, vol. 24, no. 24, pp. 14209–14214, Dec. 2008, doi: 10.1021/la802115n.

[20] T. Aumond, L. Pinard, C. Batiot-Dupeyrat, and A. Sachse, “Non-thermal plasma: A fast and efficient template removal approach allowing for new insights to the SBA-15 structure,” *Microporous Mesoporous Mater.*, vol. 296, p. 110015, Apr. 2020, doi: 10.1016/j.micromeso.2020.110015.

[21] E. W. S. J. C. Vartuli, K. D. Schmitt, C. T. Kresge, W. J. Roth, M. E. Leonowicz, S. B. McCullen, S. D. Hellring, J. S. Beck, J. L. Schlenker, D. H. Olson, “Effect of Surfactant / Silica Molar Ratios on the Formation of Mesoporous Molecular Sieves : Inorganic,” *Chem. Mater.*, vol. 6, pp. 2317–2326, 1994, doi: 10.1021/cm00048a018.

[22] S. Lechevallier *et al.*, “Luminescence properties of mesoporous silica nanoparticles encapsulating different europium complexes: Application for biolabelling,” *J. Nanomater.*, vol. 2013, 2013, doi: 10.1155/2013/918369.

[23] K. W. Gallis and C. C. Landry, “Synthesis of MCM-48 by a Phase Transformation Process,” *Chem. Mater.*, vol. 9, no. 10, pp. 2035–2038, 1997, doi: 10.1021/cm970482m.

[24] C. Y. Chen, H. X. Li, and M. E. Davis, “Studies on mesoporous materials. I. Synthesis and characterization of MCM-41,” *Microporous Mater.*, vol. 2, no. 1, pp. 17–26, 1993, doi: 10.1016/0927-6513(93)80058-3.

[25] Q. Huo *et al.*, “Organization of Organic Molecules with Inorganic Molecular Species into Nanocomposite Biphase Arrays*,” 1994. doi: 10.1021/cm00044a016.

[26] Z. Zhang, A. Mayoral, and I. Melián-Cabrera, “Protocol optimization for the mild detemplation of mesoporous silica nanoparticles resulting in enhanced texture and colloidal stability,” *Microporous Mesoporous Mater.*, vol. 220, pp. 110–119, Jan. 2016, doi: 10.1016/j.micromeso.2015.08.026.

[27] A. Lodha *et al.*, “Synthesis of mesoporous silica nanoparticles and drug loading of poorly water soluble drug cyclosporin A,” *J. Pharm. Bioallied Sci.*, vol. 4, no. SUPPL., pp. 92–94, 2012, doi: 10.4103/0975-7406.94153.

[28] S. S. Park, M. H. Jung, Y. S. Lee, J. H. Bae, S. H. Kim, and C. S. Ha, “Functionalised mesoporous silica nanoparticles with excellent cytotoxicity against various cancer cells for pH-responsive and controlled drug delivery,” *Mater. Des.*, vol. 184, p. 108187, 2019,

doi: 10.1016/j.matdes.2019.108187.

[29] M. S. Kim and J. Y. Chang, “Preparation of multifunctional mesoporous silica particles: the use of an amphiphilic silica precursor with latent amine functionality in selective functionalization of the inner surface,” *J. Mater. Chem.*, vol. 21, no. 24, p. 8766, 2011, doi: 10.1039/c1jm10440c.

[30] X. Du, L. Xiong, S. Dai, F. Kleitz, and S. Zhang Qiao, “Intracellular microenvironment-responsive dendrimer-like mesoporous nanohybrids for traceable, effective, and safe gene delivery,” *Adv. Funct. Mater.*, vol. 24, no. 48, pp. 7627–7637, 2014, doi: 10.1002/adfm.201402408.

[31] K. M. L. Taylor, J. S. Kim, W. J. Rieter, H. An, W. Lin, and W. Lin, “Mesoporous Silica Nanospheres as Highly Efficient MRI Contrast Agents,” *J. Am. Chem. Soc.*, vol. 130, no. 7, pp. 2154–2155, Feb. 2008, doi: 10.1021/ja710193c.

[32] L. Yu *et al.*, “Manganese Extraction" Strategy Enables Tumor-Sensitive Biodegradability and Theranostics of Nanoparticles,” *J. Am. Chem. Soc.*, vol. 138, no. 31, pp. 9881–9894, 2016, doi: 10.1021/jacs.6b04299.

[33] N. Lang and A. Tuel, “A fast and efficient ion-exchange procedure to remove surfactant molecules from MCM-41 materials,” *Chem. Mater.*, vol. 16, no. 10, pp. 1961–1966, 2004, doi: 10.1021/cm030633n.

[34] J. Feng, Z. Wang, B. Shen, L. Zhang, X. Yang, and N. He, “Effects of template removal on both morphology of mesoporous silica-coated gold nanorod and its biomedical application,” *RSC Adv.*, vol. 4, no. 54, pp. 28683–28690, 2014, doi: 10.1039/C4RA03122A.

[35] Q. He, J. Shi, F. Chen, M. Zhu, and L. Zhang, “An anticancer drug delivery system based on surfactant-templated mesoporous silica nanoparticles,” *Biomaterials*, vol. 31, no. 12, pp. 3335–3346, Apr. 2010, doi: 10.1016/j.biomaterials.2010.01.015.

[36] K. Möller, J. Kobler, and T. Bein, “Colloidal suspensions of nanometer-sized mesoporous silica,” *Adv. Funct. Mater.*, vol. 17, no. 4, pp. 605–612, Mar. 2007, doi: 10.1002/adfm.200600578.

[37] B. Y. Hung *et al.*, “Utilization of enzyme-immobilized mesoporous silica nanocontainers (IBN-4) in prodrug-activated cancer theranostics,” *Nanomaterials*, vol. 5, no. 4, pp. 2169–2191, Dec. 2015, doi: 10.3390/nano5042169.

[38] F. Catalano and P. P. Pompa, “Design Rules for Mesoporous Silica toward the Nanosize: A Systematic Study,” *ACS Appl. Mater. Interfaces*, vol. 11, no. 50, pp. 47237–47246, 2019, doi: 10.1021/acsami.9b16135.

[39] H. Yamada, C. Urata, E. Yamamoto, S. Higashitamori, Y. Yamauchi, and K. Kuroda, “Effective Use of Alkoxysilanes with Different Hydrolysis Rates for Particle Size Control of Aqueous Colloidal Mesostructured and Mesoporous Silica Nanoparticles by the Seed-Growth Method,” *ChemNanoMat*, vol. 1, no. 3, pp. 194–202, Jul. 2015, doi: 10.1002/cnma.201500010.

[40] H. Yamada, C. Urata, Y. Aoyama, S. Osada, Y. Yamauchi, and K. Kuroda, “Preparation of colloidal mesoporous silica nanoparticles with different diameters and their unique degradation behavior in static aqueous systems,” *Chem. Mater.*, vol. 24, no. 8, pp. 1462–1471, Apr. 2012, doi: 10.1021/cm3001688.

[41] E. Yamamoto and K. Kuroda, *Preparation and Controllability of Mesoporous Silica*

*Nanoparticles*, 1st ed., vol. 44. Elsevier Inc., 2018.

[42] L. S. Wang *et al.*, "Biofunctionalized phospholipid-capped mesoporous silica nanoshuttles for targeted drug delivery: Improved water suspensibility and decreased nonspecific protein binding," *ACS Nano*, vol. 4, no. 8, pp. 4371–4379, 2010, doi: 10.1021/nn901376h.

[43] H. Yamada, H. Ujiie, C. Urata, E. Yamamoto, Y. Yamauchi, and K. Kuroda, "A multifunctional role of trialkylbenzenes for the preparation of aqueous colloidal mesostructured/mesoporous silica nanoparticles with controlled pore size, particle diameter, and morphology," *Nanoscale*, vol. 7, no. 46, pp. 19557–19567, 2015, doi: 10.1039/C5NR04465K.

[44] E. Yamamoto, M. Kitahara, T. Tsumura, and K. Kuroda, "Preparation of size-controlled monodisperse colloidal mesoporous silica nanoparticles and fabrication of colloidal crystals," *Chem. Mater.*, vol. 26, no. 9, pp. 2927–2933, 2014, doi: 10.1021/cm500619p.

[45] C. Urata, Y. Aoyama, A. Tonegawa, Y. Yamauchi, and K. Kuroda, "Dialysis process for the removal of surfactants to form colloidal mesoporous silica nanoparticles," *Chem. Commun.*, no. 34, pp. 5094–5096, Sep. 2009, doi: 10.1039/b908625k.

[46] A. da C. Schneid, C. P. Silveira, F. E. Galdino, L. F. Ferreira, K. Bouchmella, and M. B. Cardoso, "Colloidal Stability and Redispersibility of Mesoporous Silica Nanoparticles in Biological Media," *Langmuir*, vol. 36, no. 39, pp. 11442–11449, Oct. 2020, doi: 10.1021/acs.langmuir.0c01571.

[47] Z. Zhang and I. Melián-Cabrera, "Modifying the hierarchical porosity of SBA-15 via mild-detemplation followed by secondary treatments," *J. Phys. Chem. C*, vol. 118, no. 49, pp. 28689–28698, Dec. 2014, doi: 10.1021/jp5096213.

[48] Z. Kheshti and S. Hassanajili, "Surfactant Removal from Mesoporous Silica Shell of Core-Shell Magnetic Microspheres by," 2017.

[49] Y. Liu, Y. Pan, Z. J. Wang, P. Kuai, and C. J. Liu, "Facile and fast template removal from mesoporous MCM-41 molecular sieve using dielectric-barrier discharge plasma," *Catal. Commun.*, vol. 11, no. 6, pp. 551–554, Feb. 2010, doi: 10.1016/j.catcom.2009.12.017.

[50] V. V. Potapov and L. T. Zhuravlev, "Temperature dependence of the concentration of silanol groups in silica precipitated from a hydrothermal solution," *Glas. Phys. Chem.*, vol. 31, no. 5, pp. 661–670, Sep. 2005, doi: 10.1007/s10720-005-0111-z.

[51] N. Zainuddin, I. Ahmad, H. Kargarzadeh, and S. Ramli, "Hydrophobic kenaf nanocrystalline cellulose for the binding of curcumin," *Carbohydr. Polym.*, vol. 163, pp. 261–269, May 2017, doi: 10.1016/j.carbpol.2017.01.036.

[52] D. Tarn, C. E. Ashley, M. Xue, E. C. Carnes, J. I. Zink, and C. J. Brinker, "Mesoporous Silica Nanoparticle Nanocarriers: Biofunctionality and Biocompatibility," *Acc. Chem. Res.*, vol. 46, no. 3, pp. 792–801, Mar. 2013, doi: 10.1021/ar3000986.

[53] Y.-S. Lin and C. L. Haynes, "Impacts of Mesoporous Silica Nanoparticle Size, Pore Ordering, and Pore Integrity on Hemolytic Activity," *J. Am. Chem. Soc.*, vol. 132, no. 13, pp. 4834–4842, Apr. 2010, doi: 10.1021/ja910846q.

[54] R. Kumar, H.-T. Chen, J. L. V. Escoto, V. S. Y. Lin, and M. Pruski, "Template Removal and Thermal Stability of Organically Functionalized Mesoporous Silica Nanoparticles," *Chem. Mater.*, vol. 18, no. 18, pp. 4319–4327, Sep. 2006, doi: 10.1021/cm060598v.

[55] F. Tang, L. Li, and D. Chen, “Mesoporous silica nanoparticles: Synthesis, biocompatibility and drug delivery,” *Adv. Mater.*, vol. 24, no. 12, pp. 1504–1534, 2012, doi: 10.1002/adma.201104763.

[56] J. G. Croissant, Y. Fatieiev, A. Almalik, and N. M. Khashab, “Mesoporous Silica and Organosilica Nanoparticles: Physical Chemistry, Biosafety, Delivery Strategies, and Biomedical Applications,” *Adv. Healthc. Mater.*, vol. 7, no. 4, pp. 1–75, 2018, doi: 10.1002/adhm.201700831.

[57] W. Ratirotjanakul, T. Suteewong, D. Polpanich, and P. Tangboriboonrat, “Amino acid as a biodegradation accelerator of mesoporous silica nanoparticles,” *Microporous Mesoporous Mater.*, vol. 282, no. November 2018, pp. 243–251, 2019, doi: 10.1016/j.micromeso.2019.02.033.

[58] M. Varache, I. Bezverkhyy, F. Bouyer, R. Chassagnon, F. Baras, and F. Bouyer, “Improving structural stability of water-dispersed MCM-41 silica nanoparticles through post-synthesis pH aging process,” *J. Nanoparticle Res.*, vol. 17, no. 9, 2015, doi: 10.1007/s11051-015-3147-6.

[59] Y. Choi, J. E. Lee, J. H. Lee, J. H. Jeong, and J. Kim, “A Biodegradation Study of SBA-15 Microparticles in Simulated Body Fluid and in Vivo,” *Langmuir*, vol. 31, no. 23, pp. 6457–6462, 2015, doi: 10.1021/acs.langmuir.5b01316.

[60] X. Li, F. Gao, Y. Dong, and X. Li, “Strategies to Regulate the Degradability of Mesoporous Silica-based Nanoparticles for Biomedical Applications,” *Nano*, vol. 14, no. 12, pp. 1–13, 2019, doi: 10.1142/S1793292019300081.

[61] A. Tzur-Balter, Z. Shatsberg, M. Beckerman, E. Segal, and N. Artzi, “Mechanism of erosion of nanostructured porous silicon drug carriers in neoplastic tissues,” *Nat. Commun.*, vol. 6, pp. 1–8, 2015, doi: 10.1038/ncomms7208.

[62] T. T. Hoang Thi, V. Du Cao, T. N. Q. Nguyen, D. T. Hoang, V. C. Ngo, and D. H. Nguyen, “Functionalized mesoporous silica nanoparticles and biomedical applications,” *Mater. Sci. Eng. C*, vol. 99, no. December 2018, pp. 631–656, 2019, doi: 10.1016/j.msec.2019.01.129.

[63] E. B. Ehlerding, F. Chen, and W. Cai, “Biodegradable and renal clearable inorganic nanoparticles,” *Adv. Sci.*, vol. 3, no. 2, pp. 1–8, 2015, doi: 10.1002/advs.201500223.

[64] S. Yang *et al.*, “Tumor-targeted biodegradable multifunctional nanoparticles for cancer theranostics,” *Chem. Eng. J.*, vol. 378, no. July, p. 122171, 2019, doi: 10.1016/j.cej.2019.122171.

[65] L. Li and H. Liu, “Biodegradable inorganic nanoparticles: An opportunity for improved cancer therapy?,” *Nanomedicine*, vol. 12, no. 9, pp. 959–961, 2017, doi: 10.2217/nnm-2017-0057.

[66] J. G. Croissant and C. J. Brinker, *Biodegradable Silica-Based Nanoparticles: Dissolution Kinetics and Selective Bond Cleavage*, 1st ed., vol. 43. Elsevier Inc., 2018.

[67] Q. He, J. Shi, M. Zhu, Y. Chen, and F. Chen, “The three-stage in vitro degradation behavior of mesoporous silica in simulated body fluid,” *Microporous Mesoporous Mater.*, vol. 131, no. 1–3, pp. 314–320, 2010, doi: 10.1016/j.micromeso.2010.01.009.

[68] S. Goel *et al.*, “Engineering Intrinsically Zirconium-89 Radiolabeled Self-Destructing Mesoporous Silica Nanostructures for In Vivo Biodistribution and Tumor Targeting Studies,” *Adv. Sci.*, vol. 3, no. 11, pp. 1–11, 2016, doi: 10.1002/advs.201600122.

[69] D. Shen *et al.*, "Biphase stratification approach to three-dimensional dendritic biodegradable mesoporous silica nanospheres," *Nano Lett.*, vol. 14, no. 2, pp. 923–932, 2014, doi: 10.1021/nl404316v.

[70] K. Möller and T. Bein, "Degradable Drug Carriers: Vanishing Mesoporous Silica Nanoparticles," *Chem. Mater.*, vol. 31, no. 12, pp. 4364–4378, 2019, doi: 10.1021/acs.chemmater.9b00221.

[71] V. Cauda, C. Argyo, D. G. Piercey, and T. Bein, "'Liquid-phase calcination' of colloidal mesoporous silica nanoparticles in high-boiling solvents," *J. Am. Chem. Soc.*, vol. 133, no. 17, pp. 6484–6486, May 2011, doi: 10.1021/ja1067492.

[72] Y. Yang *et al.*, "Hyperbranched Polyglycerol-Induced Porous Silica Nanoparticles as Drug Carriers for Cancer Therapy In Vitro and In Vivo," *ChemistryOpen*, vol. 6, no. 1, pp. 158–164, 2017, doi: 10.1002/open.201600072.

[73] X. Du, F. Kleitz, X. Li, H. Huang, X. Zhang, and S. Z. Qiao, "Disulfide-Bridged Organosilica Frameworks: Designed, Synthesis, Redox-Triggered Biodegradation, and Nanobiomedical Applications," *Adv. Funct. Mater.*, vol. 28, no. 26, 2018, doi: 10.1002/adfm.201707325.

[74] X. Li, L. Zhang, X. Dong, J. Liang, and J. Shi, "Preparation of mesoporous calcium doped silica spheres with narrow size dispersion and their drug loading and degradation behavior," *Microporous Mesoporous Mater.*, vol. 102, no. 1–3, pp. 151–158, 2007, doi: 10.1016/j.micromeso.2006.12.048.

[75] V. Cauda, C. Argyo, and T. Bein, "Impact of different PEGylation patterns on the long-term bio-stability of colloidal mesoporous silica nanoparticles," *J. Mater. Chem.*, vol. 20, no. 39, pp. 8693–8699, Oct. 2010, doi: 10.1039/c0jm01390k.

[76] D. Bhavsar, V. Patel, and K. Sawant, "Systemic investigation of in vitro and in vivo safety, toxicity and degradation of mesoporous silica nanoparticles synthesized using commercial sodium silicate," *Microporous Mesoporous Mater.*, vol. 284, no. January, pp. 343–352, 2019, doi: 10.1016/j.micromeso.2019.04.050.

[77] S. Seré *et al.*, "Altering the Biodegradation of Mesoporous Silica Nanoparticles by Means of Experimental Parameters and Surface Functionalization," *J. Nanomater.*, vol. 2018, 2018, doi: 10.1155/2018/7390618.

[78] J. G. Croissant, Y. Fatieiev, and N. M. Khashab, "Degradability and Clearance of Silicon, Organosilica, Silsesquioxane, Silica Mixed Oxide, and Mesoporous Silica Nanoparticles," *Adv. Mater.*, vol. 29, no. 9, 2017, doi: 10.1002/adma.201604634.

[79] H. Li *et al.*, "Nanotherapy in Joints: Increasing Endogenous Hyaluronan Production by Delivering Hyaluronan Synthase 2," *Adv. Mater.*, vol. 31, no. 46, pp. 1–8, 2019, doi: 10.1002/adma.201904535.

[80] X. Hao *et al.*, "Hybrid Mesoporous Silica-Based Drug Carrier Nanostructures with Improved Degradability by Hydroxyapatite," *ACS Nano*, vol. 9, no. 10, pp. 9614–9625, 2015, doi: 10.1021/nn507485j.

[81] L. Wang, M. Huo, Y. Chen, and J. Shi, "Iron-engineered mesoporous silica nanocatalyst with biodegradable and catalytic framework for tumor-specific therapy," *Biomaterials*, vol. 163, pp. 1–13, 2018, doi: 10.1016/j.biomaterials.2018.02.018.

[82] W. Wu *et al.*, "Enhanced Tumor-Specific Disulfiram Chemotherapy by in Situ Cu2+ Chelation-Initiated Nontoxicity-to-Toxicity Transition," *J. Am. Chem. Soc.*, vol. 141, no.

29, pp. 11531–11539, 2019, doi: 10.1021/jacs.9b03503.

[83] C. G. Liu, Y. H. Han, J. T. Zhang, R. K. Kankala, S. Bin Wang, and A. Z. Chen, “Rerouting engineered metal-dependent shapes of mesoporous silica nanocontainers to biodegradable Janus-type (sphero-ellipsoid) nanoreactors for chemodynamic therapy,” *Chem. Eng. J.*, vol. 370, no. January, pp. 1188–1199, 2019, doi: 10.1016/j.cej.2019.03.272.

[84] X. Wang *et al.*, “Biodegradable Metal Ion-Doped Mesoporous Silica Nanospheres Stimulate Anticancer Th1 Immune Response in Vivo,” *ACS Appl. Mater. Interfaces*, vol. 9, no. 50, pp. 43538–43544, 2017, doi: 10.1021/acsami.7b16118.

[85] E. Bindini *et al.*, “Following in Situ the Degradation of Mesoporous Silica in Biorelevant Conditions: At Last, a Good Comprehension of the Structure Influence,” *ACS Appl. Mater. Interfaces*, vol. 12, no. 12, pp. 13598–13612, 2020, doi: 10.1021/acsami.9b19956.

[86] D. Shao *et al.*, “Bioinspired Diselenide-Bridged Mesoporous Silica Nanoparticles for Dual-Responsive Protein Delivery,” *Adv. Mater.*, vol. 30, no. 29, pp. 1–8, 2018, doi: 10.1002/adma.201801198.

[87] M. Qian *et al.*, “Biodegradable Mesoporous Silica Achieved via Carbon Nanodots-Incorporated Framework Swelling for Debris-Mediated Photothermal Synergistic Immunotherapy,” *Nano Lett.*, vol. 19, no. 12, pp. 8409–8417, 2019, doi: 10.1021/acs.nanolett.9b02448.

[88] H. Yan, X. hu Zhang, J. ming Wu, L. qiao Wei, X. guang Liu, and B. she Xu, “The use of CTAB to improve the crystallinity and dispersibility of ultrafine magnesium hydroxide by hydrothermal route,” *Powder Technol.*, vol. 188, no. 2, pp. 128–132, Dec. 2008, doi: 10.1016/j.powtec.2008.04.024.

[89] S. Hosseini, A. B. Mohamad, A. H. KaHum, and W. R. Wan Daud, “Thermal analysis of CsH2PO4 nanoparticles using surfactants CTAB and F-68,” in *Journal of Thermal Analysis and Calorimetry*, Jan. 2010, vol. 99, no. 1, pp. 197–202, doi: 10.1007/s10973-009-0132-2.

[90] Y. Zhong, S. Chang, and G. Dong, “Preparation and characterization of a novel double-walled Na2(TiO)SiO4 nanotube by hydrothermal process with CTAB as an assistant,” *Microporous Mesoporous Mater.*, vol. 239, pp. 70–77, Feb. 2017, doi: 10.1016/j.micromeso.2016.09.041.

[91] A. M. Alswieleh, A. M. Beagan, B. M. Alsheheri, K. M. Alotaibi, M. D. Alharthi, and M. S. Almeataq, “Hybrid Mesoporous Silica Nanoparticles Grafted with 2-(tert-butylamino)ethyl Methacrylate-b-poly(ethylene Glycol) Methyl Ether Methacrylate Diblock Brushes as Drug Nanocarrier,” *Molecules*, vol. 25, no. 1, p. 195, Jan. 2020, doi: 10.3390/molecules25010195.

[92] G. E. Musso, E. Bottinelli, L. Celi, G. Magnacca, and G. Berlier, “Influence of surface functionalization on the hydrophilic character of mesoporous silica nanoparticles,” *Phys. Chem. Chem. Phys.*, vol. 17, no. 21, pp. 13882–13894, 2015, doi: 10.1039/C5CP00552C.

[93] J. Kobler, K. Möller, and T. Bein, “Colloidal Suspensions of Functionalized Mesoporous Silica Nanoparticles,” *ACS Nano*, vol. 2, no. 4, pp. 791–799, Apr. 2008, doi: 10.1021/nn700008s.

[94] J. Goworek, A. Kierys, W. Gac, A. Borówka, and R. Kusak, “Thermal degradation of CTAB in as-synthesized MCM-41,” *J. Therm. Anal. Calorim.*, vol. 96, no. 2, pp. 375–382, May 2009, doi: 10.1007/s10973-008-9055-6.

[95] R. Saha, R. V. S. Uppaluri, and P. Tiwari, “Effects of interfacial tension, oil layer break time, emulsification and wettability alteration on oil recovery for carbonate reservoirs,” *Colloids Surfaces A Physicochem. Eng. Asp.*, vol. 559, pp. 92–103, Dec. 2018, doi: 10.1016/j.colsurfa.2018.09.045.

[96] U. Nithiyanantham, S. R. Ede, M. F. Ozaydin, H. Liang, A. Rathishkumar, and S. Kundu, “Low temperature, shape-selective formation of Sb2Te3 nanomaterials and their thermoelectric applications,” *RSC Adv.*, vol. 5, no. 109, pp. 89621–89634, Oct. 2015, doi: 10.1039/c5ra17284e.

[97] M. Bera, Chandravati, P. Gupta, and P. K. Maji, “Facile one-pot synthesis of graphene oxide by sonication assisted mechanochemical approach and its surface chemistry,” *J. Nanosci. Nanotechnol.*, vol. 18, no. 2, pp. 902–912, 2018, doi: 10.1166/JNN.2018.14306.

[98] B. Kartick, S. K. Srivastava, and I. Srivastava, “Green synthesis of graphene,” *J. Nanosci. Nanotechnol.*, vol. 13, no. 6, pp. 4320–4324, Jun. 2013, doi: 10.1166/JNN.2013.7461.

[99] F. Kleitz, W. Schmidt, and F. Schüth, “Calcination behavior of different surfactant-templated mesostructured silica materials,” *Microporous Mesoporous Mater.*, vol. 65, no. 1, pp. 1–29, Oct. 2003, doi: 10.1016/S1387-1811(03)00506-7.

[100] T. Peng, D. Zhao, K. Dai, W. Shi, and K. Hirao, “Synthesis of titanium dioxide nanoparticles with mesoporous anatase wall and high photocatalytic activity,” *J. Phys. Chem. B*, vol. 109, no. 11, pp. 4947–4952, Mar. 2005, doi: 10.1021/jp044771r.

[101] G. J. D. A. A. Soler-Illia, A. Louis, and C. Sanchez, “Synthesis and characterization of mesostructured titania-based materials through evaporation-induced self-assembly,” *Chem. Mater.*, vol. 14, no. 2, pp. 750–759, 2002, doi: 10.1021/cm011217a.

[102] Y. Ding, C. Zhao, Y. Li, Z. Ma, and X. Lv, “Effect of calcination temperature on the structure and catalytic performance of the cu-mcm-41 catalysts for the synthesis of dimethyl carbonate,” *Quim. Nova*, vol. 41, no. 10, pp. 1156–1161, Dec. 2018, doi: 10.21577/0100-4042.20170291.

[103] T. Kimura, K. Kuroda, and Y. Sugahara, “Esterification of the Silanol Groups in the Mesoporous Silica Derived from Kanemite,” *J. Porous Mater.*, vol. 5, pp. 127–132, 1998.

[104] P. Riachy *et al.*, “Hybrid Hierarchical Porous Silica Templated in Nanoemulsions for Drug Release,” *Eur. J. Inorg. Chem.*, vol. 2016, no. 13–14, pp. 1989–1997, May 2016, doi: 10.1002/ejic.201501127.

[105] S. C. Feifel and F. Lisdat, “Silica nanoparticles for the layer-by-layer assembly of fully electro-active cytochrome c multilayers,” *J. Nanobiotechnology*, vol. 9, no. 1, p. 59, Dec. 2011, doi: 10.1186/1477-3155-9-59.

[106] S. B. McCullen *et al.*, “A New Family of Mesoporous Molecular Sieves,” in *Access in Nanoporous Materials*, vol. 114, no. 27, 2006, pp. 1–11.

[107] H. B. S. Chan, P. M. Budd, and T. V. De Naylor, “Control of mesostructured silica particle morphology,” *J. Mater. Chem.*, vol. 11, no. 3, pp. 951–957, 2001, doi: 10.1039/b005713o.

[108] A. Stein, B. J. Melde, and R. C. Schroden, “Hybrid inorganic-organic mesoporous

silicates-nanoscopic reactors coming of age," *Adv. Mater.*, vol. 12, no. 19, pp. 1403–1419, 2000, doi: 10.1002/1521-4095(200010)12:19<1403::AID-ADMA1403>3.0.CO;2-X.

[109] F. Lu, S.-H. Wu, Y. Hung, and C.-Y. Mou, "Size Effect on Cell Uptake in Well-Suspended, Uniform Mesoporous Silica Nanoparticles," *Small*, vol. 5, no. 12, pp. 1408–1413, Jun. 2009, doi: 10.1002/smll.200900005.

[110] X. Feng, G. E. Fryxell, L. Q. Wang, A. Y. Kim, J. Liu, and K. M. Kemner, "Functionalized monolayers on ordered mesoporous supports," *Science (80-. ).*, vol. 276, no. 5314, pp. 923–926, 1997, doi: 10.1126/science.276.5314.923.

[111] V. Nairi *et al.*, "Interactions between bovine serum albumin and mesoporous silica nanoparticles functionalized with biopolymers," *Chem. Eng. J.*, vol. 340, pp. 42–50, May 2018, doi: 10.1016/j.cej.2018.01.011.

[112] M. R. B. Paiva *et al.*, "Surface functionalized mesoporous silica nanoparticles for intravitreal application of tacrolimus," *J. Biomater. Appl.*, 2020, doi: 10.1177/0885328220977605.

[113] A. Abdel, M. S. El, and A. O. Abdelhamid, "European Journal of Chemistry," *Eur. J. Chem.*, vol. 3, no. 4, pp. 455–460, 2012, doi: 10.5155/eurjchem.3.3.359.

[114] L. Yu, Y. Chen, H. Lin, W. Du, H. Chen, and J. Shi, "Ultrasmall mesoporous organosilica nanoparticles: Morphology modulations and redox-responsive biodegradability for tumor-specific drug delivery," *Biomaterials*, vol. 161, pp. 292–305, 2018, doi: 10.1016/j.biomaterials.2018.01.046.

# CHAPTER 7: GENERAL CONCLUSIONS

# 7. GENERAL CONCLUSIONS

In the last decade, mesoporous silica nanoparticles have been widely applied to several fields, and particularly, in biomedicine and nanomedicine. This is result of their **unique properties and advantages** such as their simple, low cost, tuneable, environmentally friendly and quick synthesis; their easy and versatile functionalisation; their thermal and psychochemical stability; their high surface area and pore volume capacity for loading active pharmaceutical ingredients; their high uptake capability in vitro and in vivo, and their, in principle, biocompatibility and inertness, etc. Among the MSN developed for biomedical application, the MCM-41-type MSN are one of the most studied and promising materials.

Nevertheless, in spite of the development of a huge number of new biomedical nanodevices, in general, and MSN, in particular, there is a patent **bottleneck in their translation to the clinical use and commercialisation**. The main limitations that nanomaterials find in overcoming the approval requirements for clinical use are those related to manufacturing processes and those related to the complexity of their interaction with the biological organism. Regarding the nanodevices manufacturing, the development of robust manufacturing processes that assure good quality formulations, including stability, size uniformity, well-dispersion, scalability and reproducibility of the final product, is still an unresolved issue, especially in the case of MSN. On the other hand, concerning to the interaction of the nanomaterials with the biological organism, important issues remains unsettled. For example, the undesired tissue accumulation and immunogenicity, the long-term exposure consequences, the escape from the RES, the formation of albumin corona or the targeting to desired location still remain problematic.

Starting from this point, researchers must propose realistic goals, identify the limitations of current nanoparticles and maximising the capabilities of current nanoscopic systems. In other words, they must follow the idea of "**keep it simple**", looking for robustness, and progressing in a stepwise manner. In this context, material science plays an essential role, since it is crucial to understand the synthesis mechanism of nanomaterials, to establish the properties derived from the structure, to design nanodevices rationally and to finely control their physico-chemical properties.

As for **the MCM-41-type MSN** development, their **main weaknesses** in the biomedical context are the achievement of reproducibility in their size, morphology and functionalisation, as well as the obtaining of monodisperse, non-aggregated and biodegradable nanoparticles. The control of these parameters is required to get a suitable biodistribution, to escape from RES, to have good particle–cell interactions and cell uptake, to avoid their accumulation in the organism and to promote their degradation.

Therefore, throughout the current thesis we focused on studying the different weaknesses of MCM-41-type MSN synthesis. Thanks to that, we have obtained a comprehensive knowledge about them and have contributed to solve some of the main obstacles that researches found when are working with this type of nanoparticles.

In Chapter 3, the main objective we set was to **understand mechanism synthesis of MCM-41-type MSN** regarding the silica templating mechanism, as well as nucleation, growth and condensation processes, as the main steps involving in the formation of these nanoparticles.

First, we observed that in the first stages of MCM-41-type MSN formation the silica precursor and CTAB formed micellar complexes larger than the posterior mesostructured micelles. These observations can fit with silica polymerization model and swelling-shrinking model, by which these micelles can act as CTAB repositories meanwhile other mesostructured micelles are forming; or with cooperative assembly model, based on the rearrangement of micelles in presence of increasing amount of silica precursor, which produces smaller mesostructured micelles.

Second, we showed that the nucleation and growth processes are greatly influenced by the silica hydrolysis and condensation rates, and then, a decrease in the hydrolysis rate produces less number of initial seeds that form larger nanoparticles, and vice versa. We demonstrated that the hydrolysis and condensation rate are not only affected by the pH and temperature, as it has been widely studied, but also by the amount of TEOS added, the stirring rate and the TEOS addition rate. This influence is mediated by the following mechanism: the amount of silica available to be hydrolysed acts as limiting step at low concentrations; and low hydrolysis rate acts as limiting step downstream, namely, to the condensation step.

Third, we demonstrated that templating, nucleation and growth occur in the range from seconds to few minutes, observing well-formed nanoparticles from aliquots taken at few seconds from the reaction mixture and obtaining nanoparticles with similar characteristics to the standard ones when aging for 5 minutes.

Fourth, we showed that the aging step is required for consolidating the nanoparticles structure by increasing the percentage of siloxane bonds, and reducing the nanoparticles size dispersion by Ostwald ripening, and it is optimal at 2 hours. This consolidation strengthen the silica framework and minimise the shrinkage produced by calcination step.

In Chapter 4, the main objective was to **study the influence of some disregarded parameters** in the synthesis of MCM-41-type MSN.

First, we have shown and explained that the stirring mechanism and the flow dynamics are correlated with the nucleation, development and growth of nanoparticles. We also observed that stirring rate not only affects to the nanoparticles size, but also shape of nanoparticles or the fusions among them. Additionally, we also observed that the magnetic stirrer bar morphology and their surface, just as stirring set up are greatly influent on this issue.

Second, we studied and explained for the first time the effects of the TEOS addition rate in the nanoparticles formation. This parameter influence on the amount of silica available to be hydrolysed over time, and thus, it not only affects the size of nanoparticles, but also to their homogeneity, since different cycles of nucleation and growth are provoked if low TEOS addition rates are employed, appearing spherical, rod-like and bean-like nanoparticles. We showed the same effect when extremely low stirring rates are used, as the mixing of aqueous and organic phases is extremely slow.

Third, we demonstrated the weakness of the silica framework of the MSN when they are just formed, even after aging for 2 hours. Thus, the processes subsequent to nanoparticles formation, such as the cooling step, the neutralisation process and the separation of the solid

from the reaction media can be quite influent on MSN silica framework. In this sense, the forced neutralisation with HCl provokes a notable shrinkage of the pores.

On account of the studies performed in previous chapters, we shed some light to help to control the MCM-41-type MSN synthesis in order to **obtain more reproducible and tailored nanoparticles**.

In Chapter 5, different objectives were set relative to the obtaining of colloidal MSN.

First, we reviewed critically the reported literature about the obtaining of colloidal MSN suspensions. This review allows us to demonstrate that this issue is still unresolved. In addition, we showed that most of researchers claim to obtain colloidal MSN, but they do not apply a proper methodology to validate it.

Second, taking into account the state or the art, we get **to develop some methodologies to characterise the colloidal stability in MSN**. We compared different methods and presented their pros and cons. We decided to mostly use the measurement of light attenuation when different pulse spins are applied due to their advantages, such as their simplicity, the low time required, the capacity of quantify the percentage of suspended nanoparticles and their reproducibility.

Third, we studied the main **parameters that influence on colloidal stability of MCM-41-type MSN samples**. We observed that tuning the parameters of synthesis can explain some improvement or worsening of colloidal stability, but the main influence is obtained when tuning the sample preparation, the solvent, the nanoparticles concentration, and especially, the nanoparticles functionalisation and PEGylation.

Fourth, we **analysed the principles which govern the colloidal stability in MCM-41-type MSN** and we presented a conceptual and operational framework of MSN suspendability based on the colloidal physics principles, the reported literature and our own experience. In this context, we analyse that normally a MSN preparation are composed by three populations: a) isolated or discrete nanoparticles, b) nanoparticles agglomerated by physical interactions and c) nanoparticles fused by chemical bonds. Besides, we explained the formation of each population, how are influenced by the synthesis and manipulation parameters, and we proposed some tips to reduce the agglomerations and fusions.

In Chapter 6, the main objective was to **study systematically the implications of the use of different surfactant removal procedures in MCM-41-type MSN**. We observed that the method employed to eliminate the template is quite influent on the physicochemical properties of MSN as is listed below:

First, the efficiency in the removal of the template was demonstrated for calcined samples when the calcination temperature was at least 500 °C (finding coke residuals in those samples calcined at lower temperatures). In the case of extracted samples, though the removal of the surfactant was also efficient, we have observed the presence of ethoxy- groups after the extraction procedure, due to esterification of silanol groups.

Second, the silica condensation degree increase considerably in all calcined samples in compared with extracted samples. In the same vein, the silica structure becomes more rigid after calcination and remains more flexible after the solvent extraction.

Third, we demonstrated that independently the temperature used the calcination provokes a great shrinkage of the silica framework, which is much lower when the surfactant is removed by solvent extraction. In addition, we observed that this shrinkage is not provoked by an extra reduction of pore size, but a decrease in pore wall thickness.

Fourth, we observed that the colloidal stability of MSN improves when lower calcination temperature are used or when solvent extraction method is applied. This improvement is mainly mediated by the higher repulsion forces between nanoparticles giving that extra negative charge belonging to silanol/silanolate groups.

Fifth, the reactivity of nanoparticles was demonstrated to be greater when lower calcination temperatures are applied. Nevertheless, this effect can be counteracted for temperatures below 500 °C, because the presence of surfactant residues can disturb a subsequent functionalisation.

Sixth, the compatibility of prepared MSN for biomedical applications was analysed regarding their cytotoxicity and biodegradation. On the one hand, we demonstrated that both calcination (from 400 to 550 °C) and solvent extraction produce non-toxic nanoparticles. On the other hand, we showed that all studied samples presented signs of degradation at few weeks, such as surface roughness, decrease in size, fusion between nanoparticles and appearing of amorphous silica agglomerates. The degradation rate was found to be higher in case of calcining at lower temperatures, and even higher when surfactant was extracted.

On account of the knowledge obtained in the present thesis, we get **to distinguish the main variables and steps that affect to the use of MCM-41-type MSN in biomedical applications, regard their reproducibility, suspendability and biodegradability**. In this context, and as a final conclusion, we can suggest that the best option to obtain MSN oriented toward biomedical applications are the fine control of each step in synthesis and manipulation, following the next recommendations:

a) in the nanoparticles synthesis, to use 500 rpm as stirring rate and a plain and cylindrical magnetic bar, to add the TEOS dropwise at 5 mL $min^{-1}$, to age the nanoparticles for 2 hours;

b) in the surfactant removal, to use calcination method at 500 °C or solvent extraction (both with HCl-ethanol or $NH_4NO_3$-ethanol) in terms of functionalisation effectiveness, colloidal stability and biodegradability; nevertheless, if the concrete application of MSN requires long-term use, to use standard calcination at 550 °C for obtain particles with longer lifetime;

c) in the sample preparation, to sonicate the samples at least 1 hour to remove the higher agglomerates, which is useful in each functionalisation step, to avoid the use of high nanoparticles concentration in step susceptible to aggregate, to avoid the use of aprotic or highly saline solvents to suspend the nanoparticles;

d) in the obtaining colloidal suspension of MSN, to functionalise them with PEG or similar molecules in terms of steric hindrance, to apply spin pulses as a rapid, reproducible, cost-effective, and monitoring-enabled method to remove the higher aggregates.